UNIVERSITY OF GAZİANTEP
GRADUATE SCHOOL OF
NATURAL & APPLIED SCIENCES

CFD MODELLING OF TWO-PHASE PULSATILE TUBULAR FLOWS

A Ph. D. THESIS
IN
MECHANICAL ENGINEERING

BY
FUAT YILMAZ
JANUARY 2011

CFD Modelling of Two-Phase Pulsatile Tubular Flows

A Ph. D. Thesis
in
Mechanical Engineering
University of Gaziantep

Supervisor
Prof. Dr. M. Yaşar GÜNDOĞDU

Assist. Prof. Dr. İhsan KUTLAR
Co-Supervisor

by

Fuat YILMAZ

January 2011

T.C.
UNIVERSITY OF GAZİANTEP
GRADUATE SCHOOL OF
NATURAL & APPLIED SCIENCES
MECHANICAL ENGINEERING DEPARTMENT

Name of the thesis	:	CFD Modelling of Two-Phase Pulsatile Tubular Flows
Name of the student	:	Fuat YILMAZ
Exam date	:	31.01.2011

Approval of the Graduate School of Natural and Applied Sciences.

Prof. Dr. Ramazan KOÇ
Director

I certify that this thesis satisfies all the requirements as a thesis for the degree of Doctor of Philosophy.

Prof. Dr. L. Canan DÜLGER
Head of Department

This is to certify that we have read this thesis and that in our opinion it is fully adequate, in scope and quality, as a thesis for the degree of Doctor of Philosophy.

Assist. Prof. Dr. İhsan KUTLAR
Co-Supervisor

Prof. Dr. M. Yaşar GÜNDOĞDU
Supervisor

Examining Committee Members	signature
Prof. Dr. Kahraman ALBAYRAK	
Prof. Dr. Ali Rıza TEKİN	
Prof. Dr. Melda Ö. ÇARPINLIOĞLU	
Prof. Dr. M. Yaşar GÜNDOĞDU	
Assoc. Prof. Dr. Bahattin KANBER	

ABSTRACT

CFD MODELLING OF TWO-PHASE PULSATILE TUBULAR FLOWS

YILMAZ, Fuat
Ph.D. in Mehanical Engineering
Supervisor: Prof. Dr. M. Yaşar GÜNDOĞDU
Co-Supervisor: Assist. Prof. Dr. İhsan KUTLAR
January 2011, 208 pages

The analysis of pulsatile tubular flow problems is studied by using FLUENT CFD (Computational Fluid Dynamics) software. Modelling and analysis are realized by three main steps:

Firstly, single-phase, Newtonian, intermediate laminar pulsatile flow in rigid pipe flow at different flow conditions is studied for the evaluation of characteristic flow parameters. The computational and experimental data on axial velocity confirm each other except the near-wall region for $0.95<r/R<1.0$ and the central core region for $r/R<0.4$ at all phases of the runs.

Secondly, liquid-liquid, two-phase, non-Newtonian, steady flow is investigated to understand the suitability of various drag models cited in literature and two new drag coefficient correlation models. The Augier, and Rusche and Issa models are found to give the best agreement with experimental measurements.

Finally, two-phase, non-Newtonian, pulsatile blood flow in a geometrically realistic right coronary artery is investigated to assess the influences of three drag models in literature, and one new modified model based on own experimental data of blood flow. The results reveal that the choice of drag models has a critical effect on the prediction of red blood cells' (RBCs) distributions. Schiller and Nauman drag model not including the effects of the presence of neighboring entities estimates RBC distribution differently than the other models. Estimations of liquid-liquid models including Rusche and Issa, and modified drag model based on Cokelet and Jung's et al viscosity correlation is found to be very close to each other. Gidaspow model for solid particles underestimated a little more RBCs distribution than liquid-liquid models.

Key Words: blood flow, two-phase, pulsatile, non-Newtonian, drag, Eulerian multiphase model, coronary artery.

ÖZET

İKİ FAZLI DARBELİ BORUSAL AKIŞLARIN HAD MODELLEMESİ

YILMAZ, Fuat
Doktora Tezi, Makine Müh. Bölümü
Tez Yöneticisi: Prof. Dr. M. Yaşar GÜNDOĞDU
Yardımcı Tez Yöneticisi: Y. Doç. Dr. İhsan KUTLAR
Ocak 2011, 208 sayfa

Bazı darbeli borusal akışların analizi FLUENT hesaplamalı akışkanlar dinamiği (HAD) yazılım programı kullanılarak çalışılmıştır. Modelleme ve analiz çalışmaları üç ana adımda gerçekleştirilmiştir:

İlk olarak; farklı akım şartlarında, tek fazlı, Newton tipi, laminar-darbeli rijit boru akışının ara bölgesindeki hız alanı; hesaplamalı teknikler kullanılarak incelenmiştir. Eksenel hız üzerine hesaplamalı ve deneysel bulgular, duvara yakın bölge (0.95<r/R<1.0) ve merkezi kor bölgesi (r/R<0.4) dışında, birbirlerini bütün çalışma fazlarında doğrulamaktadır.

İkinci olarak; literatürde bulunan farklı sürükleme modelleri ve iki yeni modelin etkisinin anlaşılması için iki fazlı, sıvı-sıvı, Newton tipi olmayan, zamandan bağımsız düzenli akışın analizi yapılmıştır. Deneysel ölçümlerle en iyi uyumu Augier, ve Rusche ve Issa modellerinin sağladığı anlaşılmıştır.

Son olarak, literatürdeki üç sürükleme modeli ve bir yeni modelin etkilerini değerlendirmek için, geometrik olarak gerçekçi bir sağ koroner damarda iki-fazlı, Newton tipi olmayan, darbeli kan akışının analizi yapılmıştır. Sonuçlar, sürükleme modelinin seçiminin kan hücrelerinin dağılımı üzerinde önemli bir etkiye sahip olduğunu ortaya çıkartmıştır. Komşu parçacıkların sürükleme üzerine etkisini içermeyen Schiller ve Nauman sürükleme modeli kan hücrelerinin dağılımını diğer modellerden farklı çıkarmıştır. Rusche ve Issa modeli, ve Cokelet ve Jung vd.'lerinin viskozite korelasyonuna bağlı uyarlanmış sürükleme modelini içeren sıvı-sıvı modellerin hesaplamaları arasında çok iyi bir uyum vardır. Katı parçacıklar için kullanılan Gidaspow modeli kan hücrelerinin dağılımı sıvı-sıvı modellerden biraz daha düşük hesaplamıştır.

Anahtar Kelimeler: kan akışı, iki fazlı akış, darbeli, Newton tipi olmayan, sürükleme, Eulerian çok fazlı model, koroner damar.

ACKNOWLEDGMENTS

I would like to express my sincere gratitude to my supervisor, Prof. Dr. M. Yaşar GÜNDOĞDU, for offering me the opportunity to study on an interesting and popular topic related to human health, and his academic assistance, invaluable guidance, encouragement and advice throughout my Ph. D. study. I would like to thank my co-supervisor Assist. Prof. Dr. İhsan KUTLAR, for kindness, constructive supervision, and valuable advice. I wish to express my appreciation to the members of my thesis committee, Prof. Dr. Kahraman ALBAYRAK, and Prof. Dr. Melda Ö. ÇARPINLIOĞLU for their kindness, help in getting my thesis in the right direction. I look forward to collaborating with them on future research areas and expect continuous support.

Financial support from the Research Fund of the University of Gaziantep in terms of a research project coded as MF.07.06. is gratefully acknowledged. Furthermore, I would like to thank all of educational and technical service staffs of my department for their kind support.

I would like to express my gratitude to Assoc. Prof. Dr. Bahattin KANBER, and Assist. Prof. Dr. Ahmet ERKLİĞ, for their academic assistance. I am also grateful to all of my friends for their encouragement. Additionally, I also wish to thank many other people whose names are not mentioned here. Their help in many other ways is also greatly appreciated.

Special thanks goes to my parents, Mukadder and Mustafa, my brother Suat and everyone in my family whose love and encouragement have supported me throughout my life. Last but not least the warmest thanks from my deep in heart, to my wife Şenay, for her unconditional love, emotional and spiritual support, persistent encouragement and patience, and my children Kerem Emir and Burak Emre. There is no doubt that I would not be where I am today without you.

CONTENTS

LIST OF FIGURES

page

LIST OF TABLES

page

LIST OF SYMBOLS

a_1	evaluated constant parameter of Morsi and Alexander drag coefficient model for different particle Reynolds number
a_2	evaluated constant parameter of Morsi and Alexander drag coefficient model for different particle Reynolds number
a_3	evaluated constant parameter of Morsi and Alexander drag coefficient model for different particle Reynolds number
$a(\dot{\gamma})$	the aggregation rate
A	the equilibrium value of structural parameter which indicates the relative amount of rouleaux in blood
A_1	the first Rivlin-Ericksen Tensor
$A_{aggregation}$	a coefficient (71±2 mPa)
A_c	the cross sectional area of the duct (m)
A_r	velocity amplitude ratio; $\frac{\lvert U_{m,os,1} \rvert}{U_{m,ta}}$
A_t	the value of stress at t=1s
AA	the empirical function in Ishii and Zuber model
$b(\dot{\gamma})$	the disaggregation rate
B	the depth of the duct (m)
$B_{K_{p(t)}}$	the left Cauchy-Green elastic stretch tensor

C	the kinetic rate constant of the structural breakdown of rouleaux into individual erythrocytes induced by shearing
$C_{1\varepsilon}$	the model constants
$C_{2\varepsilon}$	the model constants
$C_{3\varepsilon}$	the model constants
C_D	the drag coefficient
C_{D0}	the drag coefficient of a single spherical drop evaluated from the Schiller and Nauman model
C_f	fibrinogen concentration of plasma in grams per deciliter
C_L	lift coefficient
C_{L0}	the lift coefficient for a spherical bubble evaluated from Legendre and Magnaudet's model
C_{VM}	virtual mass coefficient
C_μ	the model constant
d_r	the mean diameter of the drops of phase r (m)
D	pipe diameter (m)
D_c	diffusivity
D_d	diffusivity
D_{db}	the dimensionless bubble diameter
D_t	the rate of deformation tensor
De	Deborah number
f	the drag function
F	the external forces (N)

$F(D_d)$	the proposed shape factor for the lift coefficient evaluated by using the experimental data
$F(\alpha)$	a function which takes into account the effects arising from the presence of other dispersed elements on the drag coefficient of a single spherical drop
F_L	lift force (N)
F_s	dynamic shape factor
F_{VM}	virtual mass force (N)
g	the gravity (m/s^2)
g_n	the average aggregate destruction rate coefficient
G	the elasticity
$G_{k,c}$	the production of turbulent kinetic energy
HD	hydraulic diameter (m)
I	the unit tensor
I_t	the turbulence intensity at the core of a fully-developed duct flow
k_1	one of the coefficient in Rusche and Issa drag correlations
k_2	one of the coefficient in Rusche and Issa drag correlations
k_b	Boltzmann's constant
k_{dc}	the covariance of the velocities of the continuous phase and the dispersed phase
k_{kh}	one of the empirical constant in Kumar and Hartland model
K_1	one of the empirical constant in Kumar and Hartland model
K_a	the empirical function in Barnea and Mizrahi model
K_b	the empirical function in Barnea and Mizrahi model

K_η	the flux coefficients caused by gradients in the viscosity
K_c	the flux coefficients caused by gradients in the volume fraction
K_{ri} ($=K_{ir}$)	the inter-phase momentum exchange coefficient between the phases
K	the kinetic energy
ℓ	turbulence length scale
L	axial distance (m)
L_g	velocity gradient
$L_{t,c}$	the length scale of the turbulent eddies
m	the order of the structural breakdown reaction
n_i	the empirical power constants(n_i=n, $n_{1, 2, ..}$)
n_{ag}	the average aggregate size
n_{st}	the steady state value of n_{ag} at a given shear rate
N_o	number of red blood cells per unit volume
N_μ	the viscous number
p_E	parameter relating elastic shear modules
p_i	the parameters of models(p_i=p, $p_{1, 2, ..}$)
P_{wp}	the wetted perimeter of the cross section (m)
p_μ	parameter relating viscosity
P	pressure (Pa)
ΔP	pressure difference (Pa)
dP/dx	static pressure gradient (Pa/m)
ΔP /L	approximate static pressure gradient (Pa/m)

P_i	represents an inter-particle pressure as a function of volume fraction of the i-phase.
Q_c	volumetric flow rate of continuous phase (L/s)
Q_d	volumetric flow rate of dispersed phase (L/s)
r	radial distance (m)
$\bar{r}$	the ratio of the distance from tube axis to the radius of the tube
R	pipe radius (m)
R^2	coefficient of determination
R_{ri}	an interaction force between the phase-i and the other phase
Re	particle Reynolds number
Re_G	particle Reynolds number based on the shear rate
Re_{HD}	the Reynolds number based on the hydraulic diameter
Re_m	particle Reynolds number based on the mixture viscosity
Re_{ta}	Reynolds number based on time-averaged value of cross-sectional mean velocity; $\frac{U_{m,ta}D}{\upsilon}$
Re_Ω	particle Reynolds number based on the rotational speed
S	the extra stress tensor
$S_{elastic}$	the contribution to the extra stress due to the erythrocytes
Sr	the dimensionless shear rate
T	temperature (C^o)
T_a	absolute temperature (C^o)
T_c	the characteristic time of the flow
TPMA	the total plasma minus albumin

t	time (s)
t_p	period of oscillation (1/s)
u	velocity or axial velocity (m/s)
u_c	the velocity of continuous phase (m/s)
u_d	the velocity of dispersed phase (m/s)
$\vec{u}_{dr}$	the drift velocity (m/s)
$\vec{u}'_q$	the velocity correction for the q^{th} phase
$\vec{u}^*_q$	the value of $\vec{u}_q$ at the current iteration (m/s)
U_{cl}	centerline velocity (m/s)
U_m	cross-sectional mean velocity (m/s)
$U_{m,ta}$	time-averaged value of cross-sectional mean velocity (m/s)
$\lvert U_{m,os,1} \rvert$	amplitude of oscillatory cross-sectional mean velocity for the fundamental wave in the finite Fourier expansion (m/s)
U_r	the magnitude of relative velocity (m/s)
v	radial velocity (m/s)
w/w	the weight-weight percentage
W	the width of the duct (m)
We	Weissenberg number
x	x direction of cartesian coordinate system (m)
y	y direction of cartesian coordinate system (m)
z	z direction of cartesian coordinate system (m)

Greek Symbols

α	the volumetric concentration
$\alpha_{critical}$	critical hematocrit
α_e	experimental mean dispersed phase volume fraction
α_g	percolation threshold
α_i	the inlet volume fraction of the dispersed phase, $Q_d/(Q_d+Q_c)$
α_{max}	the maximum volume concentration
α_{RBC}	the concentration of red blood cells
α_{WBC}	the concentration of white blood cells
α_w	the dispersed phase concentration at the tube wall
α_o^*	the maximum packing volume fraction around the zero shear rate limit
$\alpha_{\eta_r=100}$	the dispersed phase concentration at which the relative viscosity becomes 100
$\dot{\gamma}$	the shear rate (s^{-1})
$\dot{\gamma}_c$	the characteristic shear rate (s^{-1})
δ	the Kronecker delta
ε	the dissipation rate
ζ_f	a coefficient (independent of shear rate and hematocrit)
η	the apparent viscosity (Pa·s)
$[\eta]$	the intrinsic viscosity
η_{dc}	the ratio between the Lagrangian integral time scale and the characteristic particle relaxation time is written as

θ the angle between the mean particle velocity and the mean relative velocity

θ_r the relaxation time

κ the correction factor

κ_p bulk viscosities for the plasma phase

λ the time constant

Λ_1 the relaxation times

Λ_2 the retardation times

Λ_H the Maxwell relaxation time for a single red blood cell

μ viscosity (Pa·s)

μ_c continuous phase viscosity (Pa·s)

μ_d dispersed phase viscosity (Pa·s)

μ_m mixture viscosity (Pa·s)

μ_p the plasma viscosity (Pa·s)

μ_r the relative viscosity (Pa·s)

μ_o the low shear rate viscosity (Pa·s)

$\mu_{t,c}$ the turbulent viscosity (Pa·s)

μ_∞ the high shear rate viscosity (Pa·s)

ν kinematic viscosity (m^2/s)

Π_{k_c} the term represents the influence of the dispersed phase on the continuous phase

Π_{ε_c} the term represents the influence of the dispersed phase on the continuous phase

ρ	density (kg/m^3)
ρ_{lq}	the phase reference density for the q^{th} phase (defined as the total volume average density of phase q), (kg/m^3)
ρ_0	density at t=0 (kg/m^3)
σ	the Cauchy stress tensor
σ_{dc}	a dispersion Prandtl number
σ_k	the model constant
σ_{st}	the surface tension of the bubble (N/m)
σ_ε	the model constant
τ	the shear stress (Pa)
τ^*	a characteristic shear stress for cluster break-up
$\tau_{F,dc}$	the characteristic particle relaxation time
τ_i	the i-phase stress-strain tensor
τ_r	the particle relaxation time
$\tau_{t,c}$	the characteristic time of the energetic turbulent eddies
$\tau_{t,dc}$	the Lagrangian integral time scale
τ_y	the yield stress (Pa)
φ	a time-dependent structural parameter
φ_e	an equilibrium value of the time-dependent structural parameter
ω	angular frequency of oscillation; ($2\pi / t_p$), (rad/s)
ω_d	the rotational speed of the dispersed particle
ω_v	the vorticity of undisturbed ambient flow at the center of the sphere

$\sqrt{\omega'}$	dimensionless frequency parameter (i.e., Strouhal number, Womersley parameter, Ohmi parameter); $R(\omega/\upsilon)^{1/2}$
$\sqrt{\omega'_q}$	limiting dimensionless frequency between quasi-steady and intermediate regions
$\sqrt{\omega'_t}$	limiting dimensionless frequency between intermediate and inertia dominant regions
Ω	finite shear rate

Subscripts and Others

m	cross sectional mean value
os	oscillatory component due to pulsation
q	any one of the phases
ta	long time-averaged values
1	fundamental wave in the finite Fourier expansion
$\bar{}$	ensemble-averaged value
$=$	tensor
$\rightarrow$	vector
$\angle$	phase angle (^{0})

Abbreviations

AAA	abdominal aortic aneurysm
ALE	the arbitrary Lagrangian Eulerian
ASD	the accelerated Stokesian dynamics method

BEM	the boundary element method
CFD	computational fluid dynamics
DF/FD	direct forcing fictitious domain method
DLM/FD	distributed Lagrange multiplier based fictitious domain method
DSD/SST	deforming spatial domain/stabilized space time method
EIBM	the extended immersed boundary method
EMMS	energy-minimization multi-scale
FCM	the force coupling method
FEM	finite element method
FSI	fluid structure interaction
IB	the immersed boundary
ICM	the immersed continuum method
IFEM	the immersed finite element method
IIM	immersed interface method
LBM	the lattice Boltzmann method
NITA	non-iterative time advancement
PISO	pressure-implicit with splitting of operators
RBC	red blood cell
RCA	right coronary artery
SCAFSI	sequentially coupled arterial fluid structure interaction
WSS	wall shear stress

CHAPTER 1

INTRODUCTION

1.1. Background and Motivation

Nowadays, a critical rate of deaths in developed communities results from cardiovascular diseases, most of which are associated with unusual hemodynamic conditions in arteries. Pulsatile blood flow has been of great interest due to interactions observed between vascular diseases and flow patterns through the circulation. Understanding of blood flow hemodynamics is so great importance in testing the hypothesis of disease formation, assessment and diagnosis of the cardiovascular disease, the development of risk measures on diseases, vascular surgery planning, modeling the transport of drugs through the circulatory systems and determining their local concentrations, designing more efficient cardiovascular equipment or instruments by predicting the performance of them that have not yet been built such as heart valves, stents, probes, etc., and devising better therapies of mainly coronary artery occluding, atherosclerosis, thrombosis, vasculitis or varicose, aneurysms, etc.

Pulsatile pipe flows involve some important difficulties to study them experimentally such as high cost of suitable set-up, excessive amount of flow control parameters, requirement of long-time periods for conducting limited number of experimental cases, etc. The blood flow in a human body is a typical example of pulsatile non-Newtonian multiphase flow in elastic pipes. Experimental studies on blood flow can be sub-divided as in vivo and in vitro studies. In vivo tests on humans and small mammals such as mouse, cat, rabbit, dog and pig are rather limited and only possible by permission of medical ethics commissions because of health risks to patient or animal. In vitro studies carried out in models of blood vessels have also some disadvantages caused by expensive test equipment, intensive labor, excessive number of test runs required for isolating a specific hemodynamic problem, difficulty in availability of realistic flow conditions and unreliable and inadequate medical techniques for complex regions. Medical imaging systems are widely used to display and measure both vessel wall thickness and blood velocities directly in human subjects, but this approach has only been successfully applied to relatively straight vessels due to the limitations such as the implicit assumption of uniform flow. In reality, however, most initiation and progression of vascular diseases occur in complex flow regions. Thus, these regions need more improved measurement techniques for investigation.

Computational methods have widely accepted as a vital means for investigating the blood flow at complex regions. Computational studies, however, include some difficulties such as the mathematical complexity of blood flow dynamics, the requirement of excessive numbers of finite elements to obtain sensitive solutions, and the application of realistic boundary conditions without oversimplifications. Thus, developing an efficient and reliable CFD model for blood flow is a hard task. Moreover, CFD models should be validated by accurately chosen and treated experimental data. For nearly three decades, CFD method has, however, been used by investigators to address blood flow because of their advantage in the simplicity of handling a variety of physiological flow conditions by only changing related initial and boundary conditions as well as the possibility of providing information that is hard or even impossible to measure and also they have the advantage of low cost.

1.2. Objects

The analysis of some pulsatile tubular flow problems is aimed by means of the developed CFD modeling in this thesis. Testing a variety of biological blood flow conditions is obtained by only changing related initial, boundary conditions, and adding different drag models, unsteady velocity profiles and material properties by means of user defined functions in the presented studies. The analysis of biological flow problems by means of a CFD modeling program without using any living human body enable an important contribution to the medicine or biofluid science of field.

The planned CFD model in this study is developed by using FLUENT, one of the popular conventional CFD software packages useful for analyzing dynamic flow problems. All of the study is carried on computer prompt. However some special pulsatile flow cases are analyzed by using the model and the results of analysis are also compared with the corresponding results of selected experimental studies in literature. Using Fluent and Gambit software, modeling and analysis studies are started step by step, up from simplest flow type (single phase, Newtonian, steady flow in rigid pipe) to the most difficult flow type (two-phase, non-Newtonian, pulsatile flow in a geometrically realistic artery). As a result of these test case studies, the CFD model is modified up to evaluating enough level of compatibility between the model results and the experimental results.

Firstly, intermediate laminar pulsatile pipe flow at different flow conditions is investigated for modeling in the evaluation of characteristic flow parameters such as velocity distribution, and pressure. In literature, almost all studies carried by computational methods were based on the assumption of pulsatile flow as single-phase flow. However, if industrial applications such as pneumatic conveying and drainage systems or medical applications related with blood flow are examined, the reality is that these flows include two or more phases. Therefore, our study is mainly directed to determine flow dynamics of two-phase pulsatile tubular flow. Limited number of studies directed to determination of two-phase pulsatile tubular flow dynamics by means of CFD methods have been conducted in literature, especially in the last 5 year. Our study planned to contribute the present literature in some critical points where there are gaps such as non- Newtonian viscosity modeling, the effects of the presence of neighboring entities and red blood cell's geometry and agglomeration on drag, and introduction of elastic boundary conditions. In the case of fulfilling the gaps mentioned, the model evaluated will be very useful for solution of blood flow and industrial two-phase pulsatile tubular flow problems or in design of new medical systems and equipment. Planned two-phase CFD model is prepared by using Fluent software package. The package offers readily the multiphase flow modeling, and accepts special treatments for non- Newtonian fluid models, unsteady inlet condition, and multiphase drag laws by using user defined function (UDF). Gambit software package is used for mesh generation process. Later, the suitability of various drag models cited in literature and two new drag coefficient correlation models is tested in a dense, liquid-liquid dispersed, statistically homogeneous, buoyancy driven, and co-current upward flow inside a vertical square column, as a second test case study.

Finally, a computational methodology developed for simulating two-phase blood flow in a geometrically realistic right coronary artery to obtain a quantitative understanding and characterization of blood flow. The present multiphase CFD models on blood flow have helped to understand the effects of cell structure in blood on the flow dynamics, but some existing deficiencies discussed in literature survey chapter must be remedied in order to reach efficient and reliable models of blood flows. Drag forces acting on blood cells are one of the important deficiencies for the multiphase modeling of blood flow. The present drag force models neglect the effects of the presence of neighboring entities on drag. The drag correlations should so depend on experimental data for a flow with deformable interfaces at high volume fractions. Unfortunately, no data for drag correlation of blood cells are available in the literature, but a general correlation for liquid-liquid systems and liquid-solid system would be useful for understanding the corresponding behavior of RBCs in blood. In order to evaluate proper drag law for a liquid-liquid application, three new drag coefficient correlations based on empirical blood mixture viscosity, Bedeaux's mixture viscosity, and volume average mixture viscosity are also derived and checked through this study.

1.3. Outline of the Thesis

The arrangement of this thesis mainly follows the chronological order of the tasks and has been divided into chapters as follows:

Chapter 2 analyzes and present of viewpoints on critical and commentary analysis on blood rheology, blood viscosity models, physiological flow conditions, drag and lift models recently developed for fluid-solid, fluid-fluid or liquid-liquid two-phase flows. CFD modeling of pulsatile blood flow, virtual mass effect and the effect of red blood cells, RBCs aggregation on CFD modeling of blood flow, and Fluid Structure Interaction (FSI) models are also reviewed to recognize future tendencies in this field. Understanding these basics and their applicability on the computational fluid dynamics is fundamental to meet the need for a sufficient and reliable CFD model of blood. The major gaps on these basics derived from the upcoming investigations provide potential challenging areas for future investigations.

In Chapter 3, velocity field in intermediate region of laminar-pulsatile pipe flow is investigated by using computational techniques. A part of pulsatile flow in human blood vessel is an example of this type of laminar flow. The variations of cross sectional velocity profile and static pressure difference at a test section through 30 different instants of a pulsation cycle are compared with the results of selected experimental measurements by means of a hot-wire anemometer and a pressure transducer for 29 different runs covering the ranges; $2.26\text{x}10^3\pm17\%\leq Re_{ta} \leq4.36\text{x}10^3\pm10\%$, $5.1\pm4\%\leq \sqrt{\omega'} \leq28.0\pm0.05\%$, $0.03\leq A_1 \leq0.71$. Selected four different ones of the experimental runs are analyzed computationally by using the finite-volume based Fluent software-package.

In Chapter 4, a dense, liquid-liquid dispersed, statistically homogeneous, buoyancy driven, and co-current upward flow inside a vertical square column is simulated to investigate the suitability of various drag models cited in literature. A classical Eulerian-Eulerian multiphase model (EMM) with the standard k-ε dispersed turbulence model on the Fluent v6.3.26 platform is used to predict hydrodynamic characteristics of the flow. The distribution of the dispersed phase volume fraction and the velocity profile for each phase are also predicted and then verified by comparing them by the results of different drag models together with experimental data available in literature.

In Chapter 5, the influence of the presence of neighboring entities on drag in blood flow where the dominating mechanisms are expected to be viscous, drag, and gravity forces is investigated in 3-D anatomically realistic right coronary artery. A classical Eulerian multiphase model on the Fluent v6.3.26 platform is used to model pulsatile non-Newtonian blood flow. A new drag model based on the mixture viscosity concept is developed by using the drag similarity criteria. In the literature, drag models based on the mixture viscosity concept is depended on only volume fraction and show Newtonian viscosity effects on drag. However, mixture viscosity depends on the primary independent variables such as the volume fraction and the shear rate in most of the dispersed flow like blood flow. Non-Newtonian drag effects on red blood cell are so calculated with using this new drag dependent on the volume fraction and the shear rate. This drag model depends on experimental viscosity data of human blood in the literature.

In Chapter 6, a summary of concluding remarks over the previous chapters and suggestions for future studies are given.

CHAPTER 2

LITERATURE SURVEY

2.1. Introduction

Pulsatile flows have been investigated as experimentally, theoretically, and computationally with an increasing rate. Experimental and theoretical studies on pulsatile pipe flows since the first quarter of the 20^{th} century were reviewed in great detail (Gundogdu and Carpinlioglu, 1999a), (Gundogdu and Carpinlioglu, 1999b), (Carpinlioglu and Gundogdu, 2001a). Initial studies were generally carried by mathematicians with analytical methods whereas similar studies have recently conducted densely in medicine and engineering fields. In view of these recent studies, new science fields such as bio-fluid mechanics, bioengineering, and biomedical engineering are therefore rather popular nowadays since the important contributions (cf. section 1.1 in Chapter 1) of the understanding of the pulsatile flow hemodynamics.

The arterial blood flow in the human body is typically a multiphase non-Newtonian pulsatile flow in a tapered elastic duct with the terminal side and/or small branches. The pulsatile flow is an unsteady flow in which resultant flow is composed of a mean and a periodically varying time-dependent component. Pulsatile flow is responsible for submissive effect on time-dependent viscoelastic and thixotropy behavior of blood. Studies on blood flow have been commonly performed experimentally and/or computationally. The experimental studies can be sub divided as in vivo and in vitro studies. Studies on in vivo tests on humans and small mammals such as mouse, cat, rabbit, dog and pig are rather limited and only possible by permission of medical ethics commissions because of health risks to patient or animal. In vitro studies carried out in models of blood vessels have also some disadvantages caused by expensive test equipment, intensive labor, excessive number of test runs required for isolating a specific hemodynamic problem, difficulty in availability of realistic flow conditions and unreliable and inadequate medical techniques for complex regions. Medical imaging systems are widely used to display and measure both vessel wall thickness and blood velocities directly in human subjects, but this approach has only been successfully applied to relatively straight vessels due to the limitations such as the implicit assumption of uniform flow (Steinman, 2002), (Steinman and Taylor, 2005). In reality, however, most initiation and progression of vascular diseases occur in complex flow regions. Thus, these regions need more improved techniques for investigation.

Computational methods have widely accepted as a vital means for investigating the blood flow at complex regions. Computational studies, however, include some difficulties such as the mathematical complexity of blood flow dynamics, the requirement for excessive number of finite elements to obtain sensitive solutions, and the application of realistic boundary conditions without simplifications, to be solved. Developing an efficient and reliable CFD model for blood flow is thus a hard task. Moreover, CFD models should be validated by accurately chosen and treated experimental data. For nearly three decades, CFD models have, however, been used by investigators to address blood flow because of their advantage in the simplicity of handling a variety of physiological flow conditions by only changing related initial and boundary conditions as well as the possibility of providing information that is hard or even impossible to measure (Stijnen et al, 2004) and the advantage of low cost. The CFD models have been found to be an efficient and reliable tool due to the development period during the last few decades. It is likely to continue to play an important role in hemodynamic studies.

The significant and continuous improvements in medical imaging systems, computational techniques, and computer hardware and software performances have also brought to reshape of the CFD modeling for blood flow. The CFD modeling of pulsatile blood flow was initially started with using idealized and averaged artery models together with the Newtonian fluid flow assumption. Later models have, however, included the non-Newtonian fluid rheology together with realistic artery geometries. Recent innovative models; namely, the image-based CFD models including blood flow and its arterial wall, and the multiphase CFD models based on Lagrangian and Eulerian approaches with fluid-solid interaction are now being used. The simultaneous and continuous interaction between the blood flow and the vessel wall constitutes a coupled system and plays a critical role in understanding the mechanisms that lead to various complications in the vascular system. Although these models have provided the means to model this interaction in a more physically realistic manner, its mathematical analysis seems far from complete. Computational simulation in an efficient manner is still one of the major computational challenges. On the other hand, most of the present computational studies are based on the assumption of blood flow as a single phase. However, on examination, the reality that the blood flow is multiphase becomes readily evident. Blood consists mainly of a dense suspension of elastic red cells in plasma, and its particulate nature is primarily responsible for its unique macroscopic rheology. In the last decade, several multiphase CFD models have been developed to analyze arterial blood flow and clarify the effect of the dispersed particulate phases.

The performance of CFD models is directly dependent on blood rheology and the local environment of flow medium such as physiological flow conditions, mechanical properties of blood vessels, interactive forces between blood plasma (liquid phase) and blood cells (solid-like phase), etc. The measurement of blood properties under different hemodynamic conditions has therefore gained great importance to obtain proper rheological models for CFD analysis. The studies on blood rheology are reviewed in the present study because it is accepted as an Achilles' heel for understanding the present status of blood flow modeling. After that the studies related with blood viscosity models and physiological flow conditions are also successively discussed to clarify the transfer perspective of the gained erudition from the rheological measurements up to blood CFD models. Details of some hemorheological models are available in the papers of Cho and Kensey (1991) and Zhang and Kuang (2000). This study consolidates the whole provision of current knowledge of limitations in availability of experimental data with rheometer, more recent hemorheological models and relevant data.

The blood flow models have shown critical improvements in last decade as a consequence of new findings especially those on the biomechanical properties of vessel wall structure, vessel wall-blood interaction and blood rheology. Recent studies on blood rheology and multiphase flows have led to the development of much more powerful blood viscosity and drag-lift models for blood cells that include the effects of cell shape, cell concentration, cell aggregation, and internal cell recirculation especially in flow fields of high shear gradient. Biomechanical properties of vessel wall and its interaction with blood flow, in other words integral or local boundary conditions of blood flow, have also been greatly investigated for better understanding of the causes of vascular diseases.

2.2. Blood Composition and Structure

Blood composition and structure play a vital role in blood rheology. Blood consists of a suspension of elastic particulate cells in a liquid known as plasma. Human blood plasma, the continuous phase of blood, is about 91% water, 7% proteins, 2% inorganic solutes, and other organic substances by its weight percentage (Mazumdar, 1998). Potential non-Newtonian properties of plasma were considerable debate until the early 1960 (Zydney et al., 1991), but recent studies have demonstrated that plasma is a Newtonian fluid with a viscosity of about 1.2 mPa·s at 37 °C (Pal, 2003) and its viscosity is a function of temperature (De Gruttola, 2005).

$$\mu_p = \mu_{p=37^\circ C} \exp\left[0.021(37 - T)\right] \tag{2.1}$$

The particulate second phase of blood consists of erythrocytes or red blood cells (RBCs), leukocytes or white blood cells (WBCs), and platelets as shown in Fig. 2.1. RBCs are the predominant cell type of blood and represents cellular volume fraction more than 99% (Picart et al., 1998a). The RBC volume fraction is called as the hematocrit and its normal range is 0.47±0.07 in adult human males and 0.42±0.05

in adult females (Pal, 2003). RBCs have a biconcave discoid shape and their physical properties are given in Table 2.1 (Bronzino, 2006). They consist of a thin elastic membrane enclosing hemoglobin solution that is a Newtonian fluid with a viscosity of about 6 mPa·s (Snabre and Mills, 1996) and this makes it possible for RBC to deform.

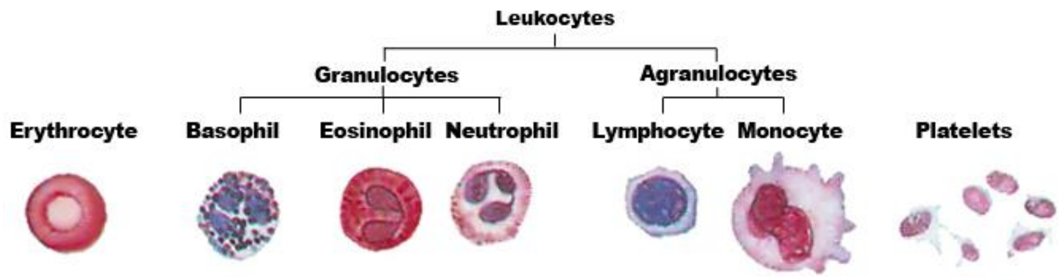

Figure 2.1. Types of blood cells

Table 2.1. The physical properties of RBCs

	Normal Physiologic Range	Typical Value
Diameter (μm)	6-9	7.5
Thickness (μm)	1.84-2.84	-
Neck (μm)	0.81-1.44	-
Surface Area (μm^2)	120-163	140
Volume (μm^3)	80-100	90
Mass Density (g/cm^3)	1.089-1.100	1.098

The aggregatable and deformable nature of the RBCs plays significant roles in blood rheology. RBC aggregation causes a large increase in viscosity at low shear rates. The size of RBC aggregation is a function of RBC concentration and shear rate (Zydney et al., 1991). The existence of aggregation also depends on the presence of fibrinogen and globulin proteins in plasma (Fung, 1993). When shear rate tends to zero, RBCs become one big aggregate, which then behaves like a solid. As the shear rate increases, RBCs aggregates tend to be broken up and the structure becomes a suspension of a cluster of RBCs aggregates in plasma. These aggregates are in turn formed from smaller units called rouleaux as shown in Fig. 2.2 (Fung, 1993). As the shear rate more increases, the average number of RBCs in each rouleaux decreases. If the shear rate is larger than a certain critical value, the rouleaux are broken up into individual cells. At subcritical shear rates, the RBCs in each rouleaux maintain their rest-state equilibrium shape, biconcave discoid shape. If the shear rate is supercritical, the RBCs are dispersed in plasma separately and tend to become elongated and line up with the streamlines (see Kang (2002) for more details). Dynamic equilibrium between cell aggregate size and applied shear stress is shown in Fig. 2.3 (Mazumdar, 1998).

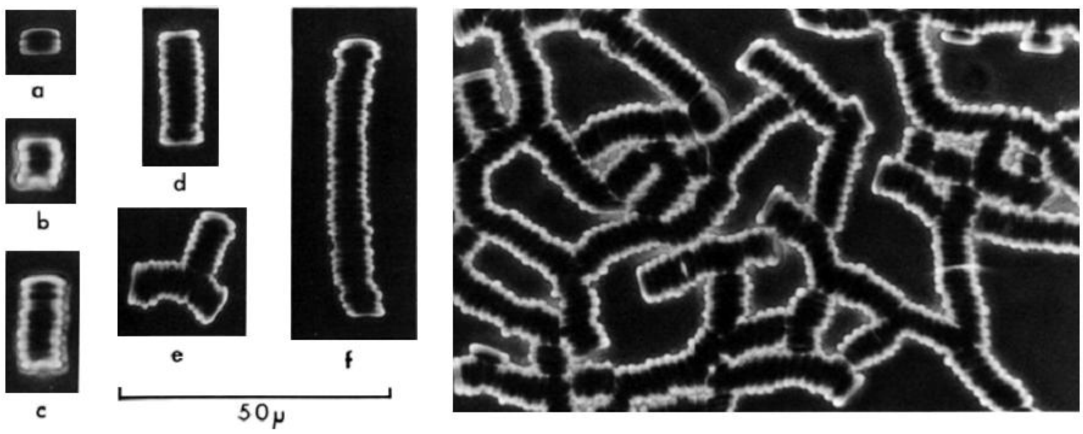

Figure 2.2. Rouleaux of human red cells photographed on a microscope slide showing single linear and branched aggregates (left part) and a network (right part). The number of cells in linear array are 2, 4, 9, 15, and 36 in a, b, c, d, f, respectively (Fung, 1993)

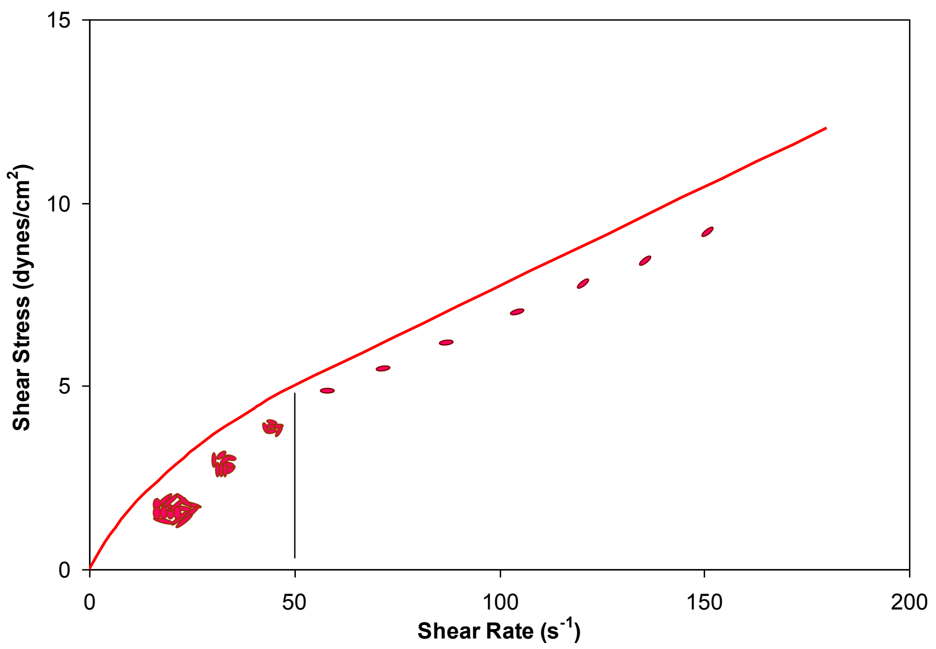

Figure 2.3. Dynamic equilibrium between cell aggregate size and shear stress applied (Mazumdar, 1998)

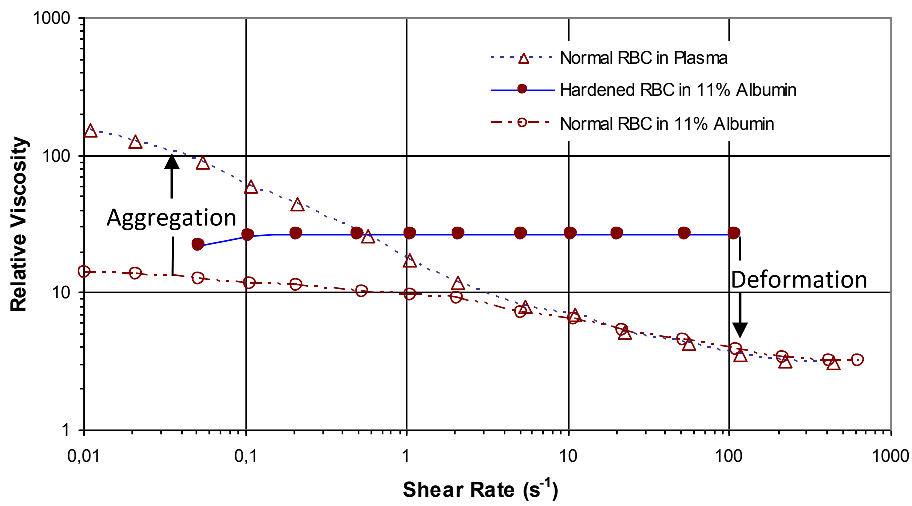

Figure 2.4. Logarithmic relations between relative apparent viscosity and shear rate in three types of RBC suspensions, each containing 45% hemotocrit value (Chien, 1970)

Fig. 2.4 illustrates the mechanisms underlying the non-Newtonian behavior of blood (Chien, 1970). It shows the relationship between relative viscosity and shear rate for three different types of RBCs suspensions namely; RBCs suspended in normal plasma (NP), RBCs suspended in albumin (NA), and hardened RBCs in albumin (HA). The relative viscosity is defined as a ratio of the suspension viscosity to the plasma viscosity. The properties of the RBCs can be altered chemically to isolate certain effects. RBCs were hardened to prevent deformation, and the albumin was used to maintain the normal cell shape. The lack of other proteins in albumin solution prevents the aggregation. In this way, the effect of aggregation and deformation of the RBCs on the blood viscosity were clarified. The difference between the NP and NA curves indicates the effect of cell aggregation, whereas that between NA and HA indicates the effect of cell deformation. Aggregation of red cells at low shear rates leads to increase of viscosity. Red cells elongation and orientation at high shear rates lead to decrease of viscosity further. In addition, the viscosity of the hardened RBC suspension seems independent of shear.

The studies related with RBC behaviors in the microcirculation (Cristini and Kassab, 2005), in the venous (Bishop et al., 2001) and in general (Baskurt and Meiselman, 2003), (Rampling et al., 2004), (Popel and Johnson, 2005) were recently reviewed. The mechanisms of RBC aggregation are figured out by the balance of aggregation and disaggregation force. Disaggregation forces mainly consist of mechanical shear force, repulsive force, and elastic energy of RBC membrane. However, the mechanism of aggregation force is unclear. As mentioned in the review articles and Baumler et al. (1999), the bridging, due to the adsorption of macromolecules onto adjacent cell surfaces, and the depletion, due to the osmotic gradient arising from the exclusion of macromolecules near the cell surface, molecular models are presently used to describe aggregation behaviors. Recently, the aggregation, deformation and dynamic motion of RBCs in shear flow is investigated by hemoreological models capable of modeling the coupled fluid structure interaction. Liu et al. (2004) used a two dimensional modeling technique that couples Navier-Stokes equations with using Morse potential to determine the cell aggregation in the framework of the immersed finite element method. Microscopic mechanism of RBC aggregation is connected to the macroscopic behaviors of the blood, such as the shear rate dependence of blood viscosity (Liu and Liu, 2006). Bagchi et al. (2005) also simulated the RBC aggregation behaviors by using bridging model and front tracking/immersed boundary method for multiple fluids. Cell to plasma viscosity ratio and the shear modules of the cell membrane determine the level of cell deformability and have a significant role on the stability and motion of the aggregate (Bagchi et al., 2005). Dupin et al. (2007) is used lattice Boltzmann method (LBM) and a harmonic spring model to simulate dense suspension of deformable RBCs. RBC deformation is also simulated by Bagchi (2007) with a large ensemble containing about 2500 RBCs. The immersed boundary method to incorporate the fluid membrane interaction has been combined with LBM investigate RBC behaviors considering the RBC membrane mechanics, plasma/cytoplasm viscosity difference, intercellular interaction and the hydrodynamic viscous force (Zhang et al., 2007b), (Zhang et al., 2008).

It can be easily understand from the studies directed on the structure of blood that the blood viscosity is dependent on the physiological flow conditions of blood and the blood composition properties such as hematocrit, temperature, shear rate, cell aggregation, cell shape, cell deformation and orientation. All of these observed dependencies should be formulated and then systematically introduced into some blood viscosity models for use in CFD analysis of blood flow. The review of the present viscosity models discussed in the following sections however showed that; the effects of cell aggregation, cell shape, cell deformation, and cell orientation have not clearly reflected in the viscosity models, although these models considers the effects of hematocrit or cell concentration, shear rate, and temperature. However, numerical studies on RBC behaviors give a hope for transferring available knowledge of microscopic hemodynamic and hemorheological behaviors to a blood viscosity model.

2.3. Blood Viscosity Models

Experimental investigations over many years showed that blood flow exhibits non-Newtonian behavior such as shear thinning, thixotropy, viscoelasticity, and yield stress. Its rheology is influenced by many factors including plasma viscosity (Baskurt and Meiselman, 2003), alignment of RBCs (Baskurt and Meiselman, 1977), level of RBC aggregation and deformability (Chien, 1970), fibrinogen (Chien et al, 1970), flow geometry and size (Thurston and Henderson, 2006), rate of shear, hematocrit, male or female, smoker or non-smoker, temperature, lipid loading, hypocaloric diet, cholesterol level, physical fitness index (Cho and Kensey, 1991), diabetes mellitus, arterial hypertension, sepsis (Meiselman and Baskurt, 2006), etc. The blood viscosity models in literature may however be discussed in two main categories namely; Newtonian viscosity models and non-Newtonian viscosity models.

2.3.1. Newtonian viscosity models

The blood behaves like a Newtonian fluid when shear rate over a limiting value. This apparent limiting viscosity or shear rate is a function of the blood composition, and is primarily modulated by hematocrit (Crowley and Pizziconi, 2005). There have been a variation in the literature on this limiting shear rate as that; 50 s^{-1} (Long et al., 2004), 100 s^{-1} (Chan et al, 2007) or in the range of 100 to 300 s^{-1} (Crowley and Pizziconi, 2005). Due to the high shear rate in large arterial blood vessels (i.e., vessel diameter ≥ 1 mm (Cho and Kensey, 1991)), blood was modeled as a Newtonian fluid in some studies by accepting the viscosity of blood to be constant and equal to the blood viscosity (generally accepted 3.5 mPa·s) corresponding to the high limiting shear rate. However, a considerable amount of attempts has been developed for estimating Newtonian viscosity of whole blood as a function of cell concentration, plasma viscosity, and maximum packing fraction for determining the relative viscosity of dispersed systems as given in Table 2.2.

As can be seen from Table 2.2, concentration dependent Newtonian models can be used to determine hematocrit dependence of the zero, μ_o and infinite, μ_∞ shear viscosity of blood. A wide variety of studies on the concentration dependence mainly extends the well-known study of Einstein on monodisperse dilute rigid spheres.

Table 2.2. Relative viscosity based on concentration dependence of dispersions

$\mu_r = 1 + 2.5\alpha$	(Einstein, 1911)
$\mu_r = 1 + 2.5\alpha + 6.2\alpha^2$	(Batchelor, 1977)
$\mu_r = 1 + 2.5\alpha + 10.05\alpha^2 + 0.00273\exp(16.6\alpha)$	(Thomas, 1965)
$\mu_r = (1.4175 + 5.878\alpha - 15.98\alpha^2 + 31.964\alpha^3)\mu_p$	(Lee and Steinman, 2007)
$\mu_r = [1 - (\alpha/\alpha_{max})]$	(Krieger, 1972)
$\mu_r = [1 - (\alpha/\alpha_{max})]^{-[\eta]\alpha_{max}}$	(Krieger and Dougherty, 1959)
$\mu_r = [1 - (\alpha/\alpha_{max})]^{-2}$	(Maron and Pierce, 1956)
$\mu_r = [1 - (\alpha/p)]^{-2}$	(Kitano et al., 1981)
$\mu_r = [1 - 0.5p\alpha]^{-2}$	(Quemada, 1978a)
$\mu_r = [1 + (1.25\,\alpha / (1 - (\alpha/\alpha_{max})))]^2$	(Eilers, 1941)
$\mu_r = 9/8((\alpha/\alpha_{max})^{1/3}/(1 - (\alpha/\alpha_{max})^{1/3}))$	(Frankel and Acrivos, 1967)
$\mu_r = [1 + 0.75(\alpha/\alpha_{max})/(1 - (\alpha/\alpha_{max}))]^2$	(Chong et al., 1971)
$\mu_r = \exp[2.5\alpha(1 - p\alpha)]$	(Mooney, 1951)
$\mu_r = \exp(p\alpha)$	(Richardson, 1933)
$\mu_r = \exp(p_1\alpha + p_2)$	(Broughton and Squires, 1938)
$\mu_r = \exp[(p\alpha)/(1 - (\alpha/\alpha_{max}))]$	(Krieger, 1972)
$\mu_r = \exp[(p_1 - p_2/\alpha_{max})\alpha]/(1 - (\alpha/\alpha_{max}))^{p_2}$	(Vocadlo, 1976)
$\mu_r = 1/(1 - \alpha^{1/3})$	(Hatschek, 1911)
$\mu_r = 1/(1 - (p\alpha)^{1/3})$	(Sibree, 1931)
$\mu_r = (1 - \alpha)^{-2.5}$	(Brinkman, 1952), (Roscoe, 1952)
$\mu_r = (1 + [(\alpha/\alpha_{\eta_r=100})/(1.187 - (\alpha/\alpha_{\eta_r=100}))])^{2.492}$	(Pal and Rhodes, 1989)
$\mu_r = 1 + 2.5\alpha[([\mu_d/\mu_c] + 0.4)/([\mu_d/\mu_c] + 1)]$	(Taylor, 1932)
$\mu_r = (1 - \alpha([\mu_d/\mu_c] + 0.4)/([\mu_d/\mu_c] + 1))^{-2.5}$	(Dintenfass, 1968)
$\mu_r = (1 + \alpha)/(1 + p\alpha)$	(Jeffery, 1922)
$\mu_r = \exp[4.1\alpha/(1.64 - \alpha)]$	(Vand, 1948)
$\mu_r = (1 - (\alpha/\alpha_{max}))^{-1.82}$ where $\alpha = (\alpha_w/\bar{r})((1 - (\alpha_w/\alpha_{max}))/(1 - (\alpha\ /\alpha_{max})))^{1.82(1-K_\eta/K_c)}$	(Phillips et al., 1992)
$\mu_r = (1 + \alpha(0.5\kappa - 1))/((1 - \kappa\alpha)^2(1 - \alpha))$	(Toda and Furuse, 2006)
$\mu_r = (1 + 1.5\alpha)/(1 - \alpha)$	(Lew, 1969)

In later developments, interactions between particles have been included by adding a quadratic terms in α, and the particle shape effects have been included by using a shape factor or maximum volume fraction, α_{max} in the range from approximately 0.5 to 0.75 even for monodisperse spheres (Barnes et al., 1989). Reformed types of Einstein equation have been used for high concentration. The effect of shear induced particle migration was also appended by using the local particle concentration, α_w (Phillips et al., 1992). Viscosities of dispersed phase, μ_d and continuous phase, μ_c have been included for deformable elastic particles. Some of these models were extended to the non-Newtonian models by taking some model parameters as shear dependent variables (Quemada, 1978a), (Wildemuth and Williams, 1984), (Snabre and Mills, 1996) and by using the differential developing effective medium approach (Pal, 2003).

2.3.2. Non-Newtonian viscosity models

The instantaneous shear rate over a cardiac cycle varies from zero to approximately 1000 s^{-1} in several large arteries (Cho and Kensey, 1991). Therefore, over a cardiac cycle, there are time periods where the blood exhibits shear thinning behavior. In addition to low shear time periods, low shear exists in some regions such as near bifurcations, graft anastomoses, stenoses, and aneurysms (Leondes, 2000). Blood in those regions appears to have non-Newtonian properties. To model the shear thinning properties of blood, a constitutive equation is necessary to define the relationship between viscosity and shear rate. The various non-Newtonian blood models have been used to relate the shear stress and rate of deformation for the blood flow in large arterial vessels. In addition to shear thinning behavior, thixotropic and elastic behaviors of blood have also been taken into account by various researchers. All of these models can be classified into two categories as time independent and time dependent flow behavior models. The constants of the time independent models were obtained by means of parameter fitting on experimental viscosity data obtained at certain shear rates under steady state conditions (Ai and Vafai, 2005), (Ballyk et al., 1994), (Braun and Rosen, 2000), (Cho and Kensey, 1991), (Cosgrove, 2005), (Fung, 1993), (Johnston et al., 2004), (Lee and Steinman, 2007), (Luo and Kuang, 1992), (Malkin, 1994), (Rao, 1999), (Rovedo et al., 1991), (Schramm, 2005), (Steffe, 1996), (Zhang and Kuang, 2000), (Zydney et al., 1991).

At this point it should be noted that; many existing viscosity data of whole blood were taken under assumption of Newtonian flow pattern in the rheometer's measurement field and ignored slip effect. In addition to these criteria, some data have been fitted and used with neglecting the effect between physiologic blood temperature and medium temperature of measurement on CFD studies. All of these assumptions can cause errors. The flow pattern and shear rates of blood in the rheometer are different from a Newtonian fluid. Overestimation of up to 20% in whole blood apparent viscosity has been observed when the shear rate is assumed to be that for a Newtonian flow pattern (Janzen et al., 2000). Therefore, apparent shear rate and viscosity data need corrections. Some correlation methods for blood or Casson fluid like blood have been used in the literature (Janzen et al., 2000), (Joye, 2003), (Zhang and Kuang, 2000), but they need to include the effect of hematocrit or void fraction. Since different flow patterns may be observed at different hematocrit values.

The slip effect is a common feature for all types of two-phase or multiphase systems like blood (Barnes, 1995). It is significant only if the slip layer is sufficiently thick or the viscosity of the slip layer is sufficiently low (Coussot, 2005). Blood has the low viscosity of the continuous phase, the high concentration of the suspensions, and finally, the relative large size of RBCs and its aggregates compared to usual wall roughness. Therefore, significant amount of slip is to be expected for blood under the appropriate conditions. Slipping of RBCs in contact with the wall in vivo and in vitro has been observed in literature (Nubar, 1971). As a result of the shear induced migration of blood cells away from wall boundaries, a cell-rich layer surrounded by a cell-deplated plasma layer at the wall occurs (Phillips et al., 1992). The interface between these layers is a rough surface due to the presence of the RBCs, and the protrusion of blood cells into the plasma layer may give additional energy dissipation (Sharan and Popel, 2001). Narrow marginal layer of plasma has a lower viscosity than the rest of the fluid and serve as a lubricant so that slip occurs. This can cause to an apparent decrease in the shear stress measured with rheometer or viscometer. In practice, in order to mitigate effect of slip, a vane type rheometer, a large enough viscometer gap size, roughening or profiling viscometer walls should be used (Barnes, 1995), (Barnes, 2000). The slip effects and the effects of fibrinogen level and hematocrit on it at low shear rates were studied (Picart et al., 1998a), (Picart et al., 1998b) and found that; migrational and slip effects are more pronounced as shear rate decreased, fibrinogen concentration is raised, and hematocrit is lowered. Aggregation behavior of RBCs at low shear rates and increase of the fibrinogen level could give rise to effective particle size, and lower hematocrit could give rise to the slip layer thickness. As a result, the slip effect can cause to experimental errors on viscosity data of whole blood if not eliminate or taken into account.

Another experimental limitation is that the viscosity models are based on experimental data obtaining the resulting shear stress response to shear rate after an acceptable amount of time has passed to allow rouleaux formation, although the time between consecutive strokes is not sufficiently long for the segregated RBC to reaggregate (O'Callaghan et al., 2006).

2.3.2.1. Time independent viscosity models

All of non-Newtonian time-independent blood viscosity models show shear thinning behavior and must meet the following model requirements. There are three distinct regions for apparent blood viscosity; a lower Newtonian region (low shear rate constant viscosity, μ_o), an upper Newtonian region (high shear rate constant viscosity, μ_∞), and a middle region where the apparent viscosity is decreasing with increasing shear rate, $\partial\mu/\partial\dot{\gamma} < 0$. Power law equation is a suitable model for the middle region. However, it does not describe the low and high shear rate regions. Herschel-Bulkley model extends the power law model to include the yield stress, τ_y. The other models which include yield stress are also shown in Table 2.3. The models that have limitation at low and high shear rates can easily figure out when shear rate in models are taken as zero or infinity. Casson, Walburn-Schneck, and Weaver models include the effect of the RBC concentration, α_{RBC}. Walburn-Schneck model also incorporates fibrinogen and globulins proteins, TPMA. A log-log plot of the apparent blood viscosity as a function of shear rate can be also used to figure out how much is closely matched each model and model parameters with healthy experimental blood viscosity data. The study on 11 viscosity models of Easthope and Brooks (1980) concluded that the Walburn and Schneck model is in well agreement in the shear rate range of 0.03-120 s^{-1}. Sugiura (1988) showed that viscosity model in that shear rate should be Weaver model. Wang and Stoltz (1994) deduced that K-L model provides the well description of hemorheological characteristic in the range of 0.2-180 s^{-1}. Zhang and Kuang (2000) found out that Bi-exponent, K-L and Quemada models can more precisely represent the hemorheological performance. Johnston et al. (2004) concluded that Ballyk model achieved a better approximation of WSS in low shear rate regions. O'Callaghan et al. (2006) showed that 9 viscosity models at high shear rates lead to similar WSS distribution while at lower shear rates they are qualitatively but not quantitatively similar. Case of study conditions (e.g., the flow rate and geometry) must be also considered for determining the shear region under investigation, and then decided the appropriate viscosity model for own studies.

Table 2.3. Time independent non-Newtonian viscosity models

Power Law	$\mu = p\left(\dot{\gamma}\right)^{n-1}$
p=14.67 $mPas^n$ and n=0.7755 (Neofytou and Tsangaris, 2006), p=0.126, n=0.8004 units in cgs system (Buchanan et al., 2000), p=9.267 $mPas^n$ and n=0.828 (Kim et al., 2000), and p=0.035 $mPas^n$ and n=0.6 (Johnston et al., 2004)	
Carreau Model	$\mu = \mu_\infty + \left(\mu_o - \mu_\infty\right)\left[1 + \left(\lambda\dot{\gamma}\right)^2\right]^{(n-1)/2}$
λ=25 s, n=0.25, μ_o=0.025 poise, μ_∞=0.035 poise (Lee and Steinman, 2007), and λ=3.313 s, n=0.3568, μ_o=0.56 poise, μ_∞=0.0345 poise (Johnston et al., 2004)	
Carreau-Yasuda Model	$\mu = \mu_\infty + \left(\mu_o - \mu_\infty\right)\left[1 + \left(\lambda\dot{\gamma}\right)^p\right]^{(n-1)/p}$
λ=1.902 s, n=0.22, p=1.25, μ_o=0.56 poise and μ_∞=0.0345 poise (Cho and Kensey, 1991), λ=0.086s, n=0.681, p=0.222, μ_o=12 mPas and μ_∞=1 mPas (Gijsen et al., 1998), λ=0.438 s, n=0.191, p=0.409, μ_o=51.9 mPas and μ_∞=4.76 mPas (van de Vosse et al., 2003), and λ=0.11s, n=0.392, p=0.644, μ_o=22 mPas and μ_∞=2.2 mPas (Chen et al., 2006a)	

Table 2.3. (Cont.)

Ballyk Model	$\mu = \lambda(\dot{\gamma})\left(\dot{\gamma}\right)^{n(\dot{\gamma})-1}$ where $\lambda\left(\dot{\gamma}\right) = \mu_\infty + \Delta\mu \exp\left[-\left(1+\lvert\dot{\gamma}\rvert/p_1\right)\exp\left(-p_2/\lvert\dot{\gamma}\rvert\right)\right]$ $n\left(\dot{\gamma}\right) = n_\infty - \Delta n \exp\left[-\left(1+\lvert\dot{\gamma}\rvert/p_3\right)\exp\left(-p_4/\lvert\dot{\gamma}\rvert\right)\right]$
μ_∞=0.0345, n_∞=1, $\Delta\mu$=0.25, Δn=0.45, p_1=50, p_2=3, p_3=50 and p_4=4 (Johnston et al., 2004), and μ_∞=0.035 poise, n_∞=1, $\Delta\mu$=0.25, Δn=0.45, p_1=35.36, p_2=2.12, p_3=35.36 and p_4=2.83 (Lee and Steinman, 2007)	
Casson Model	$\mu = \left[\left(\eta^2 J_2\right)^{1/4} + 2^{-1/2}\tau_y^{1/2}\right]^2 J_2^{-1/2}$
$\lvert\dot{\gamma}\rvert = 2\sqrt{J_2}$, τ_y=0.1(0.625α_{RBC})^3, η=μ_o(1- α_{RBC})$^{-2.5}$, μ_o=0.012 poise and α_{RBC}=0.37 (Fung, 1993)	
The Herschel Bulkley Model	$\mu = p(\dot{\gamma})^{n-1} + \left(\tau_y/\dot{\gamma}\right)$
p=8.9721 mPa·s^n, n=0.8601, τ_y=0.0175 N/m^2 (Valencia et al., 2006)	
Walburn-Schneck Model	$\mu = p_1 e^{p_2\alpha_{RBC}}\left[e^{p_4\left(TPMA/\alpha_{RBC}^{\;2}\right)}\right]\left(\dot{\gamma}\right)^{-p_3\alpha_{RBC}}$
p_1=0.00797, p_2=0.0608, p_3=0.00499 p_4=14.585 1g^{-1}, α_{RBC}=40% and TPMA=25.9 g l^{-1} (Johnston et al., 2004)	
Powell-Eyring Model	$\mu = \mu_\infty + \left(\mu_o - \mu_\infty\right)(\mathrm{Sinh}^{-1}\lambda\dot{\gamma})/(\lambda\dot{\gamma})$
λ=5.383 s, μ_o=0.56 poise and μ_∞=0.0345 poise (Cho and Kensey, 1991)	
Modified Powell-Eyring Model	$\mu = \mu_\infty + \left(\mu_o - \mu_\infty\right)\ln\left(\lambda\dot{\gamma}+1\right)/\left[\lambda\dot{\gamma}\right]^n$
λ=2.415 s, n=1.089, μ_o=0.56 poise and μ_∞=0.0345 poise (Cho and Kensey, 1991)	
Cross Model	$\mu = \mu_\infty + \left(\mu_o - \mu_\infty\right)/\left(1+\left(\lambda\dot{\gamma}\right)^n\right)$
λ=1.007 s, n=1.028, μ_o=0.56 poise and μ_∞=0.0345 poise (Cho and Kensey, 1991)	
Modified Cross Model	$\mu = \mu_\infty + \left(\mu_o - \mu_\infty\right)/\left[1+\left(\lambda\dot{\gamma}\right)^n\right]^p$
λ=8.2 s, n=0.64, p=1.23, μ_o=0.16 Pas and μ_∞=0.0035 Pas (Abraham et al., 2005), and λ=3.736 s, n=2.406, p=0.254, μ_o=0.56 and μ_∞=0.0345 poise (Cho and Kensey, 1991)	

Table 2.3. (Cont.)

Simplified Cross Model	$\mu = \mu_\infty + (\mu_o - \mu_\infty)/\left(1 + \lambda \dot{\gamma}\right)$
λ=8.0 s, μ_o=1.3 poise and μ_∞=0.05 poise (Cho and Kensey, 1991)	
Quemada Model	$\mu = \left(\sqrt{\mu_\infty} + \left(\sqrt{\tau_y}/\left(\sqrt{\lambda} + \sqrt{\dot{\gamma}}\right)\right)\right)$
μ_∞=0.02982 dyn s/cm^2, τ_y=0.2876 dyn/cm^2, λ=4.02 s^{-1} (Buchanan et al., 2003), and μ_∞=0.02654, τ_y=0.04360, λ=0.02181 units in cgs system (Buchanan et al., 2000)	
K-L Model	$\tau = \tau_y + \mu_p\left(p_1 \dot{\gamma} + p_2\sqrt{\dot{\gamma}}\right)$
Wang Model	$\tau = \mu_p\left(p_1 \dot{\gamma} + p_2\sqrt{\dot{\gamma}}\right)$
Weaver Model	$\log\mu = \log\mu_p + (0.03 - 0.0076\log\gamma)\alpha_{RBC}$
Bi-Exponent Model	$\mu = p_1 + p_2\exp\left(-\sqrt{p_3\gamma}\right) + p_4\exp\left(-\sqrt{p_5\gamma}\right)$
Ellis Model	$\tau = \dot{\gamma}/\left[(1/\mu_o) + p(\tau)^{(1/n)-1}\right]$
Sisko Model	$\mu = (\mu_\infty + p\dot{\gamma}^{n-1})$
Mizrahi-Berk Model	$\tau^{0.5} - \tau_y^{0.5} = p\dot{\gamma}^n$
Ofoli Model	$\tau^{n_1} = \tau_y^{n_1} + \mu_\infty\left(\dot{\gamma}\right)^{n_2}$
Vocadlo Model	$\tau = \left[(\tau_y)^{1/n} + p\dot{\gamma}\right]^n$
Power Series Model	$\dot{\gamma} = p_1\tau + p_2(\tau)^3 + p_3(\tau)^5 + \ldots$
Van Wazer Model	$\mu = (\mu_o - \mu_\infty)/\left(1 + p_1\dot{\gamma} + p_2\left(\dot{\gamma}\right)^n\right) + \mu_\infty$
Reiner-Philippoff Model	$\tau = \left(\mu_\infty + (\mu_o - \mu_\infty)/\left(1 + \left((\tau)^2/p\right)\right)\right)\dot{\gamma}$
Heinz-Casson Model	$\tau^n = \tau_y^n + k\dot{\gamma}^n$
Robertson-Stiff Model	$\tau = p_1\left(p_2 + \dot{\gamma}\right)^n$
Vinogradov-Malkin Model	$\mu = \mu_o/\left(1 + p_1\dot{\gamma}^n + p_2\dot{\gamma}^{2n}\right)$
Kreiger Model	$\mu = \mu_\infty + (\mu_o - \mu_\infty)/(1 + p^n)$
Prandtl-Eyring Model	$\mu = \mu_o\left(\sinh^{-1}(\lambda\dot{\gamma})/(\lambda\dot{\gamma})\right)$
Hyperbolic Tangent Model	$\mu = \mu_\infty + (\mu_o - \mu_\infty)\tanh(\lambda\dot{\gamma})^n$

2.3.2.2. Time dependent viscosity models

Time-dependent models are used to describe thixotropic and viscoelastic behavior. Thixotropy is a special condition of pseudo plasticity with or without yield stress, where the apparent viscosity also decreases when the fluid is subjected to a constant shear rate. Blood is a concentrated suspension of cells. Most of concentrated suspension system exhibits thixotropic behavior. Experimental results of whole human blood have demonstrated that blood is a thixotropic fluid to be expected (Chen et al., 1991), (Huang et al., 1987a), (Huang et al., 1987b), (Thurston, 1979). The hematocrit, gender and age are factors affecting the blood thixotropy (Chen et al., 1991), (Huang et al., 1987b). Huang developed a generalized rheological equation for thixotropic fluids. Huang model parameters were calculated from experimental data by non-linear parameter estimation technique for apparently healthy human subjects (Huang et al., 1987a). Some thixotropic models are given in Table 2.4.

Table 2.4. Time dependent thixotropic models

Huang Model	$\tau - \tau_y = \mu \dot{\gamma} + CA\dot{\gamma}^m \exp(-C\int_o^t \dot{\gamma}^m dt)$	(Huang et al., 1987a)
Weltman Model	$\tau = A_t - p\log t$	(Rao, 1999)
Tiu-Boger Model	$\tau = \varphi\tau_y + \varphi p\left(\dot{\gamma}\right)^n$ $\frac{d\varphi}{dt} = -p_1(\varphi - \varphi_e)^2$	(Rao, 1999)
Rosen Model	$\mu = p\left(\dot{\gamma}\right)^{n_1}(t)^{n_2}$	(Braun and Rosen, 2000)

In literature, viscous models obtained at steady state conditions were used under pulsatile flow conditions. These models have provided a great deal of insight into the non-Newtonian viscous behavior of blood. However, blood exhibits both viscous and elastic properties under pulsatile flow (Thurston, 1972), (Thurston, 1979). Viscosity is an assessment of the rate of energy dissipation due to cell deformation and sliding, while elasticity is an assessment of the elastic storage of energy primarily due to kinetic deformability of the RBCs (Thurston et al., 2004). There are two dimensionless numbers to measure of the tendency of a material to appear either viscous or elastic; the Deborah number and the Weissenberg number. The Deborah number is the ratio of the relaxation time to the characteristic time of the flow.

$$De = \theta_r / T_c \tag{2.2}$$

The relaxation time can be defined as a ratio of the viscosity to the elasticity;

$$\theta_r = \mu / G \tag{2.3}$$

Three ranges of Deborah number are identified as that; if De<<1, the material is viscous, if De~1, the material will act viscoelastically, and if De>>1, the material is elastic (Steffe, 1996). The Weissenberg number is defined as the ratio of the characteristic time of fluid to a characteristic convective time-scale of the flow or the characteristic shear rate times the relaxation time.

$$We = \theta_r \dot{\gamma}_c \tag{2.4}$$

If the values of De and We are above a critical value, usually in the order of one, the elastic properties of the blood have to be taken into account (Gijsen et al., 1999b). The most appropriate choice of relaxation time of the RBCs is 0.06 s and the characteristic time of the flow is equal to the period time of the physiological flow pulse (Gijsen et al., 1999b).

Blood is slightly viscoelastic, and its effect was ignored in most of the CFD studies. At low shear rates, RBCs aggregate are solid-like bodies, and has ability to store elastic energy. Its value remains constant for shear rates up to 1 s^{-1} (Thurston, 1979). At high shear rates, its effect is less prominent because the RBCs behave fluid-like bodies (Schmid-Schönbein and Wells, 1969), and lose this ability (Anand and Rajagopal, 2004). Viscoelastic models can be suitable for blood flow under certain flow conditions especially at low shear stress. It also grows in importance when flow is oscillatory (Rojas, 2007). The extra stress tensor is used to characterize the viscoelastic stress in viscoelastic models. The total stress tensor (Cauchy stress tensor) is defined in terms of the pressure (P) and the extra stress tensor (S).

$$\sigma = -PI + S \tag{2.5}$$

Some of the extra stress tensors of these models are given below. There are common definitions in the models.

$$D_t = 0.5\left(L_g + L_g^T\right) \tag{2.6}$$

The symbol $\overset{\nabla}{(.)}$ denotes the upper convected derivative.

$$\overset{\nabla}{A} = \frac{\partial A}{\partial t} + u \cdot \nabla A - (\nabla u)^T \cdot A - A(\nabla u) \tag{2.7}$$

(i) Oldroyd-B Model:

$$S + \Lambda_1 \overset{\nabla}{S} = \mu\left(D_t + \Lambda_2 \overset{\nabla}{D_t}\right) \tag{2.8}$$

(ii) Yeleswarapu Model (Yeleswarapu et al., 1998):

$$S + \Lambda_1\left[\dot{S} - L_g S - S L_g^T\right] = \mu(A_1)[A_1] + \Lambda_2\left[\dot{A}_1 - L_g A_1 - A_1 L_g^T\right] \tag{2.9}$$

$$\mu(A_1) = \mu_\infty + (\mu_o - \mu_\infty)\left[\frac{1 + \ln(1 + \eta\dot{\gamma})}{(1 + \eta\dot{\gamma})}\right] \tag{2.10}$$

$$\dot{\gamma} = \left[\frac{1}{2}\mathrm{tr}\left(A_1^2\right)\right]^{\frac{1}{2}} \tag{2.11}$$

where $A_1 = L + L^T$ is the first Rivlin-Ericksen Tensor, the dot indicates the material derivative. This model is a generalized Oldroyd-B model.

(iii) Generalized Oldroyd-B Model (Rajagopal and Srinivasa, 2000):

$$S = p_E B_{K_{p(t)}} + p_\mu D_t \tag{2.12}$$

$$S + \frac{p_\mu}{2p_E}\overset{\nabla}{S} = \eta_1\left(D_t + \frac{p_\mu}{2p_E}\overset{\nabla}{D}_t\right) + p_E \psi I \tag{2.13}$$

$$\psi = 3 \big/ \mathrm{tr}(B_{K_{p(t)}}^{-1}) \tag{2.14}$$

(iv) Generalized Maxwell Model (Rajagopal and Srinivasa, 2000):

$$S = p_E B_{K_{p(t)}} \tag{2.15}$$

$$\overset{\nabla}{B}_{K_{p(t)}} = -2\frac{p_E}{p_\mu}\left(B_{K_{p(t)}} - \psi I\right) \tag{2.16}$$

(v) Generalized Oldroyd-B Model (Anand and Rajagopal, 2004):

$$S = p_E B_{K_{p(t)}} + p_\mu D_t \tag{2.17}$$

$$\overset{\nabla}{B}_{K_{p(t)}} = -2\left(\frac{p_E}{p}\right)^{1+2n}\left(\mathrm{tr}\left(B_{K_{p(t)}}\right) - 3\psi\right)^n \left[B_{K_{p(t)}} - \psi I\right] \tag{2.18}$$

$$n = (\gamma - 1)/(1 - 2\gamma); \quad n > 0 \tag{2.19}$$

All of the Rajagopal models have a thermodynamic basis and generalized Oldroyd-B models of Rajogopal are not capable of an instantaneous elastic response.

(vi) Generalized Maxwell Model (Owens, 2006):

This model is based on homogenous flow assumption and derived from a simple structure dependent generalized Maxwell type constitutive equation for the elastic stress and identified the average aggregation size as a suitable structure variable.

$$S = \mu_p D_t + S_{elastic} \tag{2.20}$$

where $S_{elastic}$ represents the contribution to the extra stress due to the erythrocytes.

$$S_{elastic} + \Lambda_1\left(\dot{S}_{elastic} - \nabla u \cdot S_{elastic} - S_{elastic} \cdot \nabla u^T\right) = N_o k_B T_a \Lambda_1 D_t \tag{2.21}$$

$$\Lambda_1 = n_{ag}\Lambda_H \Big/ \left(1 + g_n n_{ag} \Lambda_H\right) \tag{2.22}$$

$$\frac{\partial n_{ag}}{\partial t} = -\frac{1}{2} b\left(\dot{\gamma}\right)\left(n_{ag} - n_{st}\right)\left(n_{ag} + n_{st} - 1\right) \tag{2.23}$$

$$n_{st} = \frac{\mu_o}{\mu_\infty}\left(\frac{1 + p_1 \dot{\gamma}^n}{1 + p_2 \dot{\gamma}^n}\right)\left(1 + \frac{3}{2} a\left(\dot{\gamma}\right) N_o \Lambda_H\right) \tag{2.24}$$

$$b\left(\dot{\gamma}\right) = a\left(\dot{\gamma}\right) N_o \Big/ \left(n_{st}\left(n_{st} - 1\right)\right) \tag{2.25}$$

Huang model is useful at a specific range of 0.1-10 s^{-1} (the range of blood thixotropy). Yeleswarapu model has the relaxation times, independent of shear rate as a limitation. Anand and Rajagopal (2004) determined that the best fit with experimental data for both steady and oscillatory flow is obtained with their model than Yeleswarapu and generalized Oldroyd-B models. Owens model neglect the difference between the RBC number densities across the cross section.

2.3.3. Yield stress of blood

The yield stress of blood can be taken into account in the regions of low shear rates like thixotropic and viscoelastic behavior of blood. It can supply better understanding of aggregation and deformation of blood cells. The relation of cell deformation and aggregation with yield stress was described as (Zydney et al., 1991);

$$\tau_y = \tau_{aggregation} + \zeta_f \cdot \tau_{deformation} \tag{2.26}$$

where ζ_f is a coefficient (independent of shear rate and hemotocrit) characterizing the relative contributions of these two properties. All of data in Zydney's study were obtained with stored blood. However, they were in relatively good agreement with the data obtained by fresh whole blood and suspensions of fresh RBCs. The effect of cell aggregation was described as

$$\tau_{aggregation} = A_{aggregation}(\alpha_{RBC} - 0.05)^3,\ \alpha_{RBC} \geq 0.05 \tag{2.27}$$

$$\tau_{aggregation} = 0,\ \alpha_{RBC} < 0.05 \tag{2.28}$$

where $A_{aggregation}$ is a coefficient (71±2 mPa). The effect of cell deformation was assumed to be of the form;

$$\tau_{deformation} = A_{deformation}(\alpha_{RBC} - 0.35)^3,\ \alpha_{RBC} \geq 0.35 \tag{2.29}$$

$$\tau_{deformation} = 0,\ \alpha_{RBC} < 0.35 \tag{2.30}$$

The experimental data fitted f with a deviation range of 0±0.06. This showed insignificant effect of deformation on yield stress, and aggregation effect alone provided an accurate description of yield stress. Its dependence for 0.53 to 0.95 hemotocrit ranges is given in (Picart et al., 1998a);

$$\tau_y = 26.87 \cdot \alpha_{RBC}^3 \tag{2.31}$$

There is no yield stress below a critical hemotocrit value (1-5%) (Merrill et al., 1963) and the yield stress is (Luo and Kuang, 1992);

$$\tau_y = 0 \qquad \alpha_{RBC} < \alpha_{critical} \tag{2.32}$$

$$\tau_y = 0.08(\alpha_{RBC} - \alpha_{critical})^3 \qquad \alpha_{RBC} \geq \alpha_{critical} \tag{2.33}$$

where $\alpha_{critical}$ is critical hematocrit in the range of 5-8% (Luo and Kuang, 1992) and the unit of τ_y is yield stress in pascal. The yield stress as a function of hematocrit and fibrinogen concentration is given by (Arjomandi et al., 2003);

$$\sqrt{\tau_y} = (\alpha_{RBC} - 0.1)(C_f + 0.5) \tag{2.34}$$

and with a coefficient of determination (r^2) 0.87 (Morris et al., 1989);

$$\sqrt{\tau_y} = -0.091 + 0.47 \cdot \alpha_{RBC} + 0.22 \cdot C_f - 0.14 \cdot C_f^2 + 0.48 \cdot \alpha_{RBC} \cdot C_f \tag{2.35}$$

The yield stress of aggregated RBC suspensions is given as (Snabre and Mills, 1996);

$$\tau_y = \tau^* \left(\frac{\varepsilon_o^*}{\varepsilon_{RBC}} - 1 \right)^{-2} \qquad \text{for } \alpha > \alpha_g \tag{2.36}$$

Accurately and functionally representing of blood behaviors in the viscosity models and the local hemodynamic environment are very important and increases performance of a CFD model. Therefore, there is a need for a viscosity model based on the internal structures of blood. Additionally, there are some cautions in the evaluation of accurate experimental data for blood constitutive parameters. The local environment strongly impacts the local flow patterns and hence shear rate. Expressing of accurate environment is therefore possibly essential. However, assumptions on the physiological conditions are mandatory.

2.4. Physiological Conditions

The cyclic nature of the heart pump creates pulsatile conditions in arteries, and therefore blood flow and pressure are unsteady. The pulsations of flow are damped in the small vessels, and the flow is so effectively steady in the capillaries and the veins. The arteries are not rigid tubes. It adapts to varying flow and pressure conditions by enlarging or shrinking. All of these physiologic conditions and others cause difficulties to render simulations both conceptually and computationally tractable. As a result, most CFD models of arterial hemodynamics need to make the simplifying assumptions of rigid walls, steady flow, fully developed inlet velocities, Newtonian rheology, normal and periodic flow conditions, ignoring of small side or terminal branches, using of idealized or averaged artery models, and using of in vitro experiments to validate CFD models (Steinman, 2002), (Steinman, 2004), (Steinman and Taylor, 2005). No vessel movement resulting from organ movement such as coronary arteries movement resulting from heartbeat is also possible to add these assumptions. The advantages, limitation and accuracy of the medical imaging systems used for the construction of 3D vessel geometry model were also pinned down by Steinman (2002), Steinman (2004), and Steinman and Taylor (2005).

2.5. Analogy of Single- and Multi-Phase Modeling

A great number of single phase CFD models have been proposed to meet the requirements for blood flow in the last few decades. The cell suspended structure of whole blood was ignored and it was simplified as a continuous viscous fluid. For a single phase flow, general conservation equations for mass and momentum can be respectively given as:

$$\frac{\partial \rho}{\partial t} + \nabla \cdot (\rho u) = 0 \tag{2.37}$$

$$\frac{\partial (\rho u)}{\partial t} + \nabla \cdot (\rho u u) = -\nabla P + \nabla \cdot \tau + \rho g + F \tag{2.38}$$

where ρ is the density, u is the velocity in axial direction, t is the time, P is the pressure, g is the gravity, F represents external forces, and τ is the extra shear stress tensor defined as:

$$\tau=\mu\frac{du}{dy} \tag{2.39}$$

where μ is the viscosity of blood. For a Newtonian fluid model, μ is constant and independent of the shear rate. In the case of a non-Newtonian fluid model, μ is a function of shear rate and the shear thinning behavior of blood must also be considered. Viscoelastic models can also be used to describe the elastic behavior of blood as well as its viscous behavior. However, the extra stress tensor includes an elastic stress tensor.

Above a critical shear stress, whole blood has been modeled as a dense mono-dispersion of immiscible and deformable liquid droplets enclosed with an elastic membrane in a Newtonian liquid. However, mono-dispersed structure of red blood cells, RBCs, changes to multi-dispersed structure if the shear rate decreases. The flows in the large arteries such as aorta might be treated as single-phase flow of a Newtonian fluid to obtain satisfactory results. This assumption however fails to explain the blood flow behaviors depending particular nature of blood such as Fåhraeus–Lindqvist effect, cell-free or cell-depleted layer near the wall, blunt velocity profile, phase separation effect at vessel bifurcations, particulate buildup, mass transfer to vessel, especially while flowing through small diameter vessels (2400-8 μm (Srivastava and Srivastava, 1983)). Experimental and theoretical studies (Haynes, 1960), (Cokelet, 1972) indicated that particulate effect of blood should be figured out in small size vessel (the diameter less than 1000μm). Cell-free or cell-depleted layer near the wall and a cell-rich core are experimentally observed by many investigators for blood flowing through small vessels (Bugliarello and Sevilla, 1970), (Cokelet, 1972), (Thurston, 1989). Haynes (1960) and Bugliarello and Sevilla (1970) have studied theoretically and experimentally the two-fluid models or a two-layered model treating the fluid in the core region different from the fluid in the peripheral layer for blood flow. In fact, the two-fluid model was firstly proposed by Vand (1948) for general suspensions. Sharan and Popel (2001) suggested that the viscosity in the cell-free layer is different from that of plasma due to the additional energy dissipation caused by the protrusion of red blood cells into the layer. Besides other factors, it is also function of the thickness of the cell-free layer and the core hematocrit. Sharan and Popel (2001) computed the thickness of the cell-free layer and found to be in agreement with the studies of Bugliarello and Sevilla (1970) and Reinke et al. (1987). Wang and Bassingthwaighte (2003) applied the two-layered models to blood flow in small curved tubes and found that curvature in general lowers the tube resistance, but increases the shear stress near the inside wall. In the light of the studies mentioned just above on two-fluid modeling, several researchers have studied treating the fluid in the peripheral layer as a single-phase Newtonian and the fluid in the core region as a non-Newtonian fluid such as Casson, Herschel-Bulkley, power law (Shukla et al., 1980a), (Shukla et al., 1980b), (Pralhad and Schultz, 1988), (Nair et al. 1989), (Srivastava and Saxena, 1994), (Srivastava, 1996), (Sankar and Lee, 2007). Additionally, not only particular effect on viscosity but also interaction of drag is incorporated by some investigators (Srivastava et al, 1994), (Srivastava, 1995), (Srivastava, 1996), (Chaturani and Bharatiya, 2001), (Srivastava, 2007), (Srivastava and Srivastava, 2009). Unfortunately, the studies for drag and lift forces acting on mono-dispersed blood cells or rouleaux are very limited in literature. Therefore, the drag and lift models developed for deformable and mobile interface particles such as droplets in a gas-liquid system and bubbles in a liquid-gas system would be very useful for understanding the corresponding behavior of RBCs in blood. The particular loading of RBCs (i.e., the ratio of RBC mass to the plasma mass) is approximately equal to one and represents an intermediate loading case. The phase coupling is so two-way, meaning that there is a mutual effect between the flows of plasma and blood cells. Coupling can take place through mass, momentum, and energy transfer between phases. Otherwise, the particular loading of white blood cells, WBCs, and platelets is less than 1 means that is very low loading case. The coupling between the WBCs or platelets and plasma is so one-way. The plasma carrier influences these types of cells via drag and turbulence, but the WBCs or platelets have no influence on the plasma. However, the continued collisions and hydrodynamic interactions with RBCs results in persistent lateral motion of platelets and WBCs (Kleinstreuer, 2006). There is no mass transfer between plasma and blood cells. Other side, the mass transfer to small diameter branches vessel respect to modeling vessel is generally ignored. Although the blood and the vessel wall continuously exchange substances, the effect of mass transfer from the blood to the vessel tissues is also generally disregarded and mass coupling could be treated as no coupling. Current studies results that blood flow coupled with mass transfer under the effect of hemodynamic parameter are the keys to understand atherosclerosis and as a result the importance of mass transfer at the near wall regions becomes apparent (Chakravarty and Sen, 2005), (Soulis et al, 2008). Momentum coupling is the result of interaction forces, such as drag, lift, virtual mass, and magnus lift forces between the blood cells and plasma phase. The particle response time of blood cells is in the order of 10^{-6} s. Thus, particle Stokes number is less than 1 means that cell and plasma velocity is so close each other. Therefore, RBC velocity approaches the plasma velocity and then particle Reynolds number decrease. As a result of multiphase analysis of blood flow, coupling of RBC with plasma is significant and their effects on each other cannot be ignored. Blood is a single-phase multi-component flow in actual, but for practical purposes it can be treated as a two-phase flow. In recent years, two-phase CFD models have been used to clarify the effects of cell dispersed blood structure on hemodynamic flow conditions. Dispersed flows have been modeled by using either the Lagrangian or the Eulerian approaches in literature. The Lagrangian approach was commonly applied for blood flow to study aggregation and deposition patterns of critical corpuscles such as monocytes and platelets, which play significant roles in arterial disease progression (Buchanan et al, 2000), (Hyun et al, 2000a), (Hyun et al, 2000b), (Hyun et al, 2001), (Longest and Kleinstreuer, 2003), (Buchanan et al, 2003), (Longest et al, 2004), (Longest et al, 2005). The effects of the dominant particle phase RBC on cell aggregation and deposition were commonly neglected or limited with a constant dispersion coefficient valid especially in the region of low shear stress. In healthy men, the average number of red blood cells per cubic millimeter is 5,200,000 (± 300,000); in healthy women, it is 4,700,000 (± 300,000) (Guyton and Hall, 2006). However, this model is limited to sufficiently low volume fractions and relatively small numbers of blood cells (Jung et al, 2006a). The Lagrangian approach is so impractical to use for such dense suspensions of RBC because of the heavy computational work, and time.

In recent years, Jung et al. (2006a), Jung et al, (2006b), Jung and Hassanein (2008), and Srivastava and Srivastava (2009) used two-fluid model and an Eulerian-Eulerian model to better analyze the dense suspensions of blood flow. The main difference between the Eulerian and the single-phase models is the appearance of the volume fraction for each phase in the conservation equations as well as with coupling among phases by using the mechanisms for the exchange of momentum, heat, and mass. In order to solve the conservation equations for hemodynamics, appropriate rheological properties of each phase must be specified. Eulerian-Eulerian multiphase model can be classified as mixture or heterogeneous mixture models. Heterogeneous mixture models like Eulerian and granular models are especially used for modeling the blood flow. An extension of the SIMPLE algorithm (the phase coupled SIMPLE (PC-SIMPLE) algorithm) is used for the pressure-velocity coupling through these models. Because of the volume occupied by one phase cannot be occupied by other phases, the concept of phasic volume fraction is introduced. In addition, the volume fraction is assumed to be a continuous function of space and time and their sum must be equal to one:

$$\alpha_{\text{plasma}} + \alpha_{\text{RBC}} + \alpha_{\text{WBC}} + \alpha_{\text{platelets}} = 1 \tag{2.40}$$

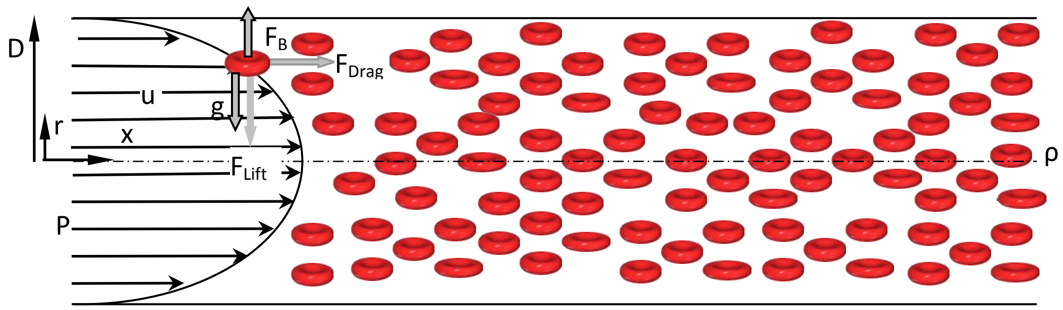

Figure 2.5. A schematic representation of two-phase blood flow

In the multiphase, non-Newtonian hemodynamic models, the continuous phase is plasma which contains water, proteins, organic and inorganic substances. The predominant dispersed (particulate) phase in the plasma is RBC at hematocrits of 37–54% in human. Leukocytes or white blood cells (WBC) and platelets occupy a total volume fraction less than one percent in blood and therefore exercise a much smaller effect than RBC on blood rheology. As a result, whole blood flow can be considered as a two-phase flow and shown schematically in Fig. 2.5.

However, multiphase modeling has been used to understand the distribution and effects of the other cells. A general mass balance by the convective mass fluxes without inter-phase mass transfer and mass source for each phase such as plasma, RBC, WBC and platelets is given by:

$$\frac{\partial(\rho_i \alpha_i)}{\partial t} + \nabla \cdot (\rho_i \alpha_i u_i) = 0 \tag{2.41}$$

where i represents any one of the phases, ρ is the density, α is the volumetric fraction, t is the time, and u is the velocity. The momentum balance equation for each phase is given by:

$$\frac{\partial(\rho_i \alpha_i u_i)}{\partial t} + \nabla \cdot (\rho_i \alpha_i u_i u_i) = -\alpha_i \nabla P + \nabla \cdot \tau_i + \alpha_i \rho_i g + \sum_{r=1}^{n} R_{ri} + F_i \tag{2.42}$$

where P is the pressure shared by all phases, τ_i is the i-phase stress-strain tensor, g is the gravity force, and F represents the external forces such as virtual mass, rotational and shear lift, electrical and magnetic forces. R_{ri} is an interaction force between the phase-i and the other phase or phases. In the Newtonian form, the stress-strain tensor for the plasma phase is given as follows:

$$\tau = \alpha_p \mu_p \left(\nabla u_p + (\nabla u_p)^T\right) + \alpha_p \left(\kappa_p - \frac{2}{3}\mu_p\right) \nabla \cdot u_p \, I \tag{2.43}$$

where, μ_p and κ_p are the shear and bulk viscosities for the plasma phase, respectively. α_p is the volume fraction of plasma, and I is a unit tensor. The bulk viscosity, κ_p can be ignored for incompressible fluids. The stress tensor for the particulate phases due to the interactions among particles is given by the form:

$$\tau = -P_i\delta + \alpha_i\mu_i\left(\nabla u_i + (\nabla u_i)^T\right) + \alpha_i\left(\kappa_i - \frac{2}{3}\mu_i\right)\nabla \cdot u_i\ I \tag{2.44}$$

where δ is the Kronecker delta and the particle-phase pressure, P_i, represents an inter-particle pressure as a function of volume fraction of the i-phase. This pressure is generated by the kinetic energy of the particle velocity fluctuations and hence collision of cells with each other or elastic or inelastic contact between cells. Since normal blood remains fluid even at a hematocrit of 98% (Fung, 1993) and since WBC and platelets are present at such low volume fraction, the inter-particle pressure of blood can be ignored (Jung and Hassanein, 2008), (Jung et al, 2006b). The inter-phase force, R_{ri} depends on the friction, pressure, cohesion, and other effects, and is subject to the conditions that $R_{ri} = -R_{ir}$, and $R_{ii} = 0$:

$$\sum_{r=1}^{n} R_{ri} = \sum_{r=1}^{n} K_{ri}(u_r - u_i) \tag{2.45}$$

where K_{ri} ($=K_{ir}$) is the inter-phase momentum exchange coefficient between the phases. A particle moving in a fluid experiences a drag force due to the viscous effects in the direction of the flow. The RBC has been considered to behave like a liquid droplet without change in the physical characteristics (volume and surface area of RBC) of the membrane (Fischer et al, 1978), (Schmid-Schönbein and Wells, 1969). The inter-phase momentum exchange coefficient for liquid-liquid dispersed flow can be written in the following general form:

$$K_{ri} = \frac{\alpha_i\alpha_r\rho_r f}{\tau_r} \tag{2.46}$$

where τ_r is the particle relaxation time given as:

$$\tau_r = \frac{\rho_r d_r^2}{18\mu_i} \tag{2.47}$$

where d_r is the mean diameter of the drops of phase r. The drag function f includes a drag coefficient C_D that is based on the Reynolds number, Re:

$$f = \frac{C_D Re}{24} \tag{2.48}$$

The drag function, f is always multiplied by the volume fraction of the continuous phase, α_i as reflected in Eq. (2.46) to enforce K_{ri}'s tendency to zero whenever the continuous phase is not present within the domain.

2.6. Drag Models

The application of statistically averaged fluid-fluid models for the simulation of blood flow requires the development of adequate models for the inter-phase momentum exchange. This situation comes with a problem at a high phase fraction of the dispersed phase. An accurate modeling of the drag force is a very critical delivery regarding the prediction of mean and turbulent features of two-phase flows, and this problem has provided an appreciable amount of literature. Various models were developed to describe the drag coefficient for fluid-fluid systems as follows:

2.6.1. Schiller and Naumann model

The well-known drag law of Stokes (i.e., C_D=24/Re) proposed for Re<1 was extended for higher particle Re numbers by means of a dimensionless multiplication factor which accounts the inertial effect on the drag force acting on a single non-deformable spherical particle in an infinite stagnant fluid at intermediate Reynolds numbers (Schiller and Nauman, 1935).

$$C_D = \begin{cases} 24(1+0.15Re^{0.687})/Re & Re \leq 1000 \\ 0.44 & Re > 1000 \end{cases} \tag{2.49}$$

where the particle Reynolds number, Re is based on the dispersed particle diameter, d, the magnitude of relative velocity, U_r between the phases, the density, ρ_c and the dynamic viscosity, μ_c of the continuous phase as that:

$$Re = \frac{\rho_c d\, U_r}{\mu_c} \tag{2.50}$$

where $U_r = \lvert u_c - u_d \rvert$ and u_c is the velocity of continuous phase and u_d is the velocity of dispersed phase. The correlation of Schiller and Naumann was also experimentally validated by Klaseboer et al. (2001) for a broader variety of liquid-liquid systems with particle Reynolds number as high as 1000. Myint et al. (2006) showed that the combination of Schiller and Naumann model and Levich (1962) model including the effects of surfactants and viscosity ratio is appropriate for spheroid drops rising through infinite stagnant liquid at intermediate Reynolds numbers.

2.6.2. Morsi and Alexander model

Morsi and Alexander (1972) also described the drag coefficient for smooth spherical particles as in the Schiller and Naumann model, but with eight different correlations over eight successive ranges of Re. In this model, Re domain is divided into eight successive Re ranges by means of adjusting eight corresponding fits to minimize the deviation between the experimental data and the fitted correlations as that:

$$C_D = a_1 + \frac{a_2}{Re} + \frac{a_3}{Re^2} \tag{2.51}$$

where Re is defined in Eq. (2.50). The values of a_1, a_2, and a_3 were evaluated as:

$$
a_1, a_2, a_3 \begin{cases} 0,24,0 & 0 < \mathrm{Re} < 0.1 \\ 3.690,22.73,0.0903 & 0.1 < \mathrm{Re} < 1 \\ 1.222,29.1667,-3.8889 & 1 < \mathrm{Re} < 10 \\ 0.6167,46.50,-116.67 & 10 < \mathrm{Re} < 100 \\ 0.3644,98.33,-2778 & 100 < \mathrm{Re} < 1000 \\ 0.357,148.62,-47500 & 1000 < \mathrm{Re} < 5000 \\ 0.46,-490.546,578700 & 5000 < \mathrm{Re} < 10000 \\ 0.5191,-1662.5,5416700 & \mathrm{Re} \geq 10000 \end{cases} \tag{2.52}
$$

The particle Reynolds number for realistic suspensions of blood cells was detected to be smaller than unity (i.e., Re<1) (Hyun et al, 2001), (Longest et al, 2004), (Longest et al, 2005), (De Gruttola et al, 2005), so the well-known Stokes formula for the drag coefficient of a spherical solid particle, or more suitable one of the above models at low Reynolds number can be used for RBC in a shear flow. However, the experimental results on drag coefficient of dispersed particles in a liquid-liquid system indicated that the effect of adjacent entities plays a significant role in accurate prediction of drag coefficient at higher concentrations proposed as $\alpha > 0.05$ (Al-Taweel et al, 2006) or $\alpha \geq 0.1$ (Rusche and Issa, 2000). These types of empirical models take into account the dispersed phase fraction, α as follows.

2.6.3. Barnea and Mizrahi model

Barnea and Mizrahi (1975) extended a drag coefficient law obtained with solid-fluid systems to liquid-liquid systems using the concept of effective viscosity and a mixture viscosity law similar to a Taylor linear law validated at a high phase fraction. Their model was found as in agreement with 12 different experimental data sources for a wide range of particle Reynolds number and phase fraction.

$$
C_D = \left(1 + \alpha^{\frac{1}{3}}\right)\left(0.63 + \frac{4.8}{\sqrt{\mathrm{Re}_m}}\right)^2 \tag{2.53}
$$

where the particle Reynolds number, Re_m is based on the mixture viscosity, μ_m instead of the continuous phase viscosity, μ_c as that:

$$Re_m = \frac{\rho_c d U_r}{\mu_m} \tag{2.54}$$

where the mixture viscosity, μ_m is evaluated from the following viscosity law:

$$\mu_m = \mu_c K_b \frac{\frac{2}{3}K_b + \frac{\mu_d}{\mu_c}}{K_b + \frac{\mu_d}{\mu_c}} \tag{2.55}$$

where μ_d is the viscosity of the dispersed phase, K_b and K_a are the empirical functions as follows:

$$K_b = \exp\left(\frac{5\alpha K_a}{3(1-\alpha)}\right) \tag{2.56}$$

$$K_a = \frac{\mu_c + 2.5\mu_d}{2.5\mu_c + 2.5\mu_d} \tag{2.57}$$

2.6.4. Ishii and Zuber model

Ishii and Zuber (1979) derived a drag law by using the same concept of mixture viscosity for particulate flows and gas-liquid systems as well as for liquid-liquid systems, including the case of distorted inclusions.

$$C_D = \frac{24}{Re_m}\left(1 + 0.1 Re_m^{0.75}\right) \tag{2.58}$$

Where the particle Reynolds number, Re_m is also based on the mixture viscosity, μ_m as in Eq. (2.54), but here the mixture viscosity is evaluated from the another mixture viscosity law:

$$\mu_m = \mu_c \left(1 - \frac{\alpha}{\alpha_{max}}\right)^{AA} \tag{2.59}$$

where α_{max} is accepted as 0.62 for solid and 1 for fluid, and the exponent AA is defined as:

$$AA = -2.5\alpha_{max} \frac{\mu_d + 0.4\mu_c}{\mu_d + \mu_c} \tag{2.60}$$

2.6.5. Kumar and Hartland model

Kumar and Hartland (1985) also proposed an empirical drag law for liquid-liquid systems based on a large number of experimental data covering important ranges of particle Reynolds number and phase fraction.

$$C_D = \left(K_1 + \frac{24}{Re}\right)\left(1 + k_{kh}\alpha^n\right) \tag{2.61}$$

where Re is defined as in Eq. (2.50), $K_1 = 0.53$, $k_{kh} = 4.56$, and $n = 0.73$.

It is important to note that the above reviewed drag models and similar can be used as a local model of the stationary drag term to be introduced into two-phase CFD models. However, the significant discrepancies observed between the proposed drag models raises the question of the choice of a particular drag law for a given liquid-liquid application such as blood flow (Rusche and Issa, 2000). The discrepancies between the all above drag models are shown in Fig. 2.6 for Reynolds numbers smaller than unity as in the case of blood flow (Hyun et al., 2001), (Longest et al., 2004), (Longest et al., 2005), (De Gruttola et al., 2005). The value of hematocrit, α_{RBC} is accepted as 0.45 through predictions. It is seen from the figure that; all of the models predict an increase in the drag coefficient when Re decreases.

The models of Schiller-Naumann (Eq. 2.49), Morsi-Alexander (Eq. 2.51), and Ishii-Zuber (Eq. 2.58) seem to predict the drag coefficient closely with each other. However, the models of Barnea-Mizrahi (Eq. 2.53) and Kumar-Hartland (Eq. 2.61) predict higher drag coefficients than those for same Re numbers.

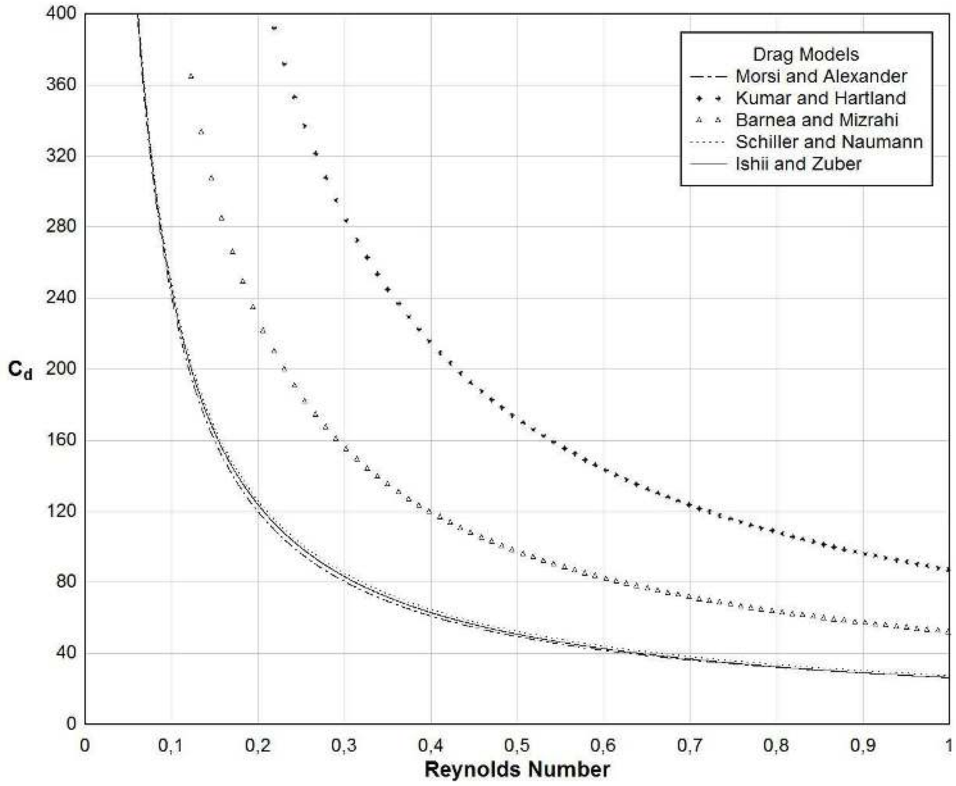

Figure 2.6. Comparison of drag models for a fluid-fluid system with Re <1.0 (α_{RBC}=0.45)

In order to evaluate proper drag law for a liquid-liquid application, it so seems necessary to test it on the basis of statistically averaged local measurements of the drag force. Augier et al. (2003a) measured the local relative velocity in a homogeneous liquid-liquid flow as a function of the local phase fraction and showed that the above mentioned classical drag coefficient laws underestimate the effect of the phase fraction on the drag coefficient. In return, the actual drag coefficient for a liquid-liquid system can be evaluated as the product of the single drop drag coefficient and a function of the local phase fraction which is well predicted by the theoretical mixture viscosity models in the creeping flow regime. It is so necessary to correlate the drag coefficient for a single sphere as the drag coefficient on systems of spheres at high volume fractions. The drag correlations should so depend on experimental data for a flow with deformable interfaces at high volume fractions (Ishii and Hibiki, 2006). Unfortunately, no data for drag correlation of blood cells are available in the literature, but a general correlation for liquid-liquid systems would be useful. The Schiller and Nauman model for a single dispersed drop was extended to describe the effect of neighboring entities by using the drag coefficient correlations as that:

$$C_D = C_{D0} F(\alpha) \tag{2.62}$$

where C_{D0} is the drag coefficient of a single spherical drop evaluated from the Schiller and Nauman model (volume fraction of dispersed phase tending towards zero) for a non-uniform flow, and $F(\alpha)$ is a function which takes into account the effects arising from the presence of other dispersed elements. The proposed $F(\alpha)$ correlation of Rusche and Issa (2000) is that:

$$F(\alpha) = e^{k_1 \alpha} + \alpha^{k_2} \tag{2.63}$$

where the values of the coefficients k_1 and k_2 for spherical droplets were determined respectively as 2.1 and 0.249 by using a non-linear fitting procedure. Another drag function correlation of Augier et al. (2003a) is also that:

$$F(\alpha) = e^{5.2\alpha} \tag{2.64}$$

for $0 < \alpha < 0.4$, and $Re < 100$. $F(\alpha)$ is here modeled for liquid-liquid systems as a function of the phase volume fraction only. However, further development of these works need to focus on effects of Archimedes, Eötvös or particle Reynolds numbers (Rusche and Issa, 2000), (Augier et al., 2003a), (Behzadi et al, 2004). However in the case of solid-fluid systems, the more specific drag correlations including the effects of both phase fraction and Reynolds number were early achieved and proposed by Wen and Yu (1966) and Wallis (1974) respectively as follows:

$$C_D = \frac{24}{Re}(1 + 0.15 Re^{0.687})(1 - \alpha)^{-1.7} \tag{2.65a}$$

$$Re = \frac{(1 - \alpha)\rho_c d U_r}{\mu_c} \tag{2.65b}$$

$$C_D = C_{D0}(1 - \alpha)^{3-2n} \tag{2.66a}$$

$$n = 4.7\frac{1 + 0.15 Re^{0.687}}{1 + 0.253 Re^{0.687}} \tag{2.66b}$$

$$Re = \frac{\rho_c d U_r}{\mu_c} \tag{2.66c}$$

2.7. Lift Force on Dispersed Phase

The lift force is a hydrodynamic force acting on a particle dispersed in a shear flow due to the particle rotation. The rotation of particle may be caused by a velocity gradient or may be imposed from some other source such as particle contact and rebound from a surface. The major parameters affecting the lift force acting on a spherical particle in a simple unbounded shear flow are (i) relative velocity between a particle and an ambient fluid, (ii) shear rate of an ambient fluid, (iii) particle rotational speed, and (iv) surface boundary condition (non-slip or slip at particle surface). Multiphase flows always involve some relative motion of one phase with respect to the others; for example, a two-phase flow problem should therefore be formulated in terms of two velocity fields. A general transient two-phase-flow problem can be formulated by using a two-fluid model; however, the greatest difficulty is associated with the establishment of constitutive relations. Additionally, the deformation of a particle causes the associated wake modification and the modified interaction with surrounding flow structures resulting in lift force modification. Thus, the modeling of the lift force in a single deformable particle system is a scientific problem (Ishii and Hibiki, 2006), (Hibiki and Ishii, 2007). The lift force acting on dispersed particle is found as significant at higher shear rates and low concentrations (Al-Taweel et al., 2006). The importance of lift force is also pointed for the flows dispersed with larger size particles and especially for quickly separable flow cases (Fluent Inc., 2006). Existing models however assume that the diameter of dispersed particle is much smaller than the inter-particle spacing and thus, the inclusion of lift forces has not yet considered properly for closely packed particles or for very small particles. The lift force acting on a particle due to velocity gradients in the flow field of the continuous phase is normal to the relative direction of flow. Therefore, a cell depleted plasma layer occurs at the wall. Lift forces in high shear rate regions like near wall environment are likely to be important. The particles in high shear rate regions have more mobility than low shear rate regions and as a result experience a reduced drag effect. This effect leads to a modification of the drag coefficient. All of these can influence the particles trajectories and the interaction between particles and the vessel wall.

The research strategy to develop the lift force model and correlation is mainly carried by means of analytical, numerical, and experimental approaches in literature. The analytical calculation of the lift force is very tedious even in asymptotic situations because it requires the consideration of the three dimensional momentum equations without major simplifications. Actually two series of analytical work have been carried out on this problem. The first one considers the effect of an inviscid rotational flow on a sphere and was initiated by Lighthill (1956) and Hall (1956). His results were improved in several subsequent works of Cousins (1970), Auton (1984), Auton (1987), and Naciri (1992). The second series of work concerns low Reynolds number flows and is related to sedimentation problems. Combining several analytical techniques, Saffman (1965) and Saffman (1968) obtained the lift force on a small rigid sphere in a linear shear flow in the limit of small Reynolds number and large shear.

2.7.1. Saffman model

The Saffman lift force is due to the pressure distribution developed on a particle due to rotation induced by a velocity gradient. His solution is based on a matched asymptotic expansion in which the flow in the inner region is modified by the inertial effects induced by the shear in the outer region. The most common correlation of Saffman's lift model can be given as:

$$F_L = 1.615 \rho_c \nu_c^{1/2} d^2 (u_c - u_d) \left| \frac{du_c}{dy} \right|^{1/2} \mathrm{sign}\left(\frac{du_c}{dy} \right) \tag{2.67}$$

where ρ_c and ν_c are the density and kinematic viscosity of continuous phase, d is the diameter of a spherical particle, u_c and u_d are the velocities of the continuous and the dispersed phases in x-direction respectively, and du_c/dy is the shear rate of the uniform flow field. The correlation requires the conditions that the particle Reynolds number, Re is much less than the shear Reynolds number, Re_G and both Reynolds numbers are much less than unity as given below:

$$Re = \frac{|u_c - u_d| d}{\nu_c} = \frac{\rho_c U_r d}{\mu_c} << 1 \tag{2.68a}$$

$$Re_G = \frac{|du_c/dy| d^2}{\nu_c} << 1 \tag{2.68b}$$

$$\beta = \frac{Re_G^{1/2}}{Re} >> 1 \tag{2.68c}$$

$$Re_\omega = \frac{\omega_d d^2}{\nu_c} << 1 \tag{2.68d}$$

where ω_d is the rotational speed of the dispersed particle. It can be easily understand that the shear rate always takes a maximum value at the pipe wall and it decreases nearer the high-velocity region around the pipe axis. Saffman's lift force model apparently cannot be applied near the wall, although there might exist a region where it can be applied. As the vessel Reynolds number increases, the dimensions of applicable region are reduced near the axis while the infringement of the constraint becomes severe near the wall. The Saffman's lift force model was therefore modified and extended to overcome its constraints by the several analytical works of McLaughlin (1991), McLaughlin (1993), Mei (1992), Drew and Lahey (1979), Drew and Lahey (1987), Drew and Lahey (1990), and Legendre and Magnaudet (1997) as follows.

2.7.2. McLaughlin model

McLaughlin (1991) and McLaughlin (1993) extended Saffman's analysis by considering the case where inertia effects related to the mean flow are of same order as those induced by the shear. The restriction on shear magnitude in Saffman's model was relaxed by means of the following expressions for the shear induced lift force on a rigid particle in an unbounded linear shear flow in the low Reynolds number regime:

$$F_L = 1.615\rho_c \nu_c^{1/2} d^2 (1-(0.287/\beta^2))(u_c - u_d)\left|\frac{du_c}{dy}\right|^{1/2} \mathrm{sign}\left(\frac{du_c}{dy}\right); \quad \text{for } \beta >> 1 \qquad (2.69)$$

$$F_L = 226.191\rho_c \nu_c^{1/2} d^2 \beta^5 \ln(\beta^2)(u_c - u_d)\left|\frac{du_c}{dy}\right|^{1/2} \mathrm{sign}\left(\frac{du_c}{dy}\right); \quad \text{for } \beta << 1 \qquad (2.70)$$

for $0.1 \le \beta \le 20$ where β is defined as in Eq. (2.68). McLaughlin's expressions also require that both Re and Re_G must be small compared to unity (i.e., Re<<1 and Re_G<<1). Legendre and Magnaudet (1997) later reconsidered Saffman's and McLaughlin's analyses for a spherical drop with a vanishing viscosity and found that the lift force is $(2/3)^{1/2}$ times that of a solid sphere.

2.7.3. Mei model

Mei (1992) proposed the following two correlations for a greater range of particle Reynolds number (0.1≤Re≤100):

$$F_L = 1.615\rho_c v_c^{1/2} d^2 \left\{ \left(1 - 0.3314\Omega^{1/2}\right)\exp\left(-Re/10\right) + 0.3314\Omega^{1/2} \right\}$$

$$* (u_c - u_d) \left|\frac{du_c}{dy}\right|^{1/2} \mathrm{sign}\left(\frac{du_c}{dy}\right) \tag{2.71}$$

for Re≤40 and;

$$F_L = 1.615\rho_c v_c^{1/2} d^2 \left\{0.0524\left(\Omega Re\right)^{1/2}\right\}(u_c - u_d) \left|\frac{du_c}{dy}\right|^{1/2} \mathrm{sign}\left(\frac{du_c}{dy}\right); \quad \text{for } Re \geq 40 \tag{2.72}$$

where finite shear rate, Ω is defined as;

$$\Omega = (Re\beta^2)/2 = Re_G/2Re = (d/2)\,|du_c/dy|/|u_c - u_d| \tag{2.73}$$

and it is limited to 0.005≤Ω≤0.4. He showed that the above empirical equation provided a reasonable fit for Mclaughlin's model. All of the above lift correlations have been derived and proposed assuming an infinite flow field in one direction and with a constant velocity gradient. This assumption can be locally satisfied when the particle is considerably smaller than the dimensions of the vessels such as blood arteries. In micro-vessels, however, the particle diameter is often comparable in size to the vessel diameter. When the velocity gradient can be varied within the scale of particle, the applicability of the correlations is not always assured. Moreover, in the curved regions of the vessel, there appear Dean vortices as secondary flow pattern. The validity of the correlations has not been investigated in such a complicated flow field (Ookawara et al., 2007).

2.7.4. Drew and Lahey model

The first attempt in analytically solving the disturbed rotational flow around the sphere was probably carried out by Drew and Lahey (1979) who invoked the frame indifference principle in order to derive a general expression for the force density acting on a dilute suspension of spheres and concluded that the conventional lift coefficient, C_L must equal to the added or virtual mass coefficient, C_{VM} defined by Darwin (1953). Even if the methodologies used by the several groups of authors (Auton, 1987), (Drew and Lahey, 1987), (Drew and Lahey, 1990), (Drew and Lahey, 1993), (Zhang and Prosperetti, 1994) are different, their results also converge in suggesting that the identity C_L=C_{VM} holds in inviscid flow (i.e., in the limit of weak shear rates). Moreover, this identity was also found to hold for ellipsoids by Naciri (1992). The proposed lift force model of Drew and Lahey is that:

$$F_L = 0.5236 C_L \rho_c d^3 (u_c - u_d) x (\nabla x u_c) \tag{2.74}$$

where C_L is accepted to be constant as 0.5 and equal to C_{VM} for an inviscid flow of an incompressible fluid. Experimental investigations however showed that the lift coefficient values are variable and significantly less than the inviscid value of 0.5, and even negative in some cases (Al-Taweel et al., 2006).

In comparison to the excessive number of above reviewed analytical approaches, the number of numerical studies directed on the lift force acting on a rigid spherical particle dispersed in a shear flow is very limited. Dandy and Dwyer (1990) obtained the first numerical estimates of the lift force for the ranges of the particle Reynolds numbers; $0.01 \leq Re \leq 100$ and the dimensionless shear rate; $0.005 \leq Sr \leq 0.4$ where the particle Reynolds number, Re is defined as in Eq. (2.50), and the dimensionless shear rate is defined as;

$$Sr = \frac{d}{|u_c - u_d|}\left(\frac{du_c}{dx}\right) \tag{2.75}$$

The lift coefficient was found approximately constant at a fixed shear rate for Re in the range of 40≤Re≤100. Their numerical predictions of the lift force were in good agreement with Saffman's solution but disagreed significantly with McLaughlin's result. While the results of Dandy and Dwyer (1990) show that when the Reynolds number increases the lift coefficient tends towards a constant positive value, those of Komori and Kurose (1996) and Kurose and Komori (1999) display completely different trends: the latter authors find that beyond a certain Reynolds number the lift coefficient becomes negative and depends strongly on the shear rate. Extension of the shear induced lift force on a rigid spherical particle to finite Reynolds numbers, of the order of few hundreds, is through numerical simulations (Bagchi and Balachandar, 2002a), (Bagchi and Balachandar, 2002b), (Zeng et al., 2009). This situation shows that the situation concerning the lift force on a rigid sphere is not clear at the present time, except in the low Reynolds number limit for which asymptotic results are available. Legendre and Magnaudet (1998) also numerically studied the 3-D flow around a spherical bubble moving steadily in a viscous linear shear flow by solving the full Navier–Stokes equations.

2.7.5. Legendre and Magnaudet model

It was assumed that the bubble surface is clean so that the outer flow obeyed a zero shear stress condition and do not induce any rotation of the bubble. The following correlation for the lift force was developed:

$$F_L = -0.5236 C_L \rho_c d^3 (u_c - u_d) \text{ x } \omega_v \tag{2.76}$$

for 0.1≤Re≤500 and 0.01≤Sr≤0.25. Here, ω_v is the vorticity of undisturbed ambient flow at the center of the sphere and the lift coefficient, C_L for a spherical bubble is given by:

$$C_L = \sqrt{\left\{C_L^{LowRe}(Re, Sr)\right\}^2 + \left\{C_L^{HighRe}(Re)\right\}^2} \tag{2.77}$$

where the lift coefficients for low and high Re ranges are respectively defined as:

$$C_L^{LowRe}(Re,Sr) = \frac{6}{\pi^2 (2ReSr)^{1/2}} \frac{2.255}{(1+0.1Re/Sr)^{3/2}} \tag{2.78}$$

$$C_L^{HighRe}(Re) = \frac{1}{2}\left(\frac{1+16Re^{-1}}{1+29Re^{-1}}\right) \tag{2.79}$$

For a solid particle, the above correlation for C_L at low Re was found approximately valid if it's numerical factor 6 replaced by 27/2. At low Re, the C_L was found strongly dependent on both Sr and Re, and for moderate to high Re such dependence was found to be very weak. Tomiyama (2004) experimentally showed that Legendre and Magnaudet's model was correct for a spherical bubble at Re<5 and at Re<1. However a slight bubble deformation with the aspect ratio in the order of 0.9 caused a noticeable deviation of the measured lift coefficients from the model and further deformation reversed the direction of the lift force acting on a bubble. Takagi and Matsumoto (1995) also pointed out this phenomenon by numerical calculation.

The previous numerical works showed that the lift force was an indispensable factor to reasonably predict the concentration effects that correspond to the experimental results. However, the adopted lift force model of Drew and Lahey (1993) based on Euler–Euler approach, was modified by Ookawara et al. (2004), Ookawara et al. (2005), and Ookawara et al. (2006) in terms of the acting direction and magnitude. By using a similarity hypothesis between the drag and the lift forces, the lift force model of Legendre and Magnaudet (1998) for a single particle system was recently modified to consider the effect of bubble deformation by Hibiki and Ishii (2007) as that:

$$C_L = F(D_{db})\, C_{L0} \tag{2.80}$$

$$F(D_{db}) = 2 - \exp(2.92\, D_{db}{}^{2.21}) \tag{2.81}$$

where C_{L0} is the lift coefficient for a spherical bubble evaluated from Legendre and Magnaudet's model, $F(D_{db})$ is the proposed shape factor for the lift coefficient evaluated by using the experimental data taken by Tomiyama et al. (2002), and the dimensionless bubble diameter, D_{db} was proposed respectively for viscous regime, distorted-particle regime, and spherical-cup bubble regime as follows:

$$D_{db} = \frac{3^{1/3}}{2^{4/3}} N_{\mu}{}^{2/3} Re^{1/3} \left(1 + 0.1 Re^{3/4}\right)^{1/3}; \quad \text{for } N_{\mu} \leq \frac{24\sqrt{2}(1 + 0.1 Re^{0.75})}{Re^2} \tag{2.82}$$

$$D_{db} = \frac{1}{4\sqrt{2}} N_{\mu} Re; \quad \text{for } N_{\mu} \leq \frac{4\sqrt{2}}{Re} \tag{2.83}$$

$$D_{db} = \frac{1}{2^{5/3}} N_{\mu}{}^{2/3} Re^{2/3}; \quad \text{for } N_{\mu} > \frac{4\sqrt{2}}{Re} \tag{2.84}$$

where Re is the particle Reynolds number defined as in Eq. (2.50) with a range; $3.68 \leq Re \leq 78.8$, and N_{μ} is the viscous number with a range of $0.0435 \leq N_{\mu} \leq 0.203$, measures the viscous force induced by an internal flow to the surface tension force and defined as that:

$$N_{\mu} = \frac{\mu_c}{\left(\rho_c \sigma_{st} \sqrt{\dfrac{\sigma_{st}}{g\,\Delta\rho}}\right)^{1/2}} \tag{2.85}$$

where g is the gravitational acceleration, $\Delta\rho$ is the density difference between the continuous and the dispersed phases, and σ_{st} is the surface tension of the bubble. The above modified lift force model in a single particle system was then also extended by Hibiki and Ishii (2007) to a multi-particle system by means of using the particle Reynolds number, Re_m, defined in Eq. (2.54), based on the mixture viscosity, $\mu_{m,}$ instead the continuous phase viscosity, μ_c. For this purpose, the mixture viscosity was evaluated from the correlation of Ishii and Chawla (1979). The applicability of both the modified and the extended lift force models were qualitatively shown for higher Reynolds numbers, but the validity of the modified lift model on slightly deformable bubbles was limited to $Re \leq 3.68$.

In the experimental approach, experimental data are utilized to obtain an empirical correlation. Starting from the first experiments of Segre and Silberberg (1962a) and Segre and Silberberg (1962b), considerable attention has gone to the understanding and quantification of shear induced lift on a particle in relative motion in an unbounded shear flow. Extensive experiments showed that relatively small and large bubbles tend to migrate toward a channel wall and center (Kariyasaki, 1987), (Zun, 1988), (Liu, 1993), (Hibiki and Ishii, 1999), (Hibiki et al., 2001), (Hibiki et al., 2003), (De Vries et al., 2002), (Sankaranarayanan and Sundaresan, 2002), (Tomiyama et al., 2002), (Tomiyama, 2004), (Shew et al., 2006), (Kulkarni, 2008). Two most important contributions on the subject among all, come from Tomiyama et al. (2002), and Sankaranarayanan and Sundaresan (2002). Tomiyama et al. (2002) measured bubble trajectories of single air bubbles in simple shear flows of glycerol–water solutions to evaluate transverse lift force acting on single bubbles. Based on the experimental result, they assumed the lift force caused by the slanted wake had the same functional form as that of the shear induced lift force, and proposed an empirical correlation of the lift coefficient. Very recent experiment done by Tomiyama (2004) implies that a slight bubble deformation might change the direction of the lift force acting on a bubble and of lateral migration even at $Re < 5$. The coupling between shear and bubble deformation (whichin turn induces the vorticity/stretching/tilting) induces lateral migration of bubbles and its direction is opposite to that of the spherical bubble. These results agree with the numerical findings by Kariyasaki (1987), Ervin and Tryggvason (1994), and Takagi and Matsumoto (1995), and Bothe et al. (2006) for a deforming bubble moving in a shear flow. Thus, in a bubble swarm, even if one ignores the hindrance by surrounding bubbles, for all the bubbles subjected to the same shear and other parameters being constant, the lift coefficient will depend upon the variation in slip velocity and bubble shapes. In majority of the cases, the liquids are never pure and hence the interfacial hydrodynamics gets modified to some extent in terms of the vorticity as well as the pressure variation on the bubble surface. The formulation of C_L for bubbles in a suspension was also derived by Sankaranarayanan and Sundaresan (2002) in terms of dimensionless numbers; namely, the particle Reynolds number, the Eotvos number, the capillary number, and the ratio of slip velocities in two orthogonal directions. The experimental observations of Kulkarni (2008) in a bubble column at different axial levels recently showed that the absolute value of C_L at the center of column is less and it increased toward the wall. Further, except in the vicinity of the wall, $C_L<0$ and it supports the radially inward motion of bubbles.

As described above, the lift and the drag forces are still poorly understood, and thus experimental and numerical efforts have further to be made to get better understanding of them on deformable particles of different sizes, in different flow fields, in dynamic situations, where the particle size would change due to absorption or reaction and also in dispersions. In order to better understanding of the lift and drag forces acting on red blood cells dispersed in plasma of the pulsatile blood flow, the critical studies of Miyazaki et al. (1995), Asmolov and McLaughlin (1999), Wakaba and Balachandar (2005), Candelier and Angilella (2006), and Candelier and Souhar (2007) considering the relative velocity between the dispersed particle and the continuous phase takes the form of a time-dependent harmonic function, should be extended for the pulsatile flow case of continuous phase and further combined with the results of above reviewed studies on dispersed deformable bubbles or droplets.

2.8. Virtual Mass Effect

The added or virtual mass effect is a concept that occurs when the dispersed phase is subjected to acceleration or deceleration. It is especially significant when the density of dispersed phase is much smaller than the continuous phase density. The virtual mass force can be evaluated from the expression:

$$F_{VM} = C_{VM}\frac{\pi d^3}{6}\rho_c\left(\frac{Du_c}{dt}-\frac{Du_d}{dt}\right); \qquad (2.86a)$$

or

$$F_{VM} = C_{VM}\frac{\pi d^3}{6}\rho_c\left\{\left(\frac{\partial u_c}{\partial t}+(u_c\cdot\nabla)u_c\right)-\left(\frac{\partial u_d}{\partial t}+(u_d\cdot\nabla)u_d\right)\right\} \qquad (2.86b)$$

where C_{VM} is the virtual mass coefficient and the term D/dt denotes the material time derivative. The well-known equality between the virtual mass coefficient and the lift coefficient holds only in the limit of weak shears and nearly steady flows (Drew and Lahey, 1979), (Drew and Lahey, 1987), (Drew and Lahey, 1990), (Zhang and Prosperetti, 1994). The value of C_{VM} is generally accepted as 0.5 for inviscid flows. Experimental investigations however showed that its value is variable and significantly less than the inviscid value of 0.5, and even negative in some cases (Al-Taweel et al., 2006). Jung et al. (2006b) and Srivastava and Srivastava (2009) proposed in their numerical analyses that the estimated shear induced lift and virtual mass forces for blood flow are negligible.

2.9. Aggregation of Blood Cells

The bridging due to the adsorption of macromolecules onto adjacent cell surfaces, and the depletion due to the osmotic gradient arising from the exclusion of macromolecules near the cell surface, are presently used as molecular models to describe the aggregation behaviors of RBC (Baumler et al., 1999), (Meiselman et al., 2007). Moreover, the predicted effects of blood composition, cellular properties and clinical conditions on aggregation (Rampling et al, 2004), (Meiselman et al, 2007), the measured aggregation tendencies (Shin et al, 2009), and the predictions on interaction forces between RBCs (Tha and Goldsmith, 1986), (Tha and Goldsmith, 1988), (Tees et al, 1993), (Zhu, 2000) have been used to understand the aggregation behavior. The effects of RBC aggregation on hemodynamics and on the other blood cells have also been investigated (Goldsmith et al, 1999), (Baskurt and Meiselman, 2007). Note that the most of the previously reviewed drag and lift models suppose that the dispersed phase particle is spherical, rigid, and having an immobile interface. RBC in blood plasma is however a biconcave disc-shaped deformable particle and it can be deformed isochorically without any change in surface area or volume. One of the important factors affecting the shape of RBC is shear rate. At lower shear rates, RBC suspension is a multi-dispersed system which contains so many aggregate parts (rouleaux) of various sizes. The shear dependent mechanisms of RBC aggregation are figured out by the balance of aggregation and disaggregation forces. However, this mechanisms and exact role of aggregation on blood flow remain unclear.

Disaggregation forces mainly consist of mechanical shear force, repulsive force, and elastic force potential of RBC membrane. Above a critical shear stress, the system becomes mono-dispersed, consisting of single cells, as RBC aggregates have broken up. Schmid-Schönbein and Wells (1969) observed the fluid drop-like behavior of single RBC. While under shear, the cells become progressively deformed into prolate ellipsoids, their long axis aligned parallel to the direction of flow, the elongation increasing with increasing shear stress. The rotational motion of its membrane about cell interior, called as tank treading motion, is also observed. The shape of RBC, whether prolate ellipsoid, biconcave disc or rouleaux, thus depends upon the shear stress and affects the drag and lift forces acting. Therefore, a dynamic shape factor is necessary to account this effect on an individual and aggregated RBCs. Jung and Hassanein (2008) recently proposed the following dynamic shape factor, F_s for the realistic range of shear rate in plasma at which RBC aggregates exist:

$$F_s = 1.5\left(1 + (\lambda \frac{du}{dy})^2\right)^{0.058697} \tag{2.87}$$

where λ is the time constant with the value as 0.11sec. This dynamic shape factor is limited to the shear rates smaller than 300 sec^{-1}. Above this limit, no expressions for a dynamic shape factor in blood can be found in the literature. A shape factor can be further derived experimentally from microscopic images of the RBC by using a high speed camera for flow at higher shear rates. Using available images, one can also evaluate shape factors for RBC of regular shape (i.e., prolate ellipsoid or ellipsoid). A shear rate dependent correlation can then be formed from these shape factors. It is expected that the degree of deformability of the RBC and the plasma viscosity will have dominant effects on the shape factor.

2.10. Hemodynamic Hypotheses on Cardiovascular Diseases

Cardiovascular diseases such as atherosclerosis and aneurysms are widely observed in the communities of the developed world and are mainly associated with unusual hemodynamic conditions in arteries in addition to arterial wall mechanics (Gessner, 1973), (Malek et al., 1999), (Wootton and Ku, 1999). The most striking feature of these diseases is that they tend to be localized in regions of curvature, bifurcation and branching in arteries. The most commonly affected arteries are the abdominal aorta, the carotid, the coronary, and the femoral arteries (Moore et al., 2001). Early investigators proposed that the focal nature of atherosclerotic lesions is correlated with local flow conditions in these sites of the arterial system. It was postulated that local hemodynamics plays a critical role in the initiation and/or progression of these lesions. Various hypotheses have been proposed relating atherosclerosis with local hemodynamics, such as pressure-related, turbulence-related, flow separation-related, and shear stress-related hypotheses.

In a review article, Gessner (1973) commented on these hypotheses and concluded that the validity of most hypotheses is highly questionable and that only shear stress-related studies show promising results. Fry (1968) and Fry (1969) were the first to propose that high wall shear stress (WSS) damaged the arterial wall and that endothelial disruption or denudation could lead to atherosclerosis. Caro et al. (1969) and Caro et al. (1971) observed that the distribution of early atherosclerotic lesions is coincident with regions of low shear, and suggested that low wall shear stress favors the enhanced residence, adhesion and infiltration of macromolecules and/or blood cells into the vessel wall. Recently, proposals of band gap WSS (Nazemi et al., 1989), oscillations in WSS (Ku et al., 1985), temporal gradients of WSS (Ojha, 1994), and spatial gradients of WSS (Lei et al., 1997) have been included in these hypotheses. The importance of WSS on the initiation, growth and rupture of aneurysms has also been reported by some investigators (Boussel et al., 2008), (Lehoux et al., 2002), (Shojima et al., 2004). Although high WSS is considered as a major factor in the initiation of aneurysms, aneurysm rupture seems to be related to a low level of WSS for its growth. In spite of the fact that much attention has been paid to hemodynamic hypotheses, the precise role and the relative importance of proposed hemodynamic parameters on vascular endothelium, pathogenesis of the atherosclerosis, and progression of the arterial lesions remain unclear.

Computational modeling of arterial biomechanics can be used in a wide variety of ways including the assessment of the effects of mural and hemodynamically induced stresses on atherogenesis, the development of risk measures for aneurysm rupture, the prediction of the progression of coronary artery disease, the improvement in interpretation of medical images, and the quantification of oxygen transport in diseased and healthy arteries (Coskun et al., 2006), (Steinman et al., 2003). Many studies proposed that hemodynamic forces regulate blood vessel structure and function (Malek et al., 1999), (Resnick et al., 2003). Understanding of arterial wall structure and mechanics in addition to blood flow, and the interaction between them are important. As a result, there is a requirement for a structural model based on arterial wall properties, as well as a blood flow model, to define mechanical interactions between blood flow and arterial wall.

2.11. Biomechanical Models of Blood Vessel Structure

Arteries are classified into three types according to the difference in their sizes and properties: elastic arteries (conducting arteries), muscular arteries (distributing arteries), and arterioles. Elastic arteries are located close to the heart (proximal arteries) and have the largest diameter. Muscular arteries are located at the periphery (distal arteries) and are intermediate-sized. Arterioles are the smallest type of arteries with a diameter of less than 0.1 mm. They are the main arterial vessels that regulate blood flow into the capillary beds of organs and tissues. Knowledge of the histology of arteries is important in that it leads to a better understanding of the mechanical characteristics of the arterial wall. Arterial walls consist of three morphologically separated concentric layers: an intima (innermost), a media (middle) and an adventitia (outermost) as shown in Fig 2.7. They consist of collagen and elastin fibers, smooth muscle cells, and water (Yamaguchi et al., 2006). The intima consists of a continuous monolayer of endothelial cells that line the lumen and form the interface between the blood and the vessel wall. It performs the secretion of vasoactive substances and the contraction and relaxation of vascular smooth muscle (Waite, 2005). The media consist of obliquely oriented smooth muscle cells in an elastin fiber and collagen bundle matrix. The elastin fibers allow distension of the artery while the collagen bundles provide tensile strength, limit distension and prevent disruption (Quarteroni et al., 2000). The boundaries between media and intima and adventitia are outlined by perforated laminae of elastic fibers that permit the transmural transfer of water, nutrients, and electrolytes as well as cellular communication between the adjacent arterial layers (Thubrikar, 2007). The adventitia consists of sparse fibroblasts intermixed with smooth muscle cells arranged between layers of elastin and collagen fibers, which add more mechanical strength to the wall. Arteries are nonlinear, anisotropic, inhomogeneous, and viscoelastic (Hayash et al., 2001), (Vito and Dixon, 2003). Viscous effects generally increase from proximal arteries of the elastic type to distal arteries of the muscular type (Gasser et al., 2006). This effect can probably be attributed to smooth muscle and is mainly developed during systole; the elastic effect to elastin fibers being predominant during diastole (Armentano et al., 1995). The media is believed to be mainly responsible for the viscoelastic behavior of an arterial segment due to the high content of smooth muscle cells (Holzapfel et al., 2002). Although the arterial wall is slightly compressible (Carew et al., 1968), it can be considered as incompressible under the physiologic conditions.

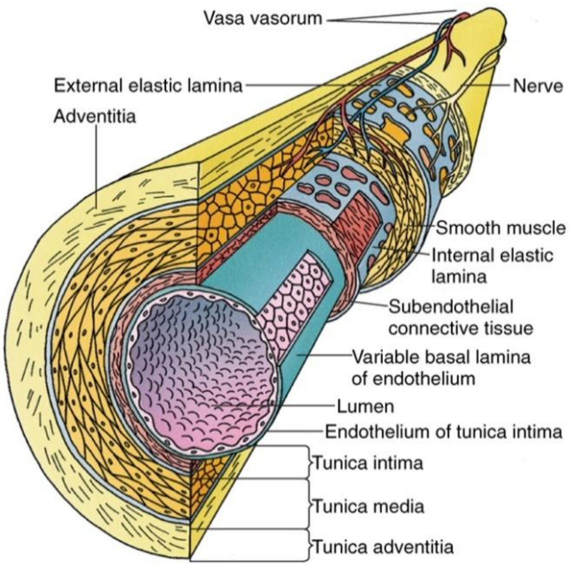

Figure 2.7. A typical artery structure (Gartner and Hiatt, 2006)

The stress distribution in the arterial wall cannot be analyzed and combined with blood flow without the constitutive models on arterial wall structure. Such constitutive models provide descriptions of the relationship between stress and strain. These models are generally evaluated by fitting data from in vivo measurements. They can be classified into four types as pseudoelastic, randomly elastic, poroelastic, and viscoelastic models. Vito and Dixon (2003) have presented a critical review of these models. Some common limitations of these models are also summarized in this study. One of them is the restricted availability of data to fit the models. Another limitation is taking no account of observed biomechanical phenomena such as smooth muscle activation, residual stress and strain, and heterogeneous fiber and cellular distribution. A comparison of the assumptions, major limitations and benefits for these models is given in Table 2.5. Zhang and Kassab (2007) have recently proposed a new strain measure definition and linearized constitutive relation for large blood vessels to overcome some disadvantages of nonlinear constitutive models. They presented a novel bilinear stress–strain relation in 2D, and extended their work to 3D (Zhang et al., 2007a). Baek et al. (2007), using methods familiar in linearized elasticity, suggested that the theory of small deformations superimposed on large deformations has potential utility in the computation of fluid-solid interactions. Stylianopoulos and Barocas (2007) presented a multiscale structural model which incorporates the fiber-fiber interactions for collagen with a requirement of the direct representation of the collagen network. Kalita and Schaefer (2008) also reviewed and discussed the approaches used to express mechanical behavior of artery walls.

As described above, there are many studies that help to understand the mechanism of the system physiology in pathogenesis and health, and can help as well with clinical study design and methods for the treatment of vascular diseases such as arterial graft selection and design, arterial clamping, angioplasty. However, they are deficient in not providing full meaningful physiological modeling. Moreover, most studies on biomechanical models of blood vessel structure need to make simplifying assumptions to overcome complexities and to render simulations both conceptually and computationally tractable thus ignoring anisotropy, nonlinear elastic, viscoelasticity, heterogeneity, residual stresses, incompressibility, vasomotion, and histological and microstructure consideration of the vessel wall.

Table 2.5. Comparison of constitutive models based on arterial wall structure (Vito and Dixon, 2003)

Type	Assumptions	Major limitation	Benefit
Pseudoelastic	The vessel is treated as one hyperelastic material in loading and another in unloading.	It separately models loading or unloading data. Data multicollinearity leads to unstable parameters and protocol dependence if incremental loading methods are used.	The approach is simple and captures vessel deformation. Pseudoelastic models form the backbone of other model types.
Randomly elastic	The strain response is centered around a definite value that lies on a well defined curve.	Data are noisier than when separately modeling loading or unloading values.	It models both loading and unloading data simultaneously.
Poroelastic	The tissue is treated as a fluid-saturated porous medium.	The movement of fluid through the porous tissue may be irrelevant within the timescale of the experiment. Nonlinear models include many unknown parameters.	It models the fluid contribution to tissue properties.
Viscoelastic	The strain response is a function of the stress history.	The response is usually modeled using a discrete number of elements. Data from one viscoelastic test may be insufficient to model characteristics from other viscoelastic tests.	It models observed viscoelastic behavior (creep, hysteresis, and stress relaxation).

Moreover, underlying mechanisms that cause and control certain properties such as vasomotion are still unknown. Geometric and mechanical properties of arteries greatly influence the velocity and pressure fields of blood flow. Additionally, pulsatile flow is responsible for the strong interaction between blood flow and arterial wall movement (Quarteroni et al., 2000). Therefore, blood flow studies have been recently combined with arterial wall mechanics. This integration can be helpful for the investigation of vascular diseases such as atherosclerosis which leads to aneurism or stenosis.

2.12. Fluid Structure Interaction

Over the last three decades, models based on coupling of fluids and structures have increasingly being used in the bioscience field such as in macroscale studies of heart mechanics, heart valves, arteries, veins, microcirculation, and pulmonary blood flow as well as in microscale studies of monocyte deposition, platelet adhesion, blood cell interactions, RBC aggregation, blood rheology, and in micro and capillary vessels (Boffi and Gastaldi, 2003), (Liu et al., 2006a), (Wang and Liu, 2004). All of these studies can be useful in the planning of vascular surgery, in diagnosis and treatment of cardiovascular disease, and in the design, evaluation and implementation of stents, artificial grafts, heart valves and probes. The popular techniques used to define fluid structure interaction for blood flow have been classified into two types depending on whether a boundary fitted mesh to solve the flow field is used or not used (Yu et al., 2006a);

i. Non-boundary-fitting methods such as the immersed boundary (IB), the distributed Lagrange multiplier based fictitious domain method (DLM/FD), the direct forcing fictitious domain method (DF/FD), the direct forcing immersed boundary method (DF/IB), the ghost cell IB methods, the lattice Boltzmann method (LBM), the accelerated Stokesian dynamics method (ASD), and the force coupling method (FCM).

ii. Boundary fitting method such as the arbitrary Lagrangian Eulerian (ALE) finite element method (FEM), and the boundary element method (BEM).

A clear virtue of the non-boundary-fitting methods is the avoiding of costly mesh updating algorithms required to track the fluid structure interface since the fluid structure interface is tracked automatically. The main drawback of the non-boundary-fitting method is the inability to capture the position of the moving fluid structure interface with high accuracy due to the necessity of using an interpolation to define the velocity field close to fluid solid interface. If one is interested in the fluid dynamic parameters close to the IB, the boundary fitting method can be a good alternative to the non-boundary-fitting method (Wood et al., 2008). The non-boundary-fitting method can be categorized into two groups according to whether or not the body force is added into the momentum equation. According to the method used for calculating the body force, there are various body force based methods such as the elastic force based IB method, and DLM/FD, DF/FD and DF/IB (Yu and Shao, 2007), (Yu et al., 2006a).

The IB method was developed by Peskin (1972) as a practical and effective solution technique for biological flow (Liu et al., 2006a). The mathematical formulation employs a mixture of Eulerian and Lagrangian variables for fluid and structure domains. Numerically, the Eulerian variables are defined on a fixed Cartesian mesh, and the Lagrangian variables are defined on a moving curvilinear mesh through the fixed Cartesian mesh without being constrained to adapt to it in any way at all (Peskin, 2002). These variables are connected by making use of the Dirac delta function in the Navier-Stokes equations. It is used to distribute the interaction force from the structure domain onto the surrounding fluid domain. The Navier Stokes equations are assumed to contain also the fiber-like one dimensional immersed elastic structure everywhere in the fluid domain. This structure may carry mass, but occupies no volume. Some disadvantages of IB method are eliminated by enhanced IB methods such as the immersed interface method (IIM) (Lee and Leveque, 2003), (Leveque and Li, 1994), (Xu and Wang, 2008), the extended immersed boundary method (EIBM) (Wang and Liu, 2004), the immersed finite element method (IFEM) (Gay et al, 2006), (Lee et al., 2008), (Liu et al., 2006a), (Liu et al., 2006b), (Zhang and Gay, 2007), (Zhang et al., 2004) and the immersed continuum method (ICM) (Wang, 2006), (Wang, 2007). Additional capabilities, flexibilities, versatilities and strengths have been obtained by using these novel methods in construction and computation such as allowing the use of non-uniform meshes, immersed solids occupying finite volumes, compressibility properties of solids and fluid, large motion of IB, using a different connection delta function with more accurate coupling. Applications of the IB method to the modeling of biological systems have recently been reviewed (Liu et al., 2006a). In later studies, the coupling of the Navier-Stokes equations and cell-to-cell interaction in the framework of the IFEM and mesh free method was used to model complex blood flows with deformable RBCs within micro and capillary vessels in three dimensions in the work of Liu and Liu (2006). Employing the IFEM, the detachment of the endothelial membrane was investigated in a pulsatile environment (Kopacz et al., 2008). Zhang and Gay (2008) used the IFEM with proper boundary conditions and material descriptions to simulate left atrium and left atrial appendage. The formation of platelet aggregates during blood clotting is modeled on both semi-discrete microscale and continuum macroscale models using the IB method (Fogelson and Guy, 2008). A 3D model based on the IB method for cell deformation to study rolling, adhesion, and deformation of multiple leukocytes in parabolic flow through micro channels has been developed with the study focusing on mechanical quantities such as fluid drag and flow resistance, and their dependence on cell deformability and cell concentration (Pappu et al., 2008).

The fictitious domain method has preferably been called the domain embedding method by some investigators. The basic idea behind the DLM/FD method is that the interior domains of the moving solid bodies are filled with the surrounding fluid, and a distributed Lagrange multiplier as a body force is introduced to impose the interior (fictitious) fluids into the solid region to satisfy the constraints of the solid body motions. The model was developed by Glowinski et al. (1999a) and (Glowinski et al. (1999b), and has been applied as an effective technique for solving particulate flow problems. Over the past decade, new formulations of DLM/FD methods have been proposed (Diaz-Goano et al., 2003), (Glowinski and Kuznetsov, 2007), (Yu, 2005), (Yu et al., 2006a), (Yu et al., 2006b) with new schemes which allow for a more efficient integration of the system of equations, such as the extension to deal with heat transfer in particulate flows in two dimensions, and the extension to deal the fluid flexible-structure interactions by replacing Newton's equations of motion for the rigid body with the continuum equations for the general solid material. Baaijens (2001) combines the ideas of the fictitious domain and the mortar element method by imposing continuity of the velocity field along an interface by Lagrange multipliers for slender bodies. Van Loon et al. (2004) have proposed a fictitious domain/adaptive meshing method in combination with another variation on the distributed Lagrange multiplier using a computationally inexpensive adaptive meshing algorithm. They have extended their model to study interactions of solids with the walls in a fluid domain (Van Loon et al., 2006). Thus, the model combines the benefits of the approaches to decrease their disadvantages without losing too much of the benefits of the Lagrange multipliers, adaptive meshing and ALE methods that adapt the fluid mesh near the boundary of the solid. A comparison between the conventional ALE method and three variations of the fictitious domain model including this method for deformable bodies has been presented to provide better insight in the strengths and the weakness of these models (Van Loon et al., 2007). De Hart et al. (2000) analyzed a 2D fluid structure interaction model of an aortic valve by using a fictitious domain method, and extended their work to a three-dimensional stented aortic valve (De Hart et al., 2003a). Later, De Hart et al. (2003b) combined fictitious domain with an arbitrary Lagrange-Eulerian method, integrated within the classical Galerkin FEM, to analyze the mechanical and hemodynamic behavior of a fiber-reinforced stentless aortic valve model. Stijnen et al. (2004) have investigated the applicability of a fictitious domain method for simulating the motion of a stiff prosthetic heart valve leaflet.

Recently, the LBM has been widely used in the area of fluid-structure and fluid-particle interactions. Feng and Michaelides (2004) applied the IB method into the LBM (IB-LBM) to utilize the desirable features of the methods. Moreover, the DLM/FD method was incorporated into LBM (LBM-DLM/FD) for 2D and 3D fluid elastic-structure interactions (Shi and Lim, 2007), (Shi and Phan-Thien, 2005). Instead of solving Navier-Stokes equations at the macroscopic level, the LBM is modeled at the microscopic level with mesoscopic kinetic equations by using particle distribution functions for simulating blood flow. The extended LBM by Chen et al. (2006b) is applied to obtain the detailed hydrodynamics in a variety of blood vessel setups, including prototype stented channels and four different human coronary artery geometries based on the images obtained from real patients. An LBM is utilized for obtaining steady and unsteady flow fields in a realistic aorta geometry evaluated from magnetic resonance angiography (Artoli et al., 2006). Zhang et al. (2007) and Zhang et al. (2008) combined the IB method to introduce the fluid membrane interaction and LBM in a 2D simulation of the deformability and aggregation of red blood cells (RBC) considering RBC membrane mechanics, plasma/cytoplasm viscosity difference, intercellular interaction, and the hydrodynamic viscous force. To study the flow-induced deformation of three-dimensional, liquid-filled capsules with elastic membranes like RBC, the immersed boundary concept is introduced into the framework of the lattice Boltzmann method, and the multi-block strategy is employed to refine the mesh near the capsule to increase the accuracy and efficiency of computation (Sui et al., 2008). Bernsdorf et al. (2008) used an extension of the LBM to compute the flow field for simulating blood coagulation. Sun and Munn (2008) developed an LBM that considers the blood as a suspension of particles in plasma, accounting for cell-cell and cell-wall interactions in order to examine the effect of the individual cells on macroscopic blood rheology. An LBM describing the microscopic behavior of moving particles was implemented into a computational code oriented towards the analysis of blood flow behavior in the presence of mechanical heart valves (Pelliccioni et al., 2007), (Pelliccioni et al., 2008).

The Lagrangian formulation can easily track interfaces or free surfaces between different materials and facilitate the handling of materials with a history-dependent constitutive relation. However, its disadvantage lies in it following large distortions of the computational domain without applying a frequent mesh update operation. The Eulerian formulation facilitates the handling of large distortion in the continuum motion. Nevertheless, the main disadvantage comes from following interfaces or free surfaces. The ALE approach is mainly used as a method of combining the advantages of both the Eulerian description of the fluid domain and the Lagrangian description of the solid domain while reducing their respective disadvantages as far as possible. In the ALE description, the nodes of the computational mesh may be moved with the continuum in a Lagrangian-like manner, or be held fixed in an Eulerian-like manner, or they can be moved in some arbitrary way to form a continuous rezoning capability. The freedom to move the computational mesh can make greater distortions of the continuum than would be allowed by a purely Lagrangian formulation, and with more resolution than that provided by a purely Eulerian formulation (Donea et al., 2004). However, some difficulties arrive such as the frequent degenerations of mesh quality due to the large motion of the interfaces, the large structure deformation, more complex geometry, the need for accurately capturing flow features in a region of high velocity gradients, and the high frequency of near collisions between particles in multiphase flow. The need for regulating the mesh, depending on the moving boundary or interface and the local or global re-meshing, requires mesh independent methods in connection with ALE to overcome these difficulties, thus increasing the robustness and accuracy for solving the problems. In practice, such regulating of the mesh can be automatically rendered by triggered mechanisms such as the element aspect ratio and the quality of the solution (Saksono et al., 2007). The mesh update process is generally difficult and a time consuming task. However, it strongly influences the success of the ALE. Therefore, a mesh generator must have the capability to build structured layers of elements around solid objects with reasonable geometric complexity for controlling the mesh resolution near solids and more accurate representation of the boundary layers. This reduces the frequency of re-meshing to an acceptable level, and produces high speed generation. Moreover, special purpose mesh generators can be used for increasing the scope, robustness, accuracy and efficiency of the specific problems when required.

In the last decade, ALE fluid structure interaction (FSI) studies related to blood flow have been widely studied. Li and Kleinstreuer (2005) and Li and Kleinstreuer (2006) have investigated post operative of endovascular stent graft treatments of abdominal aortic aneurysm (AAA), such as stent graft migration and endoleaks, to obtain quantitative criteria for optimizing endovascular stent graft designs, minimizing sac pressure magnitude, preventing endoleaks, and stent graft migration. Di Martino et al. (2001), Wolters et al. (2005), Scotti and Finol (2007), and Scotti et al. (2008) have investigated the interactions between blood flow and aneurysm wall as a guidance to assess the risk of rupture of the aneurysm by determining potential indicators of rupture or evaluative criteria for determining surgical repair to prevent rupture. Tezduyar et al. (2007), Tezduyar et al. (2008) and Tezduyar et al. (2009) have investigated the biomechanics of aortic, cerebral artery and carotid artery bifurcation aneurysms as test cases for their new method. Khanafer et al. (2009) have investigated the biomechanics of AAA under pulsatile turbulent flow condition. Torii et al. (2006a), Torii et al. (2006b), Torii et al. (2007), Torii et al. (2008), Torii et al. (2009) and Valencia et al. (2008) have emphasized the influence of hemodynamic factors and risk factors in the rupture of cerebral aneurysm. Tang et al. (1999) and Tang et al. (2002) have investigated the hemodynamics of blood flow and arterial wall mechanics in stenotic arteries. Valencia and Villanueva (2006) have investigated biomechanics of symmetric and non-symmetric stenotic cerebral arteries and mass transfer of low density lipoproteins macromolecules. Tang et al. (2008) simulated human carotid atherosclerotic plaques to quantify correlations between plaque progression as measured by wall thickness increase and plaque wall stress conditions. Kock et al. (2008) simulated carotid atherosclerotic plaques under pulsating turbulent flow conditions to facilitate estimation of the in-vivo longitudinal internal fibrous cap stresses. Valencia and Solis (2006), using constitutive wall models, simulated a representative saccular aneurysm model and one healthy model of the basilar artery to understand how the change in spatial and temporal distributions of pressure, effective wall stress, wall shear stress, and aneurysm displacement as a function of wall thickness. Chee et al. (2008) have presented a 3D fluid–structure interaction model of the RBC that can provide the means to study the FSI between the hyperelastic cell membrane and the enclosed liquid capsule. Gao and Hu (2009) modeled red blood cells as 2D elastic particles deforming in a Newtonian viscous shear flow. Most of the artery models in these studies were obtained from patients by medical imaging systems. As a result of recent studies, turbulent blood flow has been modeled using the k-w turbulence model. Computational and simulation studies have mostly been performed using the commercially available software packages such as ADINA, ANSYS ALE FSI solver, and SEPRAN. Another popular method is the deforming spatial domain/stabilized space time (DSD/SST) method (Tezduyar, 2003), an extension of ALE method and developed by Team for Advanced Flow Simulation and Modeling (T*AFSM). The stabilized space time FSI (SSTFSI) (Tezduyar and Sathe, 2007) method based on DSD/SST and an extended version of the sequentially coupled arterial fluid structure interaction (SCAFSI) for arterial fluid mechanics has now begun to be used. The assumption in the SCAFSI method is that the arterial deformation during a cardiac cycle is mostly driven by the blood pressure. Hence, a computation starts with a reference arterial deformation as a function of time, driven only by the blood pressure profile of the cardiac cycle.

Although the FSI models have been studied in great detail to understand fluid structure interactions, there is much more to be done in terms of both computational and experimental work. Studies on blood-wall interaction suffer from the limitations of biomechanical models of both vessel and blood flow. There are also some additional geometric simplifications and/or assumptions affecting the FSI models such as the assumption of uniform wall thickness, the sensitivities of medical imaging systems and segmentation algorithms. Complex variations of human vessel geometry and thus in blood flow conditions due to vessel shape and size, loading conditions, the presence of thrombus and surrounding tissues and organs are the other difficulties to be tackled in these studies. Most of the studies on blood cell plasma interactions have also contained simplifying assumptions such as no intercellular interactions and no plasma cytoplasm viscosity difference. However, the effect of microscale mechanisms on macroscale blood behavior in connection to each other has been shown. The FD method has been successfully applied to a wide range of solid particle flow problems especially in estimating drag and lift coefficients, but there has no related work on flow of elastic particles in liquids. In fact, the present FSI models applied to blood flow have not included the estimation of drag, lift, and virtual mass coefficients, the effect of the presence of neighboring entities on cell drag, the effect of a mobile interface, and the shear rate dependence of cell shape.

2.13. Conclusions

In this chapter, the physical nature of human blood and its viscosity models have reasonably well documented. An insight into the CFD modeling of two-phase blood flow is also presented. Recently, several multiphase CFD models based on Lagrangian and Eulerian approaches have been used as a means of characterizing realistic blood flow. The Lagrangian approach is applicable to blood flow modeling at relatively small concentrations of cells. The Eulerian approach, however, seems to be more suitable than the Lagrangian approach for dense suspensions of blood cells. This chapter has presented also an insight into hemodynamic hypotheses related to vascular diseases, biomechanical properties of vessel wall structures, to interaction between blood flow and vessel or cell structure, and especially into the CFD modeling of blood flow. It can be concluded that the role of CFD modeling on blood flow is very critical and expected to continue to increase in importance. Inspection of the available literature indicated that there was a need for review papers on the effect of RBC on hemodynamic of blood flow. The results of this study had been published as two international journal papers (Yilmaz and Gundogdu, 2008), (Yilmaz and Gundogdu, 2009). As referred previously in the body of the paper and the review articles, the major gaps derived from the upcoming investigations provide potential challenging areas for future investigations, as listed below;

1. Although there has been a considerable number of viscosity models in blood rheology, none of them has been commonly agreed upon or used. None of the models is fully expressing the effects of extremely complicated nature of blood rheology and its dependence of many factors. The groovy method used for obtaining the existing viscosity models is the parametric curve fitting on experimental apparent viscosity versus shear rate data, although the blood constitutive parameters in these models have been found to be related to internal structures of the blood such as RBC aggregation, RBC deformability, etc. The dependency of blood viscosity on each rheological property of the blood should be investigated and clarified separately by means of isolating the effects of remaining rheological properties.

2. The re-aggregation and viscoelastic behavior of blood detected in realistic pulsatile flows are much different from the corresponding behavior in steady flow. The blood viscosity models fitted on the data measured in the rheometer under the steady flow conditions are so not suitable for the analysis of realistic pulsatile blood flow. Observed blood apparent viscosity in the rheometers under the assumption of Newtonian flow pattern is also not suitable and the hematocrit value of tested blood also affects this pattern. The assumption of Newtonian pattern and neglecting the hematocrit effect on it can cause errors. The slip effect in the rheometers should also be prevented throughout the measurements.

3. Although there is a large number of studies on both Newtonian and non-Newtonian blood viscosity models in literature, there have been a variation on the critical value of limiting shear rate used for addressing the transition from non-Newtonian to Newtonian viscosity character of blood. Hematocrit dependence of this limiting shear rate value should be investigated for evaluating the proper application of both non-Newtonian to Newtonian viscosity models in CFD studies on blood flow.

4. Thixotropy must be considered in the regions of a substantial RBC residual time to allow the separated RBC to re-aggregate such as aneurysms and recirculation zones.

5. Viscoelasticity and thixotropy have generally accepted as less important for high shear regions. Even so, there is more need to develop in this area for low shear regions. Recent increases in study on viscoelastic models and its application in literature may be an evidence of this.

6. Making of a number of simplifying assumptions on physiologic conditions reduce very complicated construction of the realistic blood problem to a tractable problem to solve. However, each assumption grows away from realistic solution.

7. Drag and lift forces acting on blood cells are important for a realistic modeling of blood flow. Both drag and lift force models used in the present limited number of multiphase CFD models however neglect the presence of neighboring entities and suppose that the RBC is a spherical and rigid particle, and its membrane is immobile. The present study on fluid-solid and fluid-fluid or especially liquid-liquid two-phase flows has however indicated that the recently developed drag force models include the effects of dispersed particle shape and concentration, and the lift force models also include the effects of particle shape. As an initial attempt, these models can be adopted on multiphase modeling of blood flow. Moreover, the deformation, concentration, and aggregation behaviors of actual RBC at different shear rates and plasma viscosities should be further experimentally investigated so as to form more realistic drag and lift models over physiological ranges of effective parameters. The shape of the RBC and their aggregation at different shear rates and plasma viscosities should be investigated so as to obtain the dynamic RBC shape factor over a wide range of shear rates. The dependence of cell drag on volume fraction and Reynolds or Archimedes number should be determined over a physiological range of hematocrit. The effect of tank treading motion (i.e., mobility of RBC membrane) on the drag and lift forces especially at high shear rates should also be clarified.

8. The present chater on two-phase flows also shows that lift force acting on dispersed particles causes to the lateral migration of particles in a flow vessel, so it plays a key role on the traveling trajectory of dispersed particle and in the homogeneity of dispersed phase in vessel. The present multiphase CFD models of blood flow, however, do not consider the lift force or consider with a limited effect by means of using a fixed lift coefficient with the value of 0.5, accepted as equal also to the virtual mass coefficient.

9. The hemodynamic hypotheses and the related studies implied that there is a strong effect of wall shear stress (WSS) on cardiovascular diseases such as atherosclerosis and aneurysms. However, the exact role and the relative importance of proposed hemodynamic parameters on the vascular

endothelium, the pathogenesis of cardiovascular diseases, and the progression of arterial lesions remain unclear.

10. There is still lack of enough experimental data on some biomechanical conditions of vessel wall structure such as residual stresses, heterogeneity, smooth muscle activation and vasomotion. The human vessel geometry also exhibits wide variations according to shape, size, thrombus presence, loading conditions, and the presence of surrounding tissues and organs. Using some simplifying assumptions in CFD models to initiate these biomechanical and geometrical conditions of vessels therefore lead to the solution of an elastic vessel constitutive problem that also causes considerable deviations from realistic ones.

11. Many computational models have been proposed to describe various aspects of the fluid structure interaction (FSI) system. The FSI models with micro and macro scale approaches have been classified as boundary and non-boundary fitted models and recently applied to blood flow. The micro scale studies on particulate cell motion give hope for constructing macro scale models such as blood viscosity model and blood cell drag model to use within a CFD model. Most of the FSI models on interaction between blood cell and plasma also contained some simplifying assumptions such as no intercellular interaction and no plasma cytoplasm viscosity difference.

CHAPTER 3

COMPUTATIONAL INVESTIGATION OF VELOCITY FIELD FOR INTERMEDIATE REGION OF LAMINAR PULSATILE PIPE FLOW

3.1. Introduction

Pulsatile flow is composed of a positive mean and a periodically varying time-dependent component (generally sinusoidal as in nature) around the mean, whereas in oscillatory flow, time-dependent component varies around a zero mean. Investigation of these flows has of great importance especially in the biomedical science and industry. Physical characteristics of blood flow orient the researchers towards blood rheology for well analysis of the arterial blood flow (Yilmaz and Gundogdu, 2008), (Yilmaz and Gundogdu, 2009). Understanding the mechanisms of pulse generation through the pipe lines including the devices operating on reciprocating motion such as positive displacement pumps and compressors, and the fittings such as vanes, valves, junctions, etc. has also very critical. Furthermore, inertia dominant character of pulsatile pipe flow has been used as a good choice for the prevention of widely observed obstruction and choking problems through two- or multi-phase flow lines such as waste-water lines, drainage (slurry) lines, and pneumatic conveying lines.

Pulsatile and oscillatory flows in laminar regime which are two representative types of unsteady flow have been studied theoretically and experimentally since the first quarter of 20^{th} century and these investigations were reviewed in great detail (Gundogdu and Carpinlioglu, 1999a), (Carpinlioglu and Gundogdu, 2001a). Analytical and numerical solutions of the continuity, momentum, and energy equations for fluids of any kind are relatively rare due to the mathematical complexities. Analytical solutions are particularly difficult because of the increased dimensionality (Sexl, 1930), (Szymanski, 1932), (Womersley, 1955), (Womersley, 1957), (Uchida, 1956), (Linke and Hufschmidt, 1958), (Hershey and Song, 1967), (Ohmi et al., 1981), (Ohmi and Iguchi, 1981), (Donovan et al., 1991), (Donovan et al., 1994). Approximate solutions are based on modified and simplified equivalent viscosity representations for Newtonian fluids (Atabek and Chang, 1961), (Brown, 1962), (D'Souza and Olderburger, 1964), (Zielke, 1968), (Jayasinghe et al., 1974), (Ohmi et al., 1976). Experimental investigations require expensive measurement devices and excessive number of measurement runs caused by the high number of characteristic parameters such as frequency, amplitude, and Reynolds number (Richardson, 1928), (Richardson and Tyler, 1930), (Atabek et al., 1965), (Linford and Ryan, 1965), (Florio and Mueller, 1968), (Harris et al., 1969), (Denison, 1970), (Denison et al., 1971), (Gerrard and Hughes, 1971), (Hino et al., 1976), (Muto and Nakane, 1980), (Ohmi et al., 1982), (Unsal et al., 2005). Numerical exact solutions of the momentum equations based on finite-difference technique are somewhat more common for Newtonian fluids, but the constitutive complexities of non-Newtonian fluids hinder even these powerful techniques (Rosenhead, 1963), (Gerlach and Parker, 1967), (Balmer and Fiorina, 1980), (Donovan et al., 1991). Computational models based on finite-volume technique have recently accepted as a vital means for investigating the pulsatile blood flow especially in complex regions (Steinman, 2002), (Jung et al., 2006a). Computational studies may not have the disadvantages of experimental studies, but there are other difficulties to be handled such as the mathematical complexity of pulsatile flow dynamics, the requirement for an excessive number of finite elements to obtain accurate solutions, and the application of realistic boundary conditions without simplifications. Developing an efficient and reliable CFD (Computational Fluid Dynamics) model is thus a hard task. Moreover, CFD models should be validated by accurately chosen and treated experimental data. For nearly three decades, CFD models have, however, been used by investigators to address pulsatile blood flow because of their advantage in the simplicity of handling a variety of pulatile flow conditions by only changing related initial and boundary conditions, as well as the possibility of providing information that is hard or even impossible to measure. CFD models have been found to be an efficient and reliable tool during this development period. It is likely to continue to play an important role in pulsatile flow studies.

It has been understand from the above literature that the flow field of laminar pulsatile pipe flow is dependent on the dimensionless frequency parameter, $\sqrt{\omega'}$ (i.e., Strouhal number or Womersley parameter) but not on Reynolds number and amplitude (Ohmi et al., 1976). The laminar regime of pulsatile pipe flow can be classified into three sub-regions such as quasi-steady, intermediate and inertia dominant ones with respect to this frequency parameter. The limiting values of the frequency parameter were evaluated respectively as $\sqrt{\omega'_q}$ =1.32 between the quasi-steady and the intermediate regions, and as $\sqrt{\omega'_t}$ =28.0 between the intermediate and the inertia dominant regions (Ohmi et al., 1981). At low frequencies (i.e., $\sqrt{\omega'} <$ 1.32), the cross sectional distribution profile of axial velocity is parabolic so that the flow is in quasi-steady state. At high frequencies (i.e., $\sqrt{\omega'} >$ 1.32), the interaction between viscous and inertial effects alters the axial velocity profile of oscillatory and pulsatile pipe flows so that it gradually varies from parabolic shape to a rectangular-like shape with an increase in $\sqrt{\omega'}$ up to 5.0 and so it has a peak. The peak of distribution tends to approach the pipe wall gradually with further increases in $\sqrt{\omega'}$ >5.0 (Hino et al., 1976), (Muto and Nakane, 1980), (Ohmi et al., 1982). In the literature, there exists an indistinctness about the variation mechanism of the parabolic profile up to a rectangular-like shape and the movement of the distribution peak towards the pipe wall when the value of $\sqrt{\omega'}$ increases over 5.0 in the intermediate region. The unique variation mechanism proposed for it is the gradual variation by Muto and Nakane (1980) due only flow visualizations. It has also been understand from the above literature that the results of analytical, approximate, and experimental investigations on the velocity profile in the quasi-steady region of laminar regime confirms each other within a deviation range of 5%, but this deviation increases with the increase of $\sqrt{\omega'}$ in the intermediate region. However there has no any finite-difference and/or finite-volume technique based computational study on the velocity field in the intermediate region of laminar-pulsatile pipe flow. The limited numbers of the present computational studies are only directed on the variation of velocity profile as a function of the power-law index of fluid viscosity (Balmer and Fiorina, 1980) and on the flow resistance as a function of $\sqrt{\omega'}$ (Donovan et al., 1994).

In view of the literature, the present study is directed to clarify the indistinctness about the variation mechanism of the velocity profile throughout the intermediate region of laminar-pulsatile pipe flow by means of the computational techniques in order to evaluate a comparison basis between them. In the PhD study of Gundogdu (2000), the velocity profiles across the cross-section of a horizontal smooth pipe at a test section and the static pressure differences between two static taps symmetrically apart from the test section are measured through 30 different instants of a pulsation cycle by means of traversing a hot-wire probe and a pressure transducer respectively for 29 different experimental runs covering the ranges; $2.26x10^3 \pm 17\% \leq Re_{ta} \leq 4.36x10^3 \pm 10\%$, $5.1 \pm 4\% \leq \sqrt{\omega'} \leq 28.0 \pm 0.05\%$, $0.03 \leq A_r \leq 0.71$. The variation of velocity profiles are analyzed computationally by using the finite-volume based Fluent software-package v6.3.26 for the initial and the boundary conditions selected to be same with four different ones of the Gundogdu's experimental runs. Finally, the experimental and the computational velocity profiles evaluated in the present study are compared with each other and with the well-known Blasius's and Prandtl's distributions for the laminar and the turbulent regimes of the steady pipe flow respectively. As a consequence of these comparisons, evaluated results on the variation of velocity profiles with respect to the characteristic flow parameters; $\sqrt{\omega'}$, Re_{ta}, A_r and the results on the compatibility of computational technique for this flow type are discussed in view of the citations in the available literature (Hino et al., 1976), (Muto and Nakane, 1980), (Ohmi et al., 1976), (Ohmi et al., 1981), (Ohmi et al., 1982).

3.2. Experimental Study of the Test Case

Experimental study was carried out on a specially constructed test rig to determine the characteristics of pulsatile pipe flow at different flow regimes (Gundogdu, 2000). A schematic layout of the test rig is shown in Fig. 3.1. Air at ambient conditions is used in the test rig as the working fluid. The test rig is made up of the basic components; namely, steady flow generation unit, pulse generator, pipe line, flow regulation unit, measurement instruments, and an interactive data acquisition and control system. The pipe line is constructed of rigid and smooth polyvinyl chloride pipe with 50.4 mm internal diameter to enable velocity and pressure drop measurements. The pipe line is connected to the turbulence removing unit at one end and to the piston of the pulse generator at the other end by means of two bell-shaped smooth transitions. The cross-sectional areas of the transitions are designed to change steadily in the flow direction, so that the mean velocity of air changed steadily through the transitions. A honeycomb made of plastic straws preceded by a coarse screen and followed by a fine screen is used in the flow regulation unit at the air entry of the pipe line to control scale and intensity of flow turbulence in view of the investigations by Loehrke and Nagib (1976), and Farell and Youssef (1996). The operation performance of the rig is made fairly well by means of conducting a series of preliminary calibration tests based on pressure drop and velocity measurements for generated pulsatile flows with different frequency, amplitude and Reynolds numbers. The time-averaged (mean) and the oscillatory components of the pulsatile flow are generated by means of a centrifugal suction fan and a reciprocating piston driven by the slider crank of a scotch-yoke mechanism, respectively. The magnitude of the mean flow component is controlled by controlling the rotational speed of the fan by means of an AC motor speed control unit (6SE3221-3DC40, SIEMENS). The time-averaged Reynolds number, Re_{ta} of the generated pulsatile flow can thus be settled to any chosen value by adjusting the rotational speed of the fan. Pulsation frequency is controlled by adjusting the rotational speed of the slider crank by means of a second AC motor speed control unit (6SE3013-4BA00, SIEMENS). Pulsation amplitude can only be adjusted by changing the stroke of piston. Velocity measurements are made at the test section by using a hot-wire anemometer (CTA 56C01, DANTEC) in combination with the 55P11 general purpose type miniature hot-wire probe. The test section is located 125 D downstream of the flow regulation unit to obtain the fully developed laminar-pulsatile pipe flows in view of the studies of Florio and Mueller (1968), and Ohmi et al. (1976). The local axial velocity, u is measured at 14 different radial positions to obtain the velocity profile across the pipe cross section. The measurement sensitivity of u with the how-wire anemometer changes respectively from ±2% to ±0.5% when it changes from 0.15 m/s to 3 m/s in the present study. The hot-wire probe traversing mechanism used for this purpose is driven by a computer-controlled step motor with 200 steps per revolution. The step motor had a step rate of 1.8^0/digital signal pulse.

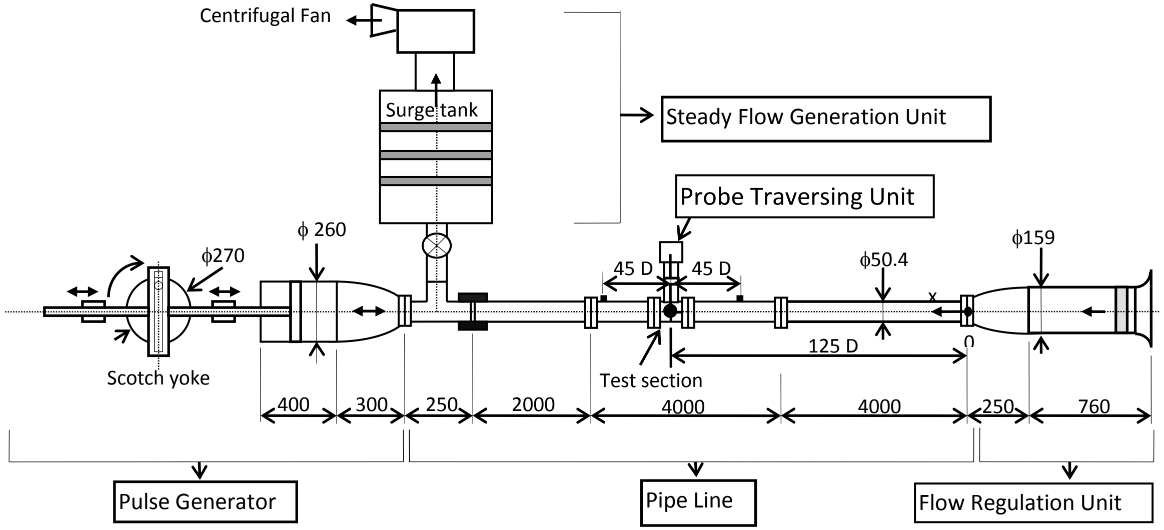

Figure 3.1. A schematic layout of the test rig

The traversing mechanism transforms rotational motion of the step motor into a linear displacement sensed by a micrometer with a dimensional sensitivity of ±2.5 micrometers. The static pressure difference between two static taps symmetrically apart from the test section with 45D axial distance is measured by using a difference type inductive pressure transducer (PD1, HBM) with a diaphragm of 300 Hz natural frequency. It has a measurement range of 0 to ±0.01bar. The HBM's 4.8 kHz carrier frequency type amplifier, MVD 2555 was also used in connection with the pressure transducer. The measurement sensitivity of ΔP changes respectively from ±5% to ±0.5% when it changes from 0.3 Pa to 5 Pa in the present study. The determination of the axial apart distance (L=90D) between the taps is done in view of the study carried by Zhao et al. (1990). The fully developed static pressure gradient dP/dx at the test section of the pipe line is then approximated by $\Delta P/L$ with accuracies better than 99%.

The period, t_p of a pulsation cycle changes with changing the pulsation frequency. So it should be made dimensionless to obtain a common comparison basis between the measurements for different pulsation periods. The non-dimensional phase parameter is used for this purpose as mostly used in literature; phase number= $\omega.t\,/(2\pi/30)$, where t is the time in seconds changes in the range $0 \leq t \leq t_p$ through the cycle and ω is the angular frequency of the pulsation in radian/seconds. The axial velocity data at 14 radial positions across the pipe and the static pressure difference data for any experimental case are accumulated at 30 different but equally spaced instants of a pulsation cycle. This timing of the data accumulation is obtained by means of the triggering time signals generated by an optical encoder (TRD-J-30-RZV, Koyo Electronics) coupled on the crank of the pulse generator. The data accumulation for each of 30 different phases in a cycle is continued through 200 cycles to obtain the data amounts allowing the treatment of an ensemble averaging. Control of the probe traversing unit of the hot-wire anemometer and all accumulation, acquisition, and processing of the measured velocity and pressure difference data in the test rig are carried by means of a fully computer-aided interactive data acquisition and control system. More detailed descriptions of the test rig, the data acquisition system, and the experimental error analysis can be found in our previous studies Carpinlioglu and Gundogdu (2001b) and Gundogdu and Carpinlioglu (2002).

Table 3.1. Characteristic parameters of the experimental runs

Run No	Re_{ta}	A_r	$\sqrt{\omega'}$	Stroke (mm)
1	1869.0	0.0582	4.899	20
2	1924.6	0.0790	7.110	
3*	**2062.6**	**0.1572**	**12.516**	
4	1901.1	0.5517	23.035	
5	2077.6	0.7113	28.001	
6	4346.6	0.0333	4.926	
7	4201.4	0.0595	7.114	
8	4131.0	0.0939	12.509	
9	4229.3	0.2733	23.035	
10	4126.6	0.4271	28.015	
11	2057.3	0.1311	5.287	40
12	2125.8	0.1634	7.088	
13	2075.3	0.4085	12.495	
14	4064.6	0.1061	5.312	
15*	**4613.2**	**0.1310**	**7.079**	
16	4210.1	0.2285	12.484	
17	2621.5	0.1903	5.312	70
18	2553.4	0.2432	7.082	
19	4786.2	0.1445	5.287	
20	3927.3	0.2391	7.082	
21	3990.7	0.4171	12.527	
22	2653.9	0.2632	5.262	100
23	1924.9	0.4793	7.079	
24	4298.9	0.1952	5.005	
25	4163.5	0.3239	7.105	
26*	**2233.0**	**0.4043**	**5.153**	130
27	1964.8	0.6449	7.129	
28*	**4240.0**	**0.2822**	**5.084**	
29	4032.8	0.4466	7.121	

*denotes the computationally analyzed runs

The velocity and pressure difference measurements of this study were planned for 50 different systematically organized runs of the test rig with 2 different time-averaged Reynolds number, Re_{ta} of $2.26x10^3 \pm 17\%$ and $4.36x10^3 \pm 10\%$, 5 different dimensionless frequency parameter, $\sqrt{\omega'}$ of 5.1±4%, 7.09±0.6%, 12.5±0.2%, 23.0±0.1%, and 28.0±0.05%, and 5 different piston strokes of 20 mm, 40 mm, 70 mm, 100 mm and 130 mm. The preliminary calibration measurements however indicated that the generated pulsatile pipe flows for 21 of the planned runs are partly or fully reversed for which the present direction-insensitive hot-wire probe can not be used (Gundogdu, 2000). The detailed velocity and pressure difference measurements are therefore conducted for the remaining 29 different runs listed in Table 3.1 as covering the intermediate region of the laminar-pulsatile pipe flow.

3.3. Computational Study

The horizontal pipe line of the experimental test rig together with the flow regulation unit at the air entry (see Fig. 3.1) is considered as a 2D axis-symmetric tubular system in order to reduce the number of grids and created by using the Gambit v2.4.6 software. The honeycomb, the coarse screen, and the fine screen present in the flow regulation unit of the test rig is not considered in the inlet section of the computational tubular domain for this study according to the requirement on excessive number of 3D grids and so extremely long solution and convergence times, but it must be noted here as a further work to evaluate absolute similarity between the experimental and the computational domains. The mirror view of the axis-symmetric geometry combined with the structured mesh of computational domain for a main flow along the x-axis is shown schematically in Fig. 3.2.

A commercial CFD software package, Fluent v6.3.26 is used to model the laminar-pulsatile viscous pipe flow. Governing equations of mass and momentum with appropriate initial and boundary conditions are adopted to solve numerically everywhere in the system. The continuity and momentum equations for 2D incompressible flows can be written respectively as follows:

$$\frac{\partial \rho}{\partial t}+\rho_o\left(\frac{\partial u}{\partial x}+\frac{\partial v}{\partial r}+\frac{v}{r}\right)=0 \tag{3.1}$$

$$\frac{\partial u}{\partial t}+u\frac{\partial u}{\partial x}+v\frac{\partial u}{\partial r}=-\frac{1}{\rho_o}\frac{\partial P}{\partial x}+\upsilon\left(\frac{\partial^2 u}{\partial x^2}+\frac{\partial^2 u}{\partial r^2}+\frac{1}{r}\frac{\partial u}{\partial r}\right)+\frac{\upsilon}{3}\frac{\partial}{\partial x}\left(\frac{\partial u}{\partial x}+\frac{\partial v}{\partial r}+\frac{v}{r}\right) \tag{3.2}$$

$$\frac{\partial v}{\partial t}+u\frac{\partial v}{\partial x}+v\frac{\partial v}{\partial r}=-\frac{1}{\rho_o}\frac{\partial P}{\partial r}+\upsilon\left(\frac{\partial^2 v}{\partial x^2}+\frac{\partial^2 v}{\partial r^2}+\frac{1}{r}\frac{\partial v}{\partial r}-\frac{v}{r^2}\right)+\frac{\upsilon}{3}\frac{\partial}{\partial x}\left(\frac{\partial u}{\partial x}+\frac{\partial v}{\partial r}+\frac{v}{r}\right) \tag{3.3}$$

where x is the axial coordinate, r is the radial coordinate, P is the static pressure, u is the axial velocity, v is the radial velocity, ρ_o is the density at t=0, υ is the kinematic viscosity. For pulsatile flow, an ensemble-averaged (i.e., short-time averaged) value has also a long-time averaged value and an oscillatory component due to the pulsation which are denoted by subscripts "ta" and "os" respectively. The instantaneous values can so be written as; $P=\overline{P}_{ta}+\overline{P}_{os}$; $u=\overline{u}_{ta}+\overline{u}_{os}$; $v=\overline{v}_{ta}+\overline{v}_{os}$.

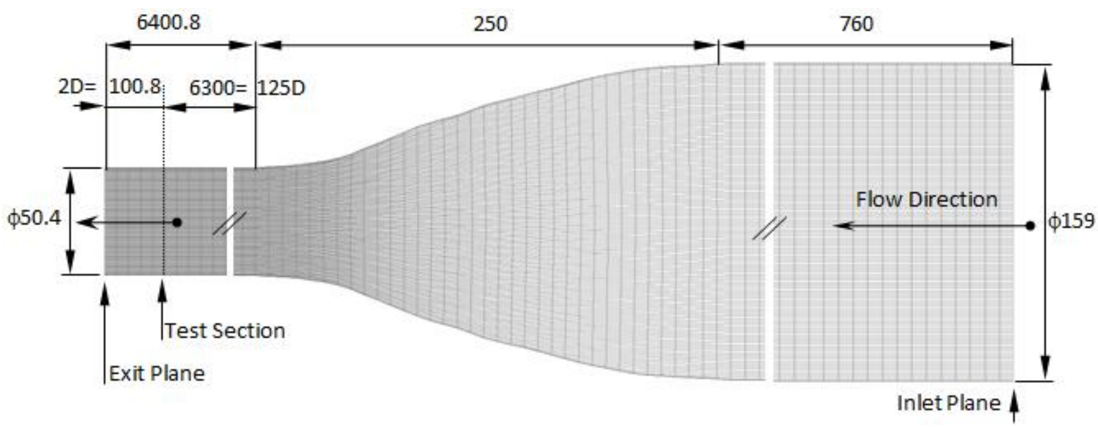

Figure 3.2. A mirror view of 2D axis-symmetric mesh of the computational domain

At the test section of the test rig, the values of cross sectional mean velocity, U_m predicted from the previously measured velocity distributions through the 30 different phases of the pulsation cycle for the selected four different runs; Run 28, Run 26, Run 15, and Run 3 as marked by the star (*) on Table 3.1 are therefore fitted with Fourier series up to sixth harmonics as follow;

$$\overline{U}_m = \overline{U}_{m,ta} + \sum_{n=1}^{6} \left|\overline{U}_{m,os,n}\right| \cos(n\omega t + \angle\overline{U}_{m,os,n}) \tag{3.4}$$

and thus, the time-averaged value $\overline{U}_{m,ta}$, the amplitude $\left|\overline{U}_{m,os,1}\right|$, and the phase angle $\angle\overline{U}_{m,os,1}$ of the fundamental wave are determined for each of the runs as follows;

$$\overline{U}_m = \overline{U}_{m,ta} + \left|\overline{U}_{m,os,1}\right| \cos(\omega t + \angle\overline{U}_{m,os,1}) \tag{3.5}$$

It is well known that the general tradition in CFD packages is applying the pressure boundary condition at the exit plane and the velocity boundary condition at the inlet plane. However, the application of the reverse of this tradition can also be possible under some circumstances as suggested by the Introductory Fluent Notes (Ansys Inc., 2006). Although the time-dependent variation of static pressure at the test section is not measured, the cross sectional velocity distribution at the test section and the static pressure difference around it are both measured previously throughout the pulsation cycles in the first part of the present study. Instead of using the general tradition about the boundary conditions, the velocity outlet and the pressure inlet boundary conditions are therefore preferred as a necessity in the computational part of the present study. The first harmonic of the U_m wave predicted from Eq. (3.5) is used to define the cross sectional mean velocity at the exit plane of the tubular computational domain shown in Fig. 3.2 as a “velocity outlet” boundary condition by specifying negative velocity as enabled by the Fluent software. This time-dependent velocity outlet condition at the exit plane is defined into the Fluent by means of a user defined function, UDF in C++ language as an interpretation. The pressure inlet boundary condition is applied at the inlet plane of the flow regulation unit of the domain by means of setting it to the atmospheric pressure. In order to eliminate the exit effects on the flow at the test section, the exit plane of the tubular domain is located at 100.8 mm (i.e., 2D) downstream of the test section as a straight buffer zone. The no-slip condition is imposed at the pipe walls.

Once the appropriate continuum structures have been defined, the pressure-based segregated algorithm with an implicit unsteady second order scheme is used together with non-iterative time advancement (NITA) option under transient controls to solve the governing equations. The momentum equations are discretized using a second order upwind discretization scheme. The pressure term is firstly discretized using a second order scheme and then both the pressure and the velocity terms are coupled with each other by using the Pressure-Implicit with Splitting of Operators (PISO) scheme. Evaluating grid independent solutions is also an important aspect to minimize the error in CFD results. So, it is practical to reach the grid independent solutions by means of several tests on computational mesh. The number of cell elements and the number of nodes in the half of the entire fluid domain are received respectively as 68100 and 69296 for the initial test of computational mesh. They are also checked respectively for the 17040 and 17639 numbers through the secondary test. Fig. 3.3 shows the results on the pressure difference at the test section after six complete pulsation cycles for these two different tests of computational mesh. It is seen from the figure that the pressure difference data for the both tests of mesh are quite similar through the all 30 phases of the cycle. This indicates that the 68100 cells are enough to reach the grid independency for the solutions and therefore the test for a greater number of cells is not required. To ensure proper temporal resolution, transient calculations are conducted by using 900 and 1800 equal time steps per cycle. Additionally, calculations are continued for the six complete pulsation cycles to ensure that cycle-to-cycle variations of pulsation become minimal. The average run time for a complete pulsation cycle was approximately 1/4 h on a personal computer having a quad processor a duo processor E6400 (2 Mb cache, 2.13 GHz) and 1 Gb ram running under a Windows 32bit system with 69296 mesh nodes.

The computational study is conducted repetitively for the four conditions kept to be same with the conditions of the selected four different experimental runs; namely, Run 28, Run 26, Run 15, and Run 3 with different characteristic flow parameters; Re_{ta}, $\sqrt{\omega'}$, and A_r. The experimental U_m data at the test section are ready for these runs to use as benchmarks for the computational study. These runs are selected to be typical examples for the intermediate region of laminar-pulsatile pipe flow (see Table 3.1). The availability of the fully-developed velocity profiles at the test section is also checked as proper before each of the computational runs. The time-dependent variations of both the cross sectional velocity profiles and the pressure difference at the test section are then received for these runs as an output of the computational study and compared with the corresponding experimental data.

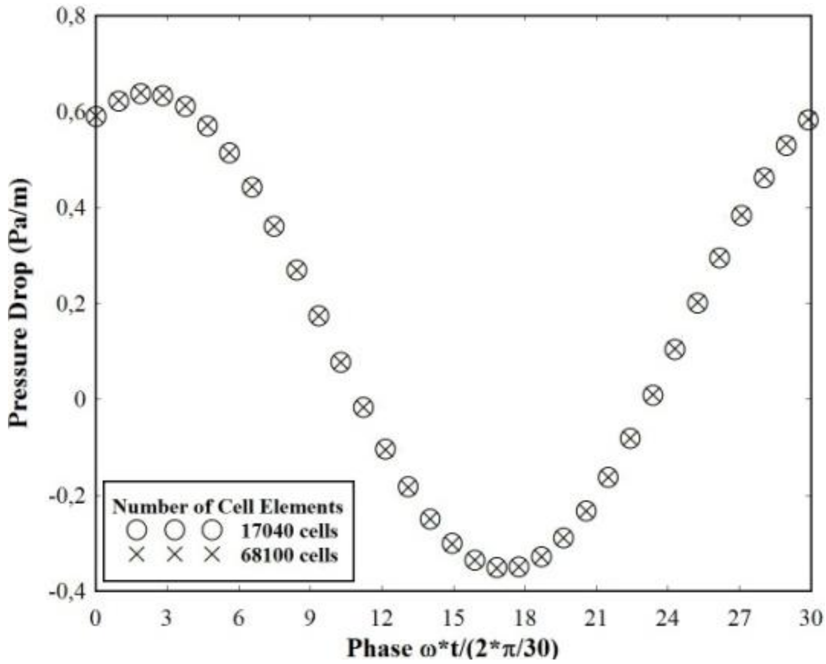

Figure 3.3. Results of ΔP/L computation for two different cell numbers

3.4. Results and Discussion

In the first part of this study, the variations of the cross sectional mean velocity, U_m and the approximate pressure gradient, ΔP/L through 30 different instants (phases) of a pulsation cycle are evaluated due to the velocity distribution and the pressure difference measurements for the 29 different runs listed in Table 3.1. In the second part, the variation of the pressure gradient, ΔP/L is also computed numerically by means of using model fits on the experimentally evaluated variation of the cross sectional mean velocity as an input parameter at the exit plane of test section to the Fluent for the Run 28, Run 26, Run 15, and Run 3. The variations of the experimentally evaluated U_m and ΔP/L data, the model fit on U_m data, and the computational output data on ΔP/L through a pulsation cycle are all shown in Figs. 3.4-3.7 for these four runs. The coefficient of determination, R^2 and the standard error of estimate are used together with the statistical models to determine and show the relationship between the measured data and the model fits on U_m. The deviations of the model fits from a standard sine wave are therefore shown in Table 3.2 for these runs.

Table 3.2. Statistics between the measured data and the model fits on U_m

Run No	R^2	Standard error
Run 28	0.9886	0.0274
Run 26	0.9894	0.0201
Run 15	0.9972	0.0068
Run 3	0.9952	0.0048

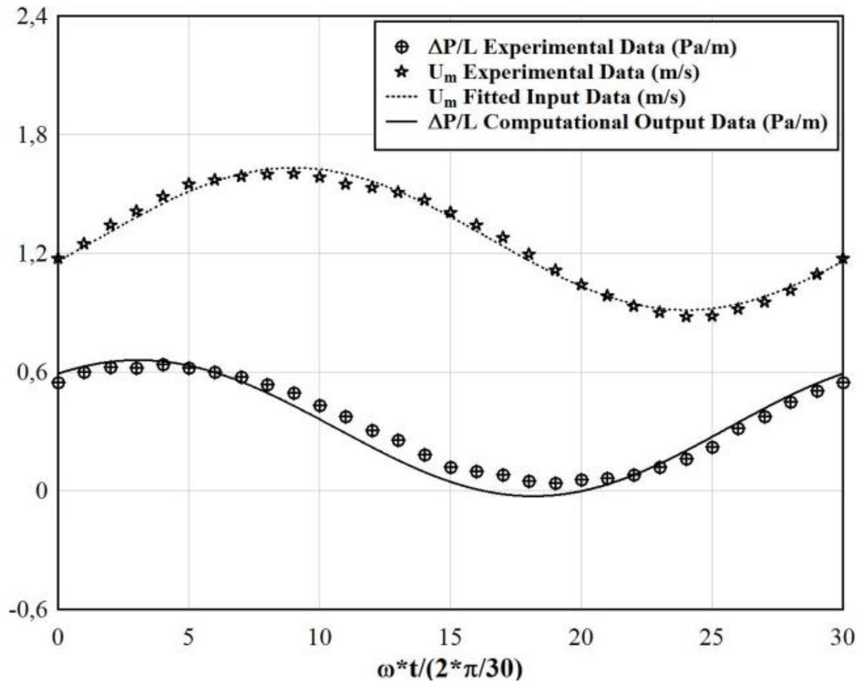

Figure 3.4. Variations of experimental and computational U_m and ΔP/L through a pulsation cycle (Run 28: Re_{ta}=4240.0, A_r=0.2822, $\sqrt{\omega'}$=5.084)

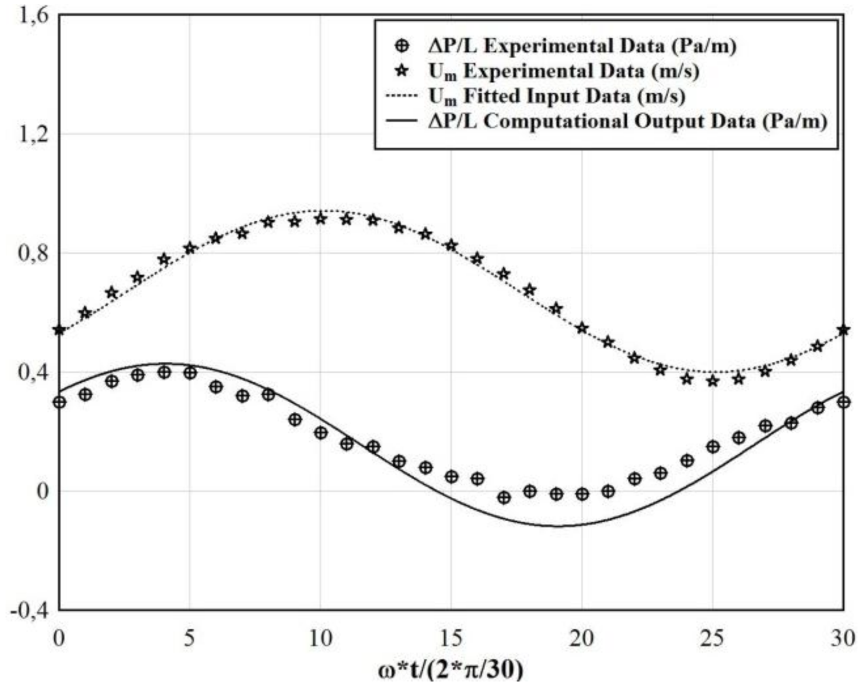

Figure 3.5. Variations of experimental and computational U_m and $\Delta P/L$ through a pulsation cycle (Run 26: Re_{ta}=2233.0, A_r=0.4043, $\sqrt{\omega'}$=5.153)

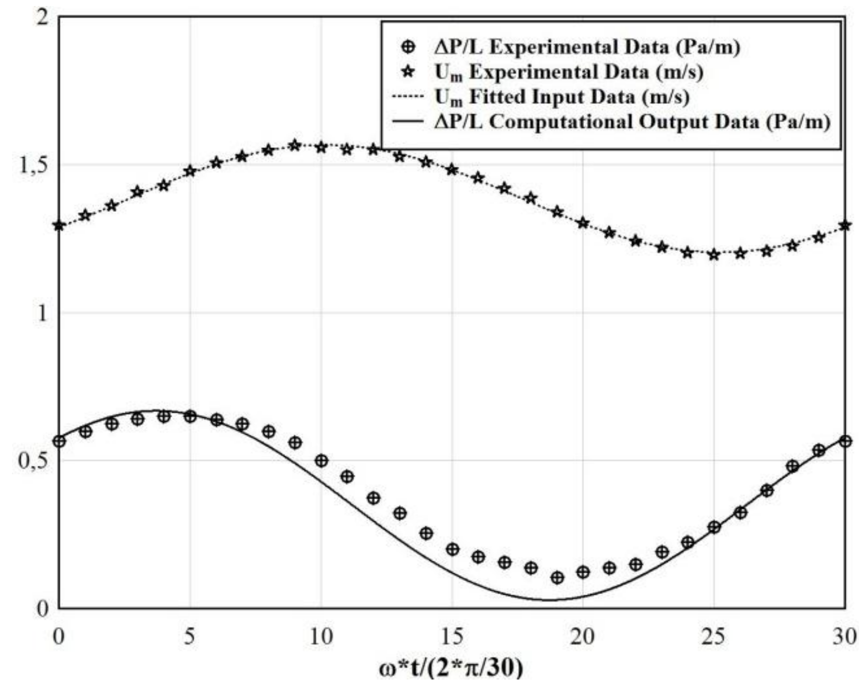

Figure 3.6. Variations of experimental and computational U_m and $\Delta P/L$ through a pulsation cycle (Run 15: Re_{ta}=4613.2, A_r=0.1310, $\sqrt{\omega'}$=7.079)

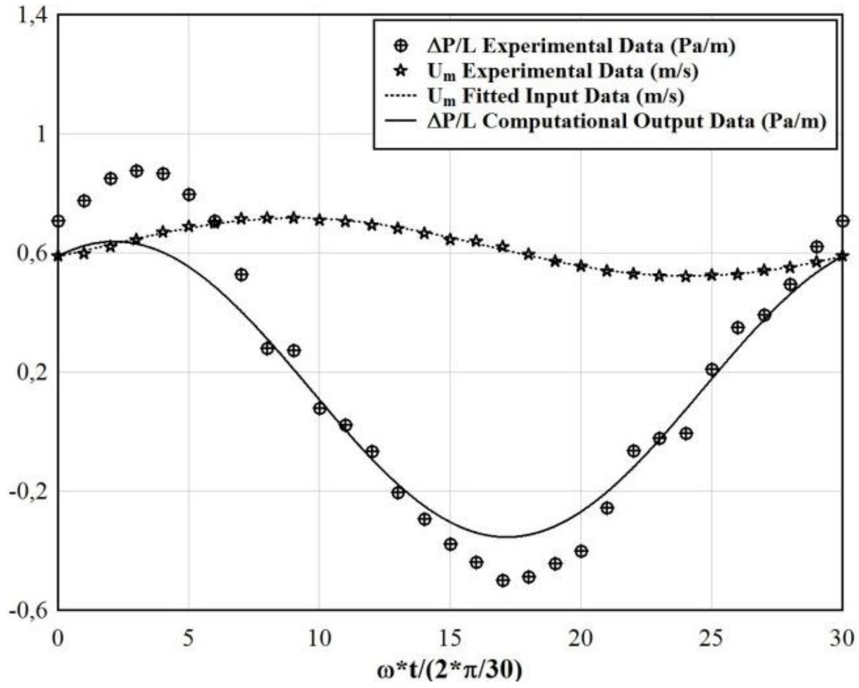

Figure 3.7. Variations of experimental and computational U_m and $\Delta P/L$ through a pulsation cycle (Run 3: Re_{ta}=2062.6, A_r=0.1572, $\sqrt{\omega'}$=12.516)

It is seen from the Figs. 3.4-3.7 that; the dimensionless phase (i.e., $\omega t/(2\pi/30)$) intervals, 0~10 and 25~30 approximately show the accelerating period of the pulsation cycle where the experimental values of $dU_m/dt > 0$. However, the phase interval, 10~25 shows the decelerating period where $dU_m/dt < 0$ for all of the studied runs. The pressure gradient, $\Delta P/L$ reaches a maximum near the middle-inflection phase (~3) of accelerating period and reaches a minimum near the middle-inflection phase (~18) of decelerating period. The phase lags of the U_m and the $\Delta P/L$ waves from the generated pulsation at the downstream pulse generator are approximately 120° and 42°-48° respectively and so the phase shift angles between them are detected to be varying between 72° and 78° for these four runs. As the $\sqrt{\omega'}$ increases, the phase shift increases slightly. The computational output data on $\Delta P/L$ show a good agreement with the corresponding experimental ones for nearly all phases of these runs except the phases near the inflection points of accelerating and decelerating periods (see especially Fig. 3.7). The bad agreement near the inflection points becomes better when $\sqrt{\omega'}$ decreases and Re_{ta} increases.

In order to show clearly the absolute deviations between the measured and the computed axial velocity data, the measured and numerically computed radial profiles of axial velocity, u at 10 different phases of a pulsation cycle are also shown in Figs. 3.8 through 3.11 for these four runs, respectively. In these figures; the experimental and the computed velocity profiles are shown by means of different data symbols and solid lines respectively for the selected 10 different phases; 0(or 30), 3, 6, 9, 12, 15, 18, 21, 24, 27 through the pulsation cycle. These ten phases are especially selected to be equally spaced in order to fully represent the variation of velocity profiles through the accelerating (0(or 30), 3, 6, 9, 27) and the decelerating (12, 15, 18, 21, 24) periods including their middle-inflection phases (3 and 18). These figures show that; the computational and experimental data on axial velocity confirm each other except the near-wall region for $0.95<r/R<1.0$ and the central core region for $r/R<0.4$ at all phases of the runs. The deviation in the near-wall region seems to be caused by the well-known wall-proximity effect on the hot-wire probe used for the velocity measurement. However in the core regions, the computed data considerably underestimate the corresponding experimental ones and the percent deviation between them reaches to a maximum at the centerline($r/R=0$). The detected maximum deviations at the centerline become 10.5 % for Run 28, 13.5 % for Run 26, 9.1 % for Run 15, 1.7 % for Run 3 at different phases. It can be detected that the percent deviation in the core region directly proportional with A_r but indirectly proportional with both of $\sqrt{\omega'}$ and Re_{ta}. It decreases when A_r decreases but when $\sqrt{\omega'}$ and Re_{ta} increase. It can be also understand that $\sqrt{\omega'}$ and A_r parameters seem to be more effective than Re_{ta} on the deviation.

For better understanding the reasons of this deviation between the experimental and the computed velocity data especially in the central core region and comparing them with the well-known Blasius's parabolic and the Prandtl's rectangular-like (i.e., blunt) shaped velocity profiles corresponding to the steady laminar and the steady turbulent pipe flows respectively, Figs. 3.12 through 3.15 are formed by means of making non-dimensional the lower axes of Figs. 3.8-3.11.

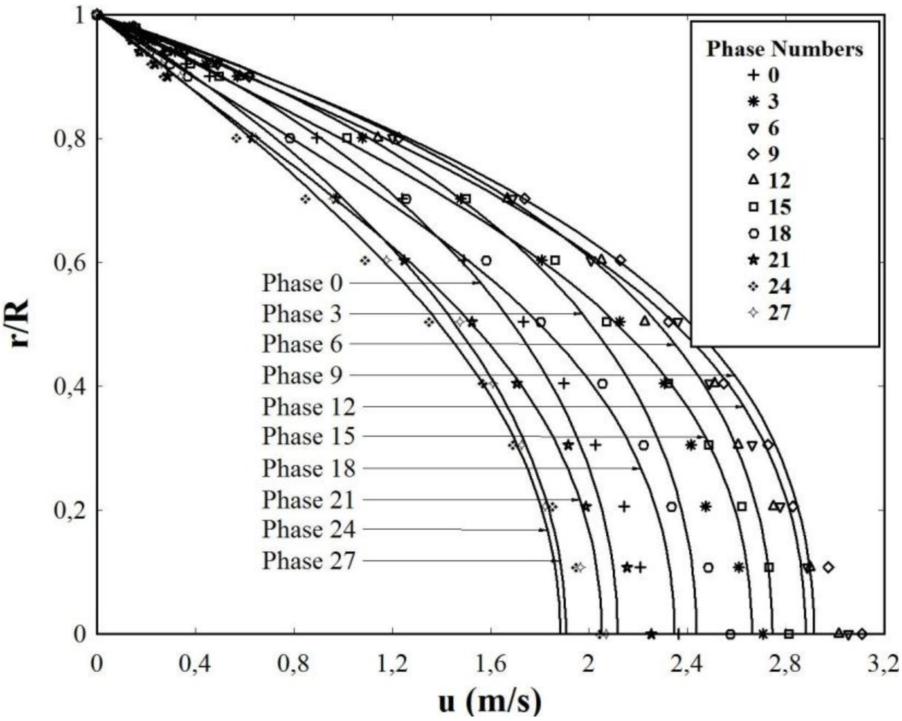

Figure 3.8. Variations of measured and computed velocity profiles with r/R at different phases (Run 28: Re_{ta}=4240.0, A_r=0.2822, $\sqrt{\omega'}$=5.084)

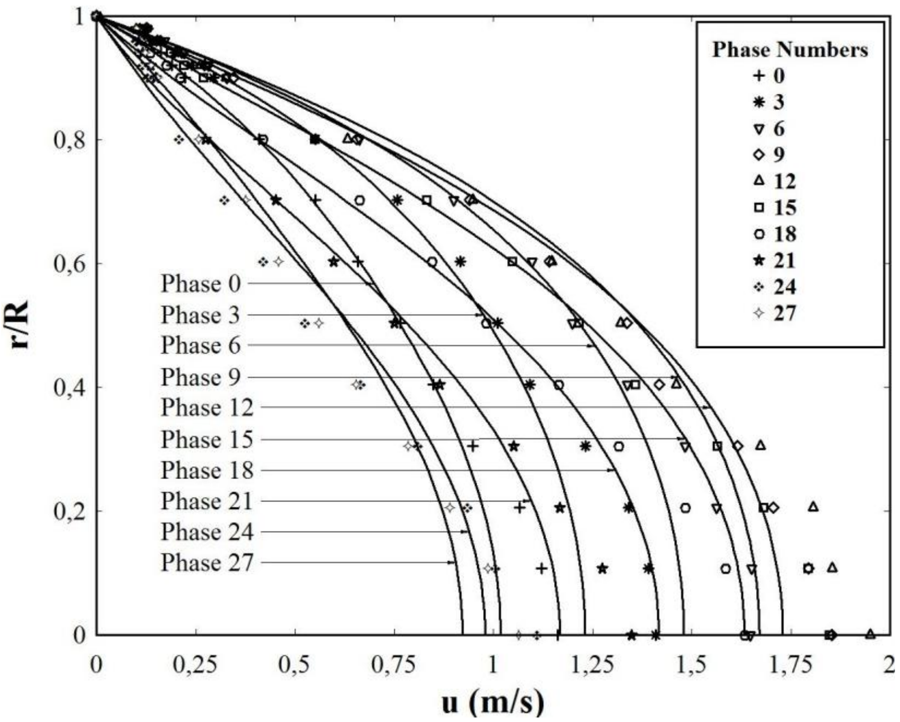

Figure 3.9. Variations of measured and computed velocity profiles with r/R at different phases (Run 26: Re_{ta}=2233.0, A_r=0.4043, $\sqrt{\omega'}$=5.15)

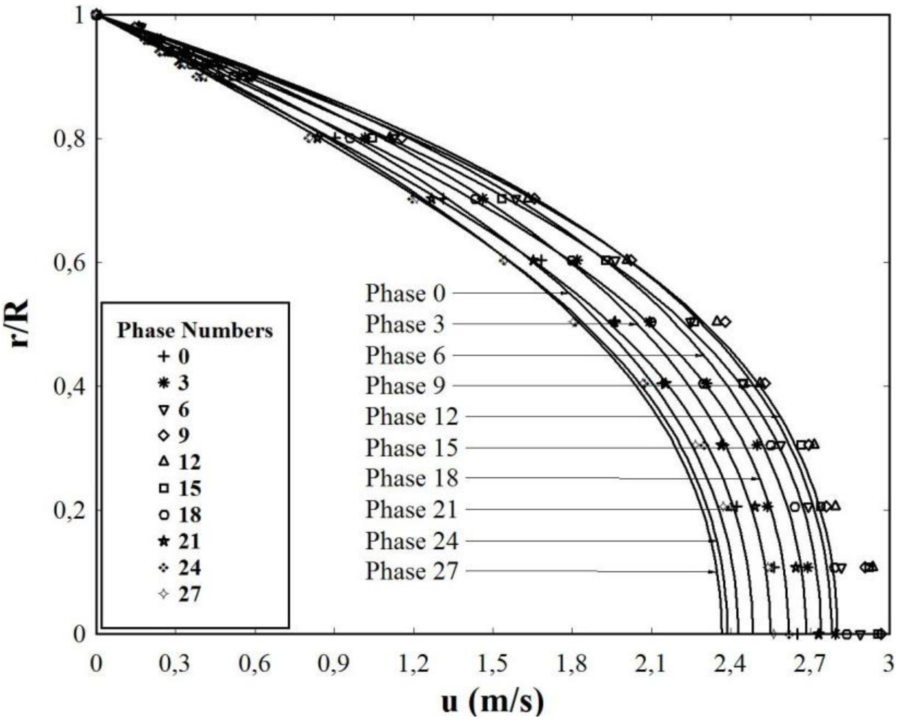

Figure 3.10. Variations of measured and computed velocity profiles with r/R at different phases (Run 15: Re_{ta}=4613.2, A_r=0.1310, $\sqrt{\omega'}$=7.079)

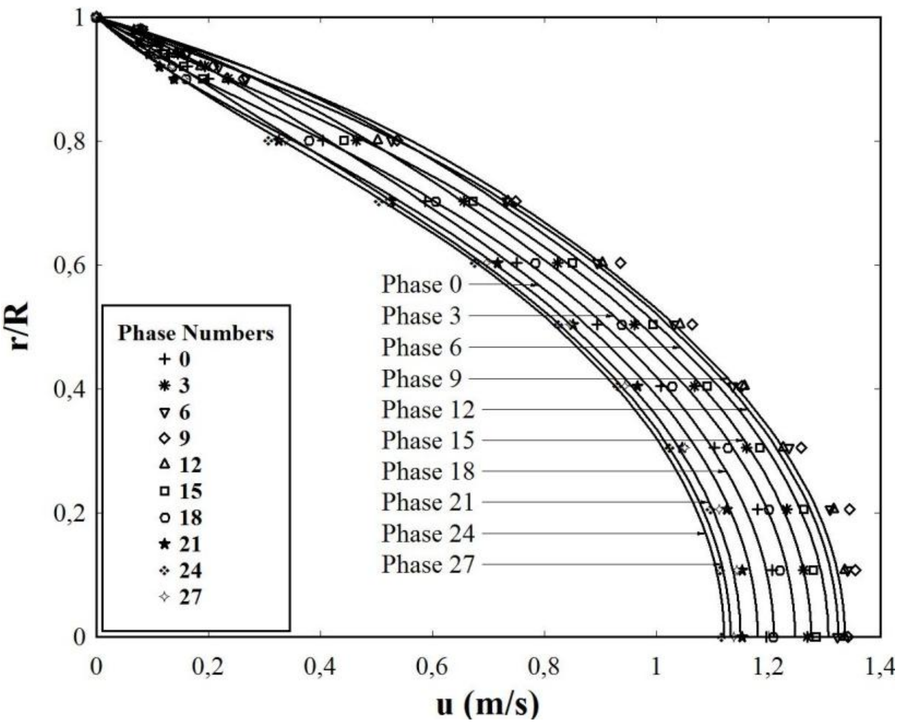

Figure 3.11. Variations of measured and computed velocity profiles with r/R at different phases (Run 3: Re_{ta}=2062.6, A_r=0.1572, $\sqrt{\omega'}$=12.516)

Additionally, Figs. 3.16 and 3.17 are also drawn for the only experimentally studied runs; Run 9 and Run 10 respectively. In these figures; the dimensionless velocity data, u/U_{cl} for both the experimental and the computational studies are plotted with respect to the dimensionless radius, r/R and labeled with different symbols and dotted lines respectively together with the corresponding phase indexes. Both the Blasius's parabolic velocity profile and the Prandtl's $1/7^{th}$-power law velocity profile are also represented with the solid and the centered lines respectively. It is seen from Figs. 3.12-3.17 that the tendency of numerically computed velocity profiles is slightly blunter than the tendency of the corresponding experimental velocity profiles for the all phases. This inconsistency between the tendencies has an order greater than the experimental error ranges of the used hot-wire anemometer system and it can be caused mainly by the preferred 2D-mesh of the tubular domain instead of using the realistic but complex 3D-mesh in the computational part of this study. Especially the turbulence removing unit that includes a honeycomb, a coarse screen, and a fine screen at the air entry of the experimental set-up should be well adapted to the numerical computation by means of a 3D-mesh of domain in a further study. Against the mentioned inconsistency, there are some critical consistent results observed as that; both the experimental and the computed velocity profiles reach to the sharpest profile (i.e., triangular-like) at the end of decelerating period or at the start of accelerating period (i.e., ~25^{th} phase (see Figs. 3.4-3.7)). Both of them become gradually blunter through the all accelerating period (i.e., between the phases; 25-30(0)-10) and almost reach to the most blunt one at the end of accelerating period (i.e., ~10^{th} phase). After that both of them become gradually sharper through the all decelerating period (i.e., between the phases; 10-25) and return to the sharpest profile at the end of decelerating period (i.e., ~25^{th} phase).

It can be also seen from Figs. 3.12-3.17 that; the general tendencies of both the experimental and the computational velocity profiles are very similar to the Blasius's distribution but differ appreciably from the Prandtl's distribution for the all six runs that are so truly considered as typical runs of the laminar-pulsatile pipe flow. Both the experimental and the computational velocity profiles become blunter than the Blasius's distribution in some phases of the pulsation cycle but become sharper than it in the remaining phases for the all runs. When $\sqrt{\omega'}$ increases over ~5.0 up to ~28.0; the sharper profiles approach to the Blasius's distribution but the blunter profiles drop below or underestimate it at the central core region (i.e., r/R<0.4) and move up to the wall in the outer region (i.e., 0.6<r/R<1.0). As can be seen especially from Figs. 3.16 and 3.17 for the $\sqrt{\omega'}$ values of ~23.0 and ~28.0, the experimental velocity profiles for the phases 6 and 9 in the second half of the accelerating period and for the phases 12 and 15 in the first half of the decelerating period approach quite close of the wall in the outer region and show almost a peak of rectangular-like velocity profile at r/R≈0.85 when $\sqrt{\omega'}\approx 28.0$.

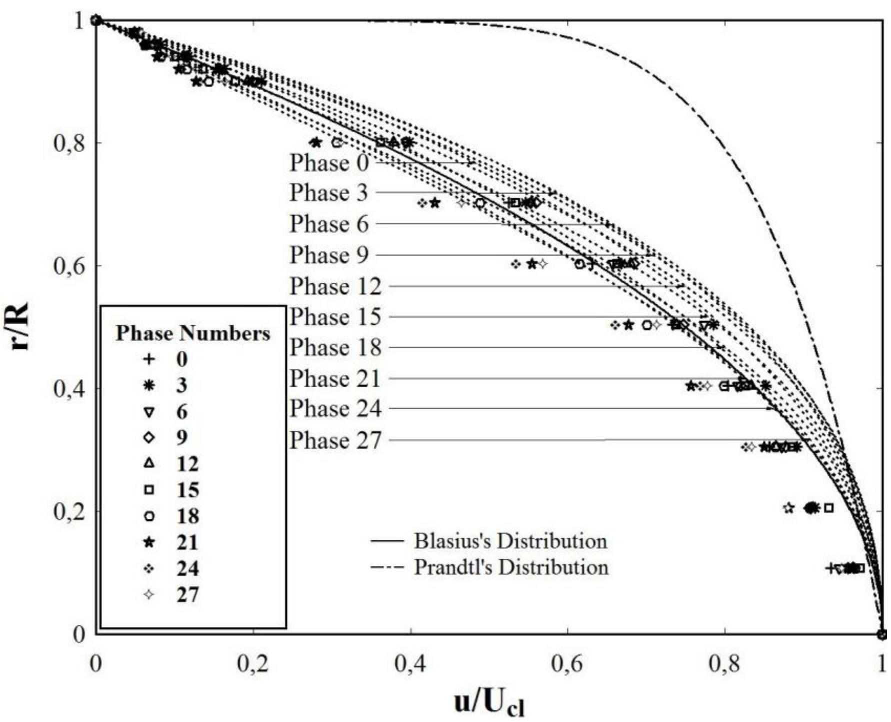

Figure 3.12. Variations of measured and computed dimensionless velocity, u/U_{cl} with r/R at different phases (Run 28: Re_{ta}=4240.0, A_r=0.2822, $\sqrt{\omega'}$=5.08)

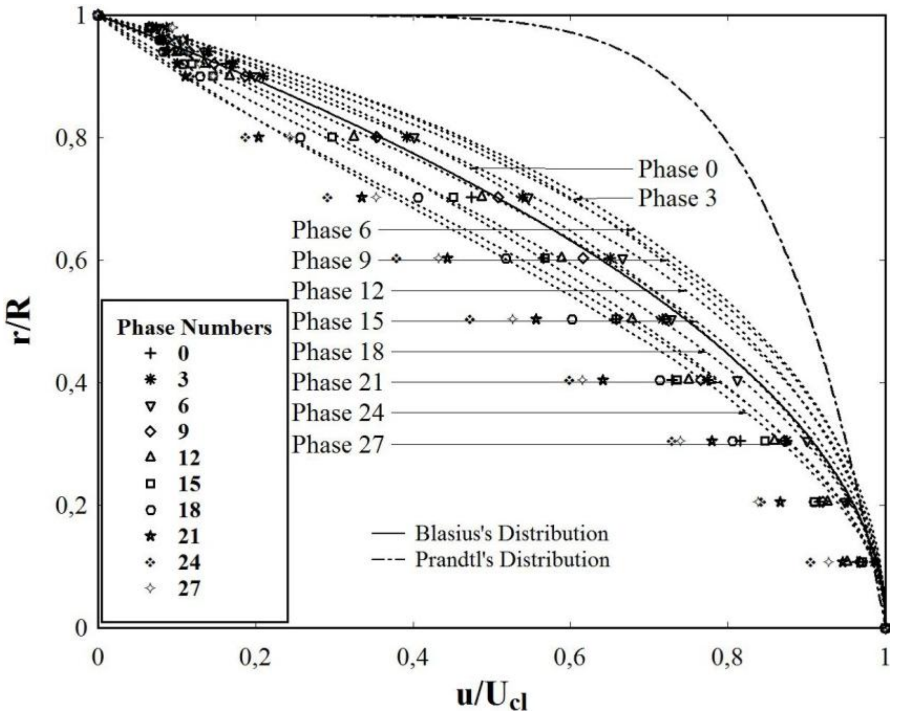

Figure 3.13. Variations of measured and computed dimensionless velocity, u/U_{cl} with r/R at different phases (Run 26: Re_{ta}=2233.0, A_r=0.4043, $\sqrt{\omega'}$=5.153)

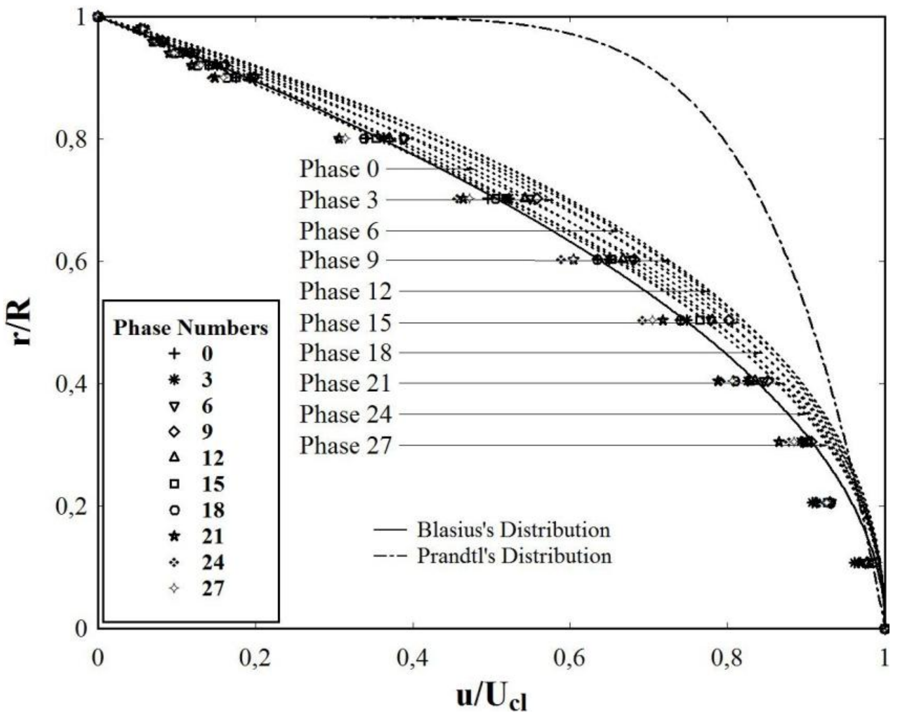

Figure 3.14. Variations of measured and computed dimensionless velocity, u/U_{cl} with r/R at different phases (Run 15: Re_{ta}=4613.2, A_r=0.1310, $\sqrt{\omega'}$=7.079)

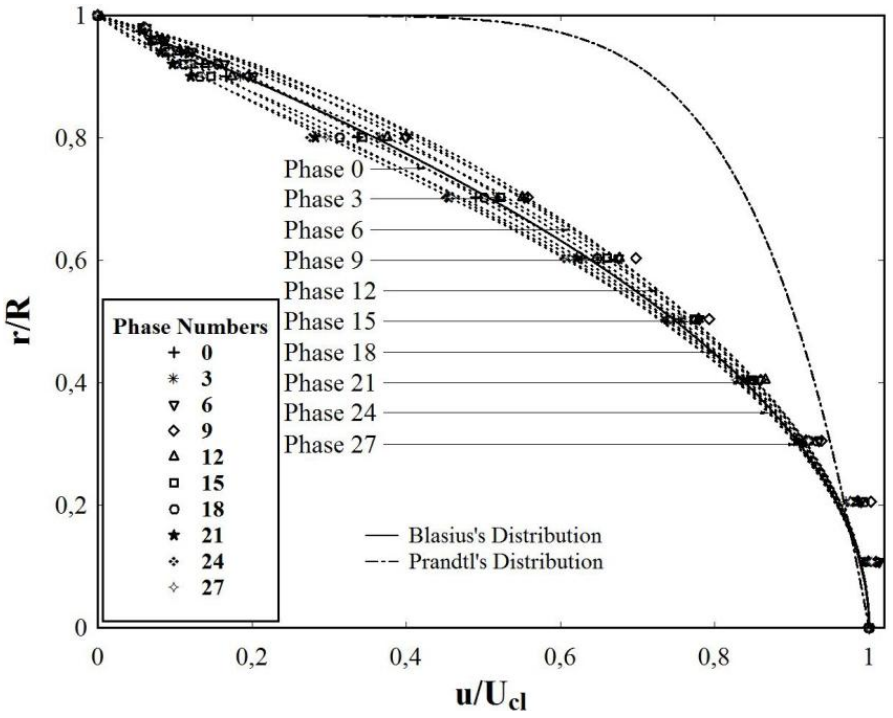

Figure 3.15. Variations of measured and computed dimensionless velocity, u/U_{cl} with r/R at different phases (Run 3: Re_{ta}=2062.6, A_r=0.1572, $\sqrt{\omega'}$=12.516)

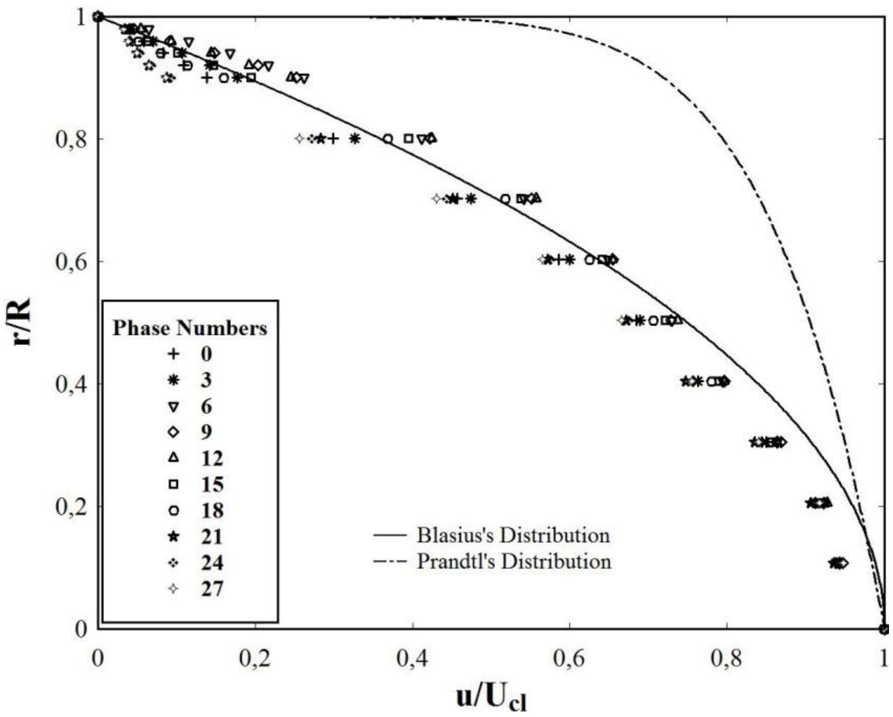

Figure 3.16. Variations of measured and computed dimensionless velocity, u/U_{cl} with r/R at different phases (Run 9: Re_{ta}=4229.3, A_r=0.2733, $\sqrt{\omega'}$=23.035)

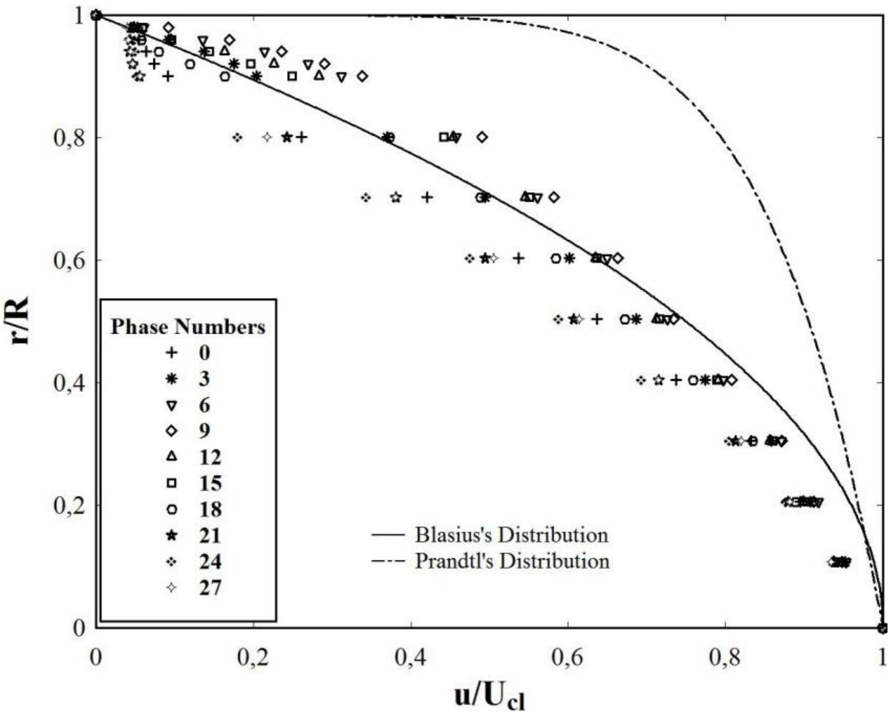

Figure 3.17. Variations of measured and computed dimensionless velocity, u/U_{cl} with r/R at different phases (Run 10: Re_{ta}=4126.6, A_r=0.4271, $\sqrt{\omega'}$=28.015)

This fact of the experimental and the computational velocity profiles in the present study show that; the limiting value of the dimensionless frequency parameter between the intermediate and the inertia dominant regions of the laminar-pulsatile pipe flow can be accepted as $\sqrt{\omega'_t}$ ≈28.0 proposed firstly by Ohmi et al. (1981a) and the peak of the velocity profile tends to gradually approach the pipe wall when $\sqrt{\omega'}$ increases from ~5.0 to the upper limit, ~28.0 of the intermediate region as addressed initially by Muto and Nakane (1980) due only flow visualizations.

3.5. Conclusions

The velocity field of fully developed laminar-pulsatile pipe flow in the intermediate region is investigated systematically by means of the computational study. The results of this study have been also published as an international journal paper (Yilmaz and Gundogdu, 2010) It can be concluded from these studies that:

1. The phase shift angles between the measured U_m and $\Delta P/L$ pulsation waves increases slightly when $\sqrt{\omega'}$ increases.

2. The computed $\Delta P/L$ data show a good agreement with the corresponding experimental ones for nearly all phases of pulsation in the intermediate laminar region except the phases near the middle-inflection points of accelerating and decelerating periods. The bad agreement near the inflection points decreases when $\sqrt{\omega'}$ decreases and Re_{ta} increases.

3. The computational and experimental data on axial velocity confirm each other except the near-wall region for $0.95<r/R<1.0$ and the central core region for $r/R<0.4$ at all phases of the runs. The deviation in the near-wall region seems to be caused by the well-known wall-proximity effect on the hot-wire probe used for the velocity measurement. However in the core regions, the computed data considerably underestimate the corresponding experimental ones and the percent deviation between them reaches to a maximum at the centerline($r/R=0$). It can be also detected that the percent deviation in the core region directly proportional with A_r but indirectly proportional with both of $\sqrt{\omega'}$ and Re_{ta}. It decreases when A_r decreases but when $\sqrt{\omega'}$ and Re_{ta} increase. It can be also understand that $\sqrt{\omega'}$ and A_r parameters seem to be more effective than Re_{ta} on the deviation.

4. The tendency of numerically computed velocity profiles is also slightly blunter than the tendency of the corresponding experimental velocity profiles for the all phases. This inconsistency between the tendencies has an order greater than the experimental error ranges of the used hot-wire anemometer system and it can be caused mainly by the used 2D-mesh of domain in the computational part of this study. Especially the flow regulation unit at the air entry of the experimental set-up should be well adapted to the computational study by means of a 3D-mesh of the tubular domain in a further study.

5. The general tendencies of both the experimental and the computational dimensionless velocity profiles are very similar to the Blasius's distribution but differ appreciably from the Prandtl's distribution for the all runs in the intermediate region of the laminar-pulsatile pipe flow. Both the experimental and the computational dimensionless velocity profiles become blunter than the Blasius's distribution in some phases of the pulsation cycle but become sharper than it in the remaining phases for the all runs. When $\sqrt{\omega'}$ increases over ~5.0 up to ~28.0; the sharper profiles approach to the Blasius's distribution but the blunter profiles drop below or underestimate it at the central core region (i.e., $r/R<0.4$) and move up to the wall in the outer region (i.e., $0.6<r/R<1.0$). The experimental velocity profiles for the phases in the second half of the accelerating period and for the phases in the first half of the decelerating period approach quite close of the wall in the outer region and show almost a peak of rectangular-like velocity profile at $r/R\approx0.85$ when $\sqrt{\omega'}\approx28.0$. This fact of the experimental and the computational velocity profiles in the present study show that; the limiting value of the dimensionless frequency parameter between the intermediate and the inertia dominant regions of the laminar-pulsatile pipe flow can be accepted as $\sqrt{\omega'}\approx28.0$ and the peak of the velocity profile tends to gradually approach the pipe wall when $\sqrt{\omega'}$ increases from ~5.0 to the upper limit, ~28.0 of the intermediate region. These facts are firstly clarified by means of both the systematic velocity measurements and the finite-volume based computations in this study.

CHAPTER 4

ASSESSMENT OF DIFFERENT LIQUID-LIQUID DRAG MODELS IN A VERTICAL DUCT BY USING CFD

4.1. Introduction

In a dispersed multiphase flow, the inter-phase momentum transfer plays an essential role in the prediction of flow behavior of each phase. The main components of inter-phase forces are composed of the drag, lift and virtual mass forces acting at the interface. In general, the drag force is the dominant component among them. Although the dispersed phase can be obtained by utilizing solid, liquid, or gas as the medium, solid dispersed phase has received by far the greater attention by researchers. The well-known reason is the fact that actual and potential industrial applications of solid dispersed phases are more frequently encountered than the others.

Nowadays, computational fluid dynamics (CFD) has proven to be a practical, efficient, and reliable tool for investigating inter-phase momentum transfer mechanisms in multiphase flows due to the advantage of low cost and simplicity in testing different drag laws. Hence, some drag laws for dense flows have been tested to understand their suitability in various industrial applications. Yang et al. (2003) employed two types of models to calculate the drag coefficient, i.e., model A (Ergun/Wen and Yu) and model B (Ergun/EMMS) for investigating the dependence of the drag coefficient on structure parameters. Du et al. (2006) assessed several widely used drag models available in literature in order to detect their effectiveness on the CFD modeling of spouted beds. Leboreiro et al. (2008) determined the impact of some drag laws on segregation predictions in systems at low gas velocities where the dominating mechanisms are expected to be drag force and gravity. Lundberg and Halvorsen (2008) studied how the different drag models influence the flow behavior in a bubbling fluidized bed. Li et al. (2009) examined the suitability of various drag models for predicting the hydrodynamics of the turbulent fluidization of FCC particles. Sobieski (2009) analyzed the influence of the model describing momentum exchange on the dynamics of the fluidized bed and height of the fountain characteristic for spouted bed grain dryer devices by using twelve different drag models. Gao et al. (2009) proposed a modified drag model based on the effective mean diameter of particle clusters together with the bed voidage profile, and compared the results with some other drag models. Vejahati et al. (2009) studied the influence of most widely used drag models on CFD simulation in the case of a 2D fluidized bed.

However, rapidly increasing industrial applications of liquid-liquid dispersed flows are being studied and attracting more and more interest in the field. The dynamics of liquid-liquid flows is much more complex than that of fluid-solid flows, the predictions of the various models are poor, i.e., large differences between the model predictions and the experimental results were encountered (Rusche and Issa 2000). The prediction of flow behavior for liquid-liquid dispersed flows is so important in industrial applications such as petrochemical (Angeli, 2001), biofluid or bioflow (Yilmaz and Gundogdu, 2008), (Yilmaz and Gundogdu, 2009), stirred vessel (Pacek et al., 1994), plate separator (Rommel et al., 1992), pharmaceuticals, polymerization, emulsification and transportation industries. The ability to predict the interfacial drag between phases is also of considerable importance for analyzing a dispersed two-phase flow under unsteady conditions. For example, blood flow is a multiphase non-Newtonian pulsatile flow in which resultant flow is composed of a mean and a periodically varying time dependent component (Gundogdu and Carpinlioglu, 1999a), (Yilmaz and Gundogdu, 2010). In the wake of unsteady flow data available, the drag coefficients developed for the steady flows have also been used for unsteady flow conditions.

Various models have been developed to describe the drag coefficient for the fluid-fluid dispersed flow systems. In literature, these models were reviewed in great detail (Rusche and Issa, 2000), (Yilmaz and Gundogdu, 2009). Drag coefficient multiplier and mixture viscosity concept are generally used modeling approach for these types of flows. In the drag coefficient multiplier approach, the single dispersed drag model is extended to include the effect of neighboring entities by using the ratio of the actual drag coefficient to its value for a single dispersed element. In the mixture viscosity approach, the effect of neighboring entities is taken into account by considering their effect on an overall mixture viscosity. The particulate Reynolds number related to the drag coefficient is based on this mixture viscosity instead of the continuous phase viscosity in this approach.

Barnea and Mizrahi (1975) extended a drag coefficient law which is obtained from solid-fluid systems to liquid-liquid systems in which the dispersed fluid particles retain substantially a spherical shape. The effective viscosity concept and mixture viscosity law similar to the Taylor linear law validated at a high phase volume fraction are used to provide the modified definitions of the drag coefficient and the Reynolds number incorporating suitable functions of the particle phase volume fraction. Their model was found to be in agreement with 12 different experimental cases having a wide range of both particle Reynolds number and phase volume fraction. Ishii and Zuber (1979) derived a drag law by using the same concept of mixture viscosity for particulate flows and gas-liquid systems as well as for liquid-liquid systems, including the case of distorted inclusions. The predicted values had been compared over 1000 experimental data, and satisfactory agreements were obtained at wide ranges of the phase volume fraction and flow Reynolds number. Considerable differences among solid-particulate, bubbly, and droplet flows were also observed in all aspects. Bedeaux (1983) derived a relation for the effective shear viscosity of a two-phase flow for arbitrary phase volume fractions in which both phases analogous to Bruggeman's formula (Bruggeman, 1935) for the dielectric constant in two-phase flows. Two new drag coefficient correlations based on both Bedeaux's mixture viscosity and volume average mixture viscosity concepts are also derived and checked in this study.

Kumar and Hartland (1985) proposed an empirical drag law for liquid-liquid systems based on drag coefficient multiplier approach. This correlation was validated against 998 published experimental results for 29 liquid-liquid systems from 14 different sources covering important ranges of particle Reynolds number and phase volume fraction. Rusche and Issa (2000) obtained the empirical correlations for the drag coefficient of droplets, particles, and bubbles to overcome the limitation that most of older correlation does not revert to a single dispersed phase element drag correlation when the phase volume fraction approaches zero. Five data sets were chosen, which cover a wide range of Archimedes numbers to validate their correlation for droplets. Another drag function correlation of Augier et al. (2003a) is not a general drag law for all liquid-liquid systems. However, this correlation depends on their experimental data used for verification of the present CFD predictions. They extended the Schiller and Nauman drag model for a single dispersed drop for the dense liquid-liquid dispersed flows. However, further developments of these studies need to focus on effects of Archimedes, Eötvös or particle Reynolds numbers (Rusche and Issa, 2000), (Augier et al., 2003a), (Behzadi et al., 2004).

Experimental investigation and simulation of two phase flows are still very difficult, which is mainly due to the complex hydrodynamic structure and the limitations of measurement techniques. During the last decade, the limitations on measurement of instantaneous local velocities and phase volume fraction in dense liquid-liquid dispersed flows have been partially solved (Augier et al., 2003a), (Augier et al., 2003b), (Powell, 2008). These recent advances now make it possible to obtain experimental data base to verify and assess against various drag model correlations on liquid-liquid dense flows. Experimental data of Augier et al (2003a) have presented the best available open literature data of their kind. They measured simultaneously both of local phase velocities and phase volume fraction fields, as well as the mean diameter of drop in a vertical co-current flow of n-heptane dispersed in an aqueous solution of glycerin by an application of PIV with a refractive index matching technique. Although, there are many investigations on drag model effects by means CFD tools, an examination regarding the effect of dense liquid-liquid drag models on CFD modeling seems unavailable. In this respect, one of the purposes of the present study is to obtain the influence of the drag laws on liquid-liquid dense dispersed flow where the dominating mechanisms are expected to be viscosity, drag force and gravity. All computations have been carried out by applying the commercial CFD package Fluent v6.3.26 in conjunction with multiphase model on a full two-fluid model including standard k-ε dispersed turbulence model with two dimensional and three dimensional grids. The so-called user defined functions are utilized in implementation of the fluid-fluid drag models.

4.2. Model Equations

4.2.1. Governing conservation equations

An Eulerian-Eulerian or two-fluid approach has been adopted to simulate and describe flow behavior of each phase inside a vertical square duct. The dispersed and the continuous phases are treated mathematically as interpenetrating continua by incorporating the concept of phase volume fractions in the Eulerian-Eulerian approach. The sum of the phase volume fractions of all contributing phases must be equal to unity. The mass and momentum balance equations are written for each phase separately. Coupling of the motion of the dispersed and the continuous phase is achieved by implementing inter-phase momentum transfer terms into the respective phase's momentum balance equations. The derivation of the conservation equations for mass, momentum and energy for each of the individual phases is done by ensemble averaging the local instantaneous balances for each of the phases. A general mass balance by the convective mass fluxes without inter-phase mass transfer and mass source for each phase is given by:

$$\frac{\partial(\rho_q \alpha_q)}{\partial t} + \nabla \cdot (\rho_q \alpha_q \vec{u}_q) = 0 \tag{4.1}$$

where q represents any one of the phases, ρ is the density, α is the phase volume fraction, t is the time, and v is the velocity. The momentum balance equation for each phase is given by:

$$\frac{\partial(\rho_q \alpha_q \vec{u}_q)}{\partial t} + \nabla \cdot (\rho_q \alpha_q \vec{u}_q \vec{u}_q) = -\alpha_q \nabla P + \nabla \cdot \overline{\overline{\tau_q}} + \alpha_q \rho_q \vec{g} + \sum_{r=1}^{n} \vec{R}_{rq} + \vec{F}_q \tag{4.2}$$

where P is the pressure and all phases share a single pressure field, $\overline{\overline{\tau_q}}$ is the q phase stress-strain tensor, g is the gravity force, and F represents the external forces such as virtual mass, rotational and shear lift, electrical and magnetic forces. $\vec{R}_{rq}$ is an interaction force between the q phase and the r phase. In the Newtonian form, the Reynolds stress tensor for the continuous phase is given as follows:

$$\overline{\overline{\tau_c}} = -\frac{2}{3}(\alpha_c \rho_c k_c + \alpha_c \rho_c \mu_{t,c} \nabla \cdot \vec{u}_c)\overline{\overline{I}} + \alpha_c \rho_c \mu_{t,c} \left(\nabla \vec{u}_c + (\nabla \vec{u}_c)^T\right) \tag{4.3}$$

where, c represents the continuous phase, $\mu_{t,c}$ is the turbulent viscosity, k is the kinetic energy, and $\overline{\overline{I}}$ is a unit tensor.

The particle-phase pressure represents an inter-particle pressure as a function of volume fraction. This pressure is generated by the kinetic energy of the particle velocity fluctuations and hence collision of drops with each other or elastic or inelastic contact between drops. Since a liquid remains fluid even at a volume fraction of 100%, the inter-particle pressure of the dispersed phase can be ignored.

4.2.2. Turbulence model equations

Turbulence effects have been predicted by using standard k-ε dispersed turbulence model. Turbulent behavior of the continuous phase is obtained by using standard k-ε model with interphase turbulent momentum transfer and extra source terms. The eddy viscosity model is used to calculate averaged fluctuating quantities in the continuous phase. Predictions of turbulence quantities for the dispersed phase are obtained using the Tchen-theory correlations.

4.2.2.1. Turbulence in the continuous phase

The turbulent viscosity $\mu_{t,c}$ is written in terms of the turbulent kinetic energy of continuous phase as:

$$\mu_{t,c} = \rho_c C_\mu \frac{k_c^2}{\varepsilon_c} \tag{4.4}$$

where k is the kinetic energy, ε is the dissipation rate, and C_μ is the model constant and equal to 0.09. The turbulent kinetic energy and dissipation rate for the continuous phase are obtained from the k-ε model:

$$\frac{\partial(\rho_c \alpha_c k_c)}{\partial t} + \nabla \cdot (\rho_c \alpha_c \vec{v}_c k_c) = \nabla \cdot \left(\alpha_c \frac{\mu_{t,c}}{\sigma_k} \nabla k_c \right) + \alpha_c G_{k,c} - \rho_c \alpha_c \varepsilon_c + \rho_c \alpha_c \Pi_{k_c} \tag{4.5}$$

and

$$\frac{\partial(\rho_c \alpha_c \varepsilon_c)}{\partial t} + \nabla \cdot (\rho_c \alpha_c \vec{v}_c \varepsilon_c) = \nabla \cdot \left(\alpha_c \frac{\mu_{t,c}}{\sigma_\varepsilon} \nabla \varepsilon_c \right)$$

$$+ \alpha_c \frac{\varepsilon_c}{k_c} \left(C_{1\varepsilon} G_{k,c} - C_{2\varepsilon} \rho_c \varepsilon_c \right) + \rho_c \alpha_c \Pi_{\varepsilon_c} \tag{4.6}$$

where $G_{k,c}$ is the production of turbulent kinetic energy. $C_{1\varepsilon}$, $C_{2\varepsilon}$, σ_k, and σ_ε are the model constants with the following default values:

$$C_{1\varepsilon}=1.44 \; C_{2\varepsilon}=1.92 \; \sigma_k=1.0 \; \sigma_\varepsilon=1.3 \tag{4.7}$$

The terms Π_{k_c} and Π_{ε_c} represent the influence of the dispersed phase on the continuous phase. They can be derived from the instantaneous equation of the continuous phase and are given by:

$$\Pi_{k_c} = \sum_{d=1}^{n} \frac{K_{dc}}{\rho_c \alpha_c} (k_{dc} - 2k_c + \vec{u}_{dc} \cdot \vec{u}_{dr}) \tag{4.8}$$

and Π_{ε_c} with the expression of Elgobashi and Abou-Arab (1983):

$$\Pi_{\varepsilon_c} = C_{3\varepsilon} \frac{\varepsilon_c}{k_c} \Pi_{k_c} \tag{4.9}$$

where n represents the number of dispersed phases, k_{dc} is the covariance of the velocities of the continuous phase and the dispersed phase (calculated by the Eq. (4.18)), $\vec{u}_{dc}$ is the relative velocity, $\vec{u}_{dr}$ is the drift velocity is the drift velocity, K_{dc} is the inter-phase momentum exchange coefficient between the phases, and $C_{3\varepsilon}$ is the model constant and equal to 1.2.

4.2.2.2. Turbulence in the dispersed phase

In the modeling of turbulence in the dispersed phase, time and length scales that characterize the motion are used to evaluate the dispersion coefficients, the correlation functions and the turbulent kinetic energy of the dispersed phase. The characteristic particle relaxation time connected with the inertial effects acting on a particulate phase is defined as

$$\tau_{F,dc} = \alpha_d \rho_c K_{dc}^{-1} \left(\frac{\rho_d}{\rho_c} + C_{VM} \right) \tag{4.10}$$

where C_V=0.5 is the virtual mass coefficient. The Lagrangian integral time scale calculated along particle trajectories, mainly affected by the crossing-trajectory effect (Csanady, 1963), is given by

$$\tau_{t,dc} = \frac{\tau_{t,c}}{\sqrt{\left(1 + C_\beta \xi^2\right)}} \tag{4.11}$$

where

$$C_\beta = 1.8 - 1.35\cos^2\theta \tag{4.12}$$

and

$$\xi = \frac{|\vec{u}_{dc}|\tau_{t,c}}{L_{t,c}} \tag{4.13}$$

where θ is the angle between the mean particle velocity and the mean relative velocity, $\tau_{t,c}$ is the characteristic time of the energetic turbulent eddies,

$$\tau_{t,c} = \frac{3}{2} C_\mu \frac{k_c}{\varepsilon_c} \tag{4.14}$$

and $L_{t,c}$ is the length scale of the turbulent eddies.

$$L_{t,c} = \sqrt{\frac{3}{2}} C_\mu \frac{k_c^{3/2}}{\varepsilon_c} \tag{4.15}$$

The ratio between the Lagrangian integral time scale and the characteristic particle relaxation time is written as

$$\eta_{dc} = \frac{\tau_{t,dc}}{\tau_{F,dc}} \tag{4.16}$$

Following Simonin and Viollet (1990) methodology, FLUENT calculates the turbulent quantities for the dispersed phase as follows:

$$k_d = k_c \left(\frac{b^2 + \eta_{dc}}{1 + \eta_{dc}} \right) \tag{4.17}$$

$$k_{dc} = 2k_c\left(\frac{b+\eta_{dc}}{1+\eta_{dc}}\right) \quad (4.18)$$

$$D_{t,dc} = \frac{1}{3}k_{dc}\tau_{t,dc} \quad (4.19)$$

$$D_d = D_{t,dc} + \left(\frac{2}{3}k_d - b\frac{1}{3}k_{dc}\right)\tau_{F,dc} \quad (4.20)$$

$$b = \left(1 + C_{VM}\right)\left(\frac{\rho_d}{\rho_c} + C_{VM}\right) \quad (4.21)$$

4.2.3. Interphase force

The interphase force, $\vec{R}_{rq}$ depends on the friction, pressure, cohesion, and other effects, and is subject to the conditions that $\vec{R}_{rq}$=-$\vec{R}_{qr}$, and $\vec{R}_{qq}$=0. The turbulent inter-phase force for two phase liquid-liquid dispersed flow can be written in the following general form;

$$\vec{R}_{dc} = K_{dc}(\vec{u}_d - \vec{u}_c) = K_{dc}\left(\vec{U}_d - \vec{U}_c\right) - K_{dc}\vec{u}_{dr} \quad (4.22)$$

where K_{dc} (=K_{cd}) is the inter-phase momentum exchange coefficient between the continuous and dispersed phase and can be written in the following general form;

$$K_{dc} = \frac{\alpha_d\rho_d f}{\tau_d} \quad (4.23)$$

where τ_d is the particle relaxation time and given as;

$$\tau_d = \frac{\rho_d d_d^2}{18\mu_c} \quad (4.24)$$

where d_d is the mean diameter of the drops. The drag function f includes a drag coefficient C_D that is based on the particle Reynolds number, Re_p:

$$f = \frac{C_D Re_p}{24} \tag{4.25}$$

The drifting velocity accounts for the dispersion of the drops due to transport by the continuous phase turbulent flow and is given by

$$\vec{u}_{dr} = -\left(\frac{D_d}{\sigma_{dc}\alpha_d} \nabla\alpha_d - \frac{D_c}{\sigma_{dc}\alpha_c} \nabla\alpha_c \right) \tag{4.26}$$

where D_d and D_c are diffusivities, and σ_{dc} is a dispersion Prandtl number. When using Tchen theory correlations in multiphase flows, Fluent software assumes $D_d=D_c=D_{t,dc}$ and the default value for the dispersion Prandtl number is 0.75.

4.2.4. Drag models

Drag coefficient resulting from the mean relative velocity between the two phases is of crucial importance for the successful simulation of a multiphase flow. To investigate the suitability of drag laws, eight different drag coefficient models are used to model the dense liquid-liquid homogeneous dispersed flow in this study. Only Schiller and Nauman drag model is available in Fluent v6.3.26. The other drag models are implemented into the CFD code by means of user defined functions.

4.2.4.1. Schiller and Nauman model

The well-known drag law of Stokes (i.e., $C_D=24/Re_p$) proposed for $Re_p<1$ is extended for higher particle Re numbers by Schiller and Nauman (1935):

$$C_D = \begin{cases} 24(1+0.15\mathrm{Re}^{0.687})/\mathrm{Re} & \mathrm{Re} \le 1000 \\ 0.44 & \mathrm{Re} > 1000 \end{cases} \tag{4.27}$$

where the particle Reynolds number, Re_p is based on the dispersed particle diameter, d, the magnitude of relative velocity, U_r between the phases, the density, ρ_c and the dynamic viscosity, μ_c of the continuous phase as that:

$$\mathrm{Re} = \frac{\rho_c d\, U_r}{\mu_c} \tag{4.28}$$

where $U_r = |u_c - u_d|$ is the velocity difference between continuous and dispersed phases. The Schiller and Naumann model validated by Klaseboer et al. (2001) for a broader variety of liquid-liquid systems with particle Reynolds number as high as 1000. The combination of Schiller and Naumann model and the Levich (1962) model was also proposed as an appropriate model for spheroid drops (Myint et al. 2006).

4.2.4.2. Barnea and Mizrahi model

Barnea and Mizrahi (1975) proposed a drag coefficient law for dense liquid-liquid systems based on the mixture viscosity concept.

$$C_D = \left(1 + \alpha^{\frac{1}{3}}\right)\left(0.63 + \frac{4.8}{\sqrt{\mathrm{Re}_m}}\right)^2 \tag{4.29}$$

where the particle Reynolds number based on the mixture viscosity, Re_m is used mixture viscosity μ_m instead of the continuous phase viscosity, μ_c as that:

$$\mathrm{Re}_m = \frac{\rho_c d U_r}{\mu_m} \tag{4.30}$$

where the mixture viscosity, μ_m is evaluated from the following viscosity law:

$$\mu_m = \mu_c K_b \frac{\frac{2}{3}K_b + \frac{\mu_d}{\mu_c}}{K_b + \frac{\mu_d}{\mu_c}} \tag{4.31}$$

where μ_d is the viscosity of the dispersed phase and K_b is an empirical function;

$$K_b = \exp\left(\frac{5\alpha K_a}{3(1-\alpha)}\right) \tag{4.32}$$

where K_a is defined as:

$$K_a = \frac{\mu_c + 2.5\mu_d}{2.5\mu_c + 2.5\mu_d} \tag{4.33}$$

4.2.4.3. Ishii and Zuber model

Ishii and Zuber (1979) proposed a drag law by using the same concept of mixture viscosity for the wide ranges of Reynolds number and flow regime.

$$C_D = \frac{24}{Re_m}\left(1 + 0.1 Re_m^{0.75}\right) \tag{4.34}$$

where the particle Reynolds number, Re_m is based on the following mixture viscosity law:

$$\mu_m = \mu_c \left(1 - \frac{\alpha}{\alpha_{max}}\right)^{AA} \tag{4.35}$$

where α_{max} is accepted as 0.62 for solid particles and 1 for fluid dispersed phase elements. The exponent A is defined as:

$$AA = -2.5\alpha_{max} \frac{\mu_d + 0.4\mu_c}{\mu_d + \mu_c} \tag{4.36}$$

4.2.4.4. Kumar and Hartland model

Kumar and Hartland (1985) proposed an empirical drag law for dense liquid-liquid systems based on a large number of experimental data covering important ranges of particle Reynolds numbers and phase volume fractions.

$$C_D = \left(K_1 + \frac{24}{Re}\right)\left(1 + k_{kh}\alpha^n\right) \tag{4.37}$$

where Re is defined as in Eq. (4.28), other model parameters are K_1 = 0.53, k_{kh} = 4.56, and n = 0.73.

4.2.4.5. Rusche and Issa model

The Schiller and Nauman model for a single dispersed drop was extended for dense flows by Rusche and Issa (2000) as:

$$C_D = C_{D0}F(\alpha) \tag{4.38}$$

where C_{D0} is the drag coefficient of a single spherical drop evaluated from the Schiller and Nauman model for a non-uniform flow, and $F(\alpha)$ is a function which takes into account the effects arising from the presence of other dispersed elements. The proposed $F(\alpha)$ correlation is that:

$$F(\alpha) = e^{k_1\alpha} + \alpha^{k_2} \tag{4.39}$$

where the values of the exponential coefficients k_1 and k_2 were extracted respectively as 2.1 and 0.249 for spherical droplets by means of a non-linear curve fitting procedure on experimental data found in available literature.

4.2.4.6. Augier model

Augier et al. (2003a) also proposed an extension of the Schiller and Nauman model and the proposed $F(\alpha)$ correlation is:

$$F(\alpha) = e^{5.2\alpha} \tag{4.40}$$

for $0 < \alpha < 0.4$, and $Re < 100$. Here $F(\alpha)$ is modeled for liquid-liquid systems as a function of the phase volume fraction only.

4.2.4.7. Bedeaux mixture viscosity based drag model

Bedeaux (1983) proposed a mixture viscosity formulation which is used to form a new drag law in this study:

$$C_D = \frac{24}{Re_m}\left(1 + 0.1 Re_m^{0.75}\right) \tag{4.41}$$

$$\frac{\mu_c - \mu_m}{\mu_c + \frac{3}{2}\mu_m}\alpha_c + \frac{\mu_d - \mu_m}{\mu_d + \frac{3}{2}\mu_m}\alpha_d = 0 \tag{4.42}$$

$$\mu_m = 0.1666\left(-2\mu_c + 3\mu_d + 5\mu_c\alpha_c - 5\mu_d\alpha_c\right)$$

$$+\sqrt{24\mu_c\mu_d + \left(2\mu_c - 3\mu_d - 5\mu_c\alpha_c + 5\mu_d\alpha_c\right)^2} \tag{4.43}$$

4.2.4.8. Volume average mixture viscosity based drag model

According to Enwald et al. (1996), the mixture viscosity may be calculated from a simple volume fraction average of the pure species' viscosities that assumes a linear relationship between the mixture viscosity and the continuous and dispersed phase viscosities. This equation is also used to compose a new drag law by using the mixture viscosity concept;

$$C_D = \begin{cases} 24(1+0.15\mathrm{Re}^{0.687})/\mathrm{Re} & \mathrm{Re} \le 1000 \\ 0.44 & \mathrm{Re} > 1000 \end{cases} \tag{4.44}$$

where Re is based on the following mixture viscosity;

$$\mu_m = \mu_c \alpha_c + \mu_d \alpha_d \tag{4.45}$$

4.2.5. Wall effects

A velocity ratio can be defined, based on constant particle dimensions, the ratio of the terminal velocity in an infinite fluid to the terminal velocity in a bounded fluid. This ratio is one of the useful measures of the effect of bounding walls on drag (Clift et al. 1978). For intermediate size drops (Eötvös number < 40), Clift et al. (1978) proposed that walls have negligible effects (less than about 2%) on terminal velocities under the following conditions:

$$\frac{d_d}{D} \le 0.08 + 0.02\log_{10}\mathrm{Re} \qquad \text{for } 0.1<\mathrm{Re}<100 \tag{4.46}$$

In the conditions imposed throughout the test cases of this study, the Reynolds number is between 10 and 100, the Eötvös number is between 1 and 2.5, and the diameter ratio is between 0.026 and 0.04. Therefore, the wall effect in these cases is accepted as negligibly small.

4.2.6. Computational grid

The vertical square duct of Augier's experimental test rig shortened in length and considered as alternatively a 2-D and/or 3-D channel system. The height of channel is considered as 0.5 m from the inlet in order to reduce the number of grids. The computational grid created by using the Gambit v2.4.6 software. The view of the geometry combined with the structured mesh of computational domain for the main flow is shown schematically in Fig. 4.1.

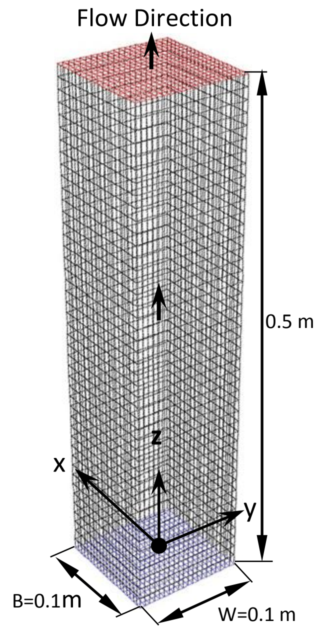

Figure 4.1. A view of 3D mesh of computational domain

Obtaining grid independent solutions is an important aspect to minimize residuals. So, several test runs were made on computational mesh to reach a grid independent solution. The number of cell elements and the number of nodes in the entire flow domain were 18000 and 20286 in the initial test of computational mesh, respectively. A secondary test run in a 6272 cell element and 7425 node case was also performed. Two monitor points at the test section are selected to check convergence of relevant quantities. The time series of the dispersed phase volume fraction and both phase velocities shown in Figs. 4.2-4.4 are recorded in the mid plane of the duct around 2.5 cm (monitor point 1) and 5 cm (monitor point 2) from the walls at an axial position of 0.2 m from the inlet. All quantities at the monitoring points start to be flat after few seconds of start-up and this clearly indicates convergence. Grid independence test studies were performed to show that increasing the number of grids does not cause noticeable changes on the simulation results. The calculated 3-D phase velocities are slightly higher, 0.3 m/s, than the results of 2-D solution. The results of 3-D and 2-D phase volume fractions seem very close to each other (cf. Fig. 4.2). The simulations performed in three dimensions are found to give better agreement with the experimental data, and therefore, the 3-D dense mesh is preferred in this study. The average run time for a 1000 iteration was approximately 1/2 h on a personal computer having a quad processor Q9450 (12 Mb cache, 2.66 GHz) and 8 Gb ram running under a Windows 64bit system with 20286 mesh nodes.

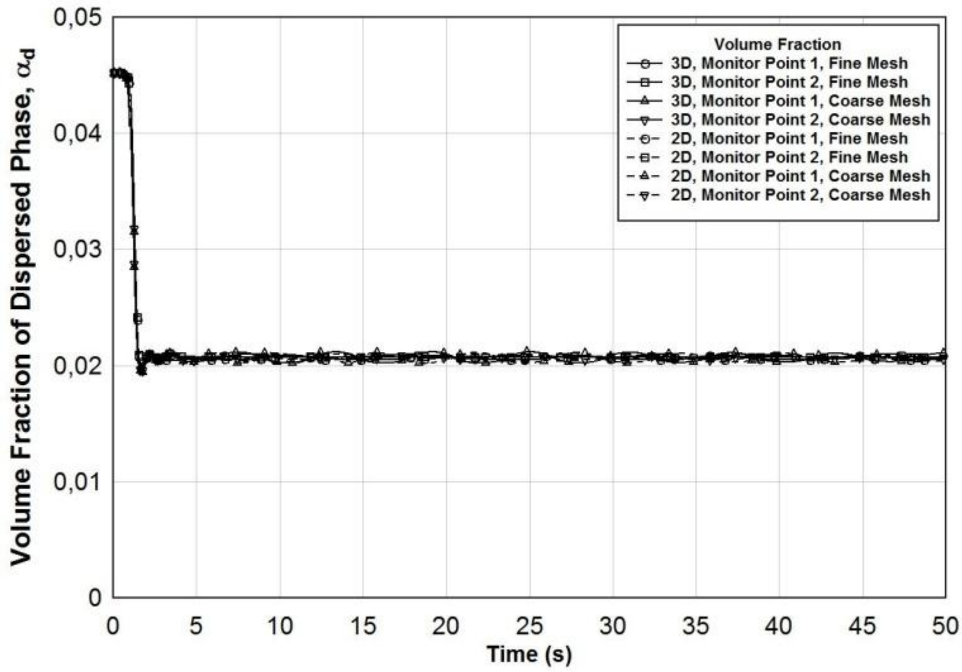

Figure 4.2. Volume fraction of dispersed phase at points 1-2 for run 1 with Augier's drag correlation

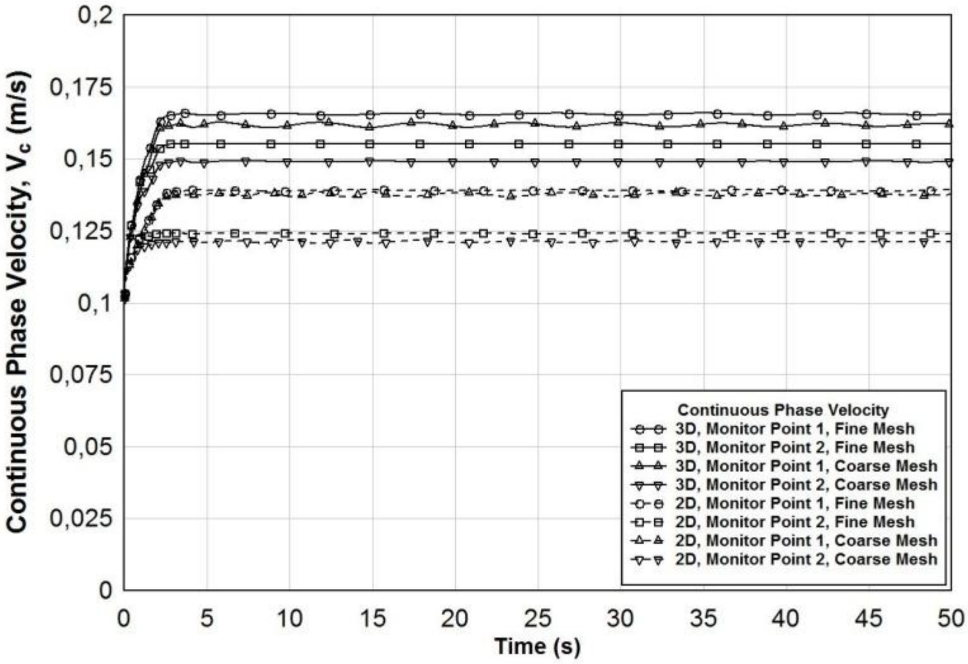

Figure 4.3. Continuous phase velocity at points 1-2 for run 1 with Augier's drag correlation

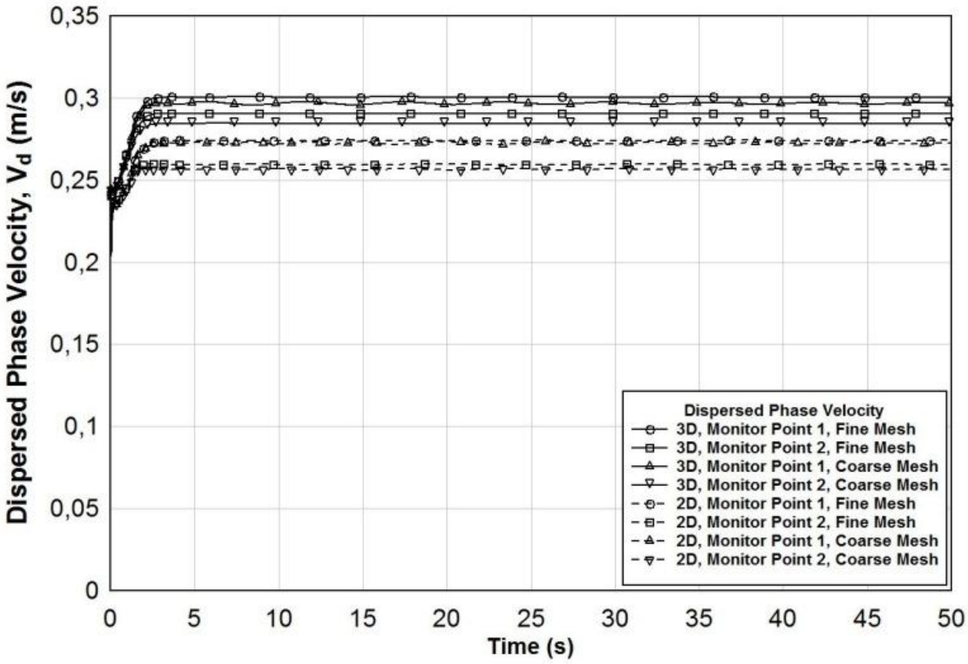

Figure 4.4. Dispersed phase velocity at points 1-2 for run 1 with Augier's drag correlation

4.2.7. Boundary conditions and fluid properties

The experimental results of Augier et al. (2003a) on dense liquid-liquid homogeneous dispersed flow are used to verify various drag models. In this experiment, phase system was composed of n-heptane as the dispersed phase, and aqueous solution of glycerin as the continuous phase inside a vertical square duct. These two immiscible liquids were maintained at a temperature of 29°C to match their refractive index in order to allow the use of a non-invasive optical measurement technique. A summary of relevant physical properties of these fluids are reported in Table 4.1.

Table 4.1. Physical properties of the experimental system fluids at 29°C

	Density ρ (kg/m^3)	Viscosity μ (Pa.s)
n-heptane	683.7	$4.5*10^{-4}$
% 50 w/w glycerol-water solution	1180	$6*10^{-3}$

The shape of the drop was observed nearly spherical and drop distribution was proposed as very close to a monodisperse distribution. The drop diameter in different cases at the test section inside buoyancy driven vertical transparent square duct was in the range of 2-4 mm. The drops of the dispersed phase are so considered as ideal spherical and monodisperse in this study. In order to provide homogeneous liquid-liquid flow at the duct inlet, the experimental setup contains two equal separated ducts having a stainless steel convergent inlet section. Each duct is 1.4 m in height, 0.1 m in width and depth. One duct was used to investigate the flow. The continuous phase enters via a stainless steel convergent section to the test duct. A 2 mm mesh grid is used after the convergent outlet. The dispersed phase was supplied through 400 stainless steel capillary tubes of 1 mm in diameter and 42 cm in length. Measurements were performed in the mid plane of the duct approximately 1 cm away from the walls at an axial position of 0.2 m from the inlet to ensure the homogeneity of the measured profiles and to eliminate the effect of the inlet conditions. The published phase volume fraction distributions and both phase velocity data for selected six different runs of Augier et al. (2003a) are used in the current study for detailed comparisons. The operation conditions of these experimental runs are summarized in Table 4.2. The detailed descriptions of the test rig and the used measurement techniques were provided in the papers of Augier et al. (2003a), Augier et al. (2003b), and Augier et al. (2007).

In Fluent software, the inlet of the duct is modeled with a velocity inlet boundary condition, requiring knowledge of inlet volume fraction and velocity of the phases, turbulent intensity, and hydraulic diameter. The inlet volume fractions of dispersed phase for the six runs are extracted from the specified experimental conditions via

$$\alpha_i = \frac{Q_d}{Q_d + Q_c} \tag{4.47}$$

and the inlet velocities for each phase are extracted by using homogenous model as

$$u_d = \frac{Q_d}{A_c \alpha_d} \tag{4.48}$$

$$u_c = \frac{Q_c}{A_c (1 - \alpha_d)} \tag{4.49}$$

where A_c is the cross sectional area of the duct, Q_c and Q_d are the volumetric flow rates of continuous and dispersed phases, respectively. According to the well-known homogenous model, the continuous and dispersed phase inlet velocities are assumed to be same. All extracted values for the inlet boundary condition are also given in Table 4.2. A turbulence intensity determination method based on the hydraulic diameter is used to estimate the inlet turbulence of the test section. The ratio of the fluctuating component of the velocity to the mean velocity is called the turbulence intensity, and is totally dependent on the upstream history of the flow. The magnitude of which is therefore difficult to predict. The turbulence intensity at the core of a fully-developed duct flow can be estimated from the following empirical correlation derived for pipe flows:

Table 4.2. Operation conditions of the experimental runs with some extracted inlet conditions

Run No	Run 1	Run 2	Run 3	Run 4	Run 5	Run 6
Experimental volumetric flow rate of continuous phase,Q_c(L/s)	1.056	1.056	1.056	1.056	1.056	0.913
Experimental Volumetric flow rate of dispersed phase, Q_d(L/s)	0.05	0.1	0.3	0.42	0.528	0.426
Experimental mean dispersed phase volume fraction, α_e	0.021	0.051	0.172	0.225	0.278	0.38
Experimental mean drop diameter, d, (m)	0.0040	0.0030	0.0031	0.0033	0.0040	0.0026
Experimental Particle Reynolds number, Re	110.9	49.3	32.3	30.2	36.7	8
Extracted inlet volume fractions of the dispersed phase, α_i	0.0452	0.0865	0.2212	0.2846	0.3333	0.3181
Extracted continuous - dispersed phase inlet velocities, (m/s)	0.1106	0.1156	0.1356	0.1476	0.1584	0.1339

$$I_t = 0.16\left(\mathrm{Re}_{HD}\right)^{-1/8} \tag{4.50}$$

where Re_{HD} is the Reynolds number based on the hydraulic diameter. The appropriate value of turbulence intensity is approximately estimated as 5% and used in simulation of the all cases. The hydraulic diameter, HD, is commonly used when handling flow through noncircular ducts:

$$HD = \frac{4A_c}{P_{wp}} \tag{4.51}$$

where A_c is the cross sectional area of the duct, and P_{wp} is the wetted perimeter. The hydraulic diameter is then calculated as 0.1 m for the present vertical duct.

The outlet of the duct is modeled as an outflow. Turbulent kinetic energy and turbulent dissipation rate are estimated using the specified turbulence intensity and length scale. The relations between them are written as

$$k = \frac{3}{2}\left(U_m I_t\right)^2 \tag{4.52}$$

and

$$\varepsilon = C_\mu^{3/4}\frac{k^{3/2}}{\ell} \tag{4.53}$$

where U_m is the mean flow velocity and turbulence length scale, ℓ, is a physical quantity related to the size of the large eddies that contain the energy in turbulent flows. In fully-developed duct flows, since the turbulent eddies cannot be larger than the duct, it is restricted by the size of the duct and can be estimated by the hydraulic diameter. An approximate relationship between ℓ and the physical size of the duct is

$$\ell = 0.07 HD \tag{4.54}$$

The factor of 0.07 is based on the maximum value of the mixing length in a fully-developed turbulent pipe flow. The no-slip condition is imposed for both phases at the duct walls.

4.2.8. Numerical Solution Method

Commercial CFD package Fluent v6.3.26 is used to simulate the liquid-liquid homogeneous co-current upward flow. The governing differential equations are solved by using an iterative solution to the discrete form of the mathematical model by means of the phase coupled semi-implicit method for pressure-linked equation (PC-SIMPLE) algorithm (Vasquez and Ivanov, 2000) for pressure-velocity coupling, which is an extension of the SIMPLE algorithm (Patankar, 1980) for multiphase flows. The quadratic upstream interpolation for the convective kinetics (QUICK) scheme of discretization is used for computing higher-order approximations for momentum, the phase volume fraction, turbulent kinetic energy and dissipation rate equations. QUICK-type schemes (Leonard and Mokhtari, 1990) are based on a weighted average of second-order-upwind and central interpolations of the variable. The velocities for both phases are solved from the coupled differential equations using the block algebraic multi-grid scheme (Weiss et al., 1999) with the governing equations solved sequentially in an implicit, unsteady fashion. Then, a pressure correction equation is built based on total volume continuity rather than mass continuity. Pressure and velocities are then corrected so as to satisfy the continuity constraint. The pressure-correction equation takes the following form for incompressible multiphase flows:

$$\sum_{q=1}^{n} \frac{1}{\rho_{lq}} \left\{ \frac{\partial}{\partial t} \alpha_q \rho_q + \nabla \cdot \alpha_q \rho_q \vec{u}'_q + \nabla \cdot \alpha_q \rho_q \vec{u}^*_q - \left(\sum_{r=1}^{n} \left(\dot{m}_{rq} - \dot{m}_{qr} \right) \right) \right\} = 0 \tag{4.55}$$

where ρ_{lq} is the phase reference density for the q^{th} phase (defined as the total volume average density of phase q), $\vec{u}'_q$ is the velocity correction for the q^{th} phase, and $\vec{u}^*_q$ is the value of $\vec{u}_q$ at the current iteration. The velocity corrections are themselves expressed as functions of the pressure corrections.

All numerical computations are time-dependent and carried out until steady state conditions have been reached. A time matching step size of 0.05 s with 20 iterations per time step is chosen. The converged solution is assumed when the scaled residuals of all variables are smaller than 10^{-3}. For near wall treatment, the non-equilibrium wall functions are used to solve the properties near the wall. It further extends the applicability of the wall function approach by including the effects of pressure gradient and strong non-equilibrium. Green-Gauss Cell based method is used to estimate gradients. Gravitational force is taken into account in these analyses.

4.3. Results and Discussion

In this section, the experimental and numerical results are presented and discussed. Several simulations have been performed to assess effectiveness of various drag models as a function of the dispersed phase volume fraction. Drag coefficient multiplier and mixture viscosity approaches have been used to obtain these drag models. Six sets of published data including mean axial velocities and phase volume fraction as a function of transverse position are used for the purpose of comparison. In order to reveal limitations and capabilities of these models, the CFD model is applied by using the transient Eulerian-Eulerian model in Fluent v6.3.26 for different dispersed phase volume fractions, ranging from the dilute ($\alpha_d \leq 0.1$) to the dense ($\alpha_d > 0.1$) flows. The experimental mean dispersed phase volume fractions (varying between 2.1% and 38%) at the test section are given as 0.021, 0.051, 0.172, 0.225, 0.278, and 0.38, respectively. It can be also seen from Table 4.2 that experimental mean dispersed phase volume fractions are less than the inlet volume fraction of the dispersed phase except the last run. The experimental and the computational dispersed phase volume fraction distributions and velocities of the both phases are shown in Fig. 4.5-4.7 by means of different data symbols. The axis of the symmetry of the test section, 2y/W=0, is also seen in these figures. These figures show that all computational data for the two halves of the test section are seemed to be symmetrically distributed. However, identity of the experimental volume phase fraction and both phase velocity data of the two sides of the symmetry axis line do not seem to be symmetrically distributed. So the un-reflection of the exact homogeneous condition of the flow regime is partly emerged. Disturbances in the profiles may be resulting from imperfections in supply system management a challenging task.

4.3.1. Results on dispersed phase volume fraction

The measured and numerically computed transverse distributions of the dispersed phase volume fractions within buoyancy driven vertical square duct for eight different drag models are shown in Figs. 4.5(a) through 4.5(f) at the six different runs. These figures show that the computational phase volume fraction distribution in the core of the square channel is nearly uniform. There are quite a number of experimental data available on uniform phase volume fraction and velocity distributions of two-phase upward flow in the core region of pipes and ducts (Lu et al., 2006). The computational results and experimental data of the dispersed phase volume fraction given in Fig. 4.5(a) agrees quite well for very dilute flow (α_e=2.1%) in a band, although some differences are noticeable. Augier et al. model reflects almost all features of the mean value of their experimental volume fraction distribution. The other models, except Rusche and Issa model, slightly underestimate the experimental mean value. In the case of Rusche and Issa model, a slight overestimation is noted. When the dispersed phase volume fraction is increased up to 5.1 percent, the dispersed phase volume fraction distributions based on the Augier et al. model and Rusche and Issa model are both found to give good estimations as shown in Fig. 4.5(b), and show a diverging tendency (cf. Figs. 4.5(b)-4.5(f)) from the other models' estimations. A similar tendency exists for the Kumar and Hartland model with increasing phase volume fraction up to 17.2 percent (cf. Figs. 4.5(c)-4.5(f)). Augier model estimation is seemed under the Rusche and Issa model estimation for dilute flows (cf. Figs. 4.5(a) and 4.5(b)). This behaviour is reversed with increasing volume fraction (cf. Figs. 4.5(c)-4.5(f)). The estimated dispersed phase volume fraction distributions of Barnea and Mizrahi, Ishii and Zuber, Schiller and Nauman, Bedeaux mixture viscosity based, and volume average mixture viscosity based drag models spread each other in a band and move away from the experimental data as the volume fraction increases. Among the investigated different drag models, the Augier et al. model is found to give quantitatively the best agreement with their experimental data for dilute and dense cases. Rusche and Issa and Kumar and Hartland models are found to give fairly well in agreement with experimental results for dilute and dense cases. All the remaining models considerably underestimate the experimental volume fraction distributions. Although, all models fail to estimate the experimental volume fraction distribution for the Run 6 having the smallest particle Reynolds number and being the densest run among all runs, Augier model is once again the closest model among them (cf. Fig. 4.5(f)). The drag correlation based on their own experimental data for the flow at high volume fractions seems to define drag in the best way.

Figures 4.5(a)-4.5(f) also show that the Schiller and Naumann model proposed to be acceptable for general use in all fluid-fluid pairs of phases is unsuitable for the dense flows. The estimated dispersed phase volume fraction data of the drag models based on mixture viscosity approach (i.e., Barnea and Mizrahi, Ishii and Zuber, volume average mixture viscosity based, and Bedeaux mixture viscosity based drag models) underestimate the experimental data. Spreading of drag models based on different estimated mixture viscosities shows that the reliable and suitable mixture viscosity model is the key parameter in this approach. However, it is not obvious how the mixture viscosity is related to the phase viscosities. Mixture viscosities of the drag models have been obtained by the phase volume fraction dependent Newtonian models and used in this study. However, most of the concentrated suspension systems, especially dense systems, exhibit non-Newtonian behavior. Therefore, Newtonian models need to extend for the non-Newtonian models. The parametric curve fitting on experimental apparent viscosity versus the phase volume fraction and the shear rate data could be used to obtain mixture viscosity (Yilmaz and Gundogdu, 2008). Unfortunately, no experimental data on the mixture viscosity of non-Newtonian two-phase flows in available literature that can be used for verification purposes of this study.

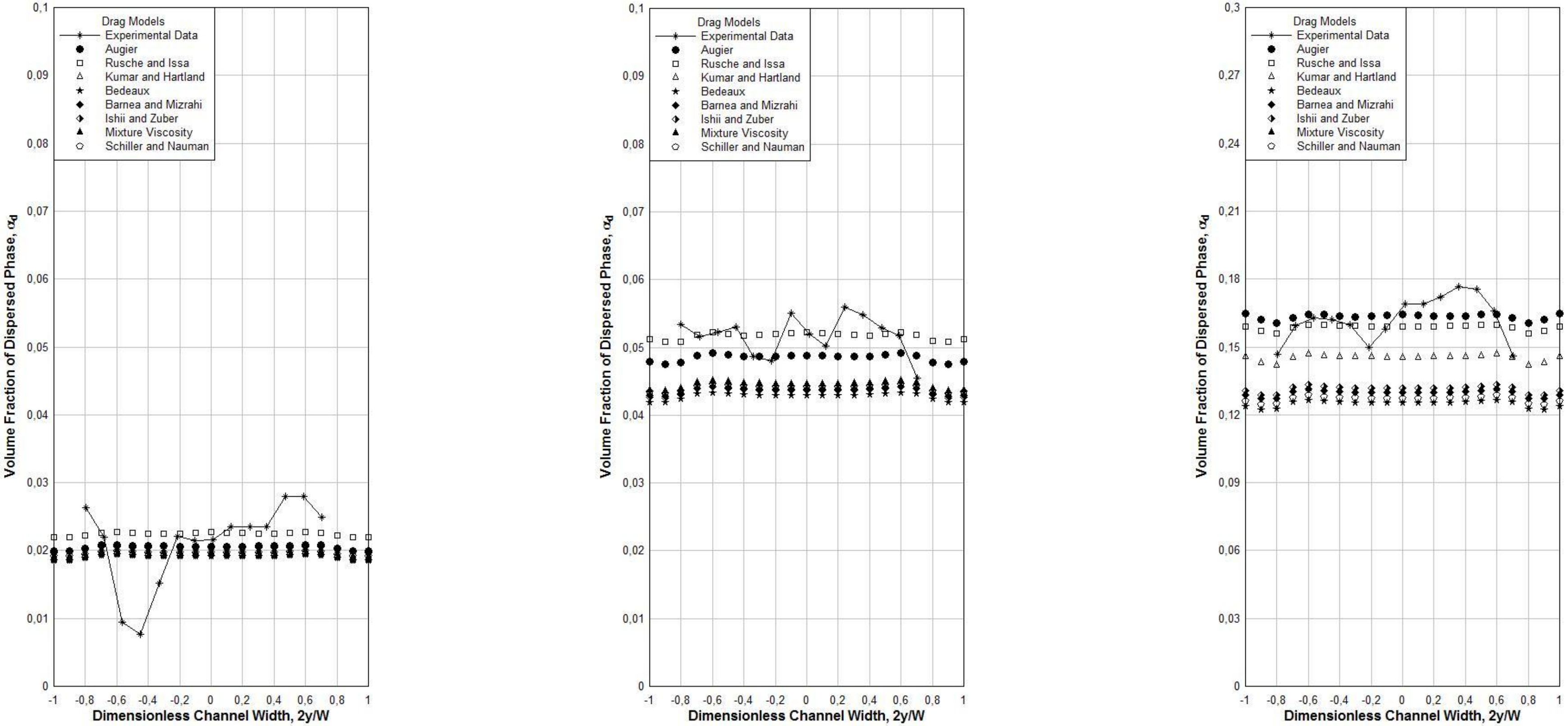

(a) Run 1 (α_e=2.1%) (b) Run 2 (α_e=5.1%) (c) Run 3 (α_e=17.2%)

Figure 4.5. Volume fraction profiles of dispersed phase for different runs

Figure 4.5. (Cont.)

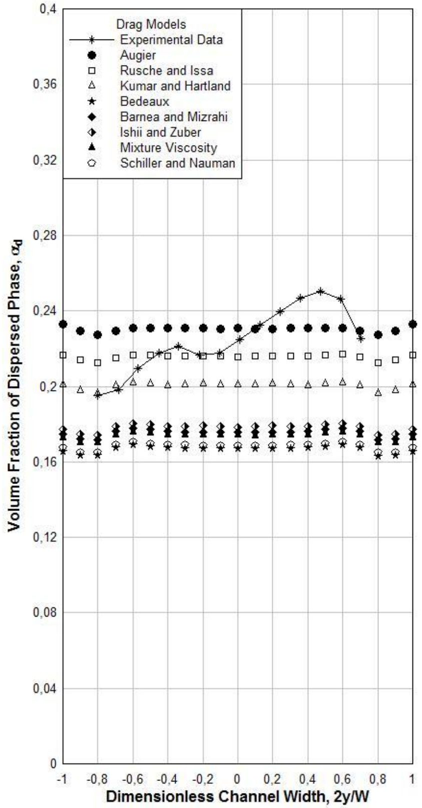

(d) Run 4 (α_e=22.5%)

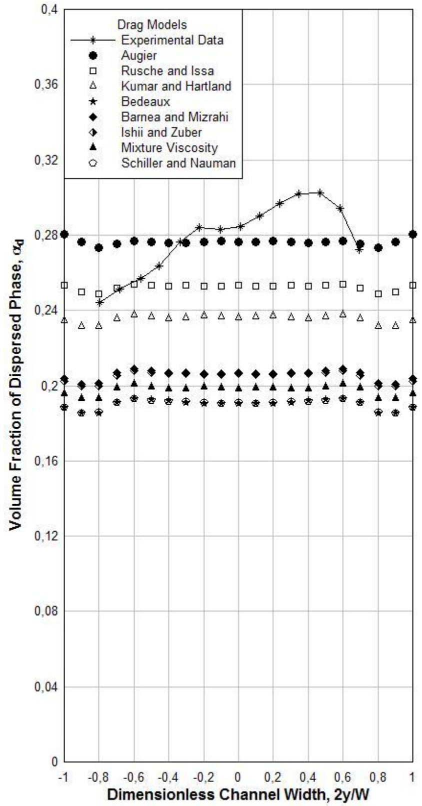

(e) Run 5 (α_e=27.8%)

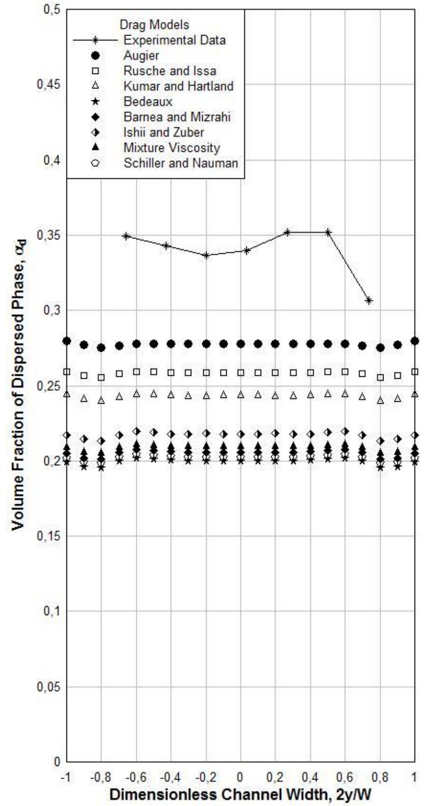

(f) Run 6 (α_e=38%)

Figure 4.5. Volume fraction profiles of dispersed phase for different runs

The drag models based on drag coefficient multiplier approach (i.e., Kumar and Hartland, Rusche and Issa, and Augier drag models) are found to give better performance than the models based on the mixture viscosity approach. Due to the limitations of measurement techniques, the addition of seeding sintered glass micro particles and of a hydrophilic fluorescent dye in the continuous phase act as surface contaminants and tend to immobilize partially the interface between these phases. As a result, the resulting drag coefficient is expected to be larger than in the case of pure interfaces and to have an effect also on the slip velocity. This effect might be an advantage for the drag coefficient multiplier approach.

The drops of the dispersed phase are considered as ideal spherical and monodispersed in this study. However, it is readily evident from the corresponding experiments that the dispersed phase element size is actually polydispersed. An illustration of drop size can be seen in the paper of Augier et al. (2003a) as a snapshot image of the experiment. To fill the gap of the lack of available adequate drag laws for polydisperse systems, monodisperse drag laws have been traditionally employed in polydisperse systems using ad hoc assumptions about the probability distribution. The simulation results of Leboreiro et al. (2008) indicate that the drag law treatment such as the polydisperse correction drag treatment plays a crucial role in the qualitative and quantitative nature of segregation predictions at low gas velocities. The effect of dispersed phase element size distribution at the cross sections of the square duct through its length, and spheroid drop shape are the basic limitations of this study. The underlying mechanisms on these limitations and adding them to drag models need further exploration.

4.3.2. Results on velocity profiles

It can be seen from Figs. 4.6 and 4.7 that all computational velocity profiles of continuous and dispersed phases descend a little in the central core region, and descend to zero at the near wall region, and ascend at the intermediate region, approximately between dimensionless channel width (2y/W) ±0.4 and ±0.6. All drag models predict the same trend. Ascending in the intermediate region and descending at the core increase with increasing phase volume fraction. These effects resemble the corresponding distributions presented in the experimental profiles. Quantitatively speaking, the simulated continuous phase velocities in Figs. 4.6(a)-4.6(f) are lower than the experimental results except the first run when the phase volume fraction is approaching to dilute flow (cf. Fig. 4.6(a)), and the last run, the densest run among all runs (cf. Fig. 4.6(f)). All drag models qualitatively follow the same trend. For dilute flow, all model predictions are the same. However, the predictions differ from each other with increasing phase volume fraction. Although the Augier, and Rusche and Issa models' predictions are found to give the closest results to the experimental data among all models, it is obvious that the differences between them are large.

Estimated distributions of dispersed phase velocity presented in Figs. 4.7(a)-4.7(f) differ significantly in dense phase simulations. The Augier, and the Rusche and Issa model predictions are found to give the closest results to the experimental data among all models except Run 2 (cf. Fig. 4.7(b)) and Run 3 (cf. Fig. 4.7(c)). The drag models based on mixture viscosity approach estimated the maximum dispersed phase velocities, since the estimated volume fractions of the dispersed phase are smaller than predicted from the drag coefficient multiplier approach.

It can be understand from the comparison Figs. 4.6 and Figs. 4.7 for corresponding runs that the estimated velocity profiles of both continuous and dispersed phases show nearly a parallel trend. As expected, the dispersed phase velocity is always larger than the continuous phase velocity, but the difference is decreasing with increase of the dispersed phase volume fraction, illustrating a qualitative agreement with the experimental tendency.

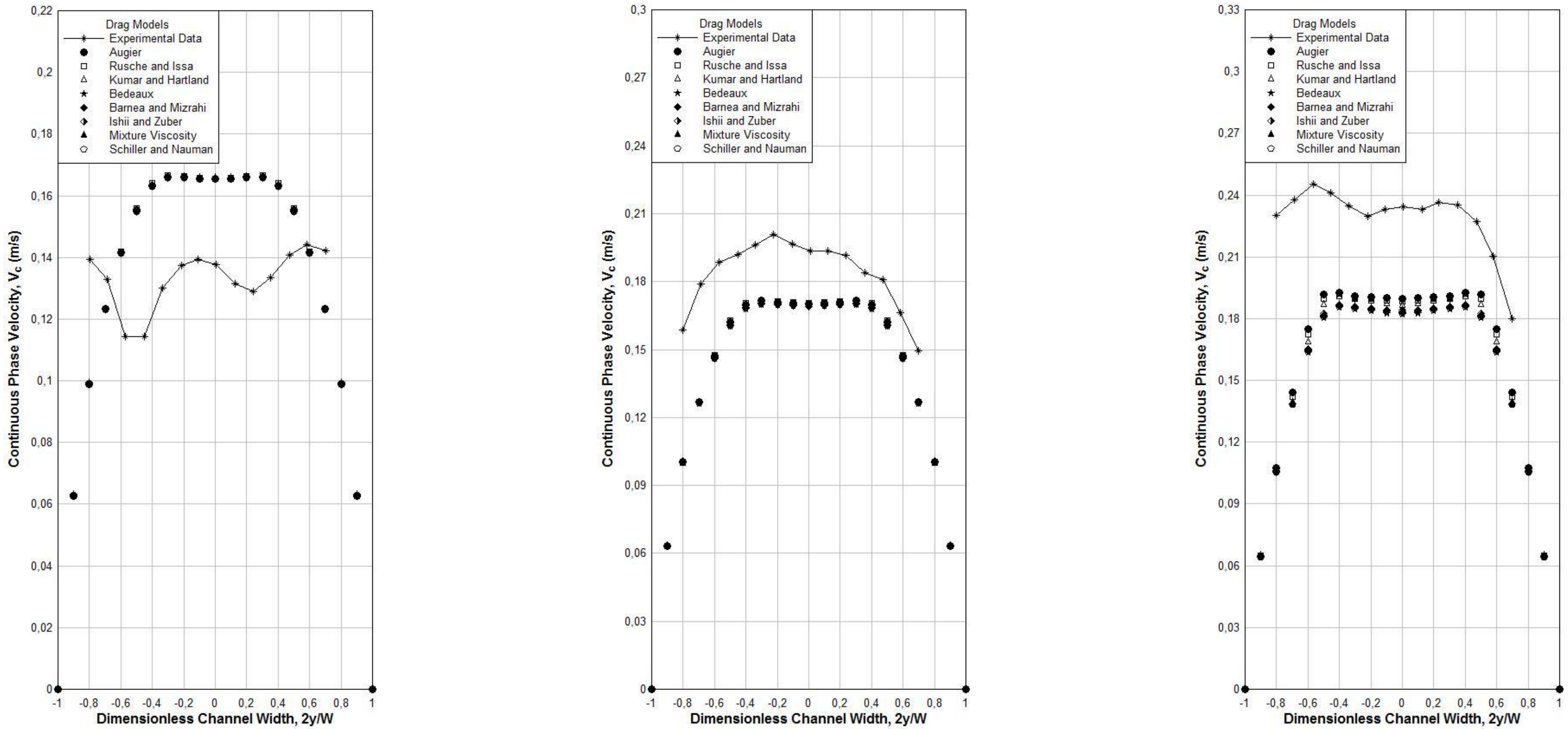

(a) Run 1 (α_e=2.1%) (b) Run 2 (α_e=5.1%) (c) Run 3 (α_e=17.2%)

Figure 4.6. Mean axial velocity profiles of continuous phase for different runs

Figure 4.6. (Cont.)

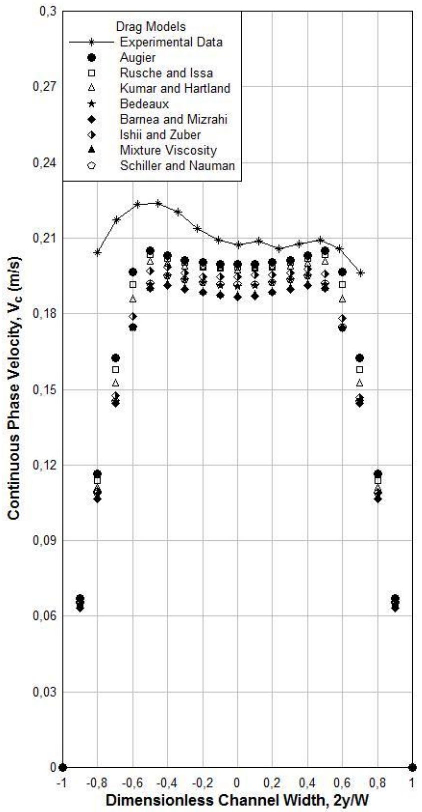

(d) Run 4 (α_e=22.5%)

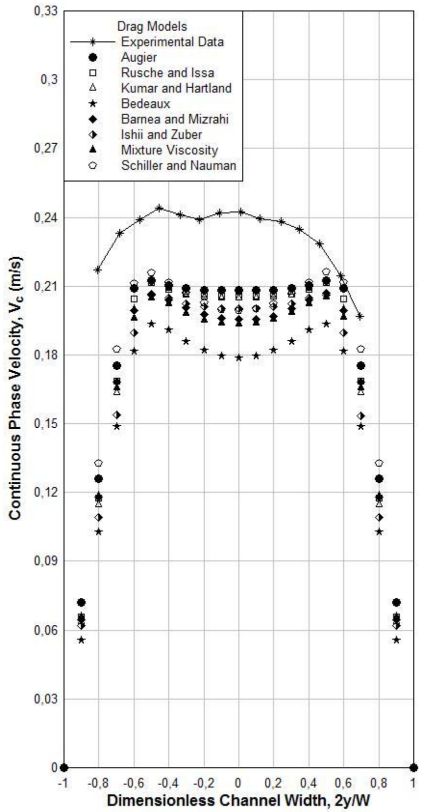

(e) Run 5 (α_e=27.8%)

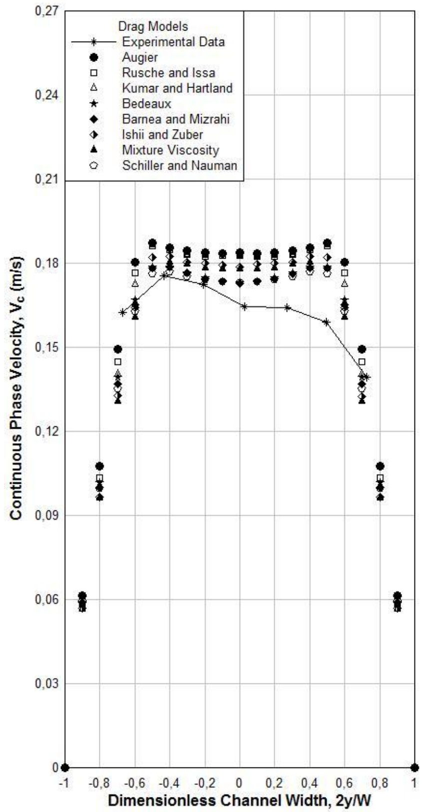

(f) Run 6 (α_e=38%)

Figure 4.6. Mean axial velocity profiles of continuous phase for different runs

4.4. Conclusions

The effectiveness of eight drag models, including two new modified models based on mixture viscosity approach, on the CFD simulation of a 2D and 3D vertical dense liquid-liquid co-current upward flow are assessed by using the Fluent platform. The dynamic flow characteristics of the two liquid phases in a turbulent two-phase flow are also investigated. The resulting hydrodynamic properties such as velocity profile of each phase and phase volume fraction profile of dispersed phase are compared with the experimental results of Augier et al. (2003a). An article about the results of this study has been in progress (Yilmaz et al., in progress, 2011a).

The results reveal that the selection of drag model in the CFD modeling of vertical dense liquid-liquid homogeneous dispersed flow significantly affects on the prediction of simulated flow patterns. All the simulated profiles show that the difference becomes more prominent as phase volume fraction increases. The Augier model is found to give quantitatively the best agreement with experimental phase volume fraction data for dilute and dense region. The drag correlations should so depend on their own experimental data for a flow with deformable interfaces at high phase volume fractions to define drag by the best way. Rusche and Issa model is found to give a good agreement relative to other drag models. The classical drag coefficient law (Schiller and Nauman drag model) underestimates the effect on the phase volume fraction, particularly at a high phase fraction. The Augier, and Rusche and Issa models are also found to give the best agreement with experimentally obtained velocity profiles in both qualitatively and quantitatively despite of some discrepancies.

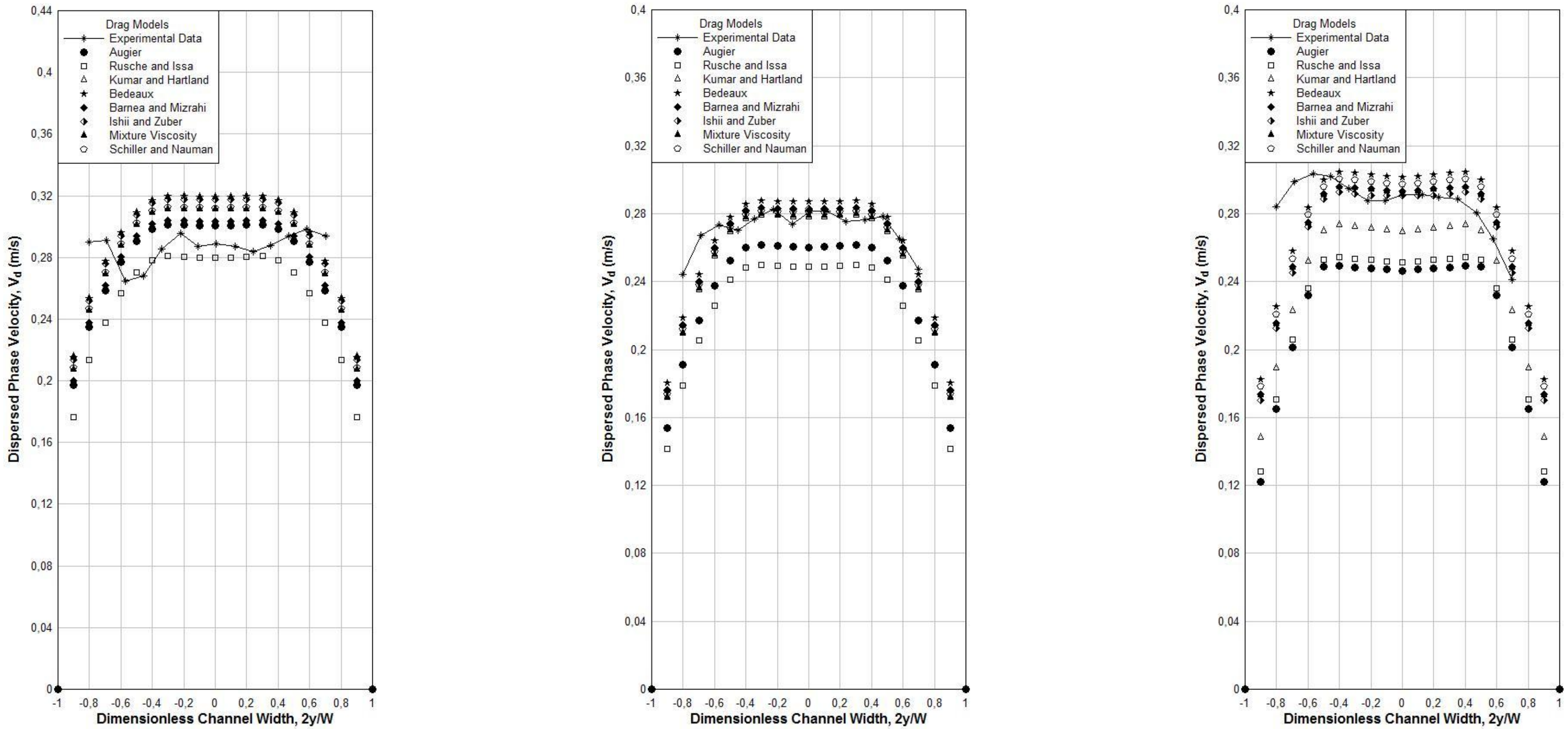

(a) Run 1 (α_e=2.1%) (b) Run 2 (α_e=5.1%) (c) Run 3 (α_e=17.2%)

Figure 4.7. Mean axial velocity profiles of dispersed phase for different runs

Figure 4.7. (Cont.)

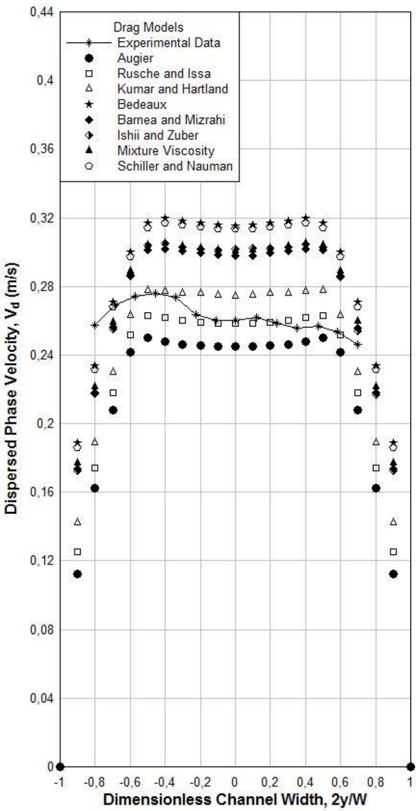

(d) Run 4 (α_e=22.5%)

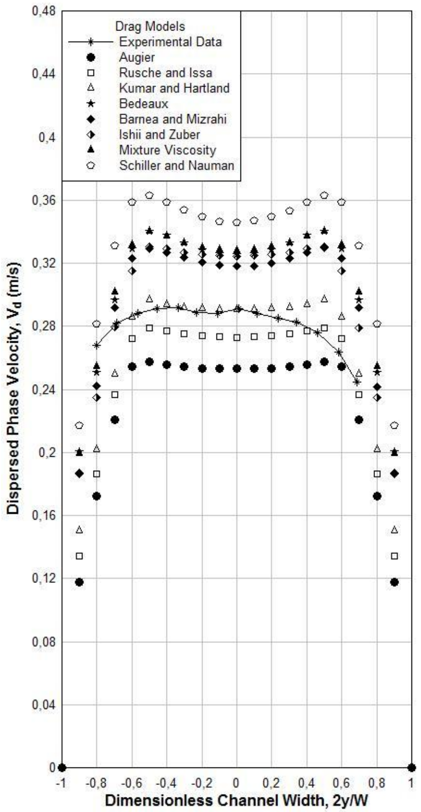

(e) Run 5 (α_e=27.8%)

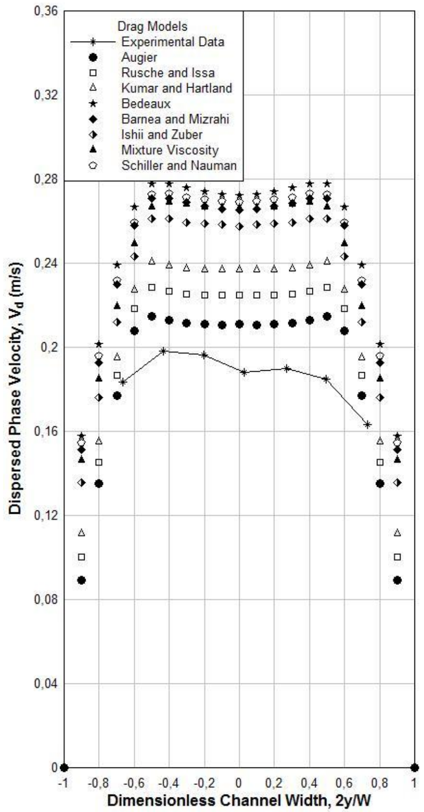

(f) Run 6 (α_e=38%)

Figure 4.7. Mean axial velocity profiles of dispersed phase for different runs

CHAPTER 5

DRAG EFFECTS ON PULSATILE BLOOD FLOW IN A RIGHT CORONARY ARTERY BY USING EULERIAN MULTIPHASE MODEL

5.1. Introduction

According to the World Health Organization (WHO), cardiovascular diseases such as heart attacks, strokes, atherosclerosis, stenosis and aneurysms have been accepted the world's highest cause of death, claiming approximately 17 million lives per year. The most commonly affected arteries are the abdominal aorta, the carotid, the coronary, and the femoral arteries (Moore et al., 2001). Unusual hemodynamic conditions in arteries in addition to arterial wall mechanics are accepted as a main reason of these diseases (Gessner, 1973), (Malek et al., 1999), (Wootton and Ku, 1999). Localization of these diseases in regions of curvature, bifurcation and branching in arteries has induced an assumption that the focal nature of these diseases is correlated with local flow conditions in these sites of the arterial system. Nowadays, it is postulated that local hemodynamics plays a critical role in the initiation and/or progression of these diseases.

Various hypotheses have been proposed relating atherosclerosis with local hemodynamics, such as pressure-related, turbulence-related, flow separation-related, and shear stress-related hypotheses. In a review article, Gessner (1973) commented on these hypotheses and concluded that the validity of most hypotheses is highly questionable and that only shear stress-related studies show promising results. Fry (1968) and Fry (1969) were the first to propose that high wall shear stress (WSS) damaged the arterial wall and that endothelial disruption or denudation could lead to atherosclerosis. Caro et al. (1969) and Caro et al. (1971) observed that the distribution of early atherosclerotic lesions is coincident with regions of low shear, and suggested that low wall shear stress favors the enhanced residence, adhesion and infiltration of macromolecules and/or blood cells into the vessel wall. Recently, proposals of band gap WSS (Nazemi et al., 1989), oscillations in WSS (Ku et al., 1985), temporal gradients of WSS (Ojha, 1994), and spatial gradients of WSS (Lei et al., 1997) have been included in these hypotheses. The importance of WSS on the initiation, growth and rupture of aneurysms has also been reported by some investigators (Boussel et al., 2008), (Lehoux et al., 2002), (Shojima et al., 2004). Although high WSS is considered as a major factor in the initiation of aneurysms, aneurysm rupture seems to be related to a low level of WSS for its growth. In spite of the fact that much attention has been paid to hemodynamic hypotheses, the precise role and the relative importance of proposed hemodynamic parameters on vascular endothelium, pathogenesis of the atherosclerosis, and progression of the arterial lesions remain unclear.

The significant and continuous improvements in medical imaging systems, computational techniques, and computer hardware and software performances have also brought reshaping of the CFD modeling for blood flow. Computational methods have widely accepted as a vital means for investigating the blood flow at complex regions of arteries. The performance of CFD models is directly dependent on blood rheology and the local environment of flow medium such as physiological flow conditions, mechanical properties of blood vessels, interactive forces between blood plasma (liquid phase) and blood cells (liquid or solid-like phase), etc. Developing an efficient and reliable CFD model for blood flow is a hard task and closely related with the way of defining hemodynamic characteristics of blood flow. Experimental investigations performed over many years have shown that blood flow exhibits non-Newtonian behavior and having properties such as shear thinning, thixotropy, viscoelasticity, and yield stress. Yilmaz and Gundogdu (2008) give a detailed description of blood structure, behavior of blood, and possible dominated condition of rheological behavior. A great number of single phase CFD models have been proposed to meet the requirements for blood flow in the last few decades. The effect of blood cell suspended structure on hemodynamic has been firstly added to the blood mixture viscosity by hematocrit dependent Newtonian viscosity. Afterwards, the shear rate dependent behavior and yield stress of blood resulting from blood cell structure has been supplemented. In some studies on thixotropy and viscoelasticity are also included. Additionally, not only particular effect on viscosity but also interaction of drag is also implemented by using two-phase theory (Jung et al. 2006a), (Jung et al, 2006b), (Jung and Hassanein 2008), (Srivastava and Srivastava 2009). In two-phase model, drag force between blood cell and plasma is the dominated force (Jung et al, 2006b) but this effect still needs more investigation.

Accurate modeling of the drag force effect is very critical with regard to the prediction of mean and turbulent features of two-phase flows, and there exist quite a number of studies on this problem in literature. The present multiphase CFD models on blood flow have helped to understand the effects of cell structure on the blood flow dynamics. Efficient analysis of drag forces acting on blood cells are one of the important deficiencies for the multiphase modeling of blood flow. The present drag force models neglect the effects of the presence of neighboring entities on drag. There is also need a dynamic RBC shape factor covering a wide range of the shear rates.

Unfortunately, the studies for drag forces acting on mono-dispersed blood cells or rouleaux are very limited in literature. The RBC has been considered to behave like a liquid droplet without any change in the physical characteristics (volume and surface area of RBC) of the membrane (Fischer et al, 1978), (Schmid-Schönbein and Wells, 1969) or solid-like phase. Therefore, the drag models developed for deformable and mobile interface particles such as droplets in a liquid-liquid system and particle in a liquid-solid system would be very useful for understanding the corresponding behavior of RBCs in blood. Various models developed to describe the drag coefficient for fluid-fluid systems have been recently reviewed (Yilmaz and Gundogdu, 2009). The influences of eight drag models based on drag coefficient multiplier and mixture viscosity concepts, including two new modified models, on the CFD simulation of a 2D and 3D vertical dense liquid-liquid co-current upward flow are assessed by using the Fluent v6.3.26 platform (Yilmaz et al., in progress, 2011a). The results reveal that the choice of drag models in the CFD modeling of vertical dense liquid-liquid homogeneous dispersed flow is significantly effective on the prediction of simulated flow patterns. The classical drag coefficient law (Schiller and Nauman drag model) underestimates the effect on the phase volume fraction, particularly at a high phase fraction. Augier et al. (2003a) and Rusche and Issa (2000) models are found to give the best agreement with experimental measurements on velocity profiles both qualitatively and quantitatively. The purpose of the present study is to reveal the influence of the effects of the presence of neighboring entities on drag in blood flow where the dominating mechanisms are expected to be viscosity, drag force and gravity.

5.2. Methods

5.2.1. Governing conservation equations

An Eulerian-Eulerian or two-fluid approach has been adopted to simulate and describe flow behavior of each phase inside a right coronary artery on the Fluent v6.3.26 platform. Each phase is treated mathematically as interpenetrating continua by incorporating the concept of phase volume fractions in the Eulerian-Eulerian approach. The sum of the phase volume fractions of all contributing phases must be equal to unity. The mass and momentum balance equations are written for each phase separately. Coupling between the motion of the dispersed and the continuous phase is achieved by implementing inter-phase momentum transfer terms into the respective phase's momentum balance equations. The derivation of the conservation equations for mass and momentum for each individual phase is done by ensemble averaging the local instantaneous balances. A general mass balance by convective mass fluxes without inter-phase mass transfer and mass source for each phase such as plasma and RBC is given by:

$$\frac{\partial(\rho_i \alpha_i)}{\partial t} + \nabla \cdot (\rho_i \alpha_i u_i) = 0 \tag{5.1}$$

where i represents any one of the phases, ρ is the density, α is the volumetric fraction, t is the time, and u is the velocity. The momentum balance equation for each phase is given by:

$$\frac{\partial(\rho_i\alpha_i u_i)}{\partial t}+\nabla\cdot(\rho_i\alpha_i u_i u_i)=-\alpha_i\nabla P+\nabla\cdot\tau_i+\alpha_i\rho_i g+\sum_{r=1}^{n}R_{ri}+F_i \tag{5.2}$$

where P is the pressure shared by all phases, τ_i is the i-phase stress-strain tensor, g is the gravitational acceleration, and F represents the external forces such as virtual mass, rotational and shear lift, electrical and magnetic forces. R_{ri} is an interaction force between the phase-i and the other phase or phases. In the Newtonian form, the stress-strain tensor for the plasma phase is given as follows:

$$\tau=\alpha_p\mu_p\left(\nabla u_p+(\nabla u_p)^T\right)+\alpha_p\left(\kappa_p-\frac{2}{3}\mu_p\right)\nabla\cdot u_p\, I \tag{5.3}$$

where, μ_p and κ_p are the shear and bulk viscosities for the plasma phase, respectively. α_p is the volume fraction of plasma, and I is a unit tensor. The bulk viscosity, κ_p can be ignored for incompressible fluids. The stress tensor for the particulate phases due to the interactions among particles is given in the form:

$$\tau=-P_i\delta+\alpha_i\mu_i\left(\nabla u_i+(\nabla u_i)^T\right)+\alpha_i\left(\kappa_i-\frac{2}{3}\mu_i\right)\nabla\cdot u_i\, I \tag{5.4}$$

where δ is the Kronecker delta and the particle-phase pressure, P_i, represents an inter-particle pressure as a function of volume fraction of the i-phase. This pressure is generated by the kinetic energy of the particle velocity fluctuations and hence collision of cells with each other or elastic or inelastic contact between cells. Since normal blood remains fluid even at a hematocrit of 98% (Fung, 1993) and since WBC and platelets are present at such low volume fraction, the inter-particle pressure of blood can be ignored (Jung and Hassanein, 2008), (Jung et al, 2006b). The inter-phase force, R_{ri} depends on the friction, pressure, cohesion, and other effects, and is subject to the conditions that R_{ri} =- R_{ir}, and R_{ii} =0:

$$\sum_{r=1}^{n}R_{ri}=\sum_{r=1}^{n}K_{ri}(u_r-u_i) \tag{5.5}$$

where K_{ri} ($=K_{ir}$) is the inter-phase momentum exchange coefficient between the phases. A particle moving in a fluid experiences a drag force due to the viscous effects in the direction of the flow. The RBC has been considered to behave like a liquid droplet without any change in the physical characteristics (volume and surface area of RBC) of the membrane (Fischer et al, 1978), (Schmid-Schönbein and Wells, 1969). The inter-phase momentum exchange coefficient for liquid-liquid dispersed flow can be written in the following general form:

$$K_{ri} = \frac{\alpha_i \alpha_r \rho_r f}{\tau_r} \tag{5.6}$$

where τ_r is the particle relaxation time given as:

$$\tau_r = \frac{\rho_r d_r^2}{18\mu_i} \tag{5.7}$$

where d_r is the mean diameter of the drops of phase r. The drag function f includes a drag coefficient C_D that is based on the Reynolds number, Re:

$$f = \frac{C_D Re}{24} \tag{5.8}$$

5.2.2. Drag models

To investigate the effectiveness of drag force model on blood flow, four different drag models are used to model the blood flow in this study. Only Schiller and Nauman drag model is available in Fluent v6.326. The other drag models are implemented into the CFD code by means of the user defined functions.

Schiller and Nauman (1935) drag model is the classical drag coefficient law not including the effects of the presence of neighboring entities.

$$C_D = \begin{cases} 24(1+0.15\mathrm{Re}^{0.687})/\mathrm{Re} & \mathrm{Re} \le 1000 \\ 0.44 & \mathrm{Re} > 1000 \end{cases} \tag{5.9}$$

$$\mathrm{Re} = \frac{\rho_c d\, U_r}{\mu_c} \tag{5.10}$$

where the particle Reynolds number, Re is based on the dispersed particle diameter, d, the magnitude of relative velocity, U_r, the density, ρ_c and the dynamic viscosity, μ_c of the continuous phase.

Rusche and Issa (2000) drag coefficient multiplier model is one of the selected model used as a general drag correlation law for all liquid-liquid dispersed flow systems and found to give good agreement with experimental measurements on velocity profiles among the other liquid-liquid dispersed models (Yilmaz et al., in progress, 2011a). Rusche and Issa (2000) extended the Schiller and Nauman model for a single dispersed drop for a dense flow.

$$C_D = C_{D0} F(\alpha) \tag{5.11}$$

where C_{D0} is the drag coefficient of a single spherical drop evaluated from the Schiller and Nauman model for a non-uniform flow, and $F(\alpha)$ is a function which takes into account the effects arising from the presence of other dispersed elements. The proposed $F(\alpha)$ correlation of Rusche and Issa (2000) is that:

$$F(\alpha) = e^{k_1 \alpha} + \alpha^{k_2} \tag{5.12}$$

where the values of the coefficients k_1 and k_2 for spherical droplets were determined respectively as 2.1 and 0.249 by using a non-linear curve fitting to five experimental data set on liquid-liquid system.

Gidaspow (1994) model is the other selected model and popularly used for solid particulate flows not only gas-solid but also fluid-solid system. It is a combination of Wen and Yu (1966) and the well-known Ergun (1952) equation. For $\alpha_{plasma} \leq 0.8$, the drag coefficient between the plasma and RBC is based on the Ergun equation to define the effects of dense solid phase on drag.

$$K_{RBC-plasma}^{Ergun} = 150\frac{\alpha_{RBC}(1-\alpha_{plasma})\mu_{plasma}}{\alpha_{plasma}d_{RBC}^{2}} + 1.75\frac{\rho_{plasma}\alpha_{RBC}\left|u_{RBC}-u_{plasma}\right|}{d_{RBC}} \tag{5.13}$$

For $\alpha_{plasma} > 0.8$, the drag coefficient is based on the work by Wen and Yu (1966)

$$K_{RBC\text{-}plasma}^{Wen\,Yu} = \frac{3}{4}C_D\frac{\rho_{plasma}\alpha_{plasma}\alpha_{RBC}\left|u_{RBC}-u_{plasma}\right|}{d_{RBC}}\alpha_{plasma}^{-2.65} \tag{5.14}$$

$$Re = \frac{\alpha_{plasma}\rho_{plasma}d_{RBC}\left|u_{RBC}-u_{plasma}\right|}{\mu_{plasma}} \tag{5.15}$$

Wen and Yu model has the same functional form as the Schiller Naumann correlation (C_D as in Eq. 5.9) but with a modified particle Reynolds number, and a power law correction. Both functions of the continuous phase volume fraction define the effects of medium and dilute solid phase (volume fraction solid phase less than % 20) on drag. To avoid an abrupt transition between the Wen-Yu and Ergun models, a switch function is used as follows (Huilin and Gidaspow, 2003)

$$\Phi = \arctan\left(\frac{150*1.75(0.2-\alpha_{RBC})}{\pi}\right)+0.5 \tag{5.16}$$

The Gidaspow model is used in the following form while implementing the user defined function code.

$$K_{RBC\text{-}plasma} = (1-\Phi)K_{RBC-plasma}^{Ergun} + \Phi K_{RBC\text{-}plasma}^{Wen\,Yu} \tag{5.17}$$

According to Ishii and Hibiki (2006), the drag correlations should depend on their own experimental data for a flow with deformable interfaces at high phase volume fractions to define drag by the best way. Augier et al. (2003a) drag correlation model based on own experimental data versus seven generic drag model estimation found to give the best agreement with experimental observation on volume fraction and velocity profiles among the other liquid-liquid dispersed models (Yilmaz et al., in progress, 2011a). The drag similarity criteria based on the mixture viscosity concept is applied to develop a new drag law dependent on the volume fraction and the shear rate. The mixture viscosity concept of the presented drag models in the literature is depended on volume fraction (Yilmaz and Gundogdu, 2009). Therefore, they show only Newtonian viscosity effects on mixture viscosity (Yilmaz and Gundogdu, 2008). However, mixture viscosity depends on the primary independent variables such as the volume fraction and the shear rate in most of the dispersed flow like blood flow.

$$C_D = \frac{24}{Re_m}\left(1 + 0.1 Re_m^{0.75}\right) \tag{5.18}$$

where the particle Reynolds number, Re_m is based on the mixture viscosity, μ_m instead of the continuous phase viscosity, μ_c as that:

$$Re_m = \frac{\rho_c d U_r}{\mu_m} \tag{5.19}$$

where the mixture viscosity, μ_m can be evaluated from the correlation of Cokelet (1987) or Jung et al. (2006a). Viscosity model with these correlations are function of both shear rate and hematocrit and not generic models. All these correlations depend on own experimental data of blood flow.

5.2.3. Fluid Properties

Blood consists of a suspension of elastic particulate cells in a liquid known as plasma. In this study, blood is assumed two-phase; one phase is plasma, the other is red blood cell. Human blood plasma, the continuous phase of blood, is about 91% water, 7% proteins, 2% inorganic solutes, and other organic substances of its weight (Mazumdar, 1998). Potential non-Newtonian properties of plasma were considerable debate until the early 1960 (Zydney et al., 1991), but recent studies have generally demonstrated that plasma is a Newtonian fluid with a viscosity of about 1.2 mPa·s at 37 °C (Pal, 2003) and its viscosity is a function of temperature (De Gruttola, 2005). The particulate second phase of blood consists of erythrocytes or red blood cells (RBCs), leukocytes or white blood cells (WBCs), and platelets. RBCs are the predominant cell type of blood and represents cellular volume fraction more than 99% (Picart et al., 1998a). The RBCs are so selected as dispersed phase. They consist of a thin elastic membrane enclosing hemoglobin solution that is a Newtonian fluid with a viscosity of about 6 mPa·s (Snabre and Mills, 1996) and this makes it possible for RBC to deform. The RBC volume fraction is called as the hematocrit and its normal range is 0.47±0.07 in adult human males and 0.42±0.05 in adult females (Pal, 2003). The plasma density 1003 kg/m^3, the RBC density 1096 kg/m^3 (Brooks et al., 1970), plasma viscosity 1 mPa·s, and an inlet hematocrit of 45% (Dill and Costill, 1974) are taken, the same as used by Jung et al. (2006a).

The effective RBC shear viscosity of particulate phase, μ_{RBC}, derived from the equation for dimensionless relative blood mixture viscosity (Jung et al., 2006a) and new drag law based on the volume fraction and the shear rate by using of mixture viscosity concepts are need a mixture viscosity model of blood. The non-Newtonian effect and also volume fraction effect of mixture viscosity can be added by variable methods. Concentration dependent Newtonian models can be extended to the non-Newtonian models by taking some model parameters as shear dependent variables (Quemada, 1978a), (Wildemuth and Williams, 1984), (Snabre and Mills, 1996). The non-Newtonian models can also be extended to show concentration effect by taking some model parameters as concentrated dependent variables.

Cokelet (1987) expressed a correlation for Quemada (1977) model. This mixture viscosity model based on the principle of minimum energy dissipation is the concentration dependent Newtonian model. The ratio of it to the plasma viscosity is given as

$$\eta_r = \left(1 - \frac{k}{2}\alpha_{RBC}\right)^{-2} \tag{5.20}$$

k is the effective intrinsic viscosity, a function of the maximum packing concentration of the RBC. This equation was extended to non-Newtonian model by taking the effective intrinsic viscosity parameter as a shear dependent variable (Quemada, 1978a), (Quemada, 1978b).

$$k = \frac{k_o + k_\infty (\dot{\gamma}/\dot{\gamma}_c)^{1/2}}{1 + (\dot{\gamma}/\dot{\gamma}_c)^{1/2}} \tag{5.21}$$

where k_o and k_∞ should be positive, $k_o > k_\infty$ for shear thinning suspension, $k=k_o$ if $\dot{\gamma} << \dot{\gamma}_c$, $k=k_\infty$ if $\dot{\gamma} >> \dot{\gamma}_c$, or $k= k_o=k_\infty$ if $\dot{\gamma}_c$ within the range of $\dot{\gamma}$ for which the suspension is Newtonian. The low shear rate intrinsic viscosity coefficient, k_o, the high shear rate coefficient, k_∞, and the critical shear rate, $\dot{\gamma}_c$ as a function of hematocrit are obtained from the experimental rheological data for human blood at 23 °C (Dufaux et al., 1980) and at 37 °C (Cokelet, 1987). The last coefficient ($\dot{\gamma}_c$) shows a more complex dependence on hematocrit, suspension phase composition, and temperature. Below given function of $\dot{\gamma}_c$ is only at physiologic blood temperature (37 °C). The data fitting of experimental data sets are shown in Figs. 5.1-5.3. Correlation of Cokelet (1987) has founded in good general agreement with Global viscosity correlation fit of Zydney et al. (1991). These correlation functions are as follows

$$\ln k_o = 3.874 - 10.410\alpha_{RBC} + 13.800\alpha_{RBC}^2 - 6.738\alpha_{RBC}^3 \tag{5.22a}$$

$$\ln k_\infty = 1.3435 - 2.803\alpha_{RBC} + 2.711\alpha_{RBC}^2 - 0.6479\alpha_{RBC}^3 \tag{5.22b}$$

$$\ln \dot{\gamma}_c = -6.1508 + 27.923\alpha_{RBC} - 25.60\alpha_{RBC}^2 + 3.697\alpha_{RBC}^3 \tag{5.22c}$$

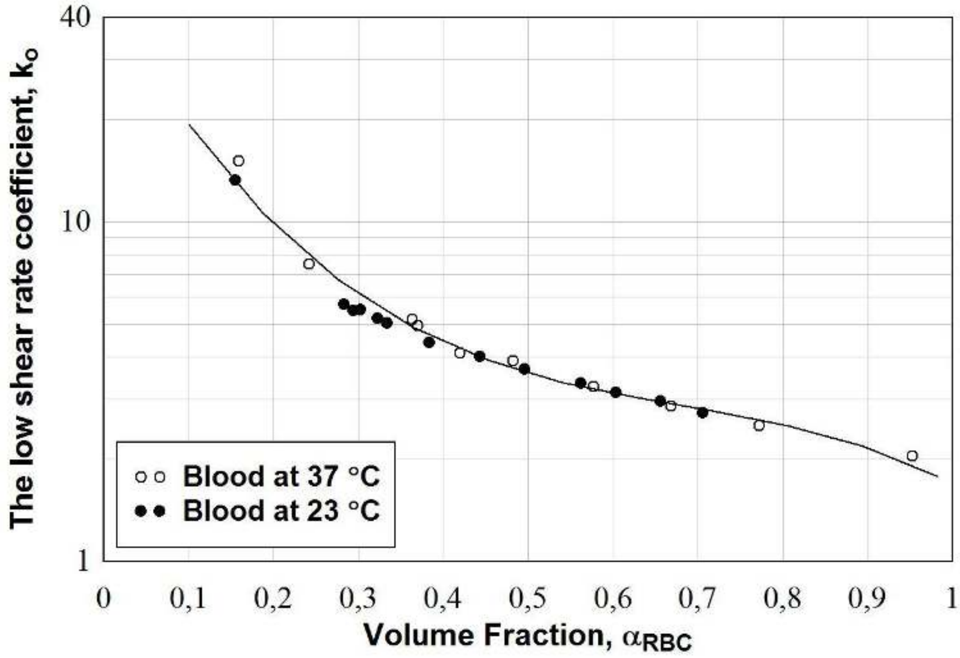

Figure 5.1. Hematocrit dependence of the low shear rate intrinsic viscosity coefficient

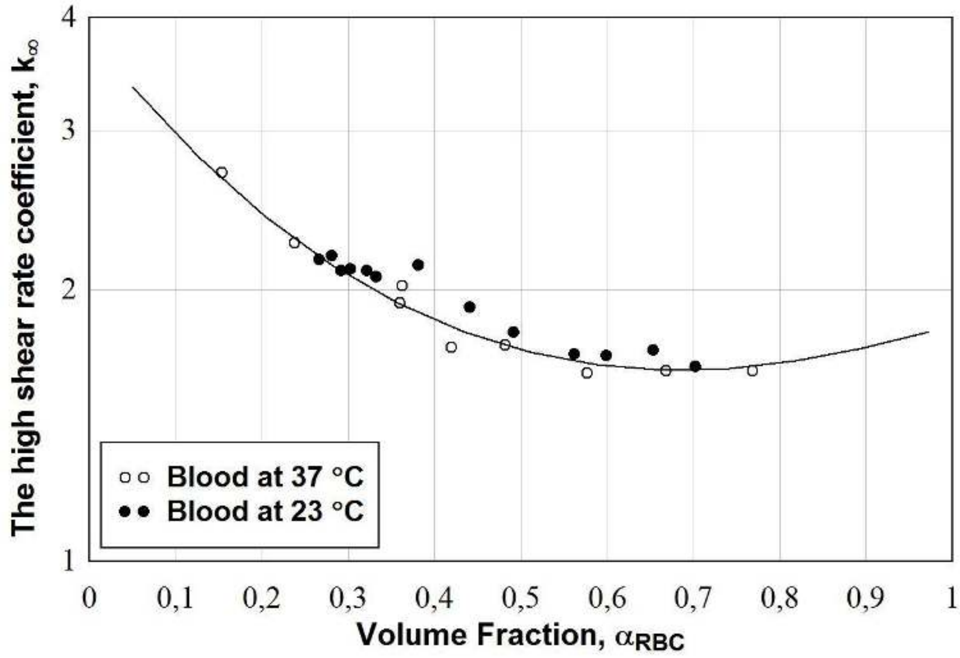

Figure 5.2. Hematocrit dependence of the high shear rate intrinsic viscosity coefficient

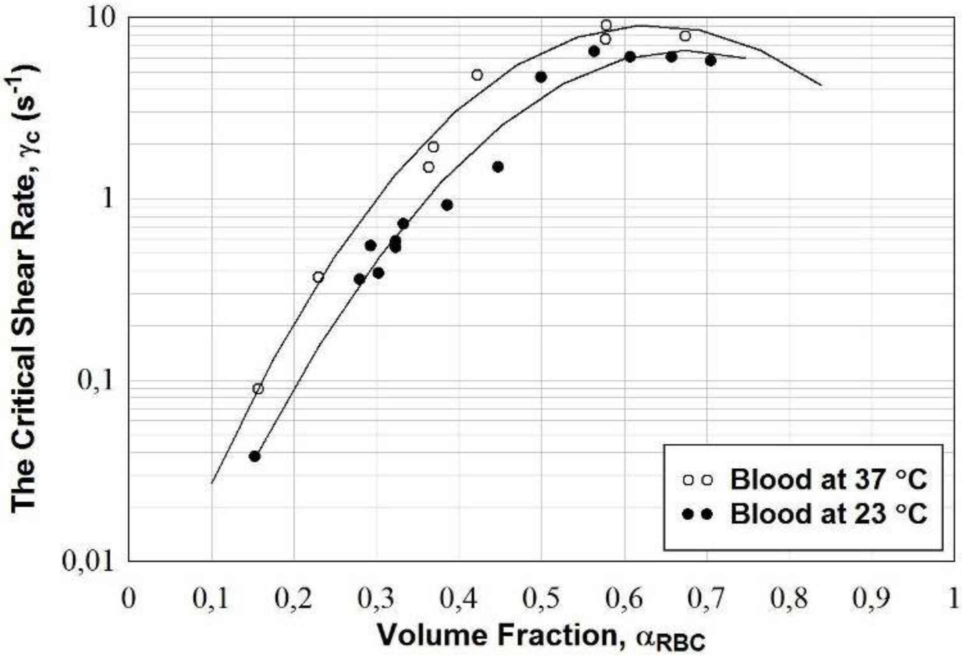

Figure 5.3. Hematocrit dependence of the critical shear rate

The non-Newtonian Carreau-Yasuda viscosity model was extended to reflect concentration effect by taking model parameters (m, n) as concentration dependent variables by Jung et al. (2006b). The modified relative mixture viscosity model is given as

$$\eta_r = m[1+(\lambda\dot{\gamma})^2]^{(n-1)/2} \tag{5.23}$$

where m, n, and λ are model parameters. The time constant, λ, is taken 0.11 s as used by Gijsen et al. (1999a). The other two parameters n and m are correlated as a function of hematocrit to obtain accurate agreement with experimental rheological data of Wojnarowski (2001) and Brooks et al. (1970) for human blood. Obtained polynomial functions are as follows

$$n = 1 - 0.3503\alpha_{RBC} - 0.8246\alpha_{RBC}^2 + 0.8092\alpha_{RBC}^3 \tag{5.24a}$$

$$m = 1 - 16.305\alpha_{RBC} - 51.213\alpha_{RBC}^2 + 122.28\alpha_{RBC}^3 \tag{5.24b}$$

Rheological measurements of Brooks et al. (1970) were taken at 25 °C, different than physiologic blood temperature. Rheological data in the paper of Wojnarowski (2001) was taken in which temperature was not given. These data sets and fitted equations at different hematocrit values are shown in Fig. 5.4.

The mixture viscosity may be calculated from a simple volume fraction average of the pure species' viscosities that assumes a linear relationship between the mixture viscosity and the continuous and dispersed phase viscosities (Enwald et al., 1996). Jung et al. (2006a) used this theory and obtained the effective RBC viscosity, μ_{RBC}.

$$\eta_r = \frac{\mu_{mix}}{\mu_{plasma}} = \frac{\mu_{RBC}\alpha_{RBC} + \alpha_{plasma}\mu_{plasma}}{\mu_{plasma}} \qquad (5.25)$$

The mixture viscosity of blood can also be easily calculated by multiplication of dimensionless relative blood mixture viscosity and plasma viscosity.

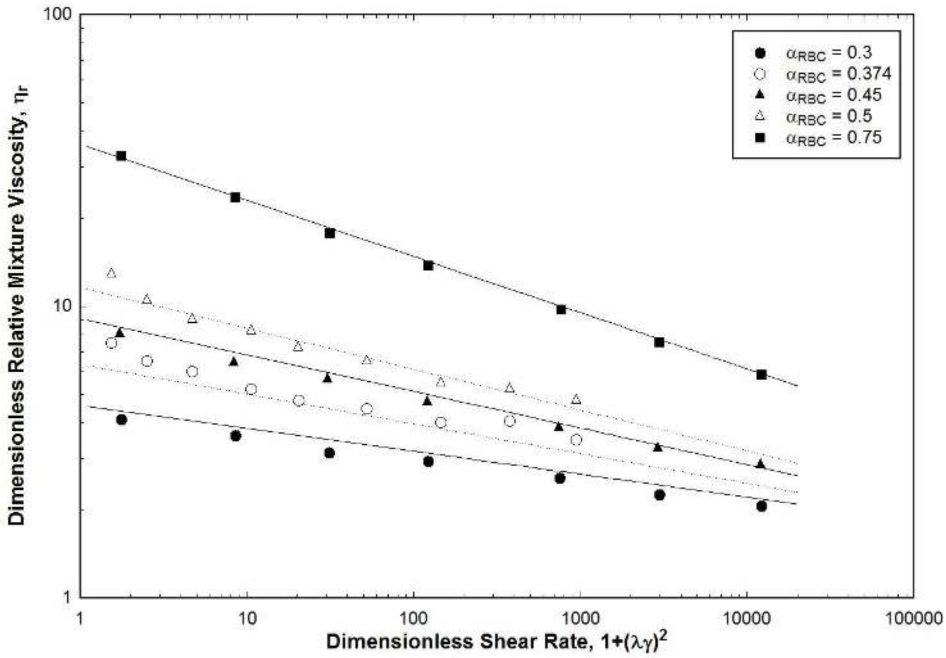

Figure 5.4. Hematocrit and shear rate relation of dimensionless relative blood viscosity

5.2.4. Computational grid

The 3-D geometry of a realistic human RCA was reconstructed by angiography in the study of Berthier et al. (2002). Reconstruction technique was close to clinical biplane angiography of Goubergrits et al. (2001). The sites of dilatation and stenosis were selected by physician to generate 30 consecutive cross sections and then these sections combined to obtain 3-D geometry of the RCA. The RCA so had different cross section along the axial direction. The total length, inlet and exit areas were 0.129 m, 15.791979 mm^2, and 2.149074 mm^2 respectively. To ensure a fully developed velocity profile at the RCA inlet, an additional 20 mm length straight tube of the same inlet diameter following a direction perpendicular to the inlet cross-section was integrated with the reconstructed RCA.

The obtained geometry of computational domain was discretized into hexahedral elements using Gambit software as shown in Fig. 5.5. To ensure better accuracy and more realistic derivation of the shear rate from the near-wall layer, a boundary layer having 3 rows, a growth factor of 1.2, and a total thickness of 0.182 mm was created on the inlet cross section, then applied a Cooper meshing scheme to the volume, using the inlet and exit faces as source faces (see Figs. 5.6 and 5.7). The total number of elements, nodes and faces used for the mesh of RCA were 36.418, 40.734, and 113277 respectively. Each of 278 cross sections in the mesh contained 131 faces. The quality of the meshes was assessed by different internal parameters. As an example, the skewness remained below 0.72, even in the most tortuous area, which was entirely satisfactory. This mesh of domain is used for the computations. It is the same as used in the studies of Berthier et al. (2002), Jung et al. (2006a), and Huang et al. (2009). The average run time for a complete cardiac cycle was approximately 3 1/4 h on a personal computer having a quad processor Q9450 (12 Mb cache, 2.66 GHz) and 8 Gb ram running under a Windows 64bit system with 40734 mesh nodes.

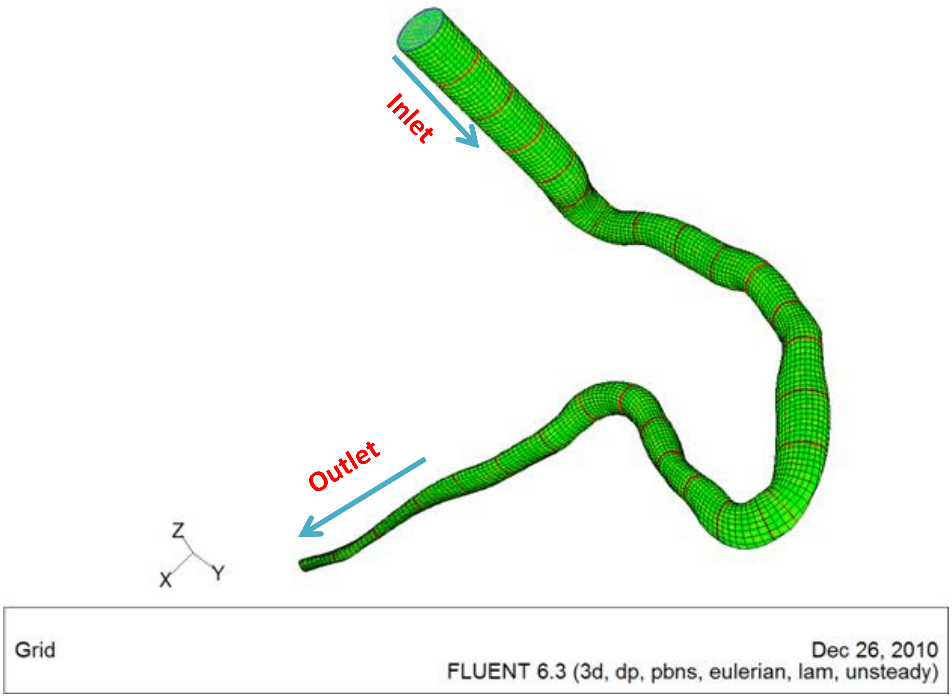

Figure 5.5. 3D-view of the right coronary artery mesh

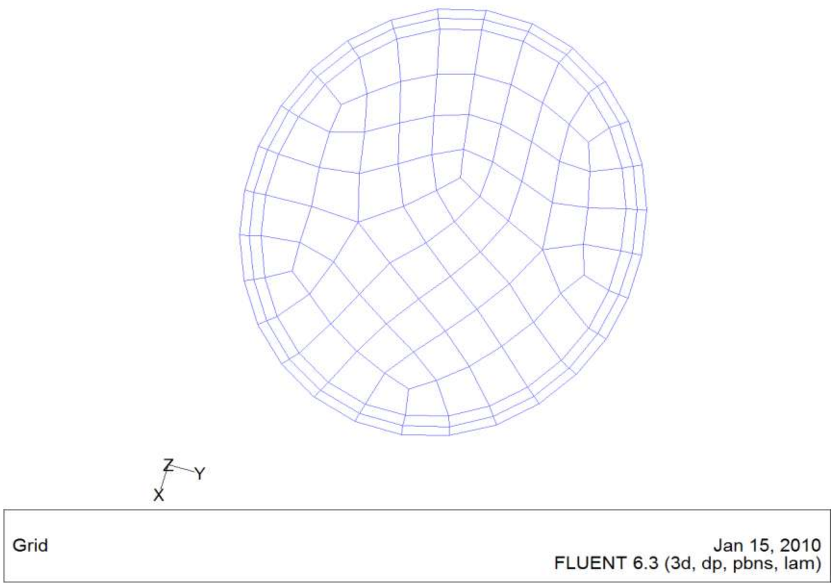

Figure 5.6. View of the grid in the entrance section with the boundary layer.

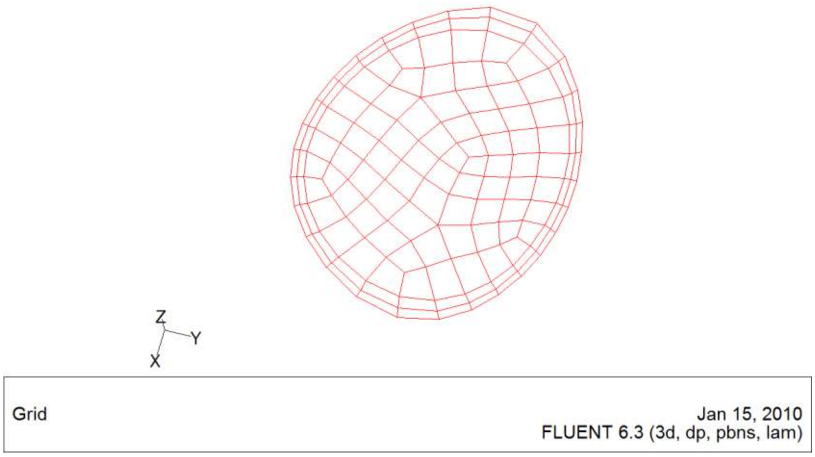

Figure 5.7. View of the grid in the exit region with the boundary layer

Evaluating grid independent solutions are also an important aspect to minimize the error in CFD results. According to the results of the mesh refinement studies of Zeng et al. (2003), Myers et al. (2001), Jung et al. (2006a), and Stewart and Lyman (2004), the used mesh in this study was accepted as essentially grid size independent by Huang et al. (2009).

5.2.5. Boundary conditions

The flow is considered as unsteady, 3-D, two-phase, non-Newtonian, and laminar. Pulsatile periodic flow condition is assumed as an inlet boundary condition for both plasma and RBC phases. A pulsatile inlet velocity waveform with a cardiac period of 0.735 s from Jung et al. (2006a) is used by developing an equation for the waveform curve, and then the equation defined into the Fluent 6.3.26 by means of a compiled user defined function, UDF in C++ language. Blood flow patterns for RCA (Nichols and O'Rourke, 1998) and in vivo pressure and flow rate measured in the ascending aorta (Cholley et al., 1995), (Poppas et al., 1997) was used to obtain this waveform by Jung et al. (2006a). Obtained mathematical function of the curve at the inlet is used to be velocity inlet as shown in Fig. 5.8. The times of end of the diastole (ED), peak of the systole (PS), end of the systole (ES), and the peak of the diastole

(PD) are 14.751 s, 14.835 s, 15.039 s, and 15.071 s for the 21st cardiac cycle. This is quite similar to the values in Huang et al. (2009). The inlet velocity profiles across the entry tube cross section are maintained as uniform.

Calculated Womersley parameters of Rappitsch et al. (1997), Gijsen et al. (1999b), Qui and Tarbell (2000), Zeng et al. (2003), and Jung et al.'s (2006a) idealized RCA model are 4.8, 7, 3, 1.82, and 3.12 respectively. All of these values are in the intermediate region of laminar pulsatile pipe flow (Gundogdu and Carpinlioglu, 1999a). Velocity field in intermediate region of laminar-pulsatile pipe flow is investigated by using experimental and computational techniques by Yilmaz and Gundogdu (2010). Both the experimental and the computational velocity profiles become blunter than the Blasius's distribution in some phases of the pulsation cycle and show a good agreement with each other.

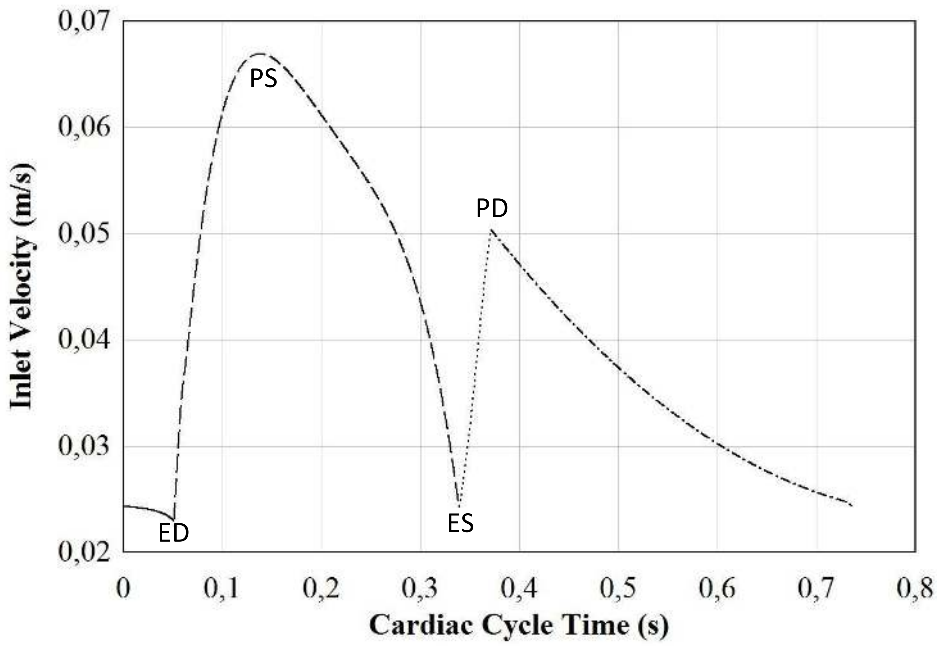

Figure 5.8. Inlet velocity waveform generated from surface monitor at inlet

The no slip wall boundary condition is applied for both RBCs and plasma. The diameter of RBCs is considered as 8μm spherical particles. For initial conditions, the inlet values at the entry are set. Outflow boundary condition are used to model flow exit where the reference pressure is set to 75 mmHg as used by Jung et al. (2006a) and Huang et al. (2009). A maximum convergence criterion of 10^{-3} for each scaled residual component is specified for the relative error between two successive iterations. A very small constant time step 10^{-4} for with maximum 20 iterations per time step is used. The hematocrit dependent non-Newtonian shear-thinning viscosity model for RBCs, and the used drag force models are programmed into the Fluent 6.3.26 as individual user defined functions. The computations are completed at the end of 21 cardiac cycles.

5.2.6. Numerical Solution Method

Fluent is a multi-purpose, unstructured, finite-volume based, Navier-Stokes CFD solver. The pressure-based solver of Fluent 6.3.26 is employed. This solver uses a co-located scheme where both the scalar and vector quantities are stored at the cell centers. The governing differential equations are solved by using an iterative solution to the discrete form of the mathematical model by means of the phase coupled semi-implicit method for pressure-linked equation (PC-SIMPLE) algorithm (Vasquez and Ivanov, 2000) for pressure-velocity coupling, which is an extension of the SIMPLE algorithm (Patankar, 1980) for multiphase flow. The quadratic upstream interpolation for the convective kinetics (QUICK) scheme of discretization is used for computing higher-order approximations for momentum and the phase volume fraction. QUICK-type schemes (Leonard and Mokhtari, 1990) are based on a weighted average of second-order-upwind and central interpolations of the variable. The velocities for both phases are solved from the coupled differential equations using the block algebraic multi-grid scheme (Weiss et al., 1999) with the governing equations solved sequentially in an implicit, unsteady fashion.

5.3. Results and Discussion

The method just described is used to simulate a multiphase pulsatile dense flow, having non-Newtonian shear thinning properties in a geometrically realistic 3-D artery by using Eulerian multiphase model in FLUENT V6.3.26. All simulations are continued up to the end of the 21^{st} cardiac cycle (15.435 s). The results are presented herein within the 21st cardiac cycle (14.7 s – 15.435 s).

Figs. 5.9-5.12 show the variation of the axial velocity profile along the length of the RCA during the cardiac period in accordance with the pulsatile flow waveform for selected different cardiac cycle times. Computed axial velocity profiles and the contour plots of RBCs obtained by using the new drag law show the development of the boundary layer in the entrance region. The color bar shows the range of related properties. The maximum and minimum values of axial velocities occur at the peak of the systole (14.84 s) and at the end of the diastole (14.75 s), respectively. Development of boundary layer is shown to be similar to the results of Jung et al. (2006b) and Huang et al. (2009). The velocity profiles of RBCs changes from a uniform profile at the entrance of the RCA to its fully developed profile at the end of the added straight tube. Thus, the entrance length of 20 mm under these flow conditions seems sufficient for the simulation of RCA. The average inlet velocity is approximately 0.042 m/s, as shown in Fig. 5.8. The computed boundary layer development of the RBC shear rate, viscosity, and volume fraction in the entrance region is also presented as contour plots in Figs. 5.13-5.15. When the radial distance in the entrance region increases towards the wall, shear rate increases (cf. Fig. 5.13), and the RBC viscosity decreases resulting from its shear thinning properties. This is opposite of the mixture viscosity computed by Huang et al. (2009) by using multiphase kinetic theory. Cell-free or cell-depleted layer near the wall and a cell-rich core are experimentally observed by many investigators for blood flowing through small vessels (Bugliarello and Sevilla, 1970), (Cokelet, 1972), (Thurston, 1989). There is a depletion layer at the top and the bottom on the XZ plane shown in Fig. 5.15. For tubes of diameter greater than about 50 times the cell diameter, or 0.5 mm tubes in the case of blood flow, the effect of the cell-depleted wall layer on viscosity is accepted as negligible by Skalak et al. (1989). A better mesh refinement can be used in the vicinity of the wall to better resolve the volume fraction distribution in it. However, the used RCA model has the diameter larger than 4 mm in the entrance region. Moreover, geometry of the tube has no longer straight and has different cross sections along the axial direction. Depletion at the bottom and cell-rich layer at the top on the XY plane may be the resulting of curvature after the entrance (cf. Fig. 5.15).

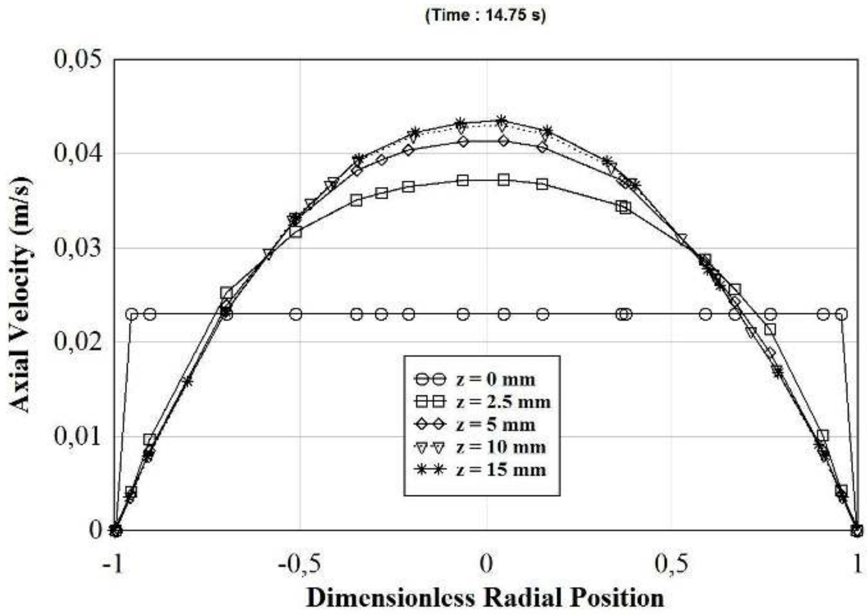

(a)

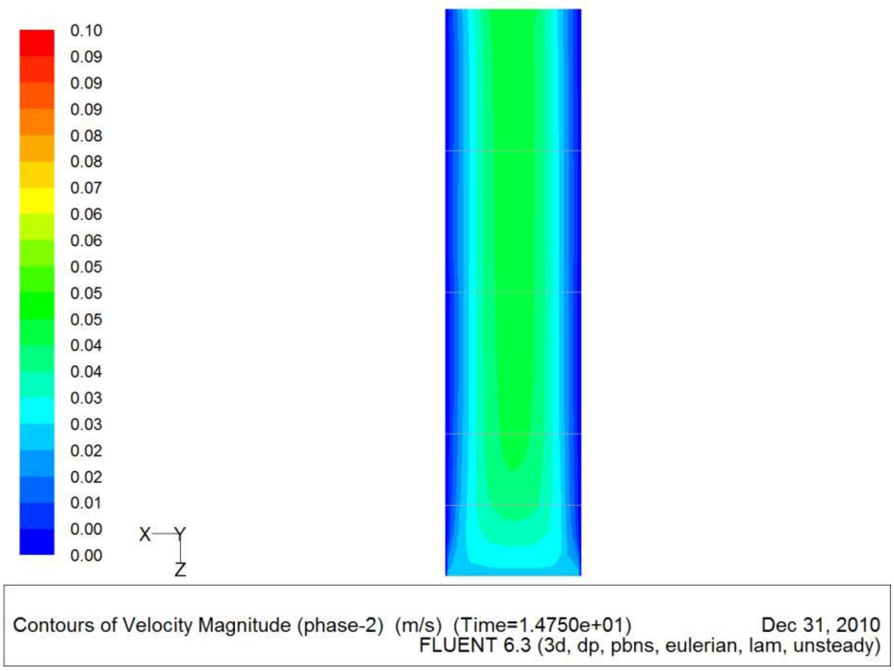

(b)

Figure 5.9. Development of RBC's inlet velocity profiles (a) and the contour plot (b) in the entrance region at beginning of the systole (14.75 s) with using modified drag correlation based on Jung' et al. (2006a) viscosity model. Flow is in the direction of the negative z-coordinate

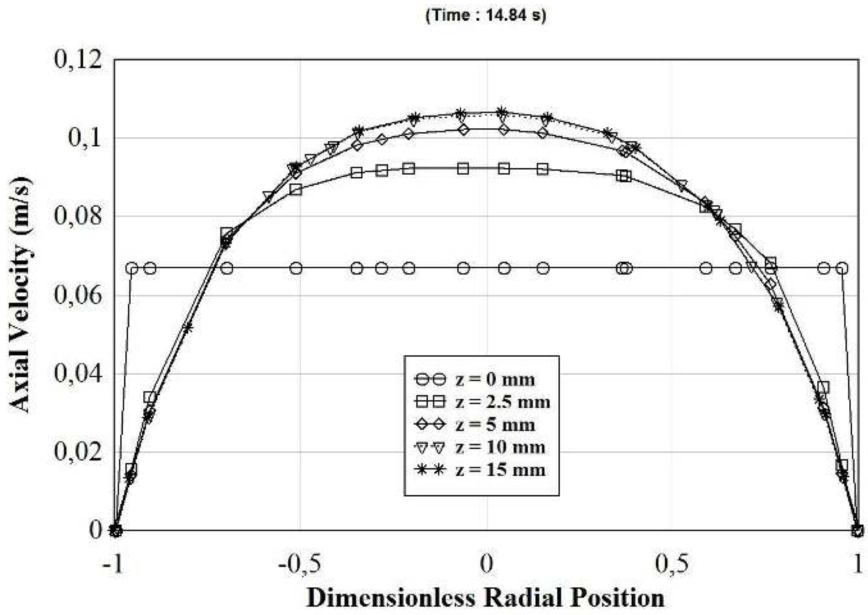

(a)

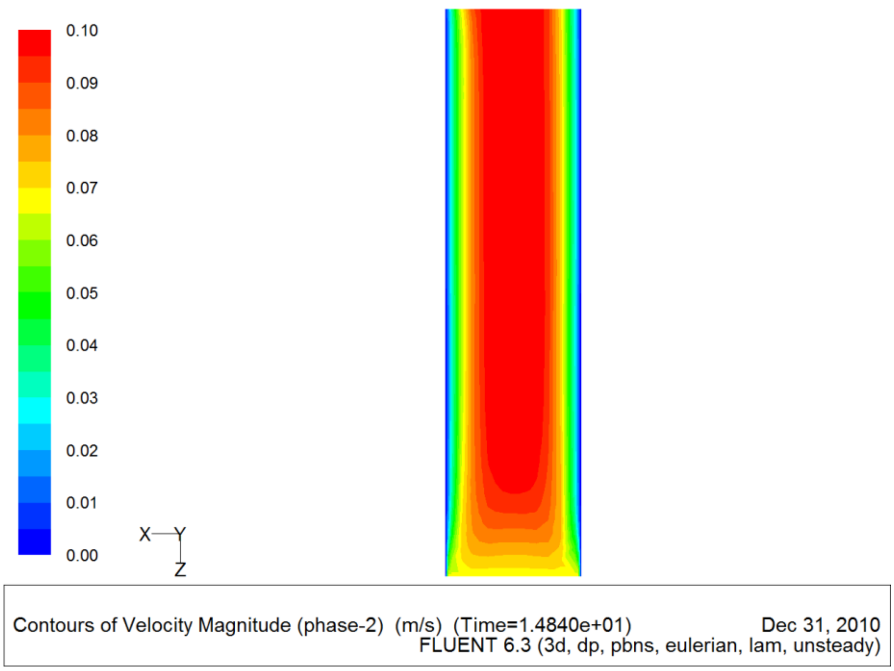

(b)

Figure 5.10. Development of RBC's inlet velocity profiles (a) and the contour plot (b) in the entrance region at peak of the systole (14.84 s) with using modified drag correlation based on Jung' et al. (2006a) viscosity model. Flow is in the direction of the negative z-coordinate

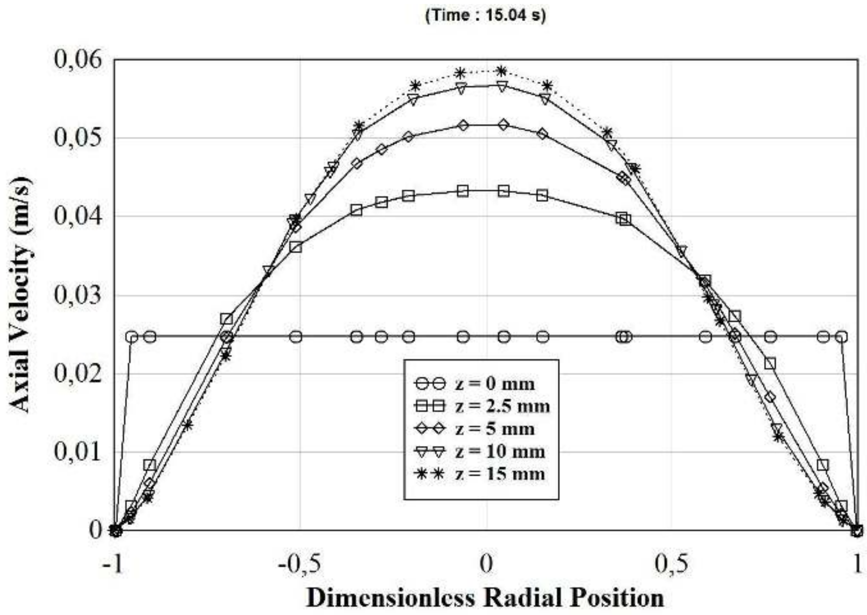

(a)

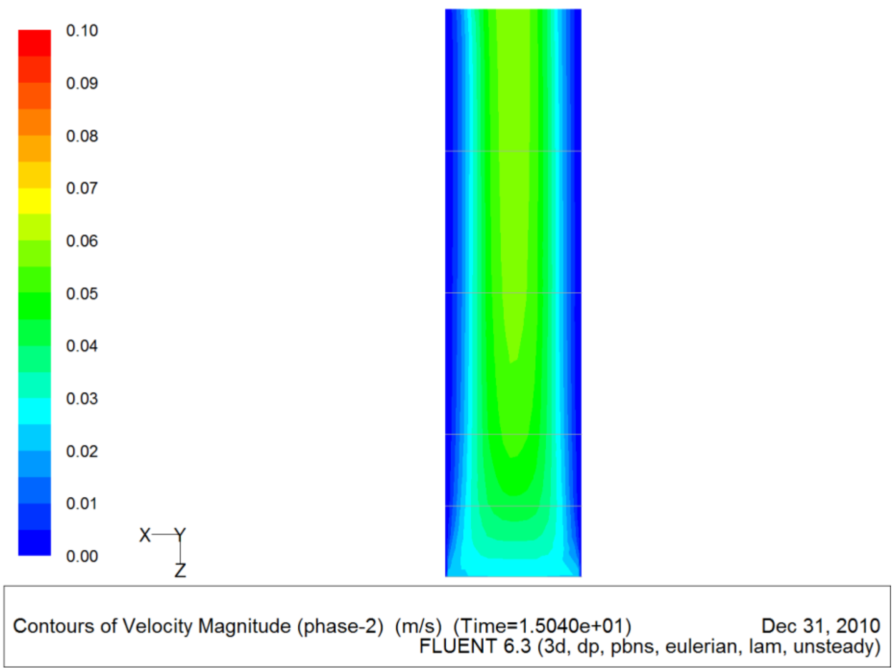

(b)

Figure 5.11. Development of RBC's inlet velocity profiles (a) and the contour plot (b) in the entrance region at beginning of the diastole (15.04 s) with using modified drag correlation based on Jung' et al. (2006a) viscosity model. Flow is in the direction of the negative z-coordinate

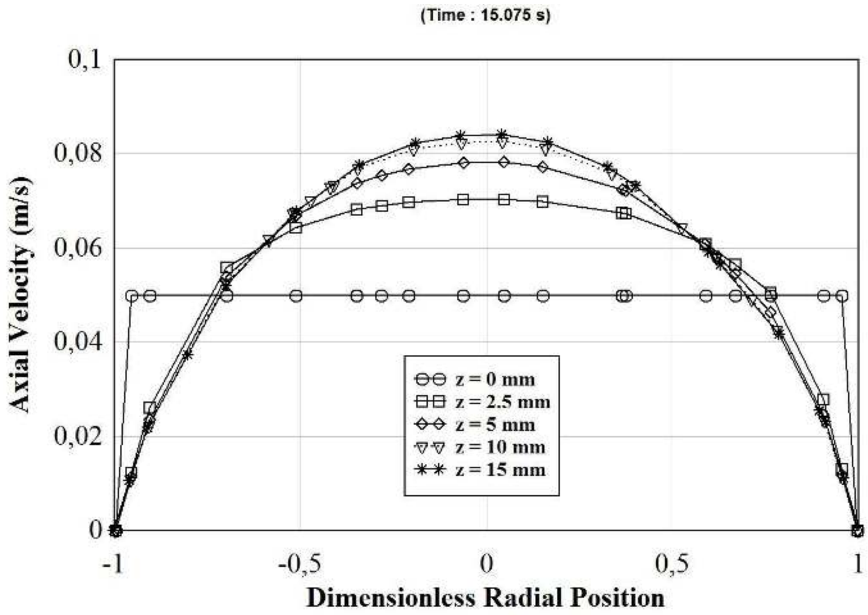

(a)

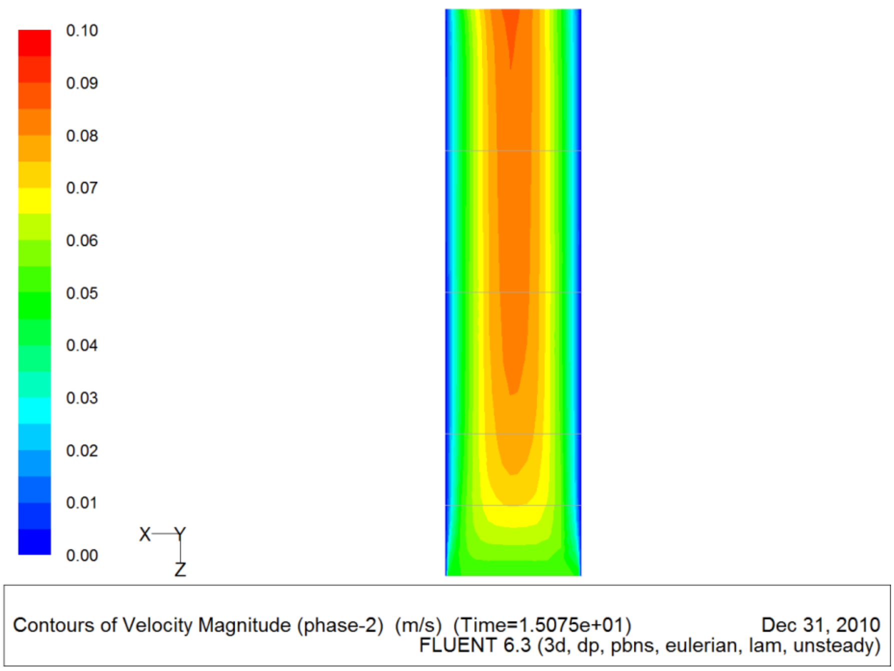

(b)

Figure 5.12. Development of RBC's inlet velocity profiles (a) and the contour plot (b) in the entrance region at peak of the diastole (15.075 s) with using modified drag correlation based on Jung' et al. (2006a) viscosity model. Flow is in the direction of the negative z-coordinate

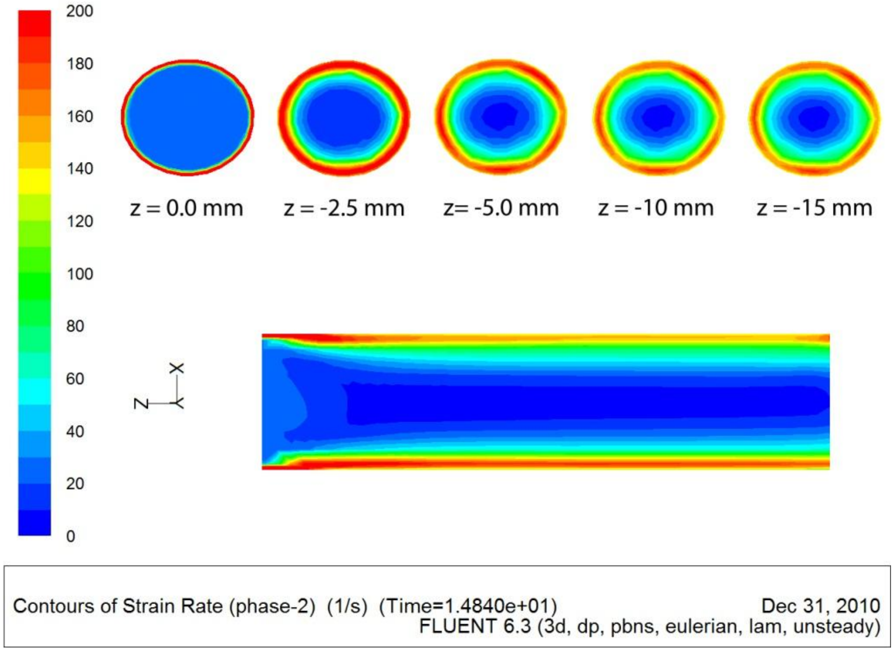

Figure 5.13. Computed boundary layer development of RBC strain rate in the entrance region of the RCA at peak of the systole (14.84 s) with using modified drag correlation based on Jung' et al. (2006a) viscosity model

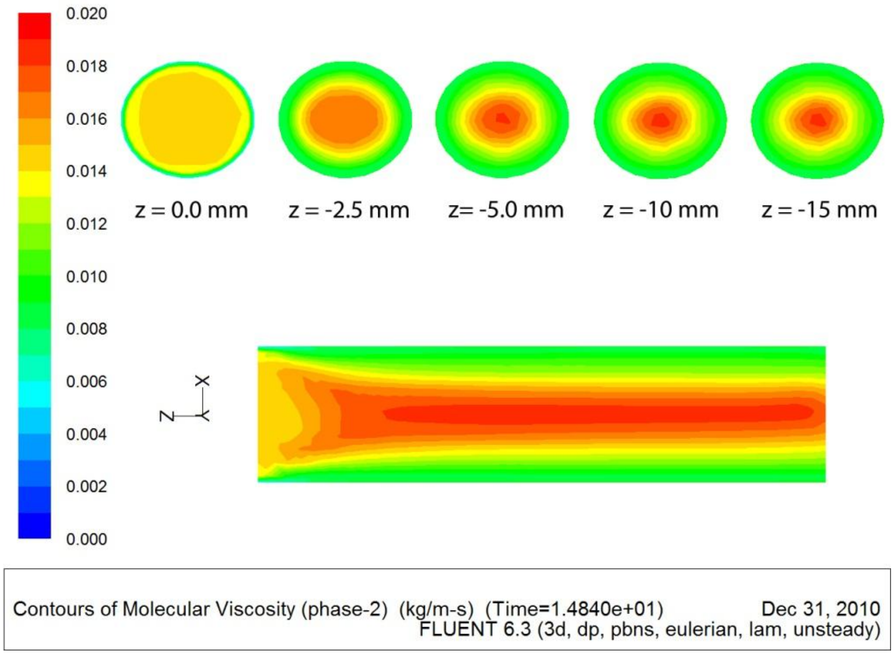

Figure 5.14. Computed boundary layer development of RBC viscosity in the entrance region of the RCA at peak of the systole (14.84 s) with using modified drag correlation based on Jung' et al. (2006a) viscosity model

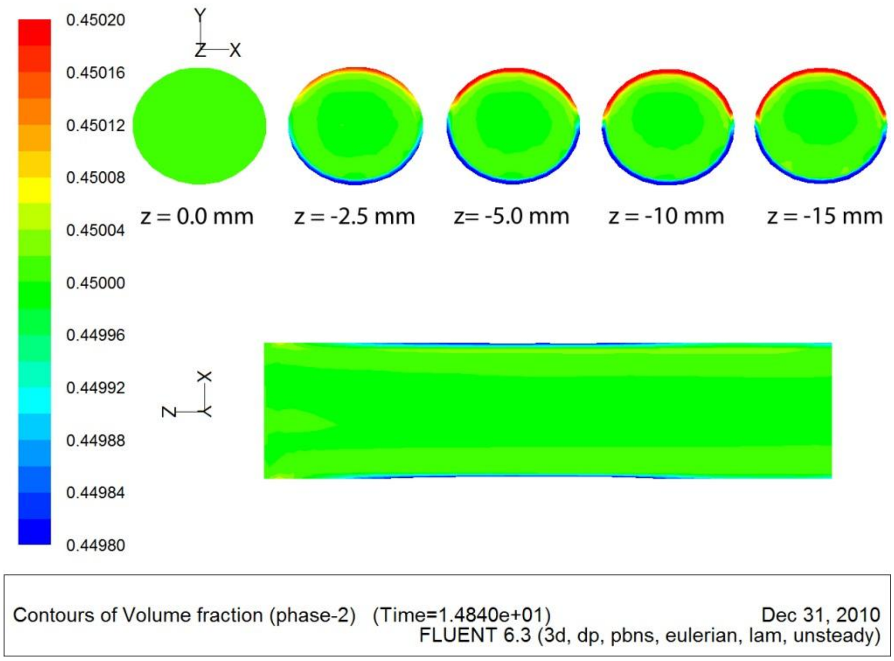

Figure 5.15. Computed boundary layer development of RBC volume fraction in the entrance region of the RCA at peak of the systole (14.84 s) with using modified drag correlation based on Jung' et al. (2006a) viscosity model

Here, the modified drag and other models, including Schiller and Nauman, Rusche and Issa, and Gidaspow are examined and compared. A reference monitoring is selected, approximately at the start of cross-sectional area decrease near the inner side of maximum curvature to check convergence and convergence history of the volume fraction of RBCs for each drag model as shown in Fig. 5.16. The volume fraction of RBCs starting from inlet with a hematocrit value (ε_{RBC}=0.45) as a function of the cardiac cycle is shown in Fig. 5.17. There is a repetition for each period of cardiac cycle (0.735 s). The volume fraction of RBCs at the monitor point starts to approach a quasisteady-state condition after 6 seconds of the cardiac cycle time, and this indicates convergence. Schiller and Nauman model overestimates volume fraction than the other models. Gidaspow model has the lowest estimation among the models. Estimations of Ruche and Issa model and modified drag models based on Jung's et al. (2006) and Cokelet (1987) are very close each other. Estimation of each model has a variation as a function of cardiac period time in a band.

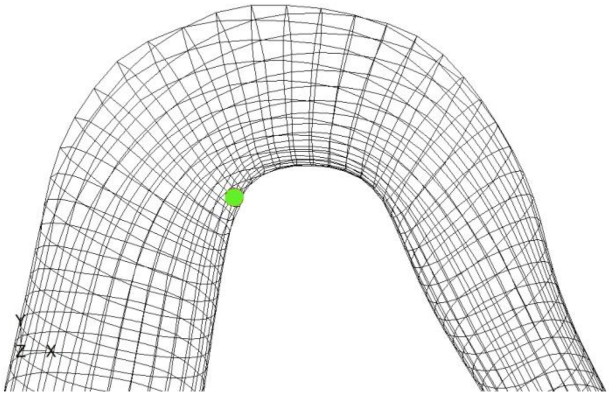

Figure 5.16. The place of monitor point on RCA

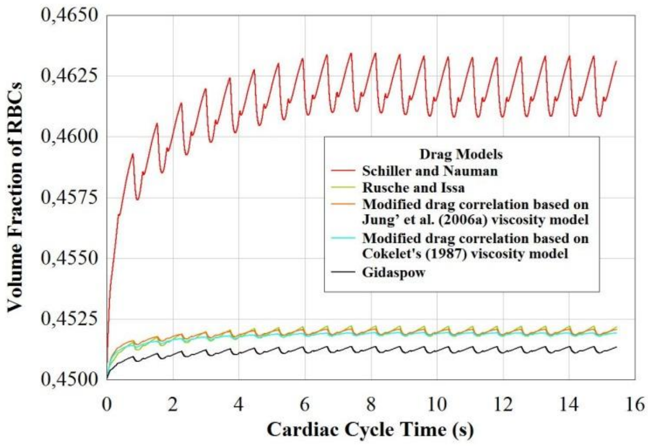

(a)

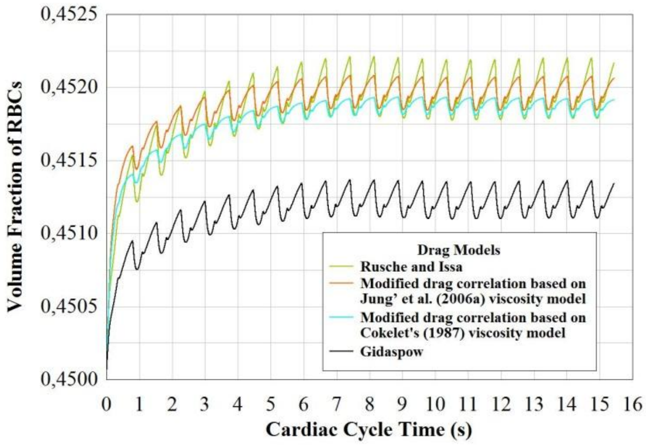

(b)

Figure 5.17. (a) RBC volume fraction as a function of cardiac cycle at the monitor point (b) a repetition to supply zoom on the close results of different drag models

Figs. 5.18-5.20 depict the contour plots of predicted RBCs volume fraction, shear stress and viscosity obtained from different drag models at peak of the systole (14.84 s), showing that these parameters vary considerably spatially along the RCA. The instantaneous distributions of RBCs volume fractions are highest during the peak of systole (14.84 s) and different for each drag model. The biggest difference in the volume fraction of RBCs is shown on the prediction of Schiller and Nauman model. The ratio of the volume fraction of RBCs in the near of the maximum curvature and the 155th cell from the entrance to the initial value is about 1.05 for this model and less than 1.01 for the other models. It should be noted that for real case where the particle diameter is not perfectly spherical and its orientation not parallel or perpendicular to its relative velocity. The particle diameter used in this study must be correlated to obtain an effective diameter and then a Stokes correction factor based on its orientation to its relative velocity must be derived. Predicted RBCs shear stress and viscosity vary considerably spatially and seem to be similar to given color band limits. Obtained results are less than the computed values in Jung et al. (2006a) and quite similar to the computed values in Huang et al. (2009).

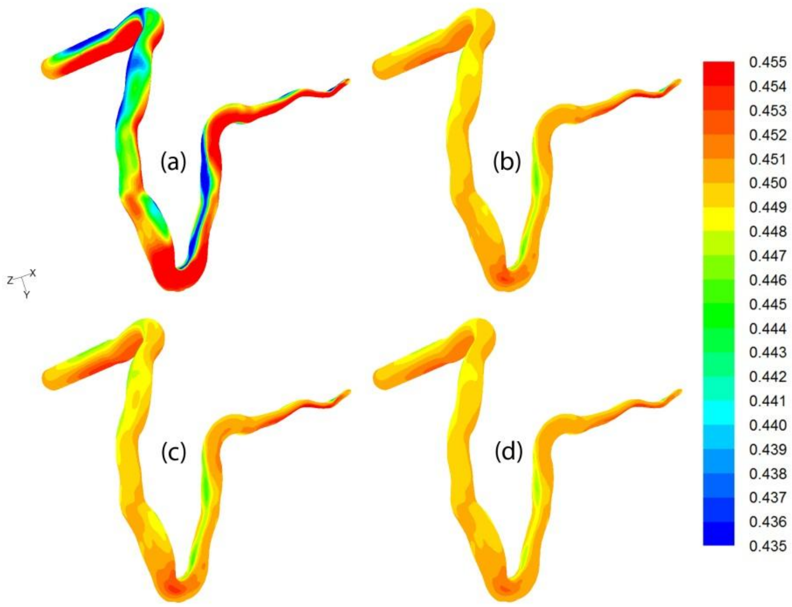

Figure 5.18. Calculated RBC volume fraction of the RCA at peak of the systole (14.84 s) with using (a) Schiller and Nauman, (b) modified drag correlation based on Jung' et al. (2006a) viscosity model, (c) Rusche and Issa, and (d) Gidaspow models

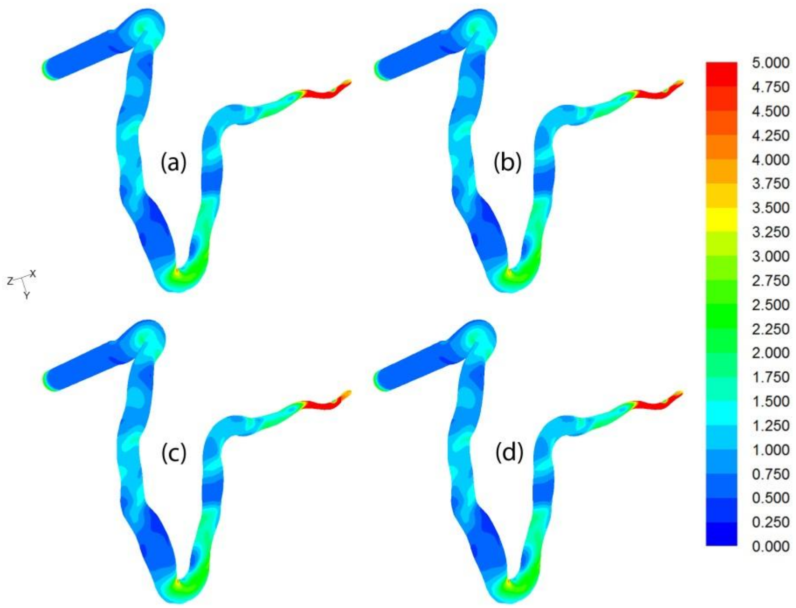

Figure 5.19. Calculated RBC shear stress of the RCA at peak of the systole (14.84 s) with using (a) Schiller and Nauman, (b) modified drag correlation based on Jung' et al. (2006a) viscosity model, (c) Rusche and Issa, and (d) Gidaspow models

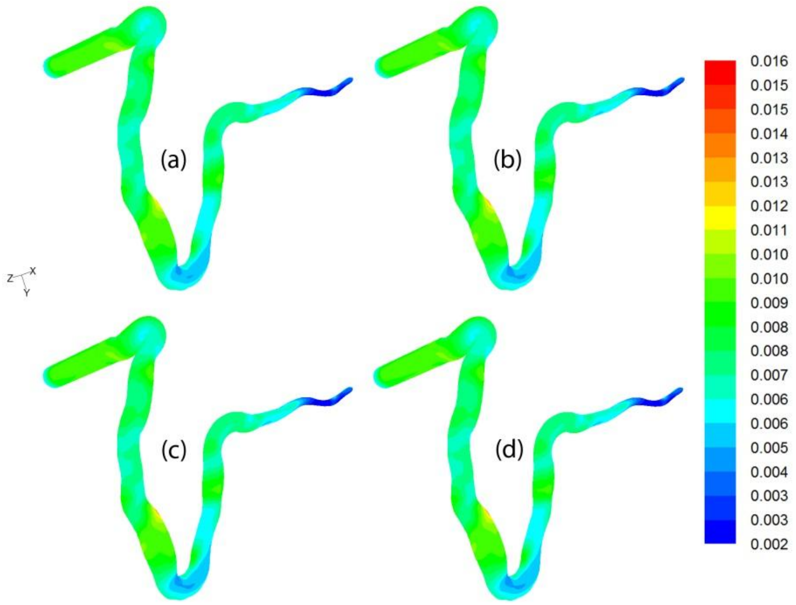

Figure 5.20. Calculated RBC viscosity of the RCA at peak of the systole (14.84 s) with using (a) Schiller and Nauman, (b) modified drag correlation based on Jung' et al. (2006a) viscosity model, (c) Rusche and Issa, and (d) Gidaspow models

Figs. 5.21-5.24 depict the contour plots of predicted RBCs volume fraction, shear stress, shear rate, and viscosity obtained from modified drag correlation based on Jung' et al. (2006a) viscosity model at beginning of the systole, peak of the systole, beginning of the diastole, and peak of the diastole showing that most of these parameters vary considerably both spatially and temporally along the RCA. RBCs volume fraction varies considerably spatially and seems to be temporally similar as shown in Fig. 5.21. The highest RBC volume fractions near the maximum curvature are computed on the side of the inside radius of curvature. The highest WSS and shear rate of RBCs, and lowest viscosity of RBC near the maximum curvature is also computed on the side of inside curvature. These results seem to be temporally similar as shown in Figs. 5.21-5.24. The WSS and shear rate of RBCs at the peak of systole and diastole is higher than the end of systole and diastole because of higher velocity, and the RBC viscosity exhibited an opposite behaviour because of a higher shear rate. The maximum spatial variation of hemodynamic parameters is also shown at the peak values of velocity.

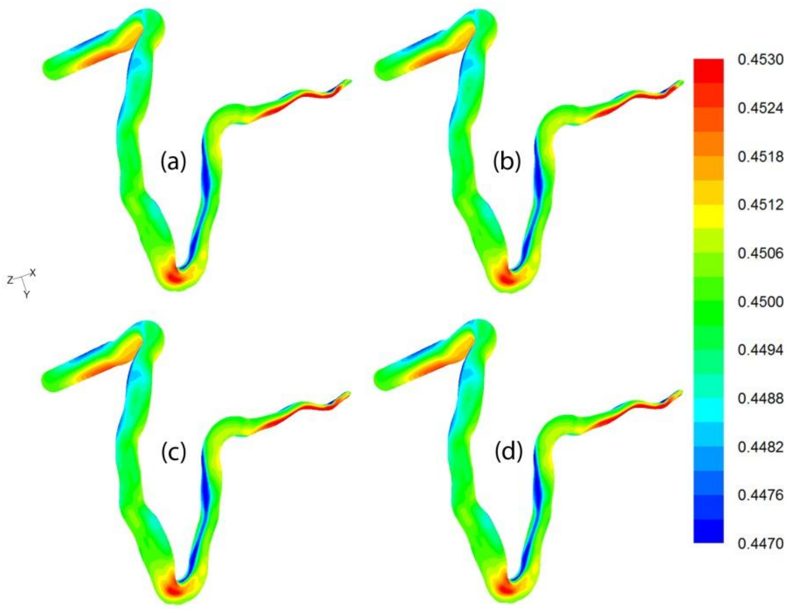

Figure 5.21. Calculated RBC volume fraction of the RCA with using modified drag correlation based on Jung' et al. (2006a) viscosity model (a) at beginning of the systole (14.75 s), (b) at peak of the systole (14.84 s), (c) at beginning of the diastole (15.04 s), and (d) at peak of the diastole (15.075 s)

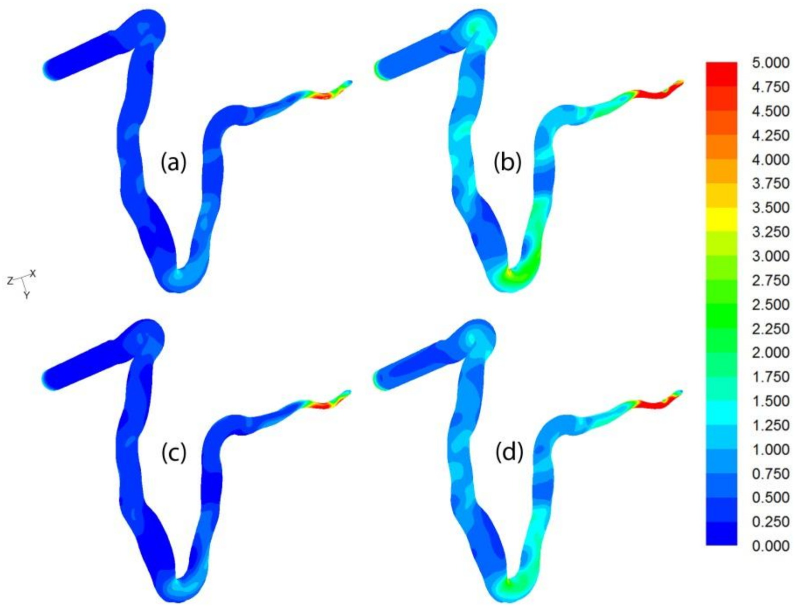

Figure 5.22. Calculated RBC shear stress of the RCA with using modified drag correlation based on Jung' et al. (2006a) viscosity model (a) at beginning of the systole (14.75 s), (b) at peak of the systole (14.84 s), (c) at beginning of the diastole (15.04 s), and (d) at peak of the diastole (15.075 s)

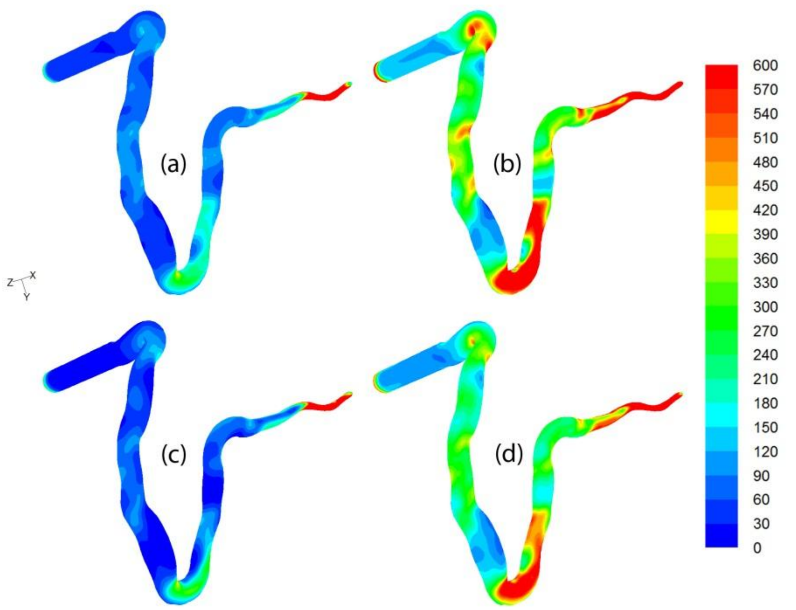

Figure 5.23. Calculated RBC shear rate of the RCA with using modified drag correlation based on Jung' et al. (2006a) viscosity model (a) at beginning of the systole (14.75 s), (b) at peak of the systole (14.84 s), (c) at beginning of the diastole (15.04 s), and (d) at peak of the diastole (15.075 s)

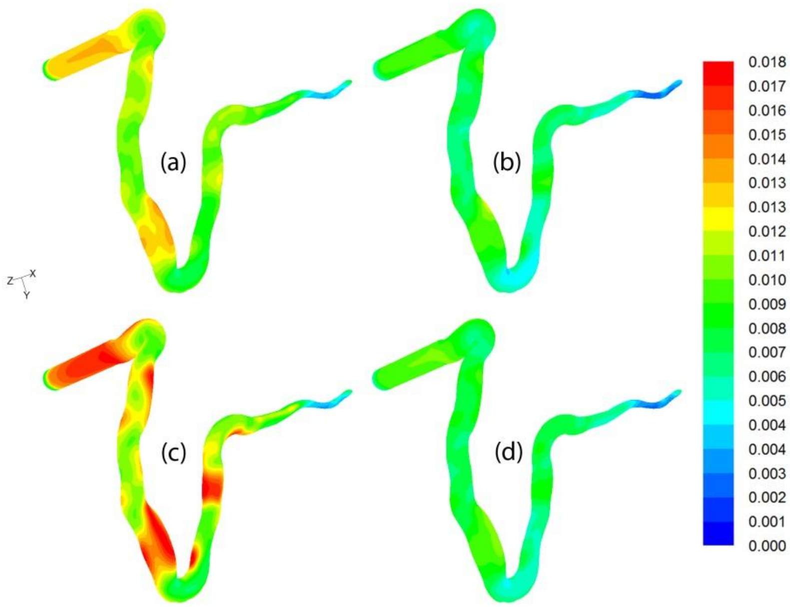

Figure 5.24. Calculated RBC viscosity of the RCA with using modified drag correlation based on Jung' et al. (2006a) viscosity model (a) at beginning of the systole (14.75 s), (b) at peak of the systole (14.84 s), (c) at beginning of the diastole (15.04 s), and (d) at peak of the diastole (15.075 s)

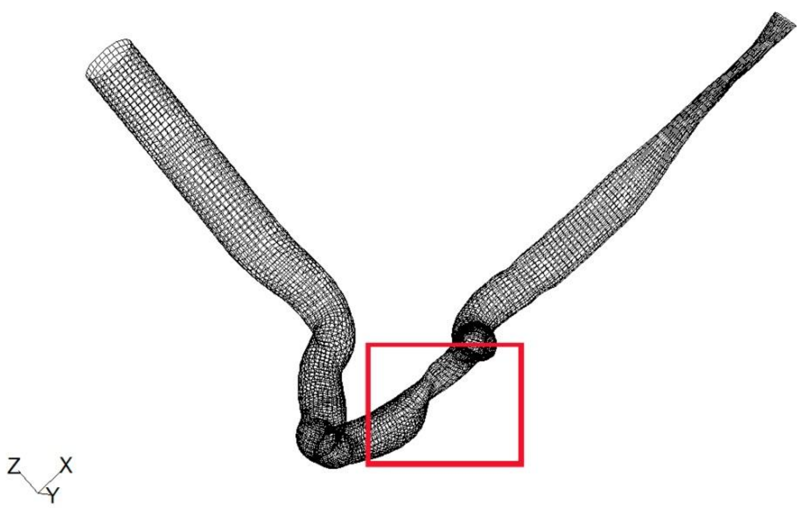

Figure 5.25. The view of point for selected region of the RCA

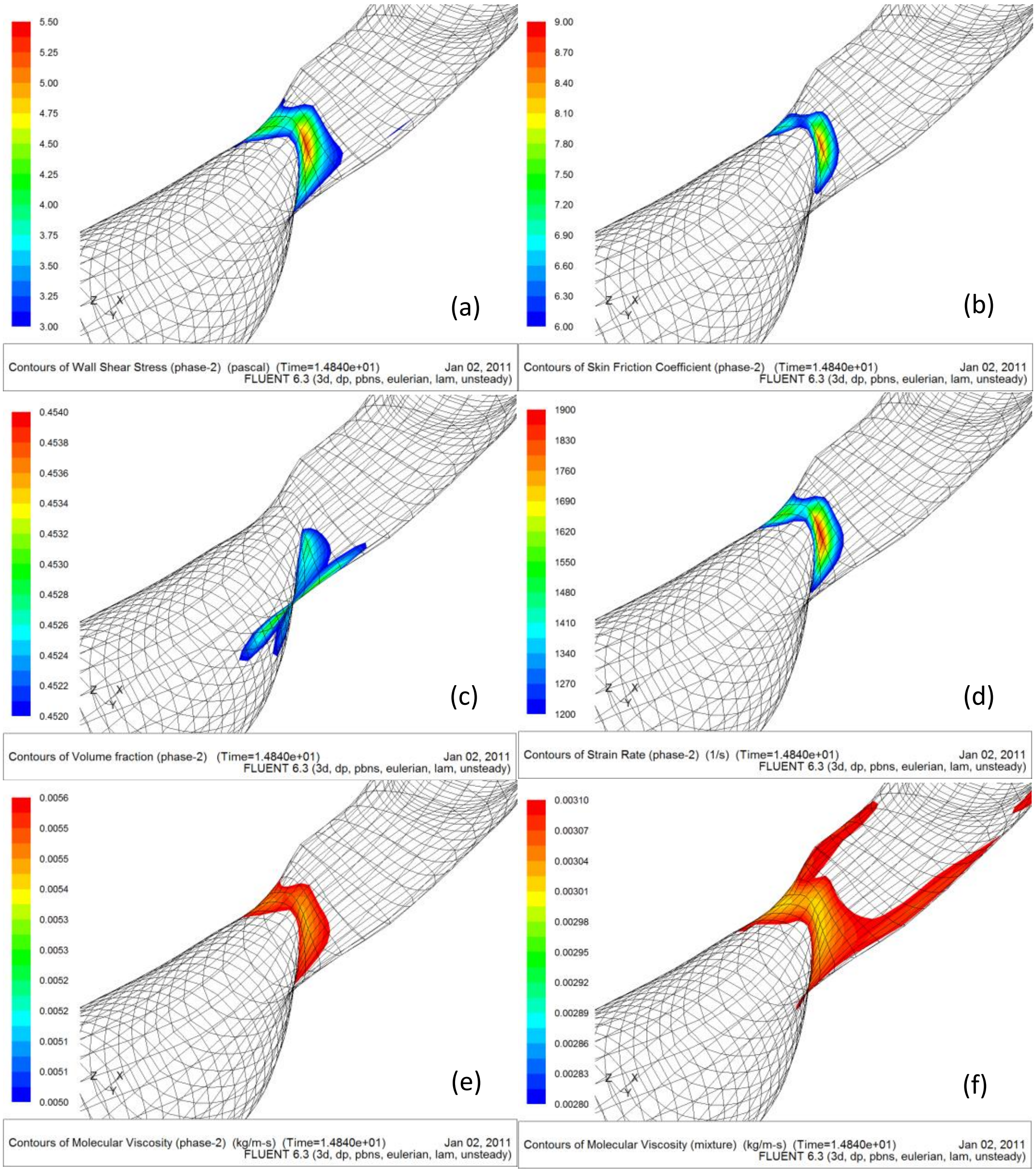

Figure 5.26. Hemodynamic Parameters with using modified drag correlation based on Cokelet (1987) viscosity model near the maximum curvature (a) WSS of RBCS phase, (b) Skin friction coefficient of RBCs phase, (c) Volume fraction of RBCs phase, (d) Strain rate of RBCs phase, (e) Molecular viscosity of RBCs phase, and (f) Molecular viscosity of the mixture phase

The marked point of the view on RCA in Fig. 5.25 is selected to investigate hemodynamic parameters on the maximum curvature region. Molecular viscosity of mixture and RBCs phase are estimated having the lowest values at the inside curvature region as shown in Fig. 5.26, and higher values of this region that are out of range are clipped to range. However, the other parameters in Fig. 5.26 are estimated having the highest values at the inside curvature region, and lower values of this region that are out of range are clipped to range. This is the inverse of previous findings for WSS computed by Jung et al. (2006a) and general expectation, where WSS was found to be high on the outside and low on the inside of an idealized RCA of uniform circular cross section with rigid walls. Johnston and Johnston (2007) found large differences in the WSS distribution in the four different human RCAs, which have been reconstructed from bi-plane angiograms. The pattern of WSS was found to be related the geometry of a particular artery. However, it is not only related arterial curvature but also lumen diameter as well as a combination of these two factors. Thus, the expansion or constriction of a realistic artery is very influential on the calculation of WSS. The constriction in the entry of maximum curvature of the modelled realistic RCA can be easily shown in Figs. 5.25-5.26. However, after the area at the maximum curvature, where the cross sectional area does not change so much, lower WSS occurs at the inside curvature.

5.4. Conclusions

The effectiveness of four drag models, including one new modified model based on mixture viscosity approach, on the CFD simulation of a 3-D RCA having different cross sections and curvatures along the axial direction are assessed on the Fluent v6.3.26 platform. The dynamic flow characteristics of the unsteady dense two-phase laminar flow in a non-uniform geometry are studied. The particulate phase is considered to behave like a liquid droplet and as a solid. The resulting hemodynamic properties such as RBCs distributions, WSS, shear rate, non-Newtonian viscosity of dispersed phase and mixture viscosity along the length of the RCA and especially near the maximum curvature are investigated. An article about the results of this study has been in progress (Yilmaz et al., in progress, 2011b).

The results reveal that the choice of drag models in the CFD modeling of blood flow has a critical effect on the prediction of RBCs distributions. Schiller and Nauman drag model not including the effects of the presence of neighboring entities estimates RBC distribution differently than the other models. Estimations of liquid-liquid models including Rusche and Issa, and modified drag model based on Cokelet and Jung's et al viscosity correlation is found to be very close to each other. Gidaspow model for solid particle underestimated a little more RBCs distribution than liquid-liquid models. This study also demonstrated that hemodynamic properties are extremely affected by curvature and sudden area change and they can commonly be found in the geometry of a RCA or an artery. The estimated hemodynamic parameters exhibited spatial variation as a function of the RCA geometry, and temporal variation as a function of pulsatile cardiac cycle. Both of these functions are also affected by biomechanical properties of blood vessel structure.

CHAPTER 6

RECOMMENDATIONS FOR FURTHER STUDIES

The conclusions of studies are already given at the end of each chapter starting from the literature survey to the final chapter. So as to avoid repetitions, here some recommendations for future studies are only given:

1. Although there has been a considerable amount of viscosity models in blood rheology, none of them has been commonly agreed upon or used. None of the models is fully expressing the effects of extremely complicated nature of blood rheology and its dependence of many factors. The dependency of blood viscosity on each rheological property of the blood should be investigated and clarified separately by means of isolating the effects of remaining rheological properties. A reliable experimental method of measuring velocity profiles and volume fraction in straight and complex geometry should be developed to determine the accurate CFD model including for characterizing blood flow.

2. The blood viscosity models fitted on the data measured in the rheometer under the steady flow conditions may not be suitable for the analysis of realistic pulsatile blood flow. Observed blood apparent viscosity in the rheometers under the assumption of Newtonian flow pattern is also not suitable and the hematocrit value of tested blood also affects this pattern. The assumption of Newtonian pattern and neglecting the hematocrit effect on it can cause inevitable errors. The slip effect in the rheometers should also be prevented throughout the measurements. A reliable experimental method of measuring blood viscosity under the pulsatile condition should be developed.

3. Proposing of a number of simplifying assumptions on physiologic conditions reduce very complicated construction of the realistic blood problem to a tractable problem to solve. However, each assumption contributes to growing deviations from realistic solution. Additionally, there is no experimental data to compare the results to investigated and clarified separately each of these effects assumed. Reliable experimental data should be provided.

4. The deformation, concentration, and aggregation behaviors of actual RBC at different shear rates and plasma viscosities under the physiological conditions should be further experimentally investigated so as to form more realistic drag and lift models over physiological ranges of effective parameters. The shape of the RBC and their aggregation at different shear rates and plasma viscosities should be investigated so as to obtain the dynamic RBC shape factor over a wide range of shear rates. The dependence of cell drag on volume fraction and Reynolds or Archimedes number should be determined over a physiological range of hematocrit. The effect of tank treading motion (i.e., mobility of RBC membrane) on the drag and lift forces especially at high shear rates should also be clarified.

5. The hemodynamic hypotheses and the related studies showed that there is a strong effect of wall shear stress (WSS) on cardiovascular diseases such as atherosclerosis and aneurysms. However, the exact role and the relative importance of proposed hemodynamic parameters on the vascular endothelium, the pathogenesis of cardiovascular diseases, and the progression of arterial lesions remain unclear. The role and importance of hemodynamic parameters resulting from flow condition and arterial geometry should be studied.

6. There is still lack of enough experimental data on some biomechanical conditions of vessel wall structure such as residual stresses, heterogeneity, smooth muscle activation and vasomotion. The human vessel geometry also exhibits wide variations according to shape, size, thrombus presence, loading conditions, and the presence of surrounding tissues and organs. Using some

simplifying assumptions in CFD models to initiate these biomechanical and geometrical conditions of vessels, therefore, lead to the solution of an elastic vessel constitutive problem that also causes considerable deviations from realistic ones. Effect of these parameters should be studied.

REFERENCES

Abraham, F., Behr, M. and Heinkenschloss, M. (2005). Shape optimization in unsteady blood flow: a numerical study of non-Newtonian effects. *Comput. Meth. Biomech. Biomed. Eng.,* **8**, 201-212.

Ai, L. and Vafai, K. (2005). An investigation of Stokes' second problem for non-Newtonian fluids. *Numer. Heat Tran. A,* **47**, 955-980.

Al-Taweel, A.M., Madhavan, S., Podila, K., Koksal, M., Troshko, A. and Gupta, Y.P. (2006). CFD Simulation of Multiphase Flow: Closure Recommendations for Fluid-Fluid Systems. *12th European Conference on Mixing*. Bologna, Italy.

Anand, M. and Rajagopal, K.R. (2004). A shear-thinning viscoelastic fluid model for describing the flow of blood. *Int. J. Cardiovasc. Med. Sci.,* **4**, 59-68.

Angeli, P. (2001). Droplet size in two-phase liquid dispersed pipeline flows. *Chem. Eng. Technol.,* **24**, 431-434.

ANSYS Inc. (2006). *Boundary Conditions, in Introductory Fluent Notes, 4-8.*

Arjomandi, H., Barcelona, S.S., Gallocher, S.L. and Vallejo, M. (2003). Biofluid dynamics of the human circulatory system. *Proceedings of the Congress on: "Biofluid Dynamics of the Human Body Systems".* Biomedical Engineering Institute, Florida International University, Miami, USA.

Armentano, R.L., Barra, J.G., Levenson, J., Simon, A. and Pichel, R.H. (1995). Arterial wall mechanics in conscious dogs: assessment of viscous, inertial, and elastic moduli to characterize the aortic wall behavior. *Circ. Res.,* **76**, 468-478.

Artoli, A.M., Hoekstra, A.G. and Sloot, P.M.A. (2006). Mesoscopic simulations of systolic flow in the human abdominal aorta. *J. Biomech.,* **39**, 873-884.

Asmolov, E.S. and McLaughlin, J.B. (1999). The inertial lift on an oscillating sphere in a linear shear flow. *Int. J. Multiphase Flow,* **25**, 739-751.

Atabek, H.B. and Chang, C.C. (1961). Oscillatory flow near the entry of a circular tube. *Zeitschrift für angewandte Mathematik und Physik,* **12**, 185-201.

Atabek, H.B., Chang, C.C. and Fingerson, L.M. (1965). Measurement of laminar oscillatory flow in the inlet of a circular tube. *Physics of Medicine Biology,* **9**, 219-227.

Augier, F., Masbernat, O. and Guiraud, P. (2003a). Slip velocity and drag law in a liquid-liquid homogeneous dispersed flow. *AIChE J.,* **49**, 2300-2316.

Augier, F., Morchain, J., Guiraud, P. and Masbernat, O. (2003b). Volume fraction gradient induced flow patterns in a two-liquid phase mixing layer. *Chem. Eng. Sci.,* **58**, 3985-3993.

Augier, F., Guiraud, P. and Masbernat, O. (2007). Velocity fluctuations in a homogeneous dispersed liquid–liquid flow at high phase fraction. *Phys. Fluids,* **19**, 057105.

Auton, T.R. (1984). *The dynamics of bubbles, drops and particles in motion in liquids.* PhD Dissertation. University of Cambridge.

Auton, T.R. (1987). The lift force on a spherical body in a rotational flow. *J. Fluid Mech.*, **183**, 199-218.

Baaijens, F.P.T. (2001). A fictitious domain: mortar element method for fluid-structure interaction. *Int. J. Numer. Meth. Fluid.,* **35**, 743-761.

Baek, S., Gleason, R.L., Rajagopal K.R. and Humphrey, J.D. (2007). Theory of small on large: Potential utility in computations of fluid–solid interactions in arteries. *Comput. Meth. Appl. Mech. Eng.,* **196**, 3070-3078.

Bagchi, P. (2007). Mesoscale simulation of blood flow in small vessels. *Biophys. J.,* **92**, 1858–77.

Bagchi, P. and Balachandar, S. (2002a). Effects of free rotation on the motion of a solid sphere in linear shear flow at moderate Re. *Phys. Fluids,* **14**, 2719-2737.

Bagchi, P. and Balachandar, S. (2002b). Shear versus vortex-induced lift force on a rigid sphere at moderate Re. *J. Fluid Mech.,* **473**, 379-388.

Bagchi, P., Johnson, P.C. and Popel, A.S. (2005). Computational fluid dynamic simulation of aggregation of deformable cells in a shear flow. *J. Biomech. Eng.,* **127**, 1070–80.

Ballyk, P.D., Steinman D.A. and Ethier, C.R. (1994). Simulation of non-Newtonian blood flow in an end-to-side anastomosis. *Biorheology,* **31**, 565–586.

Balmer, R.T. and Fiorina, M.A. (1980). Unsteady flow of an inelastic power-law fluid in a circular tube. *Journal of Non-Newtonian Fluid Mechanics,* **7**, 189-198.

Barnea, E. and Mizrahi, J. (1975). A generalized approach to the fluid dynamics of particulate systems. Part 2: Sedimentation and fluidization of clouds of spherical liquid drops. *Can. J. Chem. Eng.,* **53**, 461-468.

Barnes, H.A. (1995). A review of the slip (wall depletion) of polymer solutions, emulsions and particle suspensions in viscometers: its cause, character, and cure. *J. of Non-Newtonian Fluid Mech.,* **56**, 221-251.

Barnes, H.A. (2000). Measuring the viscosity of large-particle (and flocculated) suspensions - a note on the necessary gap size of rotational viscometers. *J. of Non-Newtonian Fluid Mech.,* **94**, 213-217.

Barnes, H.A., Hutton, J.F. and Walters, K. (1989). *An introduction to rheology*. Amsterdam: Elsevier.

Baskurt, O.K. and Meiselman, H.J. (1977). Cellular determinants of low-shear blood viscosity. *Biorheology,* **34**, 235-247.

Baskurt, O.K. and Meiselman, H.J. (2003). Blood rheology and hemodynamics. *Semin. Thromb. Hemost.,* **29,** 435-450.

Baskurt, O.K. and Meiselman, H.J. (2007). Hemodynamic effects of red blood cell aggregation. *Indian J. Exp. Biol.,* **45**, 25-31.

Batchelor, G.K. (1977). The effect of Brownian motion on the bulk stress in a suspension of spherical particles. *J. Fluid Mech.,* **83**, 97–117.

Baumler, H., Neu, B., Donath, E. and Kiesewetter, H. (1999). Basic phenomena of red blood cell rouleaux formation biorheology. *Biorheology,* **36**, 439-442.

Bedeaux, D. (1983). The effective shear viscosity for two-phase flow. *Physica A,* **121**, 345-361.

Behzadi, A., Issa, R.I. and Rusche, H. (2004). Modelling of dispersed bubble and droplet flow at high phase fractions. *Chem. Eng. Sci.,* **59**, 759-770.

Bernsdorf, J., Harrison, S.E., Smith, S.M., Lawford, P.V. and Hose, D.R. (2008). Applying the lattice Boltzmann technique to biofluids: A novel approach to simulate blood coagulation. *Comput. Math. Appl.,* **55**, 1408-1414.

Berthier, B., Bouzerar, R. and Legallais, C. (2002). Blood flow patterns in an anatomically realistic coronary vessel: Influence of three different reconstruction methods. *J. Biomech.,* **35**, 1347-1356.

Bishop, J.J., Popel, A.S., Intaglietta, M. and Johnson, P.C. (2001). Rheological effects of red blood cell aggregation in the venous network: a review of recent studies. *Biorheology,* **38**, 263–274.

Boffi, D. and Gastaldi, L. (2003). A finite element approach for the immersed boundary method. *Comput. Struct.,* **81**, 491-501.

Bothe, D., Schmidtke, M. and Warnecke, H.-J., 2006. VOF-simulation of the lift force for single bubbles in a simple shear flow. *Chem. Eng. and Techn.,* **29**, 1048-1053.

Boussel, L., Rayz, V., McCulloch, C., Martin, A., Acevedo-Bolton, G., Lawton, M., Higashida, R., Smith, W.S., Young, W.L. and Saloner, D. (2008). Aneurysm growth occurs at region of low wall shear stress. *Stroke,* **39,** 2997-3002.

Braun, D.B. and Rosen, M.R. (2000). *Rheology modifiers handbook: Practical use and application*. Noyes Publications.

Brinkman, H.C. (1952). The viscosity of concentrated suspensions and solutions. *J. Chem. Phys.,* **20**, 571–572.

Bronzino, J. D. (2006). *The biomedical engineering handbook.* (3rd ed.). CRC.

Brooks, D.E., Goodwin, J.W. and Seaman, G.V.F. (1970). Interactions among erythrocytes under shear. *J. Appl. Physiol.,* **28**, 172–177.

Broughton, G. and Squires, L. (1938). The viscosity of oil–water emulsions. *J. Phys. Chem.,* **42**, 253–263.

Brown, F.T. (1962). The transient response of fluid lines. *Journal of Basic Engineering, Transactions of the ASME, Series D,* **84**, 547-553.

Bruggeman, D.A.G. (1935). Berechnung verschiedener physikalischer Konstanten von heterogenen Substanzen. *Ann. Phys.,* **24**, 636-679.

Buchanan, J.R., Kleinstreuer, C. and Comer, J.K. (2000). Rheological effects on pulsatile hemodynamics in a stenosed tube. *Comput. Fluid,* **29**, 695-724.

Buchanan, J.R., Kleinstreuer, C., Hyun, S. and Truskey, G.A. (2003). Hemodynamics simulation and identification of susceptible sites of atherosclerotic lesion formation in a model abdominal aorta. *J. Biomech.,* **36**, 1185-1196.

Bugliarello, G. and Sevilla, J. (1970). Velocity distribution and other characteristics of steady and pulsatile blood flow in fine glass tubes. *Biorheology,* **7**, 85-107.

Candelier, F. and Angilella, J.R. (2006). Analytical investigation of the combined effect of fluid inertia and unsteadiness on low-Re particle centrifugation. *Phys. Rev. E,* **73**, 047301.

Candelier, F. and Souhar, M. (2007). Time-dependent lift force acting on a particle moving arbitrarily in a pure shear flow at small Reynolds numbers. *Phys. Rev. E,* **76**, 067301.

Carew, T.E., Vaishnav, R.N. and Patel, D.J. (1968), Compressibility of the arterial wall. *Circ. Res.,* **23,** 61-68.

Caro, C.G., Fitz-Gerald, J.M. and Schroter, R.C. (1969). Arterial wall shear and distribution of early atheroma in man. *Nature,* **223**, 1159-1161.

Caro, C.G., Fitz-Gerald, J.M. and Schroter, R.C. (1971). Atheroma and arterial wall shear: observation, correlation and proposal of a shear dependent mass transfer mechanism for atherogenesis. *Proc. R. Soc. Lond. B Biol. Sci.,* **177**, 109-159.

Carpinlioglu, M.O. and Gundogdu, M.Y. (2001a). A critical review on pulsatile pipe flow studies directing towards future research topics. *Flow Meas. Instrum.,* **12**, 163-174.

Carpinlioglu, M.O. and Gundogdu, M.Y. (2001b). Presentation of a test system in terms of generated pulsatile flow characteristics. *Flow Meas. Instrum.,* **12**, 181-190.

Chakravarty, S. and Sen, S. (2005). Dynamic response of heat and mass transfer in blood flow through stenosed bifurcated arteries. *Korea Aust. Rheol. J.,* **17,** 47-62.

Chan, W.Y., Ding, Y. and Tu, J.Y. (2007). Modeling of non-Newtonian blood flow through a stenosed artery incorporating fluid-structure interaction. *ANZIAM Journal,* **47,** C507-C523.

Chaturani, P. and Bharatiya, S.S. (2001). Magnetic fluid model for two-phase pulsatile flow of blood. *Acta Mechanica,* **149**, 97-114.

Chee, C.Y., Lee, H.P. and Lu, C. (2008). Using 3D fluid–structure interaction model to analyse the biomechanical properties of erythrocyte. *Phys. Lett. A*, **372**, 1357-1362.

Chen, H.Q., Zhong, G.H., Li, L., Wang, X.Y., Zhou, T. and Chen, Z.Y. (1991). Effects of gender and age on thixotropic properties of whole blood from healthy adult subjects. *Biorheology,* **28**, 177-183.

Chen, J., Lu, X. and Wang, W. (2006a). Non-Newtonian effects of blood flow on hemodynamics in distal vascular graft anastomoses. *J. Biomech.,* **39**, 1983-1995.

Chen, C., Chen, H. Freed, D., Shock, R., Staroselsky, I., Zhang, R., Coskun, A.U., Stone, P.H. and Feldman, C.L. (2006b). Simulation of blood flow using extended Boltzmann kinetic approach. *Phys. Stat. Mech. Appl.,* **362**, 174-181.

Chien, S. (1970). Shear dependence of effective cell volume as a determinant of blood viscosity. *Science,* **168**, 977–978.

Chien, S., Usami, S., Dellenback, R.J. and Gregersen, M.I. (1970). Shear-dependent interaction of plasma proteins with erythrocytes in blood rheology. *Am. J. Physiol.,* **219**, 143–153.

Cho, Y.I. and Kensey, K.R. (1991). Effects of the non-Newtonian viscosity of blood on hemodynamics of diseased arterial flows: Part 1, Steady flows. *Biorheology,* **28**, 241-262.

Cholley, B.P., Shroff, S.G., Sandelski, J., Korcarz, C., Balasia, B.A., Jain, S., Berger, D.S., Murphy, M.B., Marcus, R.H. and Lang, R.M. (1995). Differential effects of chronic oral antihypertensive therapies on systemic arterial circulation and ventricular energetics in African-American patients. *Circulation,* **91**, 1052-1062.

Chong, J.S., Christiansen, E.B. and Baer, A.D. (1971). Rheology of concentrated suspension. *J. Appl. Polymer Sci.,* **15**, 2007–2021.

Cokelet, G.R. (1972). The rheology of human blood. In Y.C. Fung (Ed.), *Biomechanics: lts Foundations and Objectives*. Englewood Cliffs: Prentice Hall.

Cokelet, G.R. (1987). Handbook of Bioengineering. In R. Skalak and S. Chien (Eds.) *The Rheology and Tube Flow of Blood.* New York: McGraw-Hill.

Clift, R., Grace, J.R. and Weber, M.E. (1978). *Bubbles, Drops and Particles.* New York: Academic Press.

Cosgrove, T. (2005). *Colloid science: Principles, methods and applications.* Blackwell Publishing Limited.

Coskun, A.U., Chen, C., Stone, P.H. and Feldman, C.L. (2006). Computational fluid dynamics tools can be used to predict the progression of coronary artery disease. *Phys. Stat. Mech. Appl.,* **362**, 182-190.

Cousins, R.R. (1970). A note on the shear Flow past a sphere. *J. Fluid Mech*., **40**, 543-547.

Coussot, P. (2005). *Rheometry of pastes, suspensions, and granular materials: Applications in industry and environment.* Wiley-Interscience.

Cristini, V. and Kassab, G.S. (2005). Computer modeling of red blood cell rheology in the microcirculation: A brief overview. *Ann. Biomed. Eng.,* **33**, 1724-1727.

Crowley, T.A. and Pizziconi, V. (2005). Isolation of plasma from whole blood using planar microfilters for lab-on-a-chip applications. *Lab Chip,* **5**, 922-929.

Csanady, G. T. (1963). Turbulent diffusion of heavy particles in the atmosphere. *J. Atmos. Sci.,* **20**, 201-208.

Dandy, D.S. and Dwyer, H.A. (1990). A sphere in shear flow at finite Reynolds number: effect of shear on particle lift, drag, and heat transfer. *J. Fluid Mech.,* **216**, 381–410.

Darwin, C. (1953). Note on hydrodynamics. *Cambiridge Phil. Trans*., **49**, 342-354.

De Gruttola, S., Boomsma, K. and Poulikakos, D. (2005). Computational simulation of a non-Newtonian model of the blood separation process. *Artif. Organs,* **29**, 949-959.

De Hart, J., Peters, G.W.M., Schreurs, P.J.G. and Baaijens, F.P.T. (2000). A two-dimensional fluid-structure interaction model of the aortic valve. *J. Biomech.,* **33**, 1079-1088.

De Hart, J., Peters, G.W.M., Schreurs, P.J.G. and Baaijens, F.P.T. (2003). A three-dimensional computational analysis of fluid-structure interaction in the aortic valve. *J. Biomech.,* **36**, 103-112.

De Hart, J., Baaijens, F.P.T., Peters, G.W.M. and Schreurs, P.J.G. (2003). A computational fluid-structure interaction analysis of a fiber-reinforced stentless aortic valve. *J. Biomech.,* **36**, 699-712.

De Vries, A.W.G., Biesheuvel, A. and van Wijngaarden, L. (2002). Notes on the path and wake of a gas bubble rising in pure water. *Intl. J. of Multiphase Flow,* **28**, 1823-1835.

Denison, E.B. (1970). *Pulsating laminar flow measurements with a directionally-sensitive laser velocimeter.* Ph.D. Dissertation. Purdue University.

Denison, E.B., Stevenson, W.H. and Fox, R.W. (1971). Pulsating laminar flow measurements with a directionally sensitive laser velocimeter. *AIChE Journal,* **17**, 781-787.

Di Martino, E.S. Guadagni, G. Fumero, A. Ballerini G., Spirito, R., Biglioli, P. and Redaelli, A. (2001). Fluid–structure interaction within realistic three-dimensional models of the aneurysmatic aorta as a guidance to assess the risk of rupture of the aneurysm. *Med. Eng. Phys.,* **23**, 647-655.

Diaz-Goano, C. Minev, P.D. and Nandakumar, K. (2003). A fictitious domain/finite element method for particulate flows. *J. Comput. Phys.,* **192**, 105-123.

Dill, D.B. and Costill, D.L. (1974). Calculation of percentage changes in volumes of blood, plasma, and red cells in dehydration. *J. Appl. Physiol.*, **37**, 247-248.

Dintenfass, L. (1968). Internal viscosity of the red cell and a blood viscosity equation. *Nature,* **219**, 956-58.

Donea, J., Huerta, A., Ponthot, J.-Ph. and Rodriguez-Ferran, A. (2004). Arbitrary Lagrangian-Eulerian methods, In E. Stein, R. de Borst and T.J.R. Hugues (Eds.), *Encyclopedia of Computational Mechanics.* New York: Wiley.

Donovan, F.M., Taylor, B.C. and Su, M.C. (1991). One-dimensional computer analysis of oscillatory flow in rigid tubes. *Journal of Biomechanical Engineering,* **113**, 476-484.

Donovan, F.M., McIlwain, R.W., Mittmann, D.H. and Taylor, B.C. (1994). Experimental correlations to predict fluid resistance for simple pulsatile laminar flow of incompressible fluids in rigid tubes. *Journal of Fluids Engineering,* **116**, 516-521.

Drew, D. and Lahey, R.T. (1979). Applications of general constitutive principles to the derivation of multidimensional two-phase flow equations. *Intl J. Multiphase Flow,* **5**, 243-264.

Drew, D. and Lahey, R.T. (1987). The virtual mass and lift force on a sphere in rotating and straining inviscid flow. *Intl J. Multiphase Flow,* **13**, 113-121.

Drew, D. and Lahey, R.T. (1990). Some supplemental analysis concerning the virtual mass and lift force on a sphere in a rotating and straining flow. *Intl J. Multiphase Flow,* **16**, 1127-1130.

Drew, D. and Lahey, R.T. (1993). *Analytical modeling of multiphase flow, Particulate two-phase flow.* Boston: Butterworth-Heinemann.

D'Souza, A.F. and Oldenburger, R. (1964). Dynamic response of fluid lines. *Journal of Basic Engineering, Transactions of the ASME, Series D,* **86**, 589-598.

Du, W., Bao, X., Xu, J. and Wei, W. (2006). Computational fluid dynamics (CFD) modeling of spouted bed: assessment of drag coefficient correlations. *Chem. Eng. Sci.,* **61**, 4558–4570.

Dufaux, J., Quemada, D. and Mills, P. (1980). Determination of rheological properties of red blood cells by couette viscometry. *Rev. Phys. Appliquee*, **15**, 1367-1374.

Dupin, M.M., Halliday, I., Careand, C.M., Alboul, L. and Munn, L.L. (2007). Modeling the flow of dense suspensions of deformable particles in three dimensions. *Phys. Rev. E,* **75**, 066707.

Easthope, P. and Brooks, D.E. (1980). A comparison of constitutive functions for whole human blood. *Biorheology,* **17**, 235-247.

Eilers, H. (1941). Die Viskosität von Emulsionen hochviskoser Stoffe als Funktion der Konzentration. *Kolloid-Z,* **97**, 313–321.

Einstein, A. (1911). Berichtigung zu meiner Arbeit: Eine neue Bestimmung der Moleküldimensionen. *Ann. Phys.,* **339**, 591-592.

Elghobashi, S.E. and Abou-Arab, T.W. (1983). A two-equation model for two-phase flows. *Phys. Fluids,* **26**, 931-938.

Enwald, H., Peirano, E. and Almstedt, A.-E. (1996). Eulerian Two-phase Flow Theory Applied to Fluidization. *Int. J. of Multiphase Flow,* **22**, 21-66.

Ergun, S. (1952). Fluid flow through packed columns. *Chem. Eng. Prog.,* **48**, 89-94.

Ervin, E.A. and Tryggvason, G. (1994). The rise of bubbles in a vertical shear flow. *In: Proceedings of the ASME Winter Meeting*. Fluids Engineering Div., Chicago.

Farell, C. and Youssef, S. (1996). Experiments on turbulence management using screen and honeycombs. *Trans. A.S.M.E, J. Fluids Engng.,* **118**, 26-32.

Feng, Z.G. and Michaelides, E.E. (2004). The immersed boundary-lattice Boltzmann method for solving fluid-particles interaction problems. *J. Comput. Phys.,* **195**, 602-628.

Fischer, T.M., Stöhr-Liesen, M. and Schmid-Schönbein, H. (1978). The red cell as a fluid droplet: tank tread-like motion of the human erythrocyte membrane in shear flow. *Science,* **202**, 894-896.

Florio, P. J. and Mueller, W. K. (1968). Development of a periodic flow in a rigid tube. *Journal of Basic Engineering, Transactions of the ASME, Series D,* **90**, 395-399.

Fluent Inc. (2006). *Fluent User's Guide, ver. 6.3.26.*

Fogelson, A.L. and Guy, R.D. (2008). Immersed-boundary-type models of intravascular platelet aggregation. *Comput. Meth. Appl. Mech. Eng.,* **197**, 2087-2104.

Frankel N.A. and Acrivos, A. (1967). On the viscosity of a concentrated suspension of solid particles. *Chem. Eng. Sci.,* **22**, 847–853.

Fry, D.L. (1968). Acute vascular endothelial changes associated with increased blood velocity gradients. *Circ. Res.,* **22**, 165-182.

Fry, D.L. (1969). Certain histological and chemical responses of the vascular interface to acutely induced mechanical stress in the aorta of the dog. *Circ. Res.,* **24**, 93-108.

Fung, Y.C. (1993). *Biomechanics: Mechanical properties of living tissues.* (2nd ed.). New York: Springer-Verlag.

Gao, T. and Hu, H.H. (2009). Deformation of elastic particles in viscous shear flow. *J. Comput. Phys.,* **228**, 2132-2151.

Gao, J., Lan, X., Fan, Y., Chang, J., Wang, G., Lu, C. and Xu, C. (2009). CFD modeling and validation of the turbulent fluidized bed of FCC particles. *AIChE J.,* **55**, 1680–1694.

Gartner, L.P. and Hiatt, J.L. (2006). *Color textbook of histology.* (3rd ed.). Saunders.

Gasser, T.C., Ogden, R.W. and Holzapfel, G.A. (2006). Hyperelastic modelling of arterial layers with distributed collagen fibre orientations. *J. R. Soc. Interface,* **3**, 15-35.

Gay, M., Zhang, L.T. and Liu, W.K. (2006). Stent modeling using immersed finite element method, *Comput. Meth. Appl. Mech. Eng.,* **195**, 4358-4370.

Gerlach, C.R. and Parker, J.D. (1967). Wave propagation in viscous fluid lines including higher model effect. *Journal of Basic Engineering, Transactions of the ASME, Series D,* **89**, 782-788.

Gerrard, J.H. and Hughes, M.D. (1971). The flow due to an oscillating piston in a cylindrical tube: A comparison between experiment and a simple entrance flow theory. *J. Fluid Mech.,* **50**, 97-106.

Gessner, F.B. (1973). Hemodynamic theories of atherogenesis. *Circ. Res.,* **33**, 259-266.

Gijsen, F.J.H., van de Vosse, F.N. and Janssen, J.D. (1998). Wall shear stress in backward-facing step flow of a red blood cell suspension. *Biorheology,* **35**, 263-279.

Gijsen, F.J.H., Van de Vosse, F.N. and Janssen, J.D. (1999a). The influence of the non-Newtonian properties of blood on the flow in large arteries: steady flow in a carotid bifurcation model. *Journal of Biomechanics,* **32**, 601-608.

Gijsen, F.J.H., Allanic, E., van de Vosse, F.N. and Janssen, J.D. (1999b). The influence of the non-Newtonian properties of blood on the flow in large arteries: Unsteady flow in a 90-degree curved tube. *J. Biomech.,* **32**, 705-713.

Gidaspow, D. (1994). *Multiphase flow and fluidization: Continuum and kinetic theory description.* New York: Academic Press.

Glowinski, R. and Kuznetsov, Y. (2007). Distributed Lagrange multipliers based on fictitious domain method for second order elliptic problems. *Comput. Meth. Appl. Mech. Eng.,* **196**, 1498-1506.

Glowinski, R., Pan, T.-W., Hesla ,T.I. and Joseph, D.D. (1999a). A distributed Lagrange multiplier/fictitious domain method for particulate flows. *Int. J. Multiphase. Flow*, **25**, 755-794.

Glowinski, R., Pan, T.-W., Hesla ,T.I., Joseph, D.D. and Periaux, J. (1999b). A distributed Lagrange multiplier/fictitious domain method for flows around moving rigid bodies: Application to particulate flow. *Int. J. Numer. Meth. Fluid.,* **30**, 1043-1066.

Goldsmith, H.L., Bell, D.N. Spain, S. and McIntosh, F.A. (1999). Effect of red blood cells and their aggregates on platelets and white cells in flowing blood. *Biorheology,* **36**, 461-468.

Goubergrits, L., Affeld, K., Wellnhofer, E., Zurbrugg, R. and Holmer, T. (2001). Estimation of wall shear stress in bypass grafts with computational fluid dynamics method. *International Journal of Artificial Organs,* **24**, 145-151.

Gundogdu, M.Y. (2000). *An experimental investigation on pulsatile pipe flows.* PhD Thesis. University of Gaziantep.

Gundogdu, M.Y. and Carpinlioglu, M.O. (1999a). Present state of art on pulsatile flow theory, Part 1. Laminar and transitional flow regimes. *JSME Int. J.,* **42**, 384-397.

Gundogdu, M.Y. and Carpinlioglu, M.O. (1999b). Present state of art on pulsatile flow theory, Part 2. Turbulent flow regime, *JSME Int. J.* **42**, 398-410.

Gundogdu, M.Y. and Carpinlioglu, M.O. (2002). An interactive data acquisition and control system coupled on a pulsatile pipe flow test rig. *Measurement and Control,* **35**, 43-46.

Gundogdu, M.Y., Yilmaz, F. and Kutlar A.I., (2009). Project Completion Report: *Analysis of two-phase blood flow using CFD and its application to right coronary artery*. University of Gaziantep, BAPYB, MF.07.06., December 2009.

Guyton, A.C. and Hall, J.E. (2006). *Textbook of medical physiology.* (11^{th} ed.). Elsevier Saunders.

Hall, I.M. (1956). The displacement effect of a sphere in a two-dimensional flow. *J. Fluid Mech*., **1**, 142-161.

Harris, J., Peer, G. and Wilkinson, W.L. (1969). Velocity profiles in laminar oscillating flow in tubes. *J. Phys. E. J. Sci. Instrum.,* **2**, 913-916.

Hatschek, E. (1911) Die Viskosität der Dispersoide. *Kolloid-Z,* **8**, 34–39.

Hayash, K., Stergiopulos, N., Meister, J.-J., Greenwald, S.E. and Rachev, A. (2001). Techniques in the determination of the mechanical properties and constitutive laws of arterial walls. In C.T. Leondes (Ed.), *Biomechanics Systems Techniques and Applications: Cardiovascular Techniques*, Vol. II. CRC Press.

Haynes, R.H. (1960). Physical basis on dependence of blood viscosity on tube radius. *Am. J. Physiol.,* **198**, 1193-1205.

Hershey, D. and Song, G. (1967). Friction factors and pressure drop for sinusoidal laminar flow of water and blood in rigid tubes. *AIChE Journal,* **13**, 491-496.

Hibiki, T. and Ishii, M. (1999). Experimental study on interfacial area transport in bubbly two-phase flows. *Intl J. of Heat and Mass Transfer,* **42**, 3019–3035.

Hibiki, T. and Ishii, M. (2007). Lift force in bubbly flow systems. *Chem. Eng. Sci.,* **62**, 6457-6474.

Hibiki, T., Ishii, M. and Xiao, Z. (2001). Axial interfacial area transport of vertical bubbly flows. *Intl J. of Heat and Mass Transfer,* **44**, 1869-1888.

Hibiki, T., Situ, R., Mi, Y. and Ishii, M. (2003). Local flow measurements of vertical upward bubbly flow in an annulus. *Intl J. of Heat and Mass Transfer,* **46**, 1479-1496.

Hino, M., Sawamato, M. and Takasu, S. (1976). Experiments on transition to turbulence in an oscillatory pipe flow. *J. Fluid Mech.,* **75**, 93-207.

Holzapfel, G.A., Gasser, T.C. and Stadler, M. (2002). A structural model for the viscoelastic behavior of arterial walls: Continuum formulation and finite element analysis. *Eur. J. Mech. Solid.,* **21**, 441-463.

Huang, C.R., Pan, W.D., Chen, H.Q. and Copley, A.L. (1987a). Thixotropic properties of whole blood. *Biorheology,* **24**, 795-801.

Huang, C.R., Chen, H.Q., Pan, W.D., Shih, T., Kristol, D.S. and Copley, A.L. (1987b). Effects of hematocrit on thixotropic properties of human blood. *Biorheology,* **24**, 803-810.

Huang, J., Lyczkowski, R.W. and Gidaspow, D. (2009). Pulsatile flow in a coronary artery using multiphase kinetic theory. *J Biomech.*, **42**, 743-754.

Huilin, L. and Gidaspow, D. (2003). Hydrodynamics of binary fluidization in a riser: CFD simulation using two granular temperatures. *Chemical Eng. Science,* **58**, 3777-3792.

Hyun, S., Kleinstreuer, C. and Archie, Jr. J.P. (2000a). Hemodynamics analyses of arterial expansions with implications to thrombosis and restenosis. *Med. Eng. Phys.,* **22**, 13-27.

Hyun, S., Kleinstreuer, C. and Archie, J.P. (2000b) Computer simulation and geometric design of endarterectomized carotid artery bifurcations. *Crit. Rev. Biomed. Eng.,* **28**, 53-59.

Hyun, S., Kleinstreuer, C. and Archie, Jr. J.P. (2001). Computational particle hemodynamics analysis and geometric reconstruction after carotid endarterectomy. *Comput. Biol. Med.,* **31**, 365-384.

Ishii, M. and Chawla, T.C. (1979). Local drag laws in dispersed two-phase flow. *Argonne National Laboratory Report*. ANL-79-105 (NUREG/CR-1230).

Ishii, M. and Zuber, N. (1979). Drag coefficient and relative velocity in bubbly, droplet or particulate flows. *AIChE J.,* **25**, 843-855.

Ishii, M. and Hibiki, T. (2006). *Thermo-fluid dynamics of two-phase flow.* New York: Springer.

Janzen, J., Elliott, T.G., Carter, C.J. and Brooks, D.E. (2000). Detection of red cell aggregation by low shear rate viscometry in whole blood with elevated plasma viscosity. *Biorheology,* **37**, 225-237.

Jayasinghe, D.A.P., Letelier, S.M. and Leutheusser, H.J. (1974). Frequency-dependent friction in oscillatory laminar pipe flow. *Internaional Journal of Mechanical Sciences,* **16**, 819-827.

Jeffery, G.B. (1922). The motion of ellipsoidal particles immersed in a viscous fluid. *Proc. Roy. Soc. Lond. A,* **102**, 161-179.

Johnston, B.M. and Johnston P.R. (2007). The relative effects of arterial curvature and lumen diameter on wall shear stress distributions in human right coronary arteries. *Phys. Med. Biol.,* **52**, 2531-2544.

Johnston, B.M., Johnston, P.R., Corney, S. and Kilpatrick, D. (2004). Non-Newtonian blood flow in human right coronary arteries: steady state simulations. *J. Biomech.,* **37**, 709-720.

Joye, D.D. (2003). Shear rate and viscosity corrections for a Casson fluid in cylindrical (Couette) geometries. *J. Colloid Interface Sci.,* **267**, 204-210.

Jung, J. and Hassanein, A. (2008). Three-phase CFD analytical modeling of blood flow. *Med. Eng. Phys.,* **30**, 91-103.

Jung, J., Lyczkowski, R.W., Panchal, C.B. and Hassanein, A. (2006a). Multiphase hemodynamic simulation with pulsatile flow in a coronary artery. *J. Biomech.,* **39**, 2064-2073.

Jung, J., Hassanein, A. and Lyczkowski, R.W. (2006b). Hemodynamic computation using multiphase flowdynamics in a right coronary artery. *Ann. Biomed. Eng.,* **34**, 393-407.

Kalita, P. and Schaefer, R. (2008). Mechanical models of artery walls. *Arch. Comput. Meth. Eng.,* **15**, 1-36.

Kariyasaki, A. (1987). Behavior of a single gas bubble in a liquid flow with a linear velocity profile. *Proceedings of the 1987 ASME/JSME Thermal Engineering Conference*. 261-267.

Kang, I.S. (2002). A microscopic study on the rheological properties of human blood in the low concentration limit. *Korea Aust. Rheol. J.,* **14**, 77–86.

Khanafer, K.M., Bull, J.L. and Berguer, R. (2009). Fluid–structure interaction of turbulent pulsatile flow within a flexible wall axisymmetric aortic aneurysm model. *Eur. J. Mech. B Fluid.,* **28**, 88-102.

Klaseboer, E., Chavaillier, J.P., Mate, A., Masbernat, O. and Gourdon, C. (2001). Model on experiments of drop impinging on an immersed wall. *Phys. Fluids,* **13**, 45-57.

Kleinstreuer, C. (2006). *Biofluid dynamics: Principles and selected applications.* CRC Press.

Kim S., Cho, Y.I., Jeon, A.H., Hogenauer, B. and Kensey, K.R. (2000). A new method for blood viscosity measurement. *J. Non-Newtonian Fluid Mech.,* **94**, 47-56.

Kitano, T., Kataoka, T. and Shirota, T. (1981). An empirical equation of the relative viscosity of polymer melts filled with various inorganic fillers. *Rheol. Acta,* **20**, 207-209.

Kock, S.A. Nygaard, J.V. Eldrup, N. Fründ E-T., Klaerke, A., Paaske, W.P., Falk, E. and Kim, W. (2008). Mechanical stresses in carotid plaques using MRI-based fluid–structure interaction models. *J. Biomech.,* **41**, 1651-1658.

Komori, S. and Kurose, R. (1996). The effects of shear and spin on particle lift and drag in shear flow at high Reynolds numbers. In S. Gavrilakis, L. Machiels and P. Monkewitz (Eds.), *Advances in Turbulence VI,* Kluwer.

Kopacz, A.M., Liu, W.K. and Liu, S.Q. (2008). Simulation and prediction of endothelial cell adhesion modulated by molecular engineering. *Comput. Meth. Appl. Mech. Eng.,* **197**, 2340-2352.

Krieger, I.M. (1972). Rheology of monodisperse lattices. *Adv. Colloid Interface Sci.,* **3**, 111–136.

Krieger, I.M. and Dougherty, T.J. (1959). A mechanism for non-Newtonian flow in suspension of rigid spheres. *T. Soc. Rheol.,* **3**, 137–152.

Ku, D.N., Giddens, D.P., Zarins, C.K. and Glagov, S. (1985). Pulsatile flow and atherosclerosis in the human carotid bifurcation: positive correlation between plaque formation and low oscillating shear stress. *Arteriosclerosis,* **3**, 293-302.

Kulkarni, A.A. (2008). Lift force on bubbles in a bubble column reactor: Experimental analysis. *Chem. Eng. Sci.,* **63**, 1710-1723.

Kumar, A. and Hartland, S. (1985). Gravity settling in liquid-liquid dispersions. *Can. J. Chem. Eng.,* **63**, 368-376.

Kurose, R. and Komori, S., (1999). Drag and lift forces on a rotating sphere in a linear shear flow. *J. Fluid Mech.,* **384**, 183-206.

Leboreiro, J., Joseph, G.G., Hrenya, C.M., Snider, D.M., Banejee, S.S. and Galvin, J.E. (2008). The influence of binary drag laws on simulations of species segregation in gas-fluidized beds. *Powder Technol.,* **184**, 275-290.

Lee, L. and Leveque, R.J. (2003). An immersed interface method for incompressible Navier-Stokes Equations. *SIAM J. Sci. Comput.,* **25**, 832-856.

Lee, S.W. and Steinman, D.A. (2007). On the relative importance of rheology for image-based CFD models of the carotid bifurcation. *J. Biomech. Eng.,* **129**,273-278.

Lee, T.-R., Chang, Y.-S., Choi, J.-B., Kim D.W., Liu, W.K. and Kim, Y.-J. (2008). Immersed finite element method for rigid body motions in the incompressible Navier-Stokes flow. *Comput. Meth. Appl. Mech. Eng.,* **197**, 2305-2316.

Legendre, D. and Magnaudet, J. (1997). A note on the lift force on a spherical bubble or drop in a low-Reynolds-number shear flow. *Physics of Fluids,* **9**, 3572-3574.

Legendre, D. and Magnaudet, J. (1998). The lift force on a spherical bubble in a viscous linear shear flow. *J. Fluid Mech.,* **368**, 81-126.

Lehoux, S., Tronc, F. and Tedgui, A. (2002). Mechanisms of blood flow-induced vascular enlargement. *Biorheology,* **39**, 319-324.

Lei, M., Kleinstreuer, C. and Archie, J.P. (1997). Hemodynamic simulations and computer-aided designs of graft-artery junctions. *J. Biomech. Eng.,* **119**, 343-348.

Leonard, B.P. and Mokhtari, S. (1990). Ultra-sharp nonoscillatory convection schemes for high-speed steady multidimensional flow. NASA TM 1-2568 (ICOMP-90-12), NASA Lewis Research Center.

Leondes, C.T. (Ed.). (2000). *Biomechanical systems: Techniques and applications. Volume IV: Biofluid methods in vascular and pulmonary systems: Techniques and applications: 4.* CRC Press.

Leveque R.J. and Li, Z. (1994). The immersed interface method for elliptic equations with discontinuous coefficients and singular sources. *SIAM J. Numer. Anal.,* **31**, 1019-1044.

Levich, V.G. (1962). *Physicochemical hydrodynamics.* New York: Prentice-Hall.

Lew, H.S. (1969). Formulation of statistical equation of motion of blood. *Biophys. J.,* **9**, 235-245.

Li, Z. and Kleinstreuer, C. (2005). Blood flow and structure interactions in a stented abdominal aortic aneurysm model. *Med. Eng. Phys.,* **27**, 369-382.

Li, Z. and Kleinstreuer, C. (2006). Computational analysis of type II endoleaks in a stented abdominal aortic aneurysm model. *J. Biomech.,* **39**, 2573-2582.

Li, P., Lan, X.Y., Xu, C.M., Wang, G., Lu, C.X. and Gao, J.S. (2009). Drag models for simulating gas–solid flow in the turbulent fluidization of FCC particles. *Particuology,* **7**, 269–277.

Linford, R.G. and Ryan, N.W. (1965). Pulsatile flow in rigid tubes. *Journal of Applied Physiology,* **20**, 1078-1082.

Linke, W. and Hufschmidt, W. (1958). Wärmeübergang bei pulsierender Strömung (Heat transfer in pulsating flow). *Chem. Ing. Techn.,* **30**, 159-165.

Lighthill, M.J. (1956). Drift, *J. Fluid Mech.,* **1**, 31-53.

Liu, T.J. (1993). Bubble size and entrance length effects on void development in a vertical channel. *Intl J. of Heat and Mass Transfer,* **19**, 99-113.

Liu, Y. and Liu, W.K. (2006). Rheology of red blood cell aggregation by computer simulation. *J. Comput. Phys.,* **220**, 139–154.

Liu, Y., Zhang, L., Wang, X. and Liu, W.K. (2004). Coupling of Navier–Stokes equations with protein molecular dynamics and its application to hemodynamics. *Int. J. Numer. Meth. Fluid,* **46**, 1237–52.

Liu, W.K., Liu, Y., Farrell, D., Zhang, L., Wang, X.S., Fukui, Y., Patankar, N., Zhang, Y., Bajaj, C., Lee, J., Hong, J., Chen, X. and Hsu, H. (2006a). Immersed finite element method and its applications to biological systems. *Comput. Meth. Appl. Mech. Eng.,* **195**, 1722-1749.

Liu, W.K., Kim, D.W. and Tang, S. (2006b). Mathematical foundations of the immersed finite element method. *Comput. Mech.,* **39**, 211-222.

Loehrke, R.L. and Nagib, H.M. (1976). Control of free stream turbulence by means of honeycombs: A balance between suppression and generation. *Trans. A.S.M.E, J. Fluids Engng.,* **98**, 342-353.

Long, D.S., Smith, M.L., Pries, A.R., Ley, K. and Damiano, E.R. (2004). Microviscometry reveals reduced blood viscosity and altered shear rate and shear stress profiles in microvessels after hemodilution. *PNAS,* **101**, 10060–10065.

Longest, P.W. and Kleinstreuer, C. (2003). Comparison of blood particle deposition models for non-parallel flow domains. *J. Biomech.,* **36**, 421-430.

Longest, P.W., Kleinstreuer, C. and Buchanan, J.R. (2004). Efficient computation of micro-particle dynamics including wall effects. *Comput. Fluid.,* **33**, 577-601.

Longest, P.W., Kleinstreuer, C. and Deanda, A. (2005). Numerical simulation of wall shear stress and particle-based hemodynamic parameters in pre-cuffed and streamlined end-to-side anastomoses. *Ann. Biomed. Eng.,* **33**, 1752-1766.

Lu, J., Biswas, S. and Tryggvason, G. (2006). A DNS study of laminar bubbly flows in a vertical channel. *Int. J. Multiphase Flow,* **32**, 643–660.

Lundberg, J. and Halvorsen, B.M. (2008). A review of some exsisting drag models describing the interaction between phases in a bubbling fluidized bed. *49th Scandinavian Conference on Simulation and Modeling*. Proceedings SIMS 2008.

Luo, X.Y. and Kuang, Z.B., (1992). A study on the constitutive equation of blood. *J. Biomech.,* **25**, 929-934.

Malek, A.M., Alper, S.L. and Izumo, S. (1999). Hemodynamic shear stress and its role in atherosclerosis. *JAMA,* **282**, 2035-2042.

Malkin, A.Y. (1994). *Rheology fundamentals.* ChemTec Publishing.

Maron, S.H. and Pierce, P.E. (1956). Application of Ree-Eyring generalized flow theory to suspensions of spherical particles. *J. Colloid Interface Sci.,* **11**, 80–95.

Mazumdar, J.N. (1998). *Biofluid mechanics.* World Scientific.

McLaughlin, J.B. (1991). Inertial migration of a small sphere in linear shear flows. *J. Fluid Mech*., **224**, 261-274.

McLaughlin, J.B. (1993). The lift on a small sphere in wall-bounded linear shear flows. *J. Fluid Mech.,* **246**, 249-265.

Mei, R. (1992). An approximate expression for the shear lift force on a spherical particle at finite Reynolds number. *Int. J. Multiphase Flow,* **18**, 145-147.

Meiselman, H.J. and Baskurt, O.K. (2006). Hemorheology and hemodynamics; Dove Andare? *Clin. Hemorheol. Microcirc.,,* **35**, 37-43.

Meiselman, H.J., Neu, B., Rampling, M.W. and Baskurt, O.K. (2007). RBC aggregation: Laboratory data and models. *Indian J. Exp. Biol.,* **45**, 9-17.

Merrill, E.W., Cokelet, G.C., Britten, A. and Wells, R.E. (1963). Non-Newtonian rheology of human blood - Effect of fibrinogen deduced by "subtraction". *Circ. Res.,* **13**, 48-55.

Miyazaki, K., Bedeaux, D. and Avalos, J.B. (1995). Drag on a sphere in a slow shear flow. *J. Fluid Mech.,* **296**, 373-390.

Mooney, M.J. (1951). The viscosity of a concentrated suspension of spherical particles. *J. Colloid Interface Sci.,* **6**, 162–170.

Moore, J.E. Jr, Delfino, A., Doriot, P.-A., Dorsaz P.-A. and Rutishauser, W. (2001). Arterial fluid dynamics: The relationship to atherosclerosis and application in diagnostics. In C.T. Leondes (Ed.), *Biomechanics Systems Techniques and*

Applications: Biofluid Methods in Vascular and Pulmonary Systems, *Vol. IV*. CRC Press.

Morris, C.L., Rucknagel, D.L., Shukla, R., Gruppo, R.A., Smith, C.M. and Blackshear, P. (1989). Evaluation of the yield stress of normal blood as a function of fibrinogen concentration and hematocrit. *Microvasc. Res.,* **37**, 323-338.

Morsi, S.A. and Alexander, A.J. (1972). An investigation of particle trajectories in two-phase flow systems. *J. Fluid Mech.,* **55**, 193-208.

Muto, T. and Nakane, K. (1980). Unsteady flow in circular tube; Velocity distribution of pulsatile flow. *Bulletin of JSME,* **23**, 1990-1996.

Myers, J.G., Moore, J.A., Ojha, M. and Ethier, C.R. (2001). Factors influencing blood flow patterns in the human right coronary artery. *Annals of Biomedical Engineering,* **29**, 109-120.

Myint, W., Hosokawa, S. and Tomiyama, A. (2006). Terminal velocity of single drops in stagnant liquids. *Journal of Fluid Science and Technology,* **1**, 72–81.

Naciri, M.A. (1992). *Contribution à l'étude des forces exercées par un liquide sur une bulle de gaz: portance, masse ajoutée et interactions hydrodynamiques.* PhD Thesis. L'ecole Centrale de Lyon, France.

Nair, P.K., Hellums, J.D. and Olson, J.S. (1989). Prediction of oxygen transport rates in blood flowing in large capillaries. *Microvasc. Res.,* **38**, 269-285.

Nazemi, M. Kleinstreuer, C., Archie, J.P. Jr and Sorrell, F.Y. (1989). Fluid flow and plaque formation in an aortic bifurcation. *J. Biomech. Eng.,* **111**, 316-324.

Neofytou, P. and Tsangaris, S. (2006). Flow effects of blood constitutive equations in 3D models of vascular anomalies. *Int. J. Numer. Meth. Fluid,* **51**, 489-510.

Nichols, W.W. and O'Rourke, M.F. (1998). *McDonald's blood flow in arteries*. London: Arnold.

Nubar, Y. (1971). Blood flow, slip, and viscometry. *Biophys. J.,* **11**, 252-264.

O'Callaghan, S., Walsh, M. and McGloughlin, T., (2006). Numerical modelling of Newtonian and non-Newtonian representation of blood in a distal end-to-side vascular bypass graft anastomosis. *Med. Eng. Phys.,* **28**, 70-74.

Ohmi, M. and Iguchi, M. (1981). Flow pattern and frictional losses in pulsating pipe flow. Part 6: Frictional losses in a laminar flow. *Bulletin of the JSME,* **24**, 1756-1763.

Ohmi, M., Usui, T., Fukawa, M. and Hirasaki, S. (1976). Pressure and velocity distributions in pulsating laminar pipe flow. *Bull. Jpn. Soc. Mech. Eng.,* **19**, 298-306.

Ohmi, M., Iguchi, M. and Usui, T. (1981). Flow pattern and frictional losses in pulsating pipe flow. Part 5: Wall shear stress and flow pattern in a laminar flow. *Bull. Jpn. Soc. Mech. Eng.,* **24**, 75-81.

Ohmi, M., Iguchi, M. and Urahata, I. (1982). Transition to turbulence in a pulsatile pipe flow. Part 1; Wave forms and distribution of pulsatile velocities near transition region. *Bull. Jpn. Soc. Mech. Eng.,* **25**, 182-189.

Ojha, M. (1994). Wall shear stress temporal gradient and anastomotic intimal hyperplasia. *Circ. Res.,* **74**, 1227-1231.

Ookawara, S., Street, D. and Ogawa, K. (2004). Practical application to micro-separator/classifier of the Euler-granular model. *In: International Conference on Multiphase Flow 2004*. Yokohama, Japan.

Ookawara, S., Street, D. and Ogawa, K. (2005). Quantitative prediction of separation efficiency of a micro-separator/classifier by Euler-granular model. *In: A.I.Ch.E. 2005 Spring National Meeting*. Atlanta.

Ookawara, S., Street, D. and Ogawa, K. (2006). Numerical study on development of particle concentration profiles in a curved microchannel. *Chemical Engineering Science,* **61**, 3714-3724.

Ookawara, S., Agrawal, M., Street, D. and Ogawa, K. (2007). Quasi-direct numerical simulation of lift force-induced particle separation in a curved microchannel by use of a macroscopic particle model. *Chemical Engineering Science,* **62**, 2454–2465.

Owens, R.G. (2006). A new microstructure-based constitutive model for human blood. *J. Non-Newtonian Fluid Mech.,* **140**, 57-70.

Pacek, A.W., Nienow, A.W. and Moore, I.P.T. (1994). On the structure of turbulent liquid–liquid dispersed flows in an agitated vessel. *Chem. Eng. Sci.,* **49**, 3485–3498.

Pal, R. (2003). Rheology of concentrated suspensions of deformable elastic particles such as human erythrocytes. *J. Biomech.,* **36**, 981-989.

Pal, R. and Rhodes, E. (1989) Viscosity/concentraton relationships for emulsions. *J. Rheol.,* **33**, 1021–1045.

Pappu, V., Doddi, S.K. and Bagchi, P. (2008). A computational study of leukocyte adhesion and its effect on flow pattern in microvessels. *J. Theor. Biol.,* **254**, 483-498.

Patankar, S.V. (1980). *Numerical heat transfer and fluid flow.* Washington, DC: Hemisphere Publishing Corp.

Pelliccioni, O., Cerrolaza, M. and Herrera, M. (2007). Lattice Boltzmann dynamic simulation of a mechanical heart valve device. *Math. Comput. Simulat.,* **75**, 1-14.

Pelliccioni, O., Cerrolaza, M. and Surós, R. (2008). A biofluid dynamic computer code using the general lattice Boltzmann equation. *Adv. Eng. Software,* **39**, 593-611.

Peskin, C.S. (1972). Flow patterns around heart valves: A numerical method. *J. Comput. Phys.,* **10**, 252-270.

Peskin, C.S. (2002). The immersed boundary method. *Acta Numerica,* **11**, 479-517.

Phillips, R.J., Armstrong, R.C., Brown, R.A., Graham, A.L. and Abbott, J.R. (1992). A constitutive equation for concentrated suspensions that accounts for shear-induced particle migration. *Phys. Fluid.,* **4**, 30–40.

Picart, C., Piau, J-M., Galliard, H. and Carpentier, P. (1998a). Human blood shear yield stress and its hematocrit dependence. *J. Rheol.,* **42**, 1-12.

Picart, C., Piau, J-M., Galliard, H. and Carpentier, P. (1998b). Blood low shear rate rheometry: influence of fibrinogen level and hematocrit on slip and migrational effects. *Biorheology,* **35**, 335-353.

Popel, A.S. and Johnson, P.C. (2005). Microcirculation and hemorheology. *Annu. Rev. Fluid Mech.,* **37**, 43–69.

Poppas, A., Shroff, S.G., Korcarz, C.E., Hibbard, J.U., Berger, D.S., Lindheimer, M.D. and Lang. R.M. (1997). Serial assessment of the cardiovascular system in normal pregnancy: Role of arterial compliance and pulsatile arterial load. *Circulation,* **95**, 2407-2415.

Powell, R.L. (2008). Experimental techniques for multiphase flows. *Phys. Fluids,* **20**, 040605.

Pralhad, R.N. and Schultz, D.H. (1988). Two-layered blood flow through stenosed tubes for different diseases. *Biorheology,* **25**, 715-726.

Qiu, Y. and Tarbell, J.M. (2000). Numerical simulation of pulsatile flow in a compliant curved tube model of a coronary artery. *Journal of Biomechanical Engineering,* **122**, 77-85.

Quarteroni, A., Tuveri, M. and Veneziani, A. (2000). Computational vascular fluid dynamics: problems, models and methods. *Comput. Visual. Sci.,* **2**, 163-197.

Quemada, D. (1977). Rheology of concentrated disperse systems and minimum energy dissipation principle. 1. Viscosity concentration relationship. *Rheol. Acta,* **16**, 82-84.

Quemada, D. (1978a). Rheology of concentrated disperse systems II. A model for non-newtonian shear viscosity in steady flows. *Rheol. Acta,* **17**, 632-642.

Quemada, D. (1978b). Rheology of concentrated disperse systems. III. General features of the proposed non-Newtonian model. Comparison with experimental data. *Rheol. Acta,* **17**, 643-653.

Rajagopal, K.R. and Srinivasa, A.R. (2000). A thermodynamic frame work for rate type fluid models. *J. Non-Newtonian Fluid Mech.,* **88**, 207–227.

Rampling, M.W., Meiselman, H.J., Neub, B. and Baskurt, O.K. (2004). Influence of cell-specific factors on red blood cell aggregation. *Biorheology,* **41**, 91-112.

Rao, M.A. (1999). *Rheology of fluids and semisolid foods: Principles and applications.* Springer-Verlag.

Rappitsch, G., Perktold, K. and Pernkopf, E. (1997). Numerical modeling of shear-dependent mass transfer in large arteries. *International Journal for Numerical Methods in Fluids,* **25**, 847-857.

Reinke, W., Gaehtgens, P. and Johnson, P.C. (1987). Blood viscosity in small tubes: effect of shear rate, aggregation, and sedimentation. *Am. J. Physiol.,* **253**, H540-H547.

Resnick, N., Yahav, H., Shay-Salit, A., Shushy, M., Schubert, S., Zilberman, L.C.M. and Wofovitz, E. (2003). Fluid shear stress and the vascular endothelium: for better and for worse. *Progr. Biophys. Mol. Biol.,* **81**, 177-199.

Richardson, E.G. (1928). The amplitude of sound waves in resonators. *Proceedings of the Physical Society,* **40**, 206-220.

Richardson, E.G. (1933). Über die Viskosität von Emulsionen, *Kolloid-Z,* **65**, 32-37.

Richardson, E.G. and Tyler, E. (1930). The transverse velocity gradient near the mouths of pipes in which an alternating or continuous flow is established. *Proceedings of the Physical Society,* **42**, 1-15.

Rojas, H.A.G. (2007). Numerical implementation of viscoelastic blood flow in a simplified arterial geometry. *Med. Eng. Phys.,* **29**, 491-496.

Rommel, W., Blass, E. and Meon, W. (1992). Plate separators for dispersed liquid–liquid systems: multiphase flow, droplet coalescence, separation performance and design. *Chem. Eng. Sci.,* **47**, 555–564.

Roscoe, R. (1952). The viscosity of suspensions of rigid spheres. *Br. J. Appl. Phys.,* **3**, 267–269.

Rosenhead, L. (1963). *Laminar boundary layers.* Oxford University Press.

Rovedo, C.O., Viollaz, P.E. and Suarez, C. (1991). The effect of pH and temperature on the rheological behavior of Dulce de leche, a typical dairy Argentine product. *J. Dairy Sci.,* **74**, 1497-1502.

Rusche, H. and Issa, R.I. (2000). The effect of voidage on the drag force on particles in dispersed two-phase flow, *Japanese European Two-Phase Flow Meeting*. Tsukuba, Japan.

Saffman, P.G. (1965). The lift force on a small sphere in a slow shear flow. *J. Fluid Mech.,* **22**, 385-400.

Saffman, P.G. (1968). Corrigendum to "The lift on a small sphere in a slow shear flow" *J. Fluid Mech.,* **31**, 624.

Saksono, P.H., Dettmer, W.G. and Peric, D. (2007). An adaptive remeshing strategy for flows with moving boundaries and fluid–structure interaction. *Int. J. Numer. Meth. Eng.,* **71**, 1009-1050.

Sankar, D.S. and Lee, U. (2007). Two-phase non-linear model for the flow through stenosed blood vessels. *Journal of Mechanical Science and Technology,* **21**, 678-689.

Sankaranarayanan, K. and Sundaresan, S. (2002). Lift force in bubbly suspensions. *Chemical Engineering Science,* **57**, 3521-3542.

Schiller, L. and Naumann, Z. (1935). A drag coefficient correlation. *Z. Ver. Deutsch. Ing.,* **77,** 318-320.

Schmid-Schönbein, H. and Wells, R. (1969). Fluid drop-like transition of erythrocytes under shear. *Science,* **165**, 288-291.

Schramm, L.L. (2005). *Emulsions, foams, and suspensions: Fundamentals and applications.* Wiley-VCH.

Scotti, C.M. and Finol, E.A. (2007). Compliant biomechanics of abdominal aortic aneurysms: A fluid–structure interaction study. *Comput. Struct.,* **85**, 1097-1113.

Scotti, C.M., Jimenez, J., Muluk, S.C. and Finol, E.A. (2008). Wall stress and flow dynamics in abdominal aortic aneurysms: finite element analysis vs. fluid–structure interaction. *Comput. Meth. Biomech. Biomed. Eng.,* **11**, 301-322.

Segre, G. and Silberberg, A. (1962a). Behaviour of macroscopic rigid spheres in Poiseuille flow. Part 1. Determination of local concentration by statistical analysis of particle passages through crossed light beams. *J. Fluid Mech.,* **14**, 115-135.

Segre, G. and Silberberg, A. (1962b). Behaviour of macroscopic rigid spheres in Poiseuille flow. Part 2. Experimental results and interpretation. *J. Fluid Mech.,* **14**, 136-157.

Sexl, T. (1930). Uber den von E.G. Richardson entdeckten ‘Annulareffekt’. *Zeitschrift für Physik,* **61**, 349-362.

Sharan, M. and Popel, A.S. (2001). A two-phase model for flow of blood in narrow tubes with increased effective viscosity near the wall. *Biorheology,* **38**, 415-428.

Shew, W.L., Poncet, S. and Pinton, J.F. (2006). Force measurements on rising bubbles. *J. Fluid Mech.,* **569**, 51–60.

Shi X. and Lim, S.P. (2007). A LBM-DLM/FD method for 3D fluid-structure interactions. *J. Comput. Phys.,* **226**, 2028-2043.

Shi, X. and Phan-Thien, N. (2005). Distributed Lagrange multiplier/fictitious domain method in the framework of lattice Boltzmann method for fluid-structure interactions. *J. Comput. Phys.,* **206**, 81-94.

Shin, S., Yang, Y. and Suh, J.S. (2009). Measurement of erythrocyte aggregation in a microchip stirring system by light transmission. *Clin. Hemorheol. Microcirc.,* **41**, 197-207.

Shojima, M., Oshima, M., Takagi, K., Torii, R., Hayakawa, M., Katada, K., Morita, A. and Kirino, T. (2004). Magnitude and role of wall shear stress on cerebral aneurysm, Computational fluid dynamic study of 20 middle cerebral artery aneurysms. *Stroke,* **35**, 2500-2505.

Shukla, J.B., Parihar, R.S. and Gupta, S.P. (1980a). Effects of peripheral layer viscosity on blood flow through the artery with mild stenosis. *Bulletin of Mathematical Biology,* **42**, 797-805.

Shukla, J.B., Parihar, R.S. and Rao, B.R.P. (1980b). Effects of stenosis on non-newtonian flow of the blood in an artery. *Bulletin of Mathematical Biology,* **42**, 283-294.

Sibree, J.O. (1931). The viscosity of emulsions: Part II. *Trans. Faraday Soc.,* **27**, 161-176.

Simonin, C. and Viollet, P.L. (1990). Predictions of an oxygen droplet pulverization in a compressible subsonic coflowing hydrogen flow. *Numerical Methods for Multiphase Flows, FED,* **91**, 65-82.

Skalak, R., Ozkaya, N. and Skalak, T.C. (1989). Biofluid mechanics. *Annual Review of Fluid Mechanics,* **21**, 167-200.

Snabre, P. and Mills, P. (1996). II. Rheology of weakly flocculated suspensions of viscoelastic particles. *J. Phys. III,* **6**, 1835-1855.

Sobieski, W. (2009). Momentum exchange in solid-fluid system modeling with the Eulerian multiphase model. *Drying Technol.,* **27**, 653–671.

Soulis, J.V., Giannoglou, G.D., Papaioannou, V., Parcharidis, G.E. and Louridas, G.E. (2008). Low-density lipoprotein concentration in the normal left coronary artery tree. *Biomedical Engineering On Line,* **7**, 26.

Srivastava, V.P. (1995). Particle-fluid suspension model of blood flow through stenotic vessels with applications, *International Journal of Bio-Medical Computing* **38**, 141-154.

Srivastava, V.P. (1996). Two-phase model of blood flow through stenosed tubes in the presence of a peripheral layer: Applications. *Journal of Biomechanics,* **29**, 1377-1382.

Srivastava, V.P. (2007). A theoretical model for blood flow in small vessels. *Applications and Applied Mathematics,* **2**, 51-65.

Srivastava, V.P. and Saxena, M. (1994). Two-layered model of Casson fluid flow through stenotic blood vessels: Applications to the cardiovascular system. *Journal of Biomechanics,* **27**, 921-928.

Srivastava, L.M. and Srivastava, V.P. (1983). On two-phase model of pulsatile blood flow with entrance effects. *Biorheology,* **20**, 761-777.

Srivastava, V.P. and Srivastava, R. (2009). Particulate suspension blood flow through a narrow catheterized artery. *Computers and Mathematics with Applications,* **58**, 227-238.

Srivastava, L.M., Edemeka, U.E. and Srivastava, V.P. (1994). Particulate suspension blood flow under external body acceleration. *Int. J. Biomed. Comput.,* **37**, 113-129.

Steffe, J.F. (1996). *Rheological methods in food process engineering.* (2nd ed.). Freeman Press.

Steinman, D.A. (2002). Image-based computational fluid dynamics modeling in realistic arterial geometries. *Ann. Biomed. Eng.,* **30**, 483–497.

Steinman, D.A. (2004). Image-based computational fluid dynamics: a new paradigm for monitoring hemodynamics and atherosclerosis. *Curr. Drug Targets Cardiovasc. Haematol. Disord.,* **4**, 183-97.

Steinman, D.A. and Taylor, C.A. (2005). Flow imaging and computing: Large artery hemodynamics. *Ann. Biomed. Eng.,* **33**, 1704-1709.

Steinman, D.A., Vorp, D.A. and Ethier, C.R. (2003). Computational modeling of arterial biomechanics: Insights into pathogenesis and treatment of vascular disease. *J. Vasc. Surg.,* **37**, 1118-1128.

Stewart, F.C. and Lyman, D.J. (2004). Effects of an artery/vascular graft compliance mismatch in protein transport: a numerical model. *Annals of Biomedical Engineering*, **32**, 991-1006.

Stijnen, J.M.A., de Hart, J., Bovendeerd, P.H.M. and van de Vosse, F.N. (2004). Evaluation of a fictitious domain method for predicting dynamic response of mechanical heart valves. *J. Fluid. Struct.,* **19**, 835-850.

Stylianopoulos T. and Barocas, V.H. (2007). Multiscale, structure-based modeling for the elastic mechanical behavior of arterial walls. *J. Biomech. Eng.,* **129**, 611-618.

Sugiura, Y. (1988). A method for analyzing non Newtonian blood viscosity data in low shear rates. *Biorheology,* **25**, 107-112.

Sui, Y., Chew, Y.T., Roy, P. and Low, H.T. (2008). A hybrid method to study flow-induced deformation of three-dimensional capsules. *J. Comput. Phys.,* **227**, 6351-6371.

Sun, C. and Munn, L.L. (2008). Lattice-Boltzmann simulation of blood flow in digitized vessel networks. *Comput. Math. Appl.,* **55**, 1594-1600.

Szymanski, P. (1932). Some exact solutions of the hydrodynamic equation of a viscous fluid in the case of a cylindrical tube. *J. Math. Pure Appl.,* **11**, 67-107.

Takagi, S. and Matsumoto, Y. (1995). Three dimensional calculation of a rising bubble. *In: Proceedings of the Second International Conference on Multiphase Flow*. Kyoto.

Tang, D., Yang, C., Huang, Y. and Ku, D.N. (1999). Wall stress and strain analysis using a three-dimensional thick-wall model with fluid–structure interactions for blood flow in carotid arteries with stenosis. *Comput. Struct.,* **72**, 341-356.

Tang, D., Yang, C., Walker, H., Kobayashi, S. and Ku, D.N. (2002). Simulating cyclic artery compression using a 3D unsteady model with fluid-structure interactions. *Comput. Struct.,* **80**, 1651-1665.

Tang, D., Yang, C., Mondal, S., Liu, F., Canton, G., Hatsukami, T.S. and Yuan, C. (2008). A negative correlation between human carotid atherosclerotic plaque progression and plaque wall stress: In vivo MRI-based 2D/3D FSI models. *J. Biomech.,* **41**, 727-736.

Taylor, G.I. (1932). The viscosity of a fluid containing small drops of another fluid. *Proc. Roy. Soc. Lond. A,* **138**, 41-48.

Tees, D.F.J., Coenen, O. and Goldsmith, H.L. (1993). Interaction forces between red-cells agglutinated by antibody. 4. Time and force dependence of break-up. *Biophys. J.,* **65**, 1318-1334.

Tezduyar, T.E. (2003). Computation of moving boundaries and interfaces and stabilization parameters. *Int. J. Numer. Meth. Fluid.*, **43**, 555-575.

Tezduyar, T.E. and Sathe, S. (2007). Modelling of fluid–structure interactions with the space–time finite elements: Solution techniques. *Int. J. Numer. Meth. Fluid.,* **54**, 855-900.

Tezduyar, T.E., Sathe, S., Cragin, T., Nanna, B., Conklin, B.S., Pausewang, J. and Schwaab, M. (2007). Modeling of fluid–structure interactions with the space–time finite elements: Arterial fluid mechanics, *Int. J. Numer. Meth. Fluid.,* **54**, 901-922.

Tezduyar, T.E., Sathe, S., Schwaab, M. and Conklin, B.S. (2008). Arterial fluid mechanics modeling with the stabilized space–time fluid–structure interaction technique. *Int. J. Numer. Meth. Fluid.,* **57**, 601-629.

Tezduyar, T.E., Schwaab, M. and Sathe, S. (2009). Sequentially-coupled arterial fluid–structure interaction (SCAFSI) technique. *Comput. Meth. Appl. Mech. Eng.*, **198**, 3524-3533.

Tha, S.P. and Goldsmith, H.L. (1986). Interaction forces between red-cells agglutinated by antibody. 1. Theoretical. *Biophys. J.,* **50**, 1109-1116.

Tha, S.P. and Goldsmith, H.L. (1988). Interaction forces between red-cells agglutinated by antibody. 3. Micromanipulation. *Biophys. J.,* **53**, 677-687.

Thomas, D.G. (1965). Transport characteristics of suspension: VIII. A note on the viscosity of Newtonian suspensions of uniform spherical particles. *J. Colloid Interface Sci.,* **20**, 267–277.

Thubrikar, M.J. (2007). *Vascular mechanics and pathology*, Springer-Verlag.

Thurston, G.B. (1972). Viscoelasticity of human blood. *Biophys. J.,* **12**, 1205-1217.

Thurston, G.B. (1979). Rheological parameters for the viscosity, viscoelasticity, and thixotropy of blood. *Biorheology,* **16**, 149-162.

Thurston, G.B. (1989) Plasma release-cell layering theory for blood flow. *Biorheology,* **26**, 199-214.

Thurston, G.B., Henderson, N.M. and Jeng, M. (2004). Effects of erythrocytapheresis transfusion on the viscoelasticity of sickle cell blood. *Clin. Hemorheol. Microcirc.,* **30**, 61-75.

Thurston, G.B. and Henderson, N.M. (2006). Effects of flow geometry on blood viscoelasticity. *Biorheology,* **43**, 729-746.

Toda, K. and Furuse, H. (2006). Extension of Einstein's viscosity equation to that for concentrated dispersions of solutes and particles. *J. Biosci. Bioeng.,* **102**, 524-528.

Tomiyama, A. (2004). Drag, lift and virtual mass forces acting on a single bubble. *Proceedings of the Third International Symposium on Two-phase Flow Modeling and Experimentation.* Pisa, Italy, 22-24.

Tomiyama, A. Tamai, H., Zun I. and Hosokawa, S. (2002). Transverse migration of single bubbles in simple shear flows. *Chemical Engineering Science,* **57**, 1849-1858.

Torii, R., Oshima, M., Kobayashi, T., Takagi, K. and Tezduyar, T.E. (2006a). Fluid–structure interaction modeling of aneurysmal conditions with high and normal blood pressures. *Comput. Mech.,* **38**, 482-490.

Torii, R., Oshima, M., Kobayashi, T., Takagi, K. and Tezduyar, T.E. (2006b). Computer modeling of cardiovascular fluid–structure interactions with the Deforming-Spatial-Domain/Stabilized Space–Time formulation. *Comput. Meth. Appl. Mech. Eng.,* **195**, 1885-1895.

Torii, R., Oshima, M., Kobayashi, T., Takagi, K. and Tezduyar, T.E. (2007). Influence of wall elasticity in patient-specific hemodynamic simulations. *Comput. Fluid.,* **36**, 160-168.

Torii, R., Oshima, M., Kobayashi, T., Takagi, K. and Tezduyar, T.E. (2008). Fluid–structure interaction modeling of a patient-specific cerebral aneurysm: influence of structural modeling. *Comput. Mech.,* **43**, 151-159.

Torii, R., Oshima, M., Kobayashi, T., Takagi, K. and Tezduyar, T.E. (2009). Fluid–structure interaction modeling of blood flow and cerebral aneurysm: Significance of artery and aneurysm shapes. *Comput. Meth. Appl. Mech. Eng.,* **198**, 3613-3621.

Uchida, S. (1956). The pulsating viscous flow superposed on the steady laminar motion of incompressible fluids in a circular pipe. *Z. Angew. Math. Phys.,* **7**, 403-422.

Unsal, B., Ray, S., Durst, F. and Ertunc, O. (2005). Pulsating laminar pipe flows with sinusoidal mass flux variations. *Fluid Dynamics Research,* **37**, 317-333.

Valencia, A. and Solis, F. (2006). Blood flow dynamics and arterial wall interaction in a saccular aneurysm model of the basilar artery. *Comput. Struct.,* **84**, 1326-1337.

Valencia, A. and Villanueva, M. (2006). Unsteady flow and mass transfer in models of stenotic arteries considering fluid-structure interaction. *Int. Comm. Heat Mass Trans.,* **33**, 966-975.

Valencia, A., Zarate, A., Galvez, M. and Badilla, L. (2006). Non-Newtonian blood flow dynamics in a right internal carotid artery with a saccular aneurysm. *Int. J. Numer. Meth. Fluid,* **50**, 751-764.

Valencia, A., Ledermann, D., Rivera, R., Bravo, E. and Galvez, M. (2008). Blood flow dynamics and fluid–structure interaction in patient-specific bifurcating cerebral aneurysms. *Int. J. Numer. Meth. Fluid.,* **58**, 1081-1100.

Van de Vosse, F.N., de Hart, J., van Oijen, C.H.G.A., Bessems, D., Gunther, T.W.M., Segal, A., Wolters, B.J.B.M., Stijnen, J.M.A. and Baaijens, F.P.T. (2003). Finite-element-based computational methods for cardiovascular fluid-structure interaction. *J. Eng. Math.,* **47**, 335-368.

Van Loon, R., Anderson, P.D., De Hart, J. and Baaijens, F.P.T. (2004). A combined fictitious domain/adaptive meshing method for fluid-structure interaction in heart valves. *Int. J. Numer. Method Fluid.,* **46**, 533-544.

Van Loon, R., Anderson, P.D. and Van de Vosse, F.N. (2006). A fluid-structure interaction method with solid-rigid contact for heart valve dynamics. *J. Comp. Phys.,* **217**, 806-823.

Van Loon, R., Anderson, P.D. Van de Vosse, F.N. and Sherwin, S.J. (2007). Comparison of various fluid-structure interaction methods for deformable bodies. *Comput. Struct.,* **85**, 833-843.

Vand, V. (1948). Viscosity of solutions and suspensions. 1. Theory. *J. Phys. Colloid Chem.,* **52**, 277–299.

Vasquez, S.A. and Ivanov, V.A. (2000). A phase coupled method for solving multiphase problems on unstructured meshes. *Proceedings of ASME FEDSM'00: ASME 2000*. Fluids Engineering Division Summer Meeting, Boston, June 2000.

Vejahati, F., Mahinpey, N., Ellis, N. and Nikoo, M.B. (2009). CFD simulation of gas–solid bubbling fluidized bed: A new method for adjusting drag law. *Can. J. Chem. Eng.,* **87**, 19–30.

Vito, R.P. and Dixon, S.A. (2003). Blood vessel constitutive models: 1995-2002. *Annu. Rev. Biomed. Eng.*, **5**, 413-439.

Vocadlo, J.J. (1976). Role of some parameters and effective variables in turbulent slurry flow. *Proceedings of the Hydrotransport 4 Conferenc.* BHRA, Cranfield, U.K., Paper D4, 49–62.

Waite, L. (2005). *Biofluid mechanics in cardiovascular systems.* McGraw-Hill.

Wakaba, L. and Balachandar, S. (2005). History force on a sphere in a weak linear shear flow. *Int. J. Multiphase Flow,* **31**, 996-1014.

Wallis, G.B. (1974). The terminal speed of single drops or bubbles in an infinite medium. *Int. J. Multiphase Flow,* **1**, 491-511.

Wang, X. (2006). From immersed boundary method to immersed continuum method. *Intern. J. Multiscale Comput. Eng.,* **1**, 127-146.

Wang, X.S. (2007). An iterative matrix-free method in implicit immersed boundary/continuum methods. *Comput. Struct.,* **85**, 739-748.

Wang, C.Y. and Bassingthwaighte, J.B. (2003). Blood flow in small curved tubes. *Journal of Biomechanical Engineering,* **125**, 910-913.

Wang, X. and Liu, W.K. (2004). Extended immersed boundary method using FEM and RKPM. *Comput. Meth. Appl. Mech. Eng.,* **193**, 1305-1321.

Wang, X. and Stoltz, J.F. (1994). Characterization of pathological blood with a new rheological relationship. *Clin. Hemorheol.,* **14**, 237–245.

Weiss, J.M., Maruszewski, J.P. and Smith, W.A. (1999). Implicit solution of preconditioned Navier-Stokes equations using algebraic multigrid. *AIAA J.,* **37**, 29-36.

Wen, C. and Yu, Y. (1966). Mechanics of fluidization. *Chem. Eng. Prog. Symp. Ser.,* **62**, 100-110.

Wildemuth, C.R. and Williams, M.C. (1984). Viscosity of suspensions modeled with a shear-dependent maximum packing fraction. *Rheol. Acta,* **23**, 627-635.

Wojnarowski, J. (2001). Numerical study of bileaf heart valves performance. *International Scientific Practical Conference: Efficiency of Engineering Education in XX Century*. Ukraine, Donetsk.

Wolters, B.J.B.M., Rutten, M.C.M., Schurink, G.W., Kose, U., de Hart, J. and van de Vosse, F.N. (2005). A patient-specific computational model of fluid–structure interaction in abdominal aortic aneurysms. *Med. Eng. Phys.,* **27**, 871-883.

Womersley, J.R. (1955). Method for the calculation of velocity, rate of flow and viscous drag in arteries when the pressure gradient is known. *Journal of Physiology,* **127**, 553-563.

Womersley, J.R. (1957). An elastic tube theory of pulse transmission and oscillatory flow in mammalian arteries. *WADC Technical Report.* TR56-614.

Wood, C., Gil, A.J., Hassan, O. and Bonet, J. (2008). A partitioned coupling approach for dynamic fluid-structure interaction with applications to biological membranes. *Int. J. Numer. Meth. Fluid.,* **57**, 555-581.

Wootton, D.M. and Ku, D.N. (1999). Fluid mechanics of vascular systems, diseases, and thrombosis. *Annu. Rev. Biomed. Eng.,* **1**, 299-329.

Xu, S. and Wang, Z.J. (2008). A 3D immersed interface method for fluid-solid interaction. *Comput. Meth. Appl. Mech. Eng.,* **197**, 2068-2086.

Yamaguchi, T., Ishikawa, T., Tsubota, K., Imai, Y., Nakamura, M. and Tomohiro, F. (2006). Computational blood flow analysis - New trends and methods. *J. Biomech. Sci. Eng.,* **1**, 29-50.

Yang, N., Wang, W., Ge, W. and Li, J. (2003). CFD simulation of concurrent-up gas–solid flow in circulating fluidized beds with structure-dependent drag coefficient. *Chem. Eng. J.,* **96**, 71–80.

Yeleswarapu, K.K., Kameneva, M.V., Rajagopal, K.R. and Antaki, J.F. (1998). The flow of blood in tubes: theory and experiment. *Mech. Res. Comm.,* **25**, 257-262.

Yilmaz, F. and Gundogdu, M.Y. (2008). A critical review on blood flow in large arteries; relevance to blood rheology, viscosity models, and physiologic conditions. *Korea Aust. Rheol. J.,* **20**, 197-211.

Yilmaz, F. and Gundogdu, M.Y. (2009). Analysis of conventional drag and lift models for multiphase CFD modeling of blood flow. *Korea Aust. Rheol. J.,* **21**, 161-173.

Yilmaz, F. and Gundogdu, M.Y. (2010). Experimental and computational investigation of velocity field for intermediate region of laminar pulsatile pipe flow. *J. Therm. Sci. Technol.,* **30**, 21-35.

Yilmaz, F., Kutlar, A.I. and Gundogdu, M.Y. (in progress, 2011a). Assessment of different liquid-liquid drag models in a vertical duct flow by using CFD. *Advanced Powder Technology.*

Yilmaz, F., Kutlar, A.I. and Gundogdu, M.Y. (in progress, 2011a). Drag effects on pulsatile blood flow in a right coronary artery by using Eulerian multiphase model. *Korea Aust. Rheol. J.*

Yu, Z. (2005). A DLM/FD method for fluid/flexible-body interactions, *J. Comput. Phys.,* **207**, 1-27.

Yu, Z. and Shao, X. (2007). A direct-forcing fictitious domain method for particulate flows. *J. Comput. Phys.,* **227**, 292-314.

Yu, Z., Shao, X. and Wachs, A. (2006a). A fictitious domain method for particulate flows with heat transfer. *J. Comput. Phys.,* **217**, 424-452.

Yu, Z., Wachs, A. and Peysson, Y. (2006b). Numerical simulation of particle sedimentation in shear thinning fluids with a fictitious domain method. *J. Non-Newtonian Fluid Mech.,* **136**, 126-139.

Zeng, D., Ding, Z., Friedman, M.H. and Ethier, C.R. (2003). Effects of cardiac motion on right coronary artery hemodynamics. *Annals of Biomedical Engineering,* **31**, 420-429.

Zeng, L., Najjar, F., Blachandar, S. and Fischer, P. (2009). Force on a finite-sized particle located close to a wall in a linear shear flow. *Phys. Fluids,* **21**, 033302.

Zhang, L.T. and Gay, M. (2007). Immersed finite element method for fluid-structure interactions. *J. Fluid. Struct.,* **23**, 839-857.

Zhang, L.T. and Gay, M. (2008). Characterizing left atrial appendage functions in sinus rhythm and atrial fibrillation using computational models. *J. Biomech.,* **41**, 2515-2523.

Zhang, W. and Kassab, G.S. (2007). A bilinear stres-strain relationship for arteries. *Biomaterials,* **28**, 1307-1315.

Zhang, J.B. and Kuang, Z.B. (2000). Study on blood constitutive parameters in different blood constitutive equations. *J. Biomech.,* **33**, 355-360.

Zhang, D.Z. and Prosperetti, A. (1994) Averaged equations for inviscid disperse two-phase flow. *J.Fluid Mech.,* **267**, 185-219.

Zhang, L., Gerstenberger, A., Wang, X. and Liu, W.K. (2004). Immersed finite element method. *Comput. Meth. Appl. Mech. Eng.,* **193**, 2051-2067.

Zhang, W., Wanga, C. and Kassab, G.S. (2007a). The mathematical formulation of a generalized Hooke's law for blood vessels. *Biomaterials,* **28**, 3569-3578.

Zhang, J., Johnson, P.C. and Popel, A.S. (2007b). An immersed boundary lattice Boltzmann approach to simulate deformable liquid capsules and its application to microscopic blood flows. *Phys. Biol.,* **4**, 285–295.

Zhang, J., Johnson, P.C. and Popel, A.S. (2008). Red blood cell aggregation and dissociation in shear flows simulated by lattice Boltzmann method. *J. Biomech.,* **41**, 47–55.

Zhao, T., Sanada, K., Kitagawa, A. and Takenaka, T. (1990). Real time measurement for high frequency pulsating flow rate in a pipe. *J. Dyn. Syst. Meas. Contr.,* **112**, 762-768.

Zhu, C. (2000). Kinetics and mechanics of cell adhesion. *J. Biomech.,* **33**, 23-33.

Zielke, W. (1968). Frequency-dependent friction in transient pipe flow. *Journal of Basic Engineering, Transactions of the ASME, Series D,* **90**, 109-115.

Zun, I. (1988). Transition from wall void peaking to core void peaking in turbulent bubbly flow. *Transient Phenomena in Multiphase Flow*. Hemisphere, Washington, 225-245.

Zydney, A.L., Oliver, J.D. and Colton, C.K. (1991). A constitutive equation for the viscosity of stored red blood cell suspensions: Effect of hematocrit, shear rate, and suspending phase. *J. Rheol.,* **35**, 1639-1680.

CURRICULUM VITAE

PERSONAL INFORMATION

Surname, Name: YILMAZ, Fuat
Nationality: Turkish (TC)
Date and Place of Birth: 10 April 1972, Eskişehir
Marital Status: Maried
Phone: +90 545 201 26 69
Fax: +90 342 360 11 04
email: fuatyilmaz@gantep.edu.tr

EDUCATION

Degree	Institution	Year of Graduation
MS	Gaziantep University, Graduate School of Naturel and Applied Sciences	2001
BS	Gaziantep University, Department of Mechanical Engineering	1997
High School	Adana Motor Vocational High School	1989

WORK EXPERIENCE

Year	Place	Enrollment
2005 - Present	Gaziantep University	Engineer
2002 - 2003	1010. Ordnance Base Shop	Project Engineer
1997 - 2000	Gaziantep University	Research Assistant
1997 - 1997	Özçelik Co.	R&D Engineer

FOREIGN LANGUAGES

English

PUBLICATIONS

Science Citation Index Journal Publications

[1]. Yilmaz, F. and Gundogdu, M.Y. (2008). A critical review on blood flow in large arteries; relevance to blood rheology, viscosity models, and physiologic conditions. *Korea Aust. Rheol. J.,* **20**, 197-211.

[2]. Yilmaz, F. and Gundogdu, M.Y. (2009). Analysis of conventional drag and lift models for multiphase CFD modeling of blood flow. *Korea Aust. Rheol. J.,* **21**, 161-173.

[3]. Yilmaz, F. and Gundogdu, M.Y. (2010). Experimental and computational investigation of velocity field for intermediate region of laminar pulsatile pipe flow. *J. Therm. Sci. Technol.,* **30**, 21-35.

HOBBIES

Basketball, chess, music, table tennis.